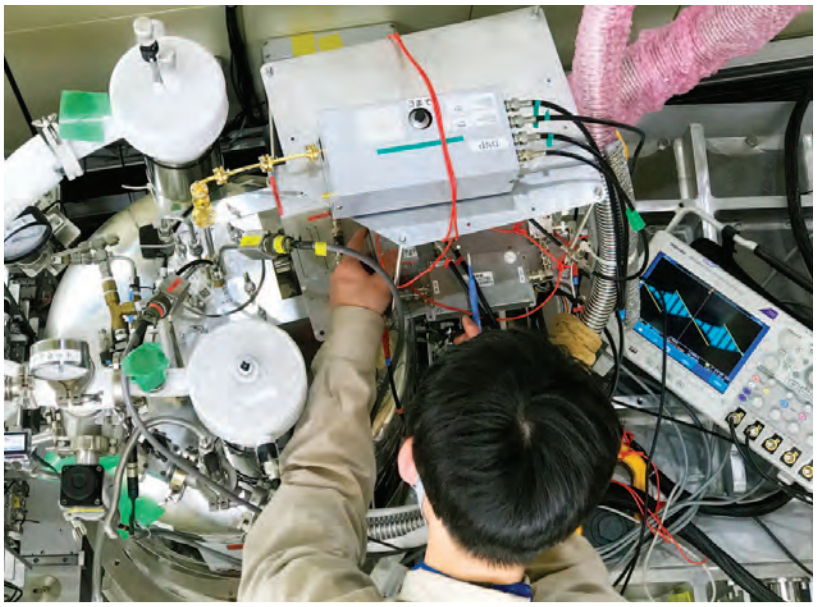

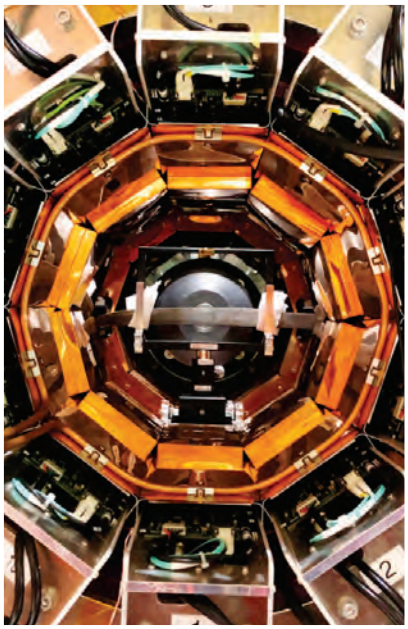

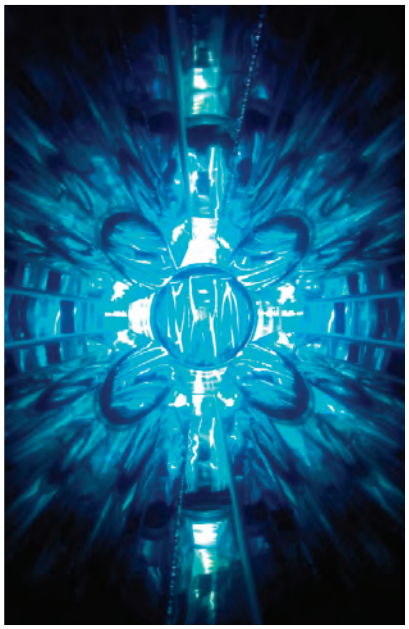

J-PARC

ANNUAL REPORT 2020

Vol.2: Materials and Life Science Experimental Facility

MLF ANNUAL REPORT

Cover photographs

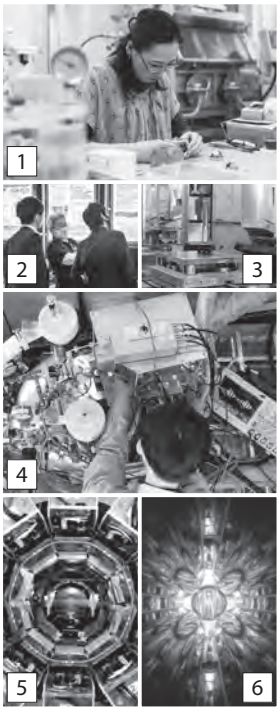

1 : Sample Preparation at BL11 PLANET

2 : Participation at the Japan Analytical & Scientific Instruments Show 2020 Exhibition

3 : Japanese Sword Neutron Imaging Analysis

4 : Dynamic Nuclear Polarization Experiment at BL17 SHARAKU

5 : Muon D1 Spectrometer

6 : Inside of a Floral Shaped Beam Duct

J-PARC MLF
Materials and Life Science Division
J-PARC Center
https://mlfinfo.jp/en

J-PARC was jointly constructed and is now operated by the High Energy Accelerator Research Organization (KEK) and the Japan Atomic Energy Agency (JAEA).

Comprehensive Research Organization for Science and Society
https://neutron.cross.or.jp/en

J-PARC 21-02

Preface

Toshiya Otomo
Division Head of Materials and Life Science Division, MLF

During the COVID-19 pandemic, a state of emergency was officially announced by the Government of Japan on April 14. J-PARC was forced to limit users visits for 47 days and imposed an unscheduled outage for 13 days in FY2020. The difficulties with the users visits affected seriously the user program of the MLF. Because domestic travel was limited and no user could visit the MLF from abroad for experiments, mail-in type experiments were performed with the dedicated support of the MLF staff. We tried to conduct as many experiments as possible in the 2020A period, however, many experiments were carried over to the 2020B period. Consequently, the available beam time to accept new proposals in the 2020B period decreased. 2020B and 2021A were called simultaneously.

Personnel exchange programs, such as AONSA Young Research Fellowship and SAKURA program with ESS, were postponed. Also, the annual meeting of industrial application at the MLF and the Neutron-Muon School were canceled. Meanwhile, Neutron Advisory Committee, Muon Advisory Committee, J-PARC International Advisory Committee, Quantum Beam Science Festa, which is an annual conference mainly for domestic users of MLF J-PARC and IMSS KEK, were held on-line.

The proton power ramp up on the neutron target and instrument upgrades were kept in progress under COVID-19. In fiscal year 2020, the beam operation started with beam power of 500 kW and the beam power was raised to 600 kW on May 18. At the end of the beam operation before the summer outage, high-power operation was maintained for 36.5 hours at 930 kW from June 25 to 27, much longer than the 10.5 hours achieved in 2019. The validity of the system design regarding a stable 1-MW operation was reconfirmed. A new detector module for a time-of-flight Laue single-crystal diffractometer installed in BL18, SENJU, was developed based on scintillator and wavelength-shifting fiber technology. The thickness was reduced to 60% of the original detector. Constructions of the muon beam lines, H-line and S2 area, progressed. Automatic and remote experiment environments of neutron beam lines were implemented to realize efficient experiments under COVID-19.

The Efforts to make the user program successfully under COVID-19 conditions will be continued by discussions with users and sharing know-hows with international facilities.

In the annual report, the research highlights and technical developments in 2020 are described in detail.

Materials and Life Science Division, Japan Proton Accelerator Research Complex
https://mlfinfo.jp/en

Preface

Mitsuhiro Shibayama
Director, CROSS

The Comprehensive Research Organization for Science and Society (CROSS), a partner organization of the Materials and Life Science Experimental Facility (MLF), is honored to release the J-PARC MLF ANNUAL REPORT 2020, which includes sections on Research and Development Highlights, Neutron Source, Neutron Science, Muon Science, and other topics. CROSS is the registered institution of the specific neutron beam facilities of J-PARC, accredited in 2011 by the Government of Japan, it also supports the activities of the MLF. CROSS is involved in operating the user program and running a fair and open proposal selection system for the seven Public Beamlines of the MLF: BL01 4SEASONS, BL02 DNA, BL11 PLANET, BL15 TAIKAN, BL17 SHARAKU, BL18 SENJU, and BL22 RADEN. It provides high-quality user support and promotes facility utilization for both academic and industrial researchers.

In FY2020, the neutron beam at the MLF was stably operated mostly at 500 – 600 kW, which ensured a highly reliable machine opera-tion. However, the COVID-19 pandemic affected the beam schedule, selection schedule, experiment styles, and so on. The neutron beam was shut down for a month from April to May, which was followed by an increase of the numbers of proxy experiments and carry-over experiments to the next beam cycle. The proposal round had to be changed to 2020B + 2021A by unifying 2020B and 2021A. The total numbers of (short term) neutron proposals submitted and accepted in the term of 2020B + 2021A were 400 and 215, respectively, and those for the Public Beamlines were 203 and 98, respectively. Regarding the outcome, 198 scientific papers (excluding proceedings) were published from the MLF in 2020, 75 of which were papers from the Public Beamlines. The details are included in the Research and Development Highlights collected in this volume. The numbers of press releases were 11 from the MLF and 4 from the Public Beamlines. These numbers illustrate the high activities of the Public Beamlines and the MLF, which have been used by a wide range of users from the academia and various industries. The special program for new users "New User Promotion (NUP)", which started in 2016, was also operated in 2020, and 5 NUP neutron users conducted experiments at the MLF. Long-Term Proposals, started in 2017B, continued its successful run in 2020. 24 FTPs (Fast Track Proposal) were accepted in 2020 and most of them were conducted at the three BLs (BL08, BL11, and BL21), that system was extended to seven BLs by adding BL16, BL17, BL18, and BL22.

Regarding public relations, I would like to address the release of a J-PARC MLF pamphlet, which introduces the performance, instru-ment scientists, and highlights of the beamlines, for the convenience of the MLF users. This pamphlet was released in December 2020 and is available through the web (https://mlfinfo.jp/ja/reports/published.html).

I hope this Annual Report would provide useful information about the current status of the MLF operations and recent scientific achievements, the technical R&D reports, and so on. On behalf of CROSS, I sincerely welcome your visit to the MLF.

Neutron Science and Technology Center, Comprehensive Research Organization for Science and Society
https://neutron.cross.or.jp/en

Contents

Research and Development Highlights

Neutron Source

Neutron Science

Muon Science

MLF Safety

MLF Operations in 2020

Organization Chart

Organization Chart of J-PARC Center

- Director, J-PARC Center
  - Deputy Director (JAEA, KEK, Safety)
    - Safety Division
  - Accelerator Division
  - Materials & Life Science Division
    - Neutron Source Section
    - Neutron Science Section
    - Neutron Instrumentation Section
    - Muon Science Section
    - Technology Development Section
  - Particle & Nuclear Physics Division
  - Nuclear Transmutation Division
  - Cryogenics Section
  - Information System Section
  - Administration Division
    - Users Office

Organization Chart of CROSS

CROSS is "Registered Institution for facility Use Promotion" for the public-access neutron beam facilities at J-PARC.

- President
  - CROSS Head Office
  - Research Center for Science and Society
  - Neutron Science and Technology Center
  - Director, Neutron Science and Technology Center
    - Science Coordinators
    - R&D Division
    - Utilization Promotion Division
    - Industrial Collaboration Promotion Division
    - Safety Division
    - Administration Division
  - New Business Creation Division

The Role of CROSS

Under the terms of the legislation that supports the Public Neutron Beam Facility, CROSS is entrusted with specific responsibilities. In practical terms, the core functions of CROSS can be summarized as follows:

- *Proposal Selection and Beamtime Allocation on the Public Beamlines*
- *User Support on the Public Beamlines*
- *Establishment of an Information Resource for Facility Users*
- *Outreach and Facility Utilization Promotion*
- *Contract Beamline Assessment and Selection*

J-PARC Map

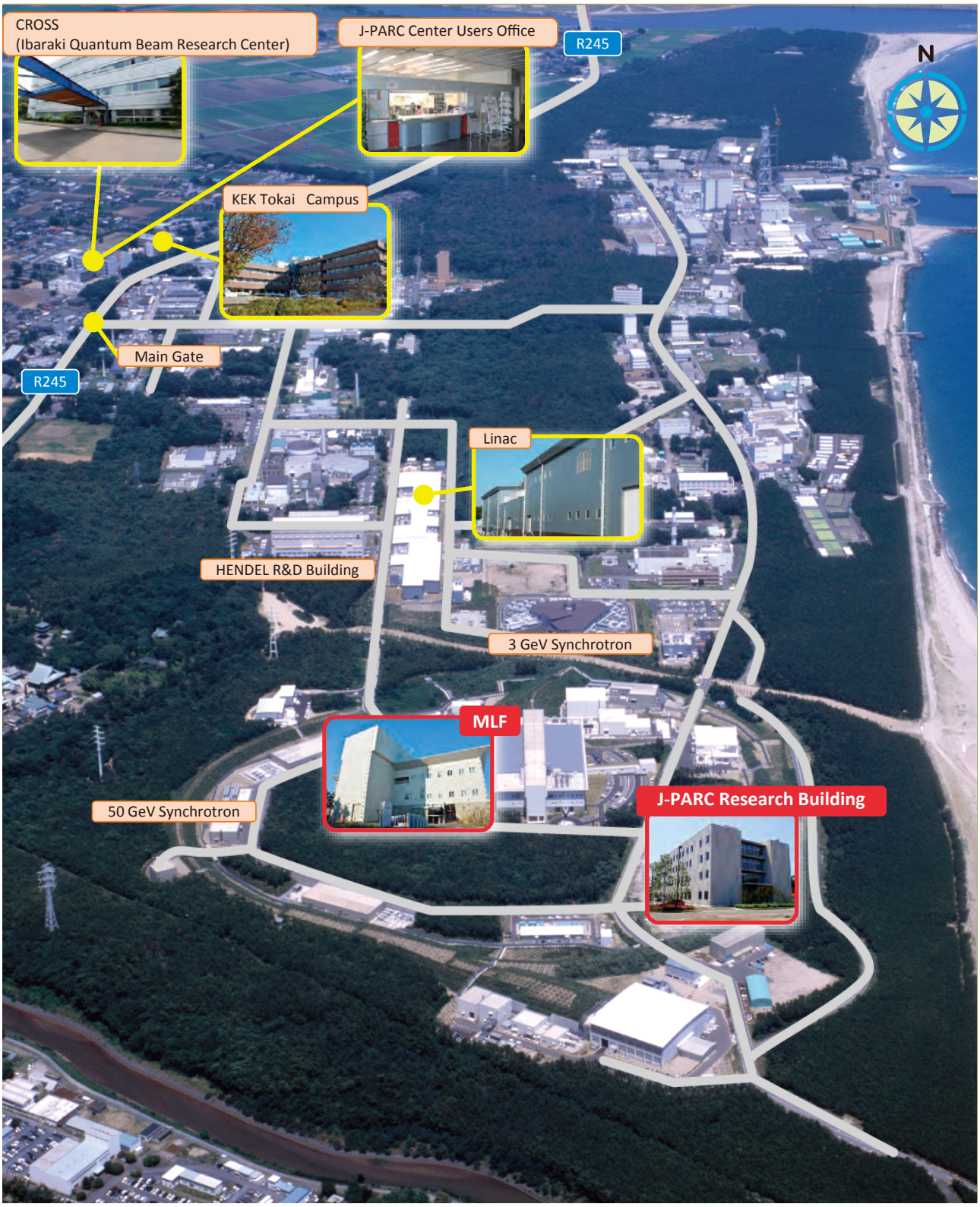
CROSS
(Ibaraki Quantum Beam Research Center)
J-PARC Center Users Office
R245
N
KEK Tokai Campus
Main Gate
R245
Linac
HENDEL R&D Building
3 GeV Synchrotron
MLF
J-PARC Research Building
50 GeV Synchrotron

Muon and Neutron Instruments

Muon Source

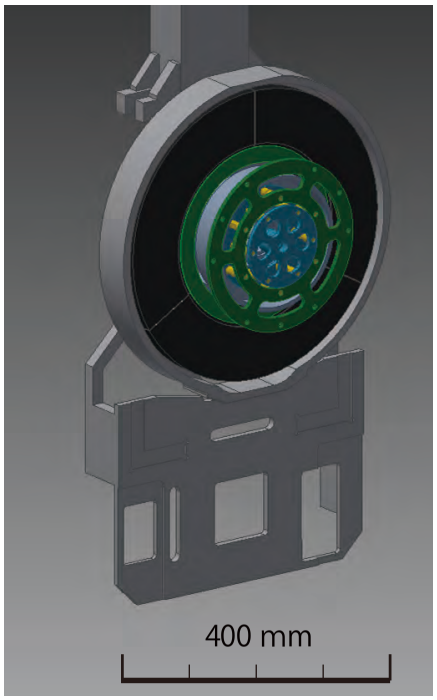

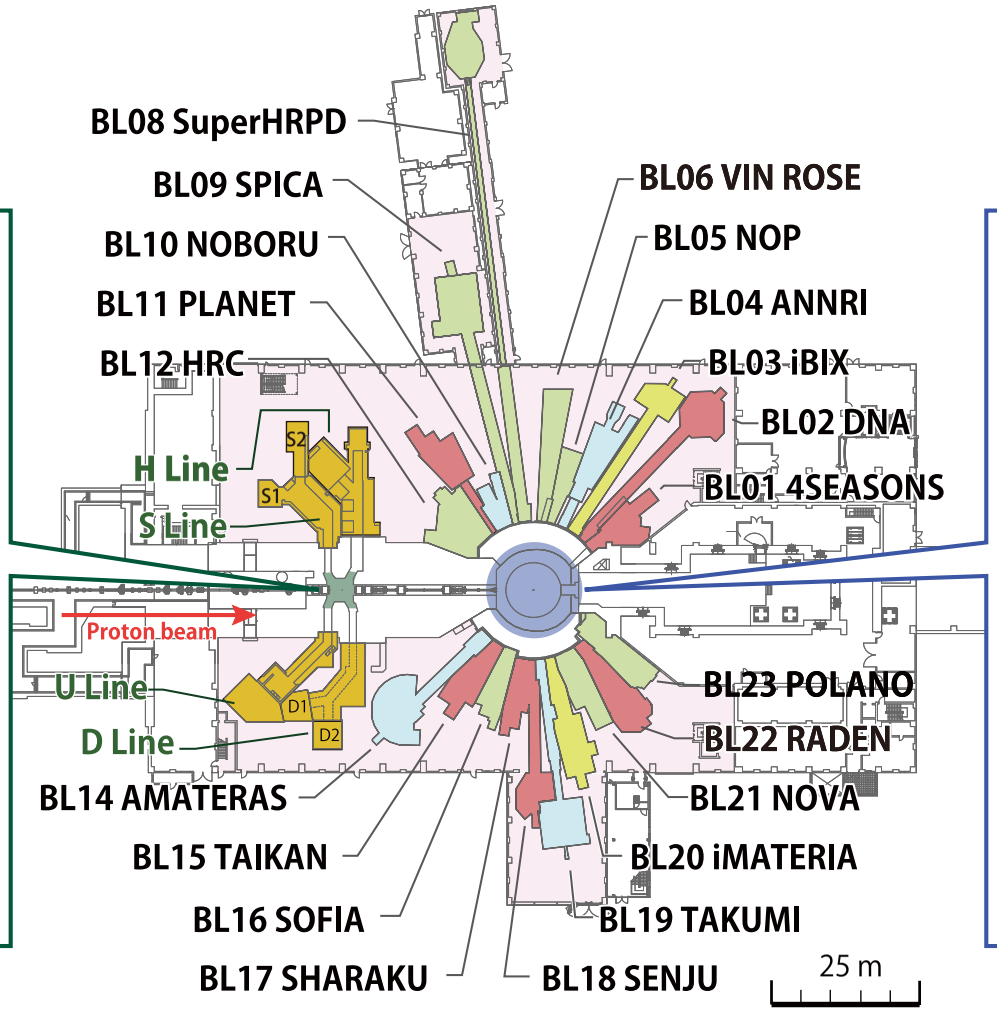

Neutron Source

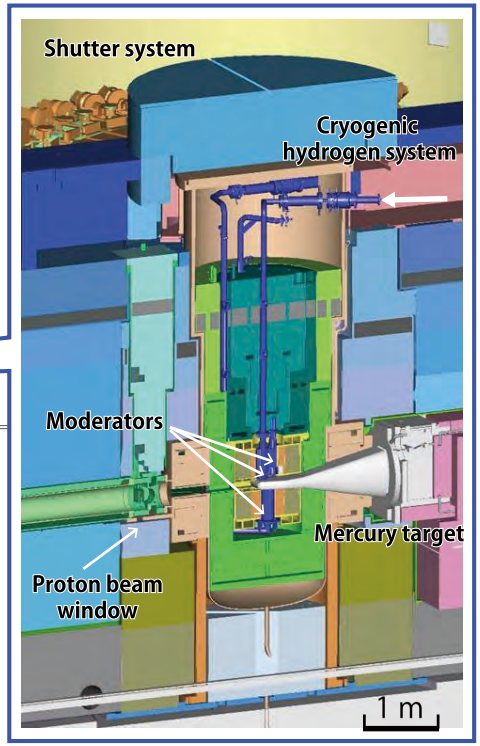

Muon Instruments

Neutron Instruments

JAEA

KEK

Public beam lines

Ibaraki Pref.

As of March 2021

Research and Development Highlights

Hierarchical Magnetic Excitations in $La_{2-x}Sr_xCuO_4$

1. Introduction

The relationship between spin correlations and superconductivity in Mott insulators remains a fascinating issue in condensed matter physics. In the hole-doped $La_{2-x}Sr_xCuO_4$ (LSCO), a magnetic excitation spectrum showing a characteristic shape called "hourglass" excitation in energy(ω)-momentum space is commonly observed in the superconducting phase [1, 2]. The waist energy of hourglass excitations increases with the superconducting transition temperature upon doping, and the shape of the waist becomes unclear in the overdoped region [3]. Thus, the origin of such characteristics is important to be clarified in connection with the mechanism of high-T_c superconductivity. There are theoretical models to reproduce the excitation spectra, such as the stripe model [4], Fermi surface nesting model [5], and the spiral model [6]. However, since the experimental resolution and the observed intensity were insufficient in the previous measurement, distinguishing adequate models was difficult. Using 4SEASONS (BL01), which provides efficient measurements with the multi-E_i method, we corrected high-quality data with sufficient statistics. An analysis based on the two-component model was performed to determine the detailed shape of magnetic excitations [7].

2. Experimental details

Inelastic neutron scattering (INS) experiments were carried out on the optimally-doped (OP) LSCO with x = 0.16. We selected the incident neutron energy of 33.7 meV and 71.1 meV with a chopper frequency of 250 Hz, yielding the energy resolution at the elastic position of 0.8 meV and 2.2 meV, respectively. Compared to the previous measurements, both the signal-to-noise ratio and statistical accuracy of the intensity are much higher in the present measurement [8]. The improvement in the data quality is due to the removal of the background and increase of the sample volume. The high-quality data obtained with better experimental conditions are essential to provide a new aspect in the magnetic excitations.

3. Results and discussion

So far, the low-ω magnetic excitation has been thought to form a hourglass dispersion as the position of the incommensurate (IC) peak gradually approaches (0.5, 0.5) reciprocal position with increasing ω and connects to outwardly dispersive high-ω spin-wave-like excitations. However, conventional analysis of our high-quality data exhibits a discontinuous behavior in incommensurability (δ) against ω in a narrow range around 25 meV (see Fig. 1). This abrupt change of δ is difficult to understand in either the stripe model or the nesting model, suggesting that the existence of only the IC component in the low-ω region is insufficient to reproduce the observed spectra. We, therefore, analyzed the data assuming the superimposition of the IC component with fixed δ and the isotropic commensurate (C) component peaked at (0.5, 0,5). As shown in Fig. 2, this two-component model reproduced the spectral shape very well. It was clarified that with increasing ω, the spectral weight of the IC component weakens toward the previously reported E_{cross} for x = 0.16, whereas the C component gains the intensity at the high-ω regions. The results of the analysis suggested a new perspective on the hourglass excitation. That is, the superposition of two components with a particular intensity balance forms an hourglass-shaped excitation, and E_{cross} corresponds to ω, where the C component becomes dominant with increasing ω.

Furthermore, we found out that the IC component disappears at high temperatures. The thermal evolution of the excitation revealed the persistence of the IC component to the pseudo-gap state [6] in which anisotropic gaps are formed in the electronic system. Such anisotropic gaps could be the origin of the steeply standing IC structure along the ω direction. Therefore, it can be inferred that the IC excitation in the low-ω region is attributed to an electron-hole pair excitation that reflects the topology near the Fermi surface. On the other hand, the C component, which is a part of spin-wave-like excitations expanding up to 300 meV, remains even at

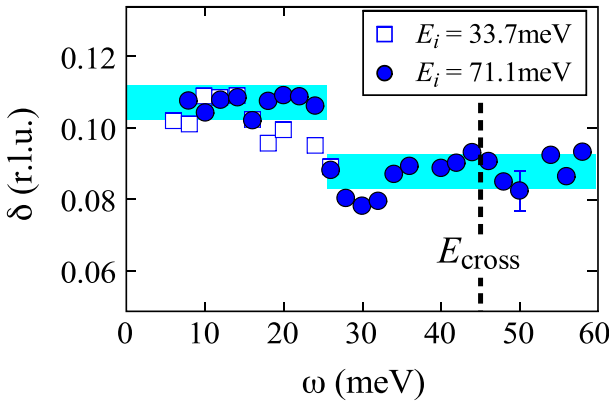

Figure 1. Incommensurability as a function of ω evaluated by assuming only an IC component.

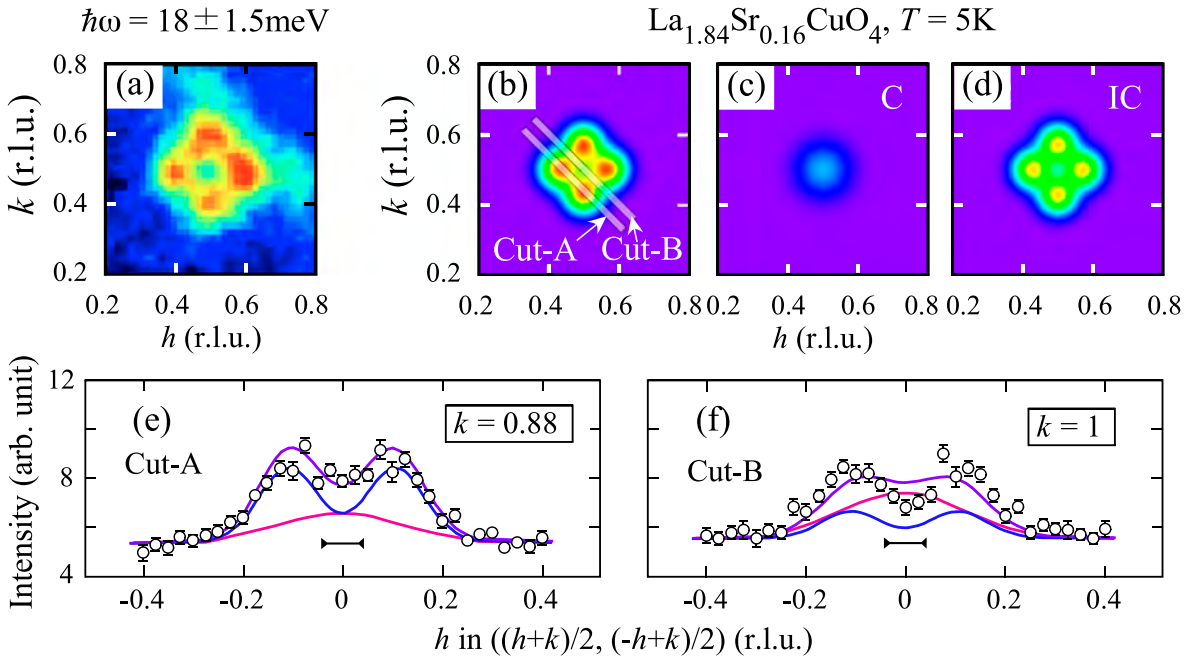

Figure 2. (a) The observed spectra for $La_{2-x}Sr_xCuO_4$ with x = 0.16 at ω = 18 meV. (b) The reproduced spectra based on the two-component model and the individual spectra for (c) the commensurate and (d) incommensurate component. (e), (f) Corresponding spectra along the directions shown in (b).

~300 K without changing the intensity. These features suggest that the C component reflects predominantly the collective mode of localized spins with a large exchange coupling, which exists in the parent material. Therefore, the hourglass excitations seen in the superconductor LSCO are composed of two types of magnetic excitation whose origin is different and has a hierarchical structure against ω. Similar results were obtained for the underdoped LSCO with x = 0.10, in which E_{cross} is ~35 meV.

The itinerant spin nature has been reported from INS measurements for the gapped low-ω excitations in nearly OP single-layer $HgBa_2CuO_{4+y}$ (Hg1201) [9] and OP double-layer $YBa_2Cu_3O_{6+y}$ [10]. Especially, Hg1201 shows a C structure. The variety of the spectral shape supports the strong influence of the structure of the Fermi surface on the low-ω magnetic excitations. By contrast, the outwardly dispersive high-ω excitation is common to copper oxides. This common feature suggests that the localized spin correlation, which robustly remains even after carrier doping, is the driving force of high-temperature superconductivity.

References

[1] J. M. Tranquada et al., Nature **429**, 534 (2004).
[2] B. Vignolle et al., Nat. Phys. **3**, 163 (2007).
[3] O. Lipscombe et al., Phys. Rev. Lett. **102**, 167002 (2009).
[4] M. Vojta and T. Ulbricht, Phys. Rev. Lett. **93**, 127002 (2004).
[5] M. R. Norman, Phys. Rev. B **63**, 092509 (2001) .
[6] Y. A. Kharkov and O. P. Sushkov, Phys. Rev. B **100**, 224510 (2019).
[7] M. Sato et al., J. Phys. Soc. Jpn. **89**, 114703 (2020).
[8] M. Sato et al., JPS. Conf. Proc. **3**, 107010 (2014).
[9] D. Reznik et al, Phys. Rev. B **78**, 132503 (2008).
[10] M. K. Chan et al., Phys. Rev. Lett. **117**, 277002 (2016).

K. Sato[1], K. Ikeuchi[2], R. Kajimoto[3], S. Wakimoto[4], M. Arai[5], and M. Fujita[6]
[1]Department of Science, Tohoku University; [2]Neutron Science and Technology Center, CROSS; [3]Neutron Science Section, Materials and Life Science Division, J-PARC Center; [4]Materials Sciences Research Center, Japan Atomic Energy Agency; [5]European Spallation Source; [6]Institute for Materials Research, Tohoku University

Spin Dynamics of a Magnetic Weyl Semimetal $Sr_{1-x}Mn_{1-y}Sb_2$

1. Introduction

Dirac semimetals are featured by two doubly degenerate linear bands crossing at the Dirac point [1–3]. The low-energy quasiparticle excitations near the Dirac point can be described by the 4 × 4 Dirac equation. Magnetic Dirac semimetals are particularly intriguing as they not only exhibit fascinating phenomena but also offer a platform for investigating the interplay between Dirac fermions and spin dynamics.

In recent years, $Sr_{1-x}Mn_{1-y}Sb_2$ has been suggested to be a prime candidate, where the net ferromagnetic moment induces the time-reversal-symmetry breaking, lifts the degeneracy of the Dirac points, and leads to the magnetic Weyl semimetal state [4]. However, whether and how the topological fermions interplay with the magnons in this particular magnetic Dirac semimetals remains an open question.

2. Topological electronic properties

We first probed the electronic properties of $Sr_{1-x}Mn_{1-y}Sb_2$ by measuring the resistivity and magnetization under an external magnetic field. As shown in Fig. 1(a), the magnetization shows very clear oscillations at moderate fields. In Fig. 1(b), we plotted the in-plane conductivity σ_{xx}, which was converted from the ρ_{xx} and ρ_{xy}, using $\sigma_{xx} = \rho_{xx}/(\rho^2_{xx} + \rho^2_{xy})$. By subtracting the background, we obtained the oscillatory component σ_{xx}, as shown in the inset of Fig. 1(b). These strong de Haas van Alphen (dHvA) and Shubnikov de Hass (SdH) oscillations at moderate magnetic field suggest the high mobility and light effective mass of the carriers.

We have fitted the temperature dependence of the amplitude of ***M***, and the results are shown in Fig. 1(c). We obtained an effective mass of 0.10(3)m_0 for the sample by averaging the results obtained at several fields. We further analyzed the dHvA data with a two-frequency Lifshitz-Kosevich (LK) model, and the results are shown in Fig. 1(d). From the LK fit, we obtained the Berry phase of 0.3π and π corresponding to the bands of 73.2 and 57.2 T, respectively. These strongly indicate that the band structure is topologically nontrivial.

3. INS spectra

By performing inelastic neutron scattering (INS) measurements on high-quality single crystals of $Sr_{1-x}Mn_{1-y}Sb_2$ on 4SEASONS of J-PARC [Figs. 2(a) and (b)] and MERLIN of ISIS [Figs. 2(c) and (d)], we obtained comprehensive spectra that revealed the spin dynamics

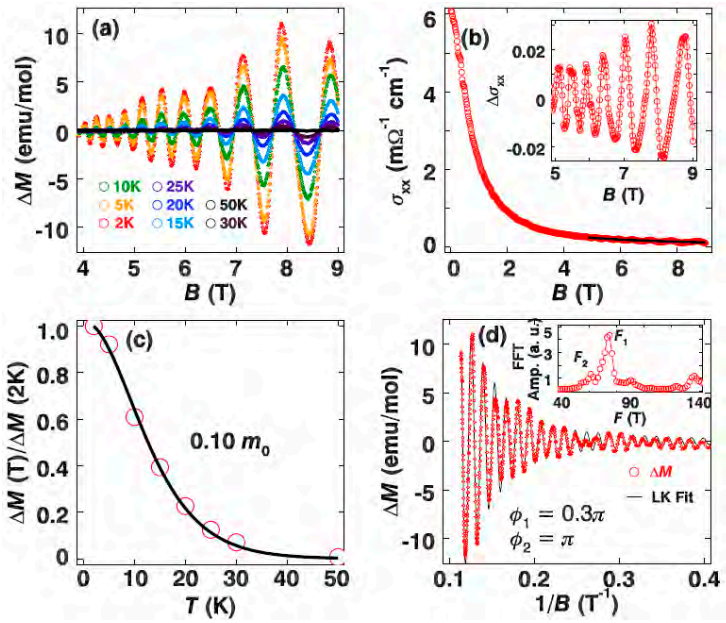

Figure 1. (a) Oscillatory component of the magnetization (ΔM) by subtracting the background at various temperatures. (b) Magnetic-field dependence of the in-plane conductivity (σ_{xx}). The solid line indicates the smooth background. The inset is the oscillatory component ($\Delta\sigma_{xx}$) by subtracting the smooth background. (c) Temperature dependence of the oscillatory amplitude, normalized by ΔM at 2K. The solid line through data is the fit. (d) ΔM at 2K plotted as a function of 1/B. The inset shows the fast Fourier transform spectra of ΔM which show two oscillating frequencies. The solid line is the fit to ΔM with a two-frequency Lifshitz-Kosevich formula.

of the material.

In Figs. 2(a) and (b), we present magnetic dispersions along two high-symmetry directions of [100] and [110], respectively, measured with an incident energy E_i of 100.1 meV at 6K. Along the [100] direction, the excitation spectra disperse from the antiferromagnetic ordering wavevector (1, 0, 0) and reach the band top at about 76 meV at (0.5, 0, 0) and (−1.5, 0, 0) [Fig. 2(a)]. Note that the (1, 0, 0) peak is structurally forbidden, and only appears below the antiferromagnetic transition temperature T_N of 304K, so these excitations are not contributed by phonons but are purely magnetic. The weak spectral weight for wave vectors ***Q***s ranging from (−0.5, 0, 0) to (0.5, 0, 0) is due to the small magnetic structure factor.

The signal at the point with $H = 0$ is expected to be weak due to the antiferromagnetic structure [4]. The spin waves remain well defined up to about 70 meV. Along the [110] direction, the band top is reduced to about 50 meV, as shown in Fig. 2(b), indicating the strong anisotropy within the *a*-*b* plane. The dispersion shows a local minimum at (−0.5, 0.5, 0). To probe the low-energy excitations, we used an E_i of 16 meV, and the obtained dispersion along the [100] direction is shown in Fig. 2(c). The dispersion in the left panel of Fig. 2(c) clearly shows a spin gap of 6 meV. The gap is also evident from the cut at (100) along the energy axis [right panel of Fig. 2(c)]. In Fig. 2(d), we plot the dispersion along the [001] direction. The out-of-plane dispersion also exhibits a clear spin gap at 6 meV, and the total band width is about 5 meV, an order of magnitude smaller than those in the plane shown in Figs. 2(a) and (b), consistent with the quasi-two-dimensional crystal structure of this material. These spin-wave excitations remain well defined at high energies, distinct from some iron-based superconductors where the high-energy excitations are strongly damped and the spin waves decay into a Stoner continuum

The INS spectra can be well described by a localized Heisenberg model with $SJ_1 \sim 28.0$ meV, $SJ_2 \sim 9.3$ meV, $SJ_c \sim -0.1$ meV and $SD \sim -0.07$ meV, with no effect from the topological Weyl electrons as revealed by our transport results.

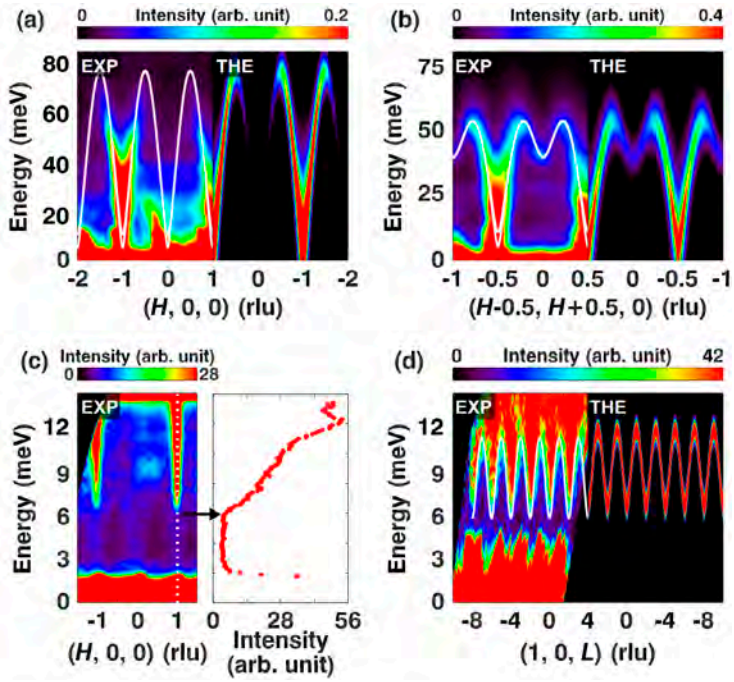

Figure 2. Magnetic dispersions of $Sr_{1-x}Mn_{1-y}Sb_2$ measured at 6K together with the theoretical calculation results. (a, b) Dispersions along the [100] and [110] directions, respectively, obtained on 4SEASONS with $E_i = 100.1$ meV. (c, d) Dispersions along the [100] and [001] directions obtained on MERLIN with $E_i = 16$ meV. Panel (c) focuses on the low-energy part of (a) to show the spin gap. In panels (a), (b), and (d), solid lines are the calculated dispersions. The calculated dispersions with intensities are shown on the right-hand side of each panel to be compared with the experimental data on the left-hand side. Data in (a) and (c) were integrated with K = [−0.2, 0.2] rlu, and all available Ls; data in (b) with a thickness of 0.1 rlu about each momentum along the [−110] direction; data in (d) with H = [0.8, 1.2] rlu, and K = [−0.2, 0.2] rlu. The dashed line in (c) illustrates an energy scan at (100). The scan profile is plotted on the right-hand side with the energy and intensity being the y and x axis, respectively. The arrow indicates the gap value. In (d), the low-energy part below about 4.5 meV is due to the Bragg peaks and some spurious signals, and the broad experimental data can be reproduced by spin-wave calculations convoluting the instrumental resolution.

4. Discussions and conclusions

In $Sr_{1-x}Mn_{1-y}Sb_2$, the magnetic excitations are resulting from the local moments in the Mn layers, whereas the itinerant electrons are contributed by the Sb layers, which are separated from the former [4-8]. The material has a quasi-two-dimensional structure with a large *c*-axis constant of 23.1359 Å. The large SdH oscillation amplitude also indicates that the electronic structure for $Sr_{1-x}Mn_{1-y}Sb_2$ is two-dimensional like. Furthermore, the spin-wave spectra indicate that the magnons are quasi-two-dimensional as well. Our fitting indicates that SJ_1 and SJ_2 are 28.0 and 9.27 meV, respectively, while J_c is only −0.10 meV, two orders of magnitude smaller. Taking these into account, it is not surprising that we did not observe the effect of the itinerant electrons on the spin dynamics.

To conclude, while our electrical transport and magnetization measurements indicate that $Sr_{1-x}Mn_{1-y}Sb_2$ is a topological semimetal, our INS data reveal well-defined spin waves resulting from the Mn local moments, which can be nicely described using a Hamiltonian including SJ_1 ~ 28.0 meV, SJ_2 ~ 9.3 meV, SJ_c ~ −0.1 meV, and SD ~ −0.07 meV. Our results suggest that the topological fermions do not impact the magnons. We propose this to be due to the separated layers of the localized spins and itinerant carriers and the weak interlayer coupling.

References

[1] N. P. Armitage et al., Rev. Mod. Phys., **90** 015001 (2018).
[2] T. O. Wehing et al., Dirac material, Adv. Phys., **63** 1 (2014).
[3] O. Vafek and A. Vishwanath, Annu. Rev. Condens. Matter Phys., **5** 83 (2014).
[4] J. Y. Liu et al., Nat. Mater., **16** 905 (2017).
[5] J. Park et al., Phys. Rev. Lett., **107** 126402 (2011).
[6] M. C. Rahn et al., Phys. Rev. B, **95** 134405 (2017).
[7] J. R. Soh et al., Phys. Rev. B, **100** 144431 (2019).
[8] M. A. Farhan et al., J. Phys.: Condes. Matter, **26** 042201 (2014).

Zhengwei Cai[1], Song Bao[1], Wei Wang[1], Zhen Ma[1], Zhao-Yang Dong[2], Yanyan Shangguan[1], Jinghui Wang[1], Kejing Ran[1], Shichao Li[1], Kazuya Kamazawa[3], Mitsutaka Nakamura[4], Devashibhai Adroja[5], Shun-Li Yu[1], Jian-Xin Li[1], and Jinsheng Wen[1]

[1]National Laboratory of Solid State Microstructures and Department of Physics, Nanjing University; [2]Department of Applied Physics, Nanjing University of Science and Technology; [3]Neutron Science and Technology Center, CROSS; [4]Technology Development Section, Materials and Life Science Division, J-PARC Center; [5]ISIS Facility, Rutherford Appleton Laboratory

Magnetism Induced by Interlayer Electrons in the Quasi-Two-Dimensional Electride Y_2C

1. Introduction

The electride is a special type of ionic crystal in which electrons serve as anions. In contrast to the nearly free electrons in a metal, the anionic electrons in electrides are loosely bound at the interstitial spaces, which leads to the unique physical properties of electrides. A low work function in electrides, especially provides a fertile field of applications, such as electron injection layers in organic light-emitting diodes and catalysts for ammonia synthesis [1].

Y_2C is a quasi-two-dimensional electride. As shown in Fig. 1, Y_2C exhibits the anti-$CdCl_2$ type structure with the space group R-3m. The standard valence states of Y and C are Y^{3+} and C^{4-}, respectively; therefore, there are two excess electrons per formula unit to preserve the charge neutrality. Density functional theory (DFT) calculations [2] and angle-resolved photoemission spectroscopy [3] have established that these excess electrons in Y_2C are mostly confined to the interlayers of $[Y_2C]^{2+}$ as anionic electrons, and that the anionic *s*-like orbitals hybridize with the Y 4*d* orbitals to form 'electride bands' at the Fermi level.

Magnetism arising from the anionic electrons has been a fundamental issue since the discovery of electrides in the 1980s. Among the reported electrides, Y_2C exhibits unusual magnetic features. For example, although the magnetic susceptibility of Y_2C has Curie-Weiss-like temperature dependence, the effective magnetic moments are highly sample dependent. Moreover, the estimated Weiss temperatures are negative, as is the case with antiferromagnets, which stands in sharp contrast with the prediction of the DFT calculations that Y_2C is a weak itinerant ferromagnet. More importantly, which one is the magnetic moment carrier, anionic electrons or Y 4*d* electrons?

In order to investigate the unusual magnetism of Y_2C, we performed inelastic neutron scattering experiments [4].

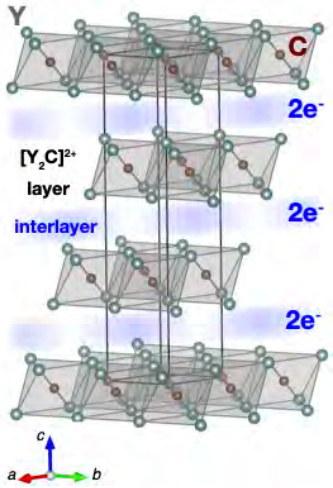

Figure 1. Crystal structure of Y_2C and schematics of an anionic electron layer [4].

2. Experiments

A polycrystalline sample of Y_2C was synthesized by an arc melting method. A 2.2 g polycrystalline ingot was clamped to an Al plate and sealed in an Al sample cell with He gas. The inelastic neutron scattering measurement was performed by the time-of-flight method using a near-backscattering spectrometer with high energy resolution, DNA, installed at BL02 in the MLF, J-PARC. To survey the range of energy transfer (E) up to 1 meV while maintaining the high energy resolution (ΔE ~ 3.6 μeV) and high signal-to-noise ratio (ca. 10^5) of DNA, five phases of a pulse shaping chopper were employed. The intensities were normalized to absolute units with incoherent scatterings after background subtraction.

3. Results and discussion

We observed weak but clear magnetic scattering around Q ~ 0 at both 7 and 120 K, while no magnetic order was observed down to 7 K. These results indicate that the observed scattering comes from ferromagnetic spin fluctuations rather than spin waves in the ferromagnet. Figure 2(a) shows the E dependence of the scattering function $S(Q, E)$ for different values of the momentum transfer Q at 7 K. The observed $S(Q, E)$ are well fitted by the conventional function to describe the paramagnetic state of itinerant electrons (see Ref. [4] for more details).

In the nearly ferromagnetic metal, where spin fluctuations with small $|Q|$ and E are dominant, an inverse lifetime of spin fluctuation Γ_Q, which is contained in the above function, is proportional to $|Q|(Q^2+\kappa^2)$, where κ is the inverse correlation length. On the other hand, in the case of a localized moment (Heisenberg) system, Γ_Q in the paramagnetic phase is often proportional to $Q^2(Q^2+\kappa^2)$. We found that the proportionality of Γ_Q to $|Q|(Q^2+\kappa^2)$ (Fig. 2(b)) is more plausible than that of

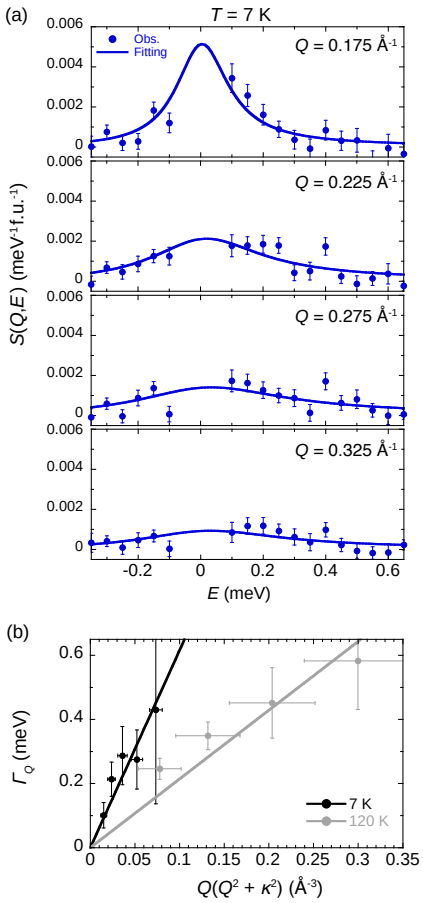

Figure 2. (a) E dependence of $S(Q, E)$ at 7 K. The elastic components between $E \pm 0.05$ meV are masked. (b) Γ_Q as a function of $Q(Q^2+\kappa^2)$ [4].

$Q^2(Q^2+\kappa^2)$. Therefore, we concluded that Y_2C is a nearly ferromagnetic metal.

Figure 3 shows the estimated Q dependence of the squared magnetic form factor, which is determined from the relative magnitude of the magnetic scattering intensity around the 003 Bragg point ($Q \sim 1.05$ Å^{-1}). The magnetic form factor in Y_2C decays faster than that of a 4*d* electron in a single Y atom. This result provides direct experimental evidence that the magnetism in Y_2C does not originate from Y 4*d* electrons, but the anionic electrons in the interlayers.

As we have shown, the magnetic moments are carried by anionic electrons with substantial spatial extension (itinerancy); therefore, it is natural to invoke the mode-coupling effect of spin fluctuations as the origin, as described by the self-consistent-renormalization

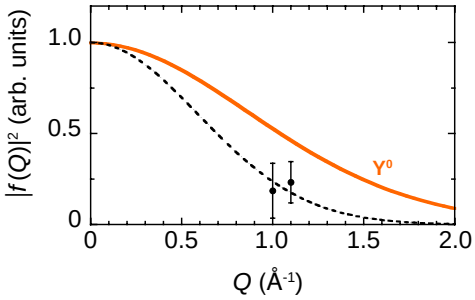

Figure 3. Estimate of the squared magnetic form factor. For comparison, the magnetization distribution of a 4*d* electron in a single Y atom is also shown (orange curve). A dotted line is a guide for the eyes [4].

(SCR) theory [5]. In the case where the parameters of the system do not reach the so-called Stoner condition for ferromagnetism, the ground state remains paramagnetic. In such a case, being close to the ferromagnetic ground state, $1/\chi(T)$ in the SCR theory increases almost linearly with T at high temperature, which appears like the Curie-Weiss law with a negative value for the apparent Weiss temperature [5]. This theoretical consequence is in approximate agreement with the reported property of Y_2C.

4. Conclusion

We performed the inelastic neutron scattering experiments to investigate the unusual magnetism in polycrystalline Y_2C. Ferromagnetic spin fluctuations were successfully observed over a wide temperature range. Our analyses of the dynamical susceptibility and the magnetic form factor demonstrated that Y_2C is a nearly ferromagnetic metal, and the magnetism in Y_2C originates from anionic electrons in the interstitial sites, rather than from Y 4*d* electrons. The Curie-Weiss-like behavior of the magnetic susceptibility is ascribed to the mode coupling effect as described by the SCR theory.

References

[1] C. Liu, et al., J. Mater. Chem. C, **8** 10551 (2020).
[2] T. Inoshita, et al., Phys. Rev. B, **92** 201109(R) (2015).
[3] K. Horiba, et al., Phys. Rev. B, **96** 045101 (2017).
[4] H. Tamatsukuri, et al., Phys. Rev. B, **102** 224406 (2020).
[5] T. Moriya, *Spin Fluctuations in Itinerant Electron Magnetism* (Springer-Verlag, Berlin, 1985).

H. Tamatsukuri[1,*], Y. Murakami[1,2], Y. Kuramoto[1], H. Sagayama[1], M. Matsuura[3], Y. Kawakita[4], S. Matsuishi[2], Y. Washio[2], T. Inoshita[2,5], N. Hamada[6], and H. Hosono[2]

[1]*Condenced Matter Research Center and Photon Factory, Institute of Materials Structure Science, KEK;* [2]*Materials Research Center for Element Strategy, Tokyo Institute of Technology;* [3]*Neutron Science and Technology Center, CROSS;* [4]*Neutron Science Section, Materials and Life Science Division, J-PARC Center;* [5]*National Institute for Materials Science;* [6]*Faculty of Science and Technology, Tokyo University of Science;* [*]*Present affiliation: Neutron Science Section, Materials and Life Science Division, J-PARC Center*

Dynamics of Proteins with Different Structure in Solution Studied by Quasielastic Neutron Scattering

1. Introduction

Under physiological condition (solution state), proteins are not fixed to certain configurations. In other words, there is protein internal dynamics (internal dynamics) [1], which could be deeply relevant to the development of their own functions. Hence, the clarification of this internal dynamics is indispensable for unveiling the mechanism of their functions. It should be noted that hydrogen (H) atoms are uniformly distributed in protein; it is possible to determine the internal dynamics from H atoms in it through incoherent quasielastic neutron scattering (QENS). We then apply QENS to two proteins with different molecular architecture to study their internal dynamics. One is globular domain protein (GDP) and the other is intrinsically disordered protein (IDP). Through the characterizations of their internal dynamics, we can elucidate their origin.

2. Experimental

As examples of GDP and IDP, we selected MurD [2] and the intrinsically disordered region of helicase-associated endonuclease for fork-structured DNS (Hef-IDR) [3]. Both samples were prepared in D_2O buffer in order to suppress the scattering from the buffer. Protein solutions of MurD and Hef-IDR (52.0 and 8.0 mg/mL, respectively) were prepared for the present study. The QENS measurements were performed using an inverted geometry time-of-flight spectrometer (BL02 DNA) [4] installed at the Materials and Life Science Experimental Facility (MLF) in J-PARC, Tokai, Japan. The magnitude of the scattering vector Q ($Q = 4\pi\sin\theta/\lambda_f$, where 2θ and λ_f, = 6.26 Å are the scattering angle and the wavelength of the analyzed neutron, respectively) ranged from 0.12 to 1.78 Å^{-1}. From the measurement of vanadium, the resolution function was determined and the energy resolution (δE) was calculated to be 12 μeV. The measurements were performed at 298 K.

3. Results and discussion

Figure 1 shows the dynamics scattering laws ($S(Q, \omega)$) from the MurD and Hef-IDR solutions, respectively. Compared to the resolution function, the spectra from both samples broadened, meaning that the dynamics within the present temporal and spatial scales was detected. It was determined that the observed $S(Q, \omega)$ consisted of approximately three representative dynamics, translational diffusion, rotational diffusion and internal dynamic. Namely, we took into consideration the contribution of translational diffusion and rotational diffusion to the observed $S(Q, \omega)$. For this purpose, we had to obtain the translational diffusion (D_t) and rotational diffusion (D_r) constants through an appropriate procedure. Then, we performed small-angle X-ray scattering (SAXS) measurements on both samples to solve their structures in solution. Thanks to the assistance of recent state-of-the art computational approaches [5, 6], the solution structures of both samples were solved. Utilizing such solved solution structures, D_t and D_r values were computed utilizing the software "HYDROPRO" [7]. Following the procedures proposed by Pérez et al. [8], we computed the $S(Q, \omega)$ originating from the translational and rotational diffusions, as shown by green lines in Fig. 1. It is clearly seen that only the contribution of the translational and rotational diffusions could not reproduce the observed $S(Q, \omega)$, meaning the detection

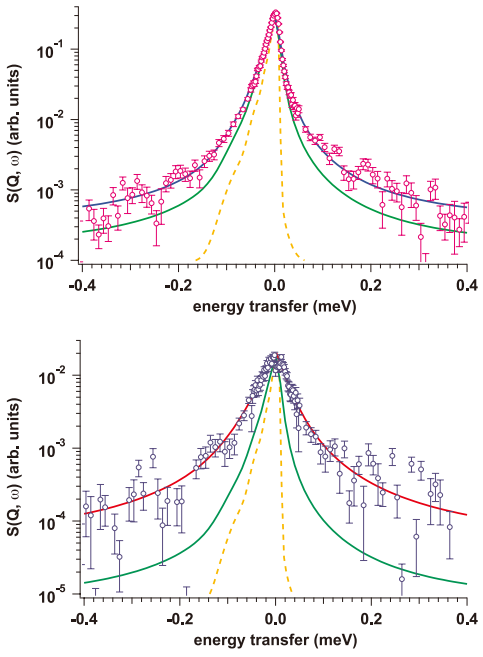

Figure 1. (a) Pink circles show $S(Q, \omega)$ of MurD at Q =1.0 Å^{-1}. Broken orange, solid green and solid blue lines correspond to the resolution function, $S(Q, \omega)$ originating from the translational and rotational diffusion and curve fit with model function [9], respectively. (b) Blue circles show the experimental $S(Q, \omega)$ of Hef-IDR at Q =1.0 Å^{-1}. Broken orange, solid green, and solid red lines correspond to the resolution function, $S(Q, \omega)$ originating from the translational and rotational diffusion and curve match the model function [9], respectively.

of internal dynamics of both samples. Referring to the work by Sarter et al. [9], we then adopted the model function, which included the contribution of the translational diffusion, rotational diffusion and internal dynamic in order to reproduce the observed $S(Q, \omega)$ from both samples. The details of this model function have been covered in our paper [10]. The pink and blue lines in Fig. 1 show how the results matched our model function for MurD and Hef-IDR, respectively, indicating that both $S(Q, \omega)$s were correctly described by this function. From the results of the match with the model function, two parameters: relaxation rate (Γ) and elastic incoherent structure factor ($A(Q)$) were obtained. Figure 2 (a) shows the Q^2 dependence of Γ values from both samples. In agreement with our expectations, the Γ-values of Hef-IDR were found to be larger than those of MurD. It means that the internal dynamics of Hef-IDR is much faster than that of MurD. We also focused on the Q dependence of $A(Q)$ in Fig. 2 (b) and analyzed it using the following equation:

$$A(Q)=p*\exp(-<u^2>Q^2)+(1-p),$$

where p and $<u^2>$ correspond to the fraction and the mean square displacement of mobile H atoms, respectively. The p and $<u^2>$ values were calculated to be 0.33±0.07 and 2.1±0.4 Å^2 for MurD, and 0.85±0.05 and 2.1±0.2 Å^2 for Hef-IDR, respectively. Although the $<u^2>$ values of both samples coincided within the experimental error, the fraction of mobile H atoms was higher in Hef-IDR than that in MurD. This fact must be the origin of the internal dynamics' differences between them.

It is considered that the H atoms located at the solvent's accessible surface possess a higher mobility than those buried inside the protein [11]. We then computed the solvent's accessible surface areas (SASA) [10] of the constituent amino acid residues of MurD and Hef-IDR based on the solution structures resolved by SAXS measurements. The mean SASA values of MurD and Hef-IDR were calculated to be 44.1 and 117.2 Å^2, respectively, meaning that the mean value of SASA of Hef-IDR was higher than that of MurD. This made us consider the possibility of a correlation between the internal dynamics and SASA. Then, we adopted the idea that amino acid residues exposed to a solvent could affect the internal dynamics. The detailed procedures for determining whether or not H atoms in constituent amino acid residues are located at solvent's accessible surface, have been covered in our paper [10]. Finally, we defined successfully the appropriate parameter that can satisfy the results from SAXS and QENS without inconsistency. Figure 3 shows the schematic view of amino acid residues in both MurD and Hef-IDR located at the solvent's accessible surface area. Such amino acid residues were predominantly segregated on the surface of MurD, on the other hand, they were homogenously distributed in the whole structure of Hef-IDR. This finding supports the idea that the amino acid residues at a surface with access to a solvent plays a main role for the internal dynamics of proteins regardless of protein's molecular architectures.

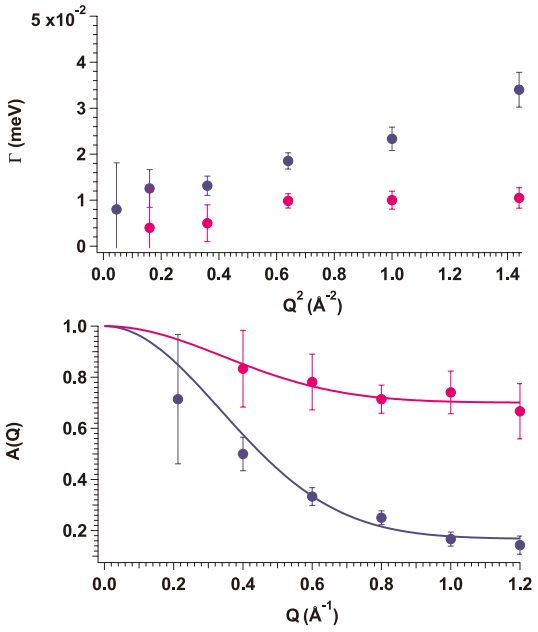

Figure 2. (a) Q^2 dependences of the Γ values of MurD (pink filled circle) and Hef-IDR (blue filled circle), respectively. (b) Q dependences of $A(Q)$s of MurD (pink filled circle) and Hef-IDR (blue filled circle), respectively. Solid lines correspond to the matches the equation in the main text for MurD (pink line) and Hef-IDR (blue line), respectively.

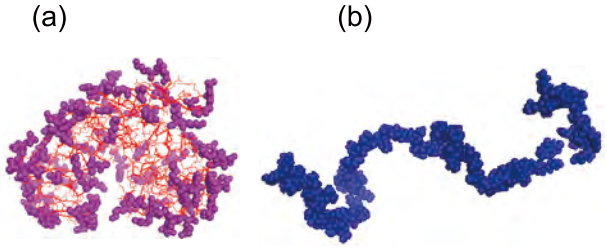

Figure 3. Schematic view of solvent-exposed amino acid residues for (a) MurD (pink sphere) and (b) Hef-IDR (blue sphere). The red line corresponds to the whole structure of MurD.

4. Outlook

Through the application of the QENS technique, we succeeded in unveiling the origin of internal dynamics of protein. We will also apply our established analytical approach to a biologically significant sample in order to figure out how the dynamics triggers the functions of that sample.

References

[1] J. A. McCammon and S. Harvey, Dynamics of Proteins and Nucleic Acids (Cambridge UniversityPress, Cambridge,1987).
[2] T. Saio et al., Sci. Rep. **5**,16685 (2015).
[3] S. Ishino, et al., J. Biol. Chem. **289**, 21627 (2014).
[4] K. Shibata et al., JPS Conf. Proc. **8**,036022 (2015).
[5] S. Grudinin, M. Garkavenko, and A. Kazennov, Acta Cryst. D **73**, 449 (2017).
[6] D. Schneidman-Duhovny, M. Hammel, J. A. Tainer, and A. Sali, Nucleic Acids Res. **44**, W424 (2016).
[7] J. Torre, De La. García, M. L. Huertas and B. Carrasco, Biophys. J. **78**, 719 (2000).
[8] J. Pérez, J. M. Zanotti, and D. Durand, Biophys. J. **77**, 454–469 (1999).
[9] M. Sarter et al., J. Phys. Chem. B **124**, 324 (2020).
[10] R. Inoue et al., Sci. Rep. **10**,21678 (2020).
[11] R. Fraczkiewicz and J. Braun, J. Comp. Chem. **19**, 319 (1998).

R. Inoue[1], T. Oda[2,3], H. Nakagawa[4,5], T. Tominaga[6], T. Saio[7], Y. Kawakita[5], M. Shimizu[1], A. Okuda[1], K. Morishima[1], N. Sato[1], R. Urade[1], M. Sato[2], and M. Sugiyama[1]

[1]*Institute for Integrated Radiation and Nuclear Science, Kyoto University;* [2]*Graduate School of Medical Life Science, Yokohama City University;* [3]*Rikkyo University;* [4]*Materials Sciences Research Center, JAEA;* [5]*Neutron Science Section, Materials and Life Science Division, J-PARC Center;* [6]*Neutron Science and Technology Center, CROSS;* [7]*Institute of Advanced Medical Sciences, Tokushima University*

Disorder in Crystal Structures of Poly(vinyl Alcohol) and Its Iodine Complex as Revealed by Concerted WAXD/ WAND Data Analysis

1. Introduction

Poly(vinyl alcohol) [PVA, -(-$CH_2CH(OH)$-)$_n$-] was synthesized in Germany in 1924 and industrialized for the first time in Japan in 1950 by the Kuraray company. Since then, PVA (commercial name POVAL) has been utilized in a variety of application fields. PVA in its amorphous state is soluble in hot water because of the presence of many OH groups. On the other hand, the high-temperature annealing of PVA increases the water resistance because of the increment of crystalline phase population. In this way, the property of PVA changes sensitively between the hydrophobicity and hydrophilicity depending on the relative content of the crystalline region. This means that the basic knowledge of the crystalline phase is indispensable for the development of practical usage of PVA as one of the most typical multipurpose-polymers.

The study of the crystal structure of PVA was started in 1930s or in the earliest stage of polymer science. The most plausible crystal structure was reported by Dr. C. W. Bunn of England in 1948 by the quantitative analysis of X-ray diffraction data [1]. As shown in Fig. 1, the planar-zigzag chains are packed face to face so that the intermolecular hydrogen bonds are formed effectively between these chains. The thus-proposed model has been utilized without almost any doubt as the most basic structural information in the physicochemical research of PVA in the last 70 years.

In general, the crystal structures of synthetic polymers are determined by the quantitative analysis of the wide-angle X-ray diffraction (WAXD) data, but the reliability of the thus-proposed structure is not very high. It is because of the relatively poor X-ray diffraction data of a semi-crystalline polymer substance with small crystallites of low regularity. Different from the single crystals of small molecules giving several thousands of sharp diffraction spots, the observable X-ray diffraction peaks of the polymer are only several tens in number, broad and diffuse as a whole. The same situation is observed in the present PVA case. It might be difficult to refine the structure model proposed by Dr. Bunn as long as only the X-ray diffraction data are focused as the target of analysis. We have to change our strategy to increase the reliability of the X-ray analyzed structure from a different point of view.

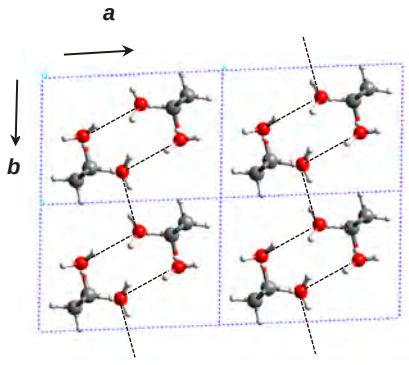

Figure 1. Crystal structure of PVA proposed by Bunn [1]

2. Combination of WAXD and WAND

We had challenges to utilize the wide-angle neutron diffraction (WAND) data. The large difference in the atomic scattering power (or cross-sectional area) between the X-ray and neutron scatterings may give us a chance to judge the quality of the proposed crystal structure from a different viewpoint. However, one serious problem was encountered at the starting point of the WAND experiment: we needed to use the fully deuterated PVA sample, because the deuterium gives strong coherent elastic neutron scattering comparable to that of C and O atoms, which is in a strong contrast with the hydrogen atom giving a substantially high incoherent scattering as a background. The deuterated PVA sample was kindly synthesized by the Kuraray company. The 2D-WAND patterns were measured for the highly-oriented deuterated PVA and its iodine-complex samples using the BIX-3 diffractometer of JRR-3 and also the iBIX system of the MLF, J-PARC. The thus-obtained WAND data were analyzed in various ways to check the reliability of the Bunn's model. However, the observed neutron diffraction profile along the equatorial line, for example, was not reproduced very well, in strong contrast to the good agreement in the WAXD profiles between the observed and calculated ones.

A similar situation was also observed in the PVA-iodine complex sample, which was prepared by immersing the oriented PVA film in an iodine aqueous solution. The PVA-iodine complex is popular as an optical polarizer, which is utilized for liquid-crystal TV screens, sunglasses etc. The crystal structure of the complex is

indispensable for the physicochemical study of the polarizer. The crystal structure derived from the X-ray diffraction data analysis could not reproduce the WAND data at all [Fig. 2 (a) and (b)]. Different from neutron scattering, X-ray scattering power is larger for an atom that has larger number of electrons. The scattering power of the iodine atom is overwhelmingly stronger than that of C and O atoms (D, H << C ~ O << I). Therefore, the X-ray diffraction pattern is governed mostly by the iodine ion positions in the unit cell. The positions of PVA chains are difficult to determine precisely. On the other hand, when the neutron diffraction data are used in the structure analysis, the neutron scattering power is in the order of D ~ C ~ O >> I. The crystal structure model of the PVA-iodine complex must reproduce consistently the observed data of WAXD and WAND. In other words, the combination of these two different kinds of diffraction data may allow us to determine the positions of PVA and iodine ions without any problem.

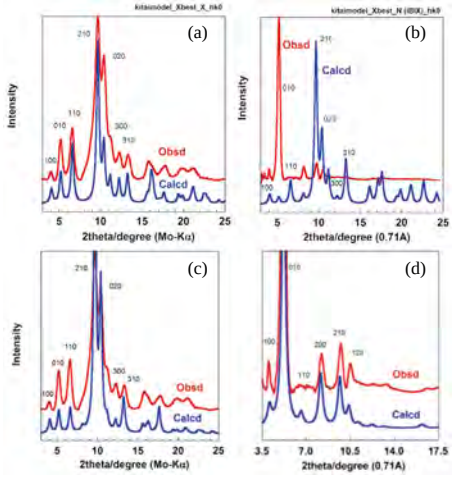

Figure 2. Comparison of WAXD and WAND profiles of PVA-iodine complex between the observed and calculated ones [2]. (a)(b): regular model and (c)(d): slipped-domain model.

3. New structure models of PVA and PVA-Iodine complex

After many trial-and-error procedures, we came up with one new idea, *i.e.*, introduction of disorder in the crystal lattice. The crystal lattice is assumed to consist of the aggregation of domains built up by a finite number of unit cells with the regular packing structure (Fig. 1). But these domains are mutually slipped along the 110 plane as illustrated in Fig. 3. The slipped-domain

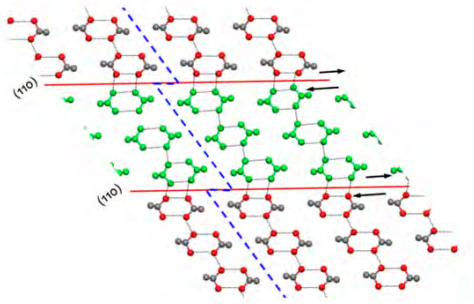

Figure 3. Slipped-domain model of PVA [2]

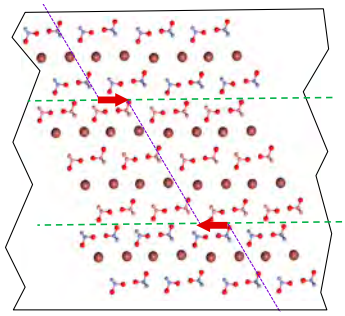

Figure 4. Crystal structure of the PVA-iodine complex consisting of the slipped-domains [2]

model satisfied quite well and consistently the observed diffraction profiles for both the WAXD and WAND data. The slippages are retained even after the formation of the PVA-iodine complex (Fig. 4). Different from the case of the regular structure model [Fig. 2 (a)(b)], the slipped-domain model of the PVA-iodine complex reproduced also both of WAXD and WAND data without any problem [Fig. 2 (c)(d)].

4. Future prospective

As described here, the harmonic combination of WAXD and WAND may lead us to the consistent determination of the crystal structure models of crystalline polymers. However, the actual success stories have been limited to only a few cases: polyethylene, poly(lactic acid), polyoxymethylene, poly(ethylene oxide), PVA, and so on [2, 3]. The determination of the accurate structure is indispensable for the quantitatively-reliable prediction of physical property of these polymers. Of course, the simultaneous analysis of vibrational spectral data combined with WAXD and WAND data is more suitable for this purpose.

References

[1] C. W. Bunn, Nature, **161**, 929 (1948).
[2] K. Tashiro et al., Macromolecules, **53**, 6656 (2020).
[3] K. Tashiro et al., Kobunshi Ronbunshu, **71**, 508 (2014).

Kohji Tashiro[1,2] and Katsuhiro Kusaka[3]
[1]*Professor emeritus, Toyota Technological Institute;* [2]*Guest Professor, Ibaraki University;* [3]*Frontier Research Center for Applied Atomic Sciences, Ibaraki University*

Neutron Crystallography Reveals Unprecedented Active-site Structure in Copper Amine Oxidase

1. Introduction

Focusing micro structures is one of the major strategies to unveil principles and fundamentals of biological phenomena. Starting with microscopic observation of cells or bacteria, we are now able to see the smallest atom, hydrogen/proton, in protein structures. Chemical reactions in solution, including an enzyme-catalyzing one, show crucial involvement of protons [1]. Redox enzymes facilitate the catalytic reactions by proton transfers with electron movements. Therefore, great attention has been paid to neutron crystallography because it can visualize the specific positions of hydrogen/proton in protein crystal structures [2]. At extremely high resolution over 1 Å, X-ray crystallography can also detect a part of hydrogen atoms, but not all are detected.

A target enzyme of the present work is copper amine oxidase (CAO) that catalyzes oxidative deamination of primary amines, having various functions, such as assimilation of primary amines in bacteria and degradation of bioactive primary amines in animals [3]. All CAOs are the homodimers of a ~70–95-kDa subunit. The active site in each subunit contains Cu^{2+} and redox cofactor topaquinone (TPQ) that is generated from a specific Tyr residue through autocatalytic posttranslational modification only requiring Cu^{2+} and molecular oxygen. It is known that TPQ has a flat structure and a visible absorption band around 480 nm due to its conjugated system. The catalytic reaction is divided into the initial reductive half-reaction involving $2e^-$ and $2H^+$ transfer from amine substrate to the oxidized TPQ (TPQ_{ox}) and the subsequent oxidative half-reaction involving the $2e^-$ and $2H^+$ transfer to molecular oxygen for cofactor reoxidation. According to involvement of protons, the catalytic reaction is significantly influenced by pH and the protonation state of dissociative groups in the active site. For CAO from *Arthrobacter globiformis* (AGAO), the neutron crystal structure having TPQ_{ox} was determined at high resolution to elucidate the catalytic mechanism (Fig. 1A) [4].

2. Unprecedented cofactor structure

The neutron crystal structure of AGAO was determined at 1.72/1.14-Å resolution by joint refinement with neutron/X-ray diffraction data for an extra-large crystal after hydrogen-deuterium exchange in deuterated buffer at pD 7.4 (Fig. 1A) [4]. Subunit size of AGAO (70 kDa/638 residues) is the largest in the neutron crystal structures reported so far, transcending the previous limitation for molecular size. The crystal structure unambiguously provides protonation state of dissociable

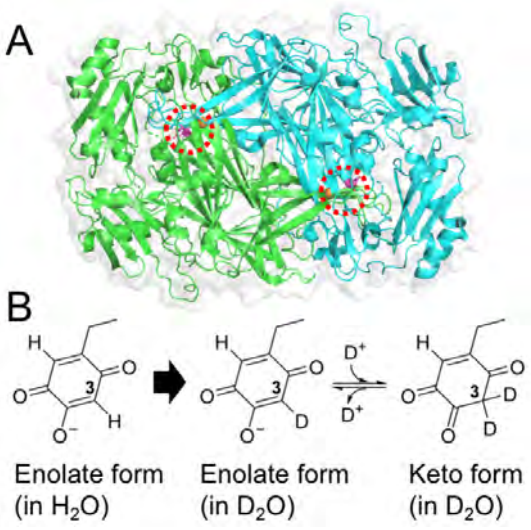

Figure 1. Neutron crystal structure and TPQ equilibrium of copper amine oxidase from *Arthrobacter globiformis* (AGAO). A: Homo-dimeric structure of AGAO. The two active sites are presented by dotted red circles. B: Equilibrium between enolate and keto forms of TPQ. H-D exchange found in the crystal structure is shown.

groups and hydrogen-bond networks in the entire structure.

Electron density (ED) and neutron scattering length density (SLD) maps revealed striking features in the active-site cofactor [4] (Fig. 2A). In contrast with the previous findings, the TPQ ring was apparently bent with non-planar geometry. Moreover, the positive SLD expanded beside the ring C3 position in nearly perpendicular direction against the TPQ plane. These facts suggest that two deuterium atoms derived from solvent D_2O are covalently attached to the C3 atom, and that the conjugated system of the TPQ ring is partially broken. It is apparent that the keto form of TPQ is generated form the enolate form that has been so far believed as only a chemical structure of TPQ_{ox}. We finally refined the TPQ structure as equilibrated mixture of the keto (41%) and enolate forms (59%) (Fig. 1B). Interestingly, the side chain of Asn381 most likely has two conformers, proving the enolate/keto equilibrium (Fig. 2A) [4]. The refined occupancies were 56% and 44% for the conformers *a* and *b* of Asn381, respectively, which are related through flipping around the Cβ-Cγ rotation. Steric hindrance is induced between the C3 deuterium atom of the keto form and the amide protons of the conformer *a*, causing rotation of the amide group to the conformer *b*. Thus, the occupancy of the alternative conformer *b* (44%) of Asn381 was comparable to that of the keto form (41%).

3. Unusual "levitated" proton

Another striking finding is the presence of a residual positive SLD with a spherical shape between TPQ O5 and a conserved Asp residue (Asp298) (Fig. 2B) [4,5]. The SLD was not assigned as a water molecule due to the absence of accompanied ED and the short distances from the surrounding atoms. Following a careful examination, we assigned this SLD as a delocalized deuterium ion (deuteron, D^+). It is likely that the D^+ is "levitated" at unusual position among three O atoms as follows. The D^+ resides nearly coplanar with three oxygen atoms (Oδ1 and Oδ2 of Asp298 side chain, and O5 of TPQ), but the distance from either Oδ1 (2.0 Å), Oδ2 (1.6 Å), or O5 (1.6 Å) far exceeded the length of a typical O-H covalent bond (ca. 0.95 Å) (Fig. 2B), clearly indicating that the D^+ ion is non-covalently interacted with the surrounding oxygen atoms. In addition, the distance between O5 of TPQ and Oδ1 (3.5 Å) or Oδ2 (2.7 Å) of Asp298 is clearly longer than that of a typical low-barrier hydrogen bond (2.2–2.5 Å) [6]. Thus, these results suggest that the detected D^+ ion (H^+ in H_2O) is a triply shared deuteron (proton) in hydrogen bonds. While TPQ O2 and O4 are fixed

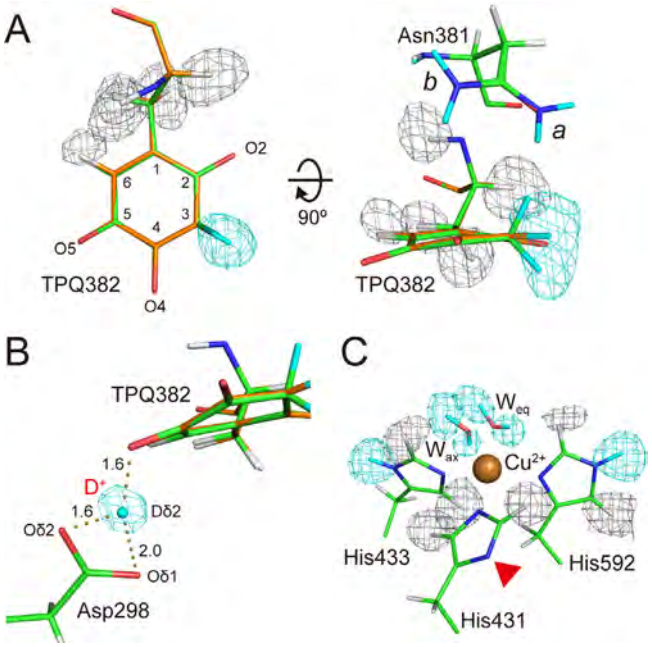

Figure 2. Three unprecedented structures found in AGAO. A: Bent structure of TPQ_{ox} and deuterium atoms covalently attached at the C3 position. The enolate and keto forms of TPQ_{ox} are indicated. B: Unusual levitated proton. C: Metal-induced deprotonation of His431. His431 is assigned as an imidazolate anion (full deprotonated form). A red triangle indicates the deprotonated His431 Nδ1. In all panels, gray meshes (negative SLD omit maps) and cyan meshes (positive SLD omit maps) represent the presence of hydrogen and deuterium atoms, respectively.

by tight hydrogen bonds with two water molecules and Tyr284 phenolic OH, respectively, it is predicted that the third tight hydrogen-bond interactions via the shared proton tether the O5 moiety of TPQ toward Asp298, forcing the TPQ ring to bend. We are unable to find another shared proton in AGAO, suggesting the specific role of D^+ ion on the catalytic mechanism. Interestingly, several similar shared protons are being identified in the active site of the other enzymes including HIV protease [7] and cholesterol oxidase [8] by neutron crystallography. Any common mechanism buried in the enzyme structure might generate shared protons as an essential chemical species to enhance the catalytic reaction.

4. Unusual histidine deprotonation

An interesting protonation state was also found in Cu^{2+}-ligands (His431, His433, His592, and two water molecules) taking a distorted pyramidal geometry as shown in the previous structures (Fig. 2C) [9]. Three imidazole side chains coordinate to Cu^{2+} through the lone pair of deprotonated Nε2 of His431, Nε2 of His433, and Nδ1 of His592. The other imidazole nitrogen atoms of His433 and His592 were identified as a single protonated form. However, SLD was undetected only for Hδ1 of His431. We assigned His431 as an imidazolate anion (full deprotonated form) despite of extreme high pK_a (=14) for the second proton dissociation of free imidazole (Fig. 2C) [4]. It is suggested that Cu^{2+} can attract electrons of the imidazole ring to significantly lower its apparent pK_a (metal-induced histidine deprotonation). The apparent pK_a for the second proton of His431 is estimated to be significantly lower than 7.4. All other His side chains were single- or double-protonated in the entire AGAO, suggesting specific environments of His431. The findings with high-resolution SLD map unambiguously provided the first structural evidence for the metal-induced deprotonation. Similar pK_a-lowering effect was also found for axially Cu^{2+}-coordinated water (W_{ax}). The positive SLD for one of two deuterium atoms covalently bound to the oxygen atom of W_{ax} showed a significantly lower than the other SLD. While the pK_a of bulk water is 14, it is consistent with the fact that pK_a of the water molecule coordinating to the Cu^{2+} ion is estimated to be 7.5 [9], that is close to data collection pD (= 7.4).

5. Conclusions

The present study reveals unprecedented structural features in the active-site structure of AGAO. These have not been identified by previous X-ray crystallographic studies. Especially, protons (bare hydrogen nuclei) are impossible to detect by X-ray crystallography since the X-ray reflection depends on the interaction with electrons. In contrast, neutron crystallography can detect even protons because neutrons interact with atomic nuclei. We expect that there are unprecedented structures or unique protons within the other reaction intermediates of AGAO or the other proteins. Neutron crystallography at high resolution will be an essential tool to reveal such unique micro structures.

References

[1] M. Eigen, Angew. Chem. Int. Ed. Engl. **3** 1 (1964).
[2] W. B. O'Dell, et al., Arch. Biochem. Biophys., **602** 48 (2016).
[3] G. Floris, and B. Mondovi, Copper Amine Oxidases: Structures, Catalytic Mechanisms and Role in Pathophysiology, (C.R.C. Press, Inc., Boca Raton, FL, 2009).
[4] T. Murakawa, et al., Proc. Natl. Acad. Sci. U.S.A., **117** 10818 (2020).
[5] Y. C. Chiu, et al., Biochemistry **45** 4105 (2006).
[6] W. W. Cleland, Arch. Biochem. Biophys., **382** 1 (2000).
[7] O. Gerlits, Angew. Chem. Int. Ed., **55** 4924 (2016).
[8] E. Golden, et al., Sci. Rep., **7** 40517 (2017).
[9] S. Kishishita, et al., J. Am. Chem. Soc., **125** 1041 (2003).

T. Murakawa[1], K. Kurihara[2], T. Tamada[2], K. Kusaka[3], M. Adachi[2], and T. Okajima[4]
[1]*Faculty of Medicine, Osaka Medical and Pharmaceutical University;* [2]*Institute for Quantum Life Science, National Institutes for Quantum Science and Technology;* [3]*Frontier Research Center for Applied Atomic Sciences, Ibaraki University;* [4]*SANKEN, Osaka University*

Features of Neutron Resonance Spin Echo Spectrometer using Time of Flight Method

1. Introduction

Neutron spin echo (NSE) [1] is a neutron scattering spectroscopy method with a high energy resolution from picoseconds to sub-microseconds in the time domain. The NSE method, in which the neutron spin is manipulated by RF fields, is called neutron resonance spin echo (NRSE) [2]. For measurements covering a wide space-time range and a variety of sample types, two resonance type spectrometers, named NRSE and MIEZE, were constructed at the J-PARC MLF BL06 (Village of neutron resonance spin echo spectrometers; VIN ROSE). In the MIEZE instruments, the required spin manipulation to obtain an echo signal is done before the sample position. This feature is especially useful to examine the spin dynamics and MIEZE spectroscopy was employed to study the spin fluctuations of the magnetic Skyrmion [3].

In the commissioning of the MIEZE instrument at BL06 (Fig. 1), the features of resonance spin echo spectrometers using the time of flight (TOF) method in pulsed neutron sources were studied analytically and experimentally. We demonstrated that the derivative of the phase of echo signals with respect to TOF was equal to the frequency shift in off-echo conditions deviated from the spin echo condition, in which neutrons of all wavelengths are in phase.

We report the features of MIEZE spectroscopy using the TOF method (TOF-MIEZE), which are interesting and can be used to perform an accurate measurement.

2. Experimental setup

The experiment was performed in a simple MIEZE system with two $\pi/2$ spin flippers. The frequencies of the first (RSF1) and second (RSF2) flippers were set as f_1 = 200 kHz and f_2 = 400 kHz, respectively, and the MIEZE frequency was $f_2 - f_1$ = 200 kHz. To test a wide neutron wavelength band available in the spallation source of the MLF, the second frame mode, in which the pulse repetition frequency is 12.5 Hz, was used, while the original one at the MLF is 25 Hz. The spin echo condition of the system is given by $f_1 L_{12} = (f_2 - f_1) L_{2d}$, where L_{12} and L_{2d} denote distances between RSF1 and RSF2, and RSF2 to the detector, respectively. The deviation from the echo condition can be represented by a detuning parameter [4]: $\Omega = [-f_1 L_{12} + (f_2 - f_1)\, L_{2d}]/L_{0d}$. L_{0d} denotes the total flight path length of the neutrons. To investigate the phase and frequency of the TOF-MIEZE signals when the system deviated from the echo condition ($\Omega = 0$), the positions of RSF1, RSF2 and the detector were changed.

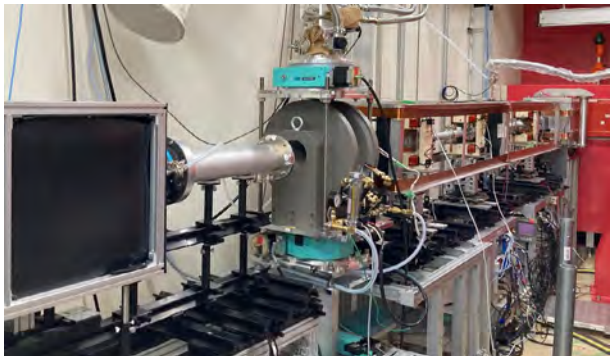

Figure 1. The MIEZE-type spin echo spectrometer at BL06 at J-PARC MLF.

3. Results and discussion

Figure 2 shows the observed frequency shifts and TOF (wavelength) dependency of the phase of the TOF-MIEZE signals in various Δy_d. In the echo condition, (c) $\Delta y_d = 0$, the phase is nearly constant over all neutron wavelengths. In off-echo conditions ($\Delta y_d \neq 0$), the phases of the TOF-MIEZE signal change linearly with the TOF. The slope of phase vs. TOF plot, $\Delta\varphi/\Delta t$ increases as the spatial displacement increases. Good quantitative agreement was found between the slope, $\Delta\varphi/\Delta t$ and the frequency shift, Ω with our analytical model.

These understandings of the phase shift of the TOF-MIEZE signals are important to realize a phase correction in the detector plane. The phase of the MIEZE signal depends on the neutron path length and the phase difference becomes larger as the MIEZE frequency and neutron wavelength increases for high resolution measurements. Figures 3 (a) and (b) illustrate the path length differences of scattered neutrons on the detector plane. Unless the detector has a perfect spherical surface, the phase of the MIEZE signal has a position dependence on the detector plane as shown in Fig. 3 (c). This phase difference can be corrected by applying a time shift on the signal according to the neutron wavelength and MIEZE frequency: $\Delta t = \Delta L / v$. Here, ΔL and v denotes the path length difference and neutron velocity. After the phase correction, the phase becomes much less dependent on the position, as shown in Fig. 3 (d).

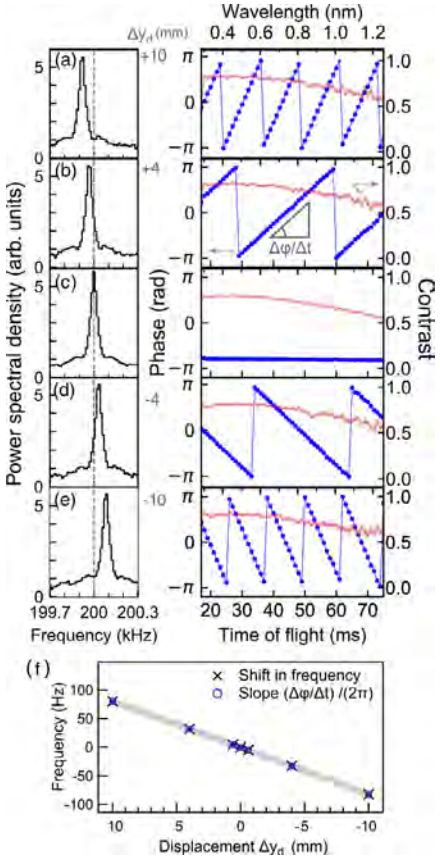

Figure 2. Phase and frequency shift of the TOF-MIEZE signals in off-echo conditions with Δy_d = +10 (a), +4.0 (b), 0.0 (c), −4.0 (d), −10 mm (e). The left column shows the Fourier transforms of the TOF-MIEZE signal. The right column shows the TOF dependency of the phase (blue closed circles) and contrast (red lines).

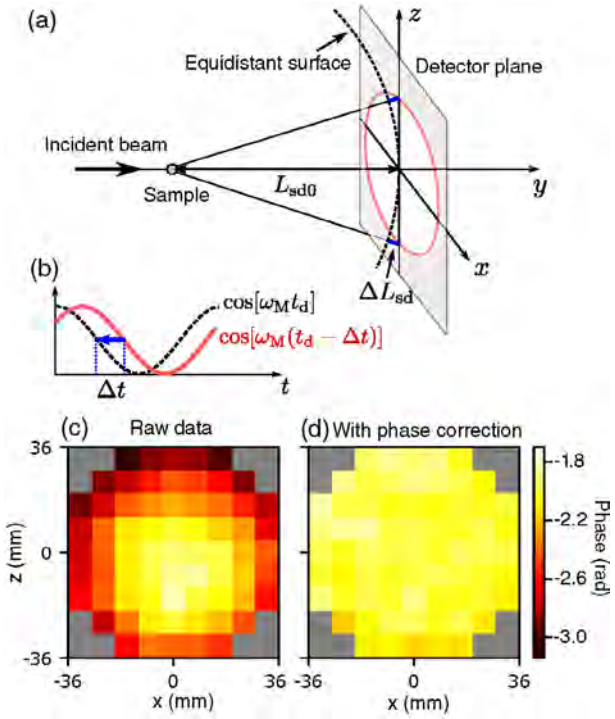

Figure 3. (a) layout of a scattering experiment. (b) Phase shift between the actual MIEZE signal (solid line) and that on the virtual equidistant surface (dashed line). (c, d) Phase maps on the detector plane of MIEZE signal for neutron wavelength λ = 0.8 nm without/with the phase correction.

4. Summary

Features of the TOF-MIEZE spectroscopy are reported. The detuning parameter Ω can be a useful indicator for the deviation from the spin echo condition. The findings enable the accurate and precise tuning of a TOF-MIEZE instrument and contribute to the data analysis of the spectroscopy.

Acknowledgements

This study was conducted in collaboration with M. Hino, Y. Kawabata (Kyoto University), H. Endo, and H. Seto (KEK). We thank S. Sato, H. Ohshita, T. Seya, and Y. Yasu (KEK) for the valuable technical support. The neutron scattering experiment was approved by the Neutron Scattering Program Advisory Committee of IMSS, KEK (Proposal Nos. 2009S07, 2014S07 and 2019S07). Device developments are supported by the program of the Development of System and Technology for Advanced Measurement Analysis (SENTAN), JST, the Photon and Quantum Basic Research Coordinated Development Program, MEXT Japan, and the Neutron Scattering Program Advisory Committee of IMSS, KEK (Proposal Nos. 2009S07 and 2014S07). This work is partly supported by JSPS KAKENHI Grants No. JP17K14133, JP19K20601, and JP19H01856.

References

[1] F. Mezei, Z. Phys. **255**, 146 (1972).
[2] R. Gähler, R. Golub, and T. Keller, Physica B **180**, 899 (1992).
[3] T. Nakajima, T. Oda, M. Hino, H. Endo, K. Ohishi, K. Kakurai, A. Kikkawa, Y. Taguchi, Y. Tokura, and T. Arima, Phys. Rev. Research **2**, 043393 (2020).
[4] T. Oda, M. Hino, H. Endo, H. Seto, and Y. Kawabata, Phys. Rev. Applied **14**, 054032 (2020).

T. Oda
Institute for Integrated Radiation and Nuclear Science, Kyoto University (Present address: Institute for Solid State Physics, The University of Tokyo)

Effect of Annealing on the Crystal Structure of Li_2MnO_3-type Cathode Material for Lithium-ion Batteries

1. Introduction

Layered manganese oxides, such as $LiMnO_2$ (monoclinic, $C2/m$ or orthorhombic, $Pmmn$), Li_2MnO_3 (monoclinic, $C2/m$) and Li_2MnO_3-$LiMO_2$ (M = Co, Mn, Ni; hexagonal, $R\bar{3}m$) solid solution, are attractive cathode materials for lithium-ion batteries because they are safer, cheaper, less toxic, and have a higher operating voltage than $LiCoO_2$ and $LiNiO_2$. The Li_2MnO_3-type cathode materials have attracted much attention among the layered manganese oxides. We have synthesized the Li_2MnO_3-type materials with and without the substitution of Co. It was found that the charge-discharge capacity did not degrade even after repeated charge-discharge cycles in the Co-substituted material [1] and that the charge-discharge capacity increased when the charge-discharge cycles in the Li_2MnO_3 material were repeated without the substitution of Co [2]. Recently, we found that annealing in a controlled oxygen atmosphere improved the charge-discharge capacity of the Ni-substituted Li_2MnO_3 material. The purpose of this study is to analyze the changes by annealing in the crystal structure of the Ni-substituted Li_2MnO_3 material.

2. Experimental

The Ni-substituted Li_2MnO_3 samples with the composition of $Li_{1.87}Mn_{0.94}Ni_{0.19}O_3$ were synthesized by coprecipitation technique [1] and annealed at 900°C under an oxygen partial pressure of 10^{-2} torr. Neutron powder diffraction data of the samples before and after annealing were taken at room temperature on the time-of-flight neutron powder diffractometer SuperHRPD. The diffraction data were analyzed using a Rietveld refinement program Z-Rietveld (version 1.1.10) [3, 4] on the basis of the Li_2MnO_3-type structure model [1, 2]. The coherent scattering lengths, b, used for Rietveld refinement, were -1.90 fm (Li), -3.75 fm (Mn) and 10.3 fm (Ni).

3. Results and discussion

The Li_2MnO_3-type structure has two sites (Li1 and Li2) on the Li layer and a periodic arrangement of the Li3 and Mn sites on the MnO_2 layer, which makes it different from the $LiCoO_2$-type structure (hexagonal, $R\bar{3}m$) that simply has alternating layers of Li and CoO_2 (Fig. 1). We have investigated which cation (Li, Mn and Ni) is substituted at each site (Li1, Li2, Li3 and Mn), based on the structure model of the previous studies [1, 2]. We can determine whether Mn or Ni is likely to be substituted at each site by refining the occupancies of Li because the neutron coherent scattering length increases in the order of Mn, Li and Ni. The occupancies were constrained so that the cation ratio determined from the occupancies was the same as the composition of the samples.

Table 1 shows the R factors, lattice parameters and occupancies of the cations. Figure. 2 shows the Rietveld refinement patterns. The fitting is good and the structure model is supported. While there was no substitution of Ni at the Li2 and Li3 sites in the sample before annealing, the substitution of Ni at the Li2 site was observed in the sample after annealing. The arrangement of Li and Mn on the MnO_2 layer also differed between the samples before and after annealing (Fig. 3). While 37% of Mn was substituted at the Li1 site in the sample before annealing, the amount of the substitution of Mn at the Li1 site became 16% and Li was almost eliminated from the Mn site in the sample after annealing. When the occupancies of the sample after annealing are refined, the amount of Li determined from the occupancies exceeds the composition due to the larger occupancy of

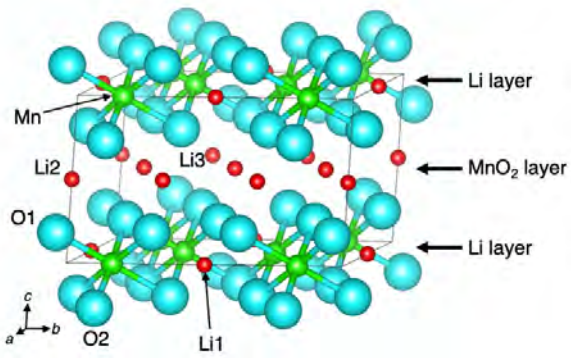

Figure 1. Crystal structure of Li_2MnO_3.

Table 1. *R* factors, lattice parameters and occupancies of $Li_{1.87}Mn_{0.94}Ni_{0.19}O_3$ before and after annealing.

Sample	Before annealing	After annealing
R factors		
S	2.29	2.13
R_{wp}	5.25%	4.46%
R_P	4.20%	3.59%
R_B	5.83%	6.08%
R_F	11.61%	9.56%
R_e	2.29%	2.09%
Lattice parameters		
a / Å	4.9435(2)	4.94463(16)
b / Å	8.5516(4)	8.5593(3)
c / Å	5.02758(13)	5.03135(10)
β / °	109.270(4)	109.224(3)
Occupancies		
Li1	Li: 0.63(4), Mn: 0.37(4)	Li: 0.84, Mn: 0.16
Li2	Li: 1, Ni: 0	Li: 0.890(5), Ni: 0.110(5)
Li3	Li: 1, Ni: 0	Li: 1, Ni: 0
Mn	Li: 0.054(18), Mn: 0.756(18), Ni: 0.19	Li: 0.00, Mn: 0.86, Ni: 0.14

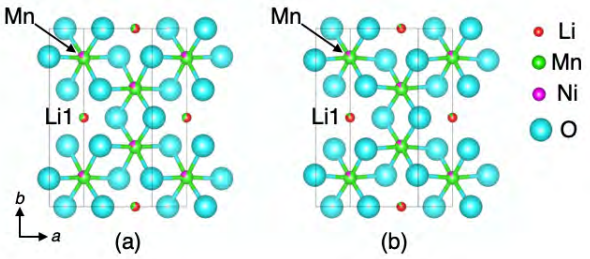

Figure 3. Structure of the MnO_2 layer of $Li_{1.87}Mn_{0.94}Ni_{0.19}O_3$ (a) before and (b) after annealing. The area inside the circle shows the amount of the substitution of each ion.

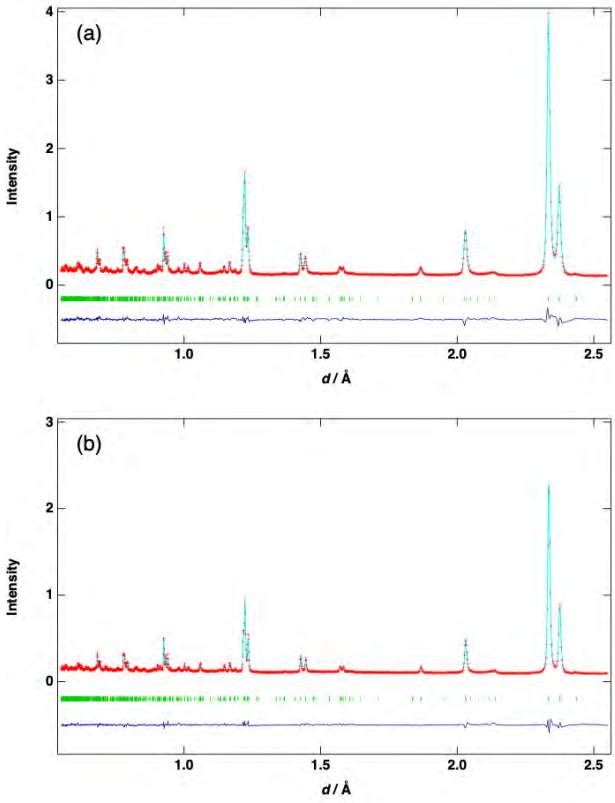

Figure 2. Rietveld analysis patterns for $Li_{1.87}Mn_{0.94}Ni_{0.19}O_3$ (a) before and (b) after annealing.

Li at the Li1 site. The occupancies at the Li1 and Mn sites were fixed in the sample after annealing. The findings indicate that the arrangement of Li and Mn in the MnO_2 layer is ordered by annealing. Refining the occupancies of oxygen at the O1 and O2 site showed no significant deficiency in both samples.

4. Conclusions

The crystal structure of the $Li_{1.87}Mn_{0.94}Ni_{0.19}O_3$ cathode material, whose capacity is improved by annealing, before and after annealing was analyzed by neutron powder diffraction. The results show that the annealing promoted the ordering of Li and Mn on the MnO_2 layer and the substitution of Ni at the Li2 site.

T. Mochiku
National Institute for Materials Science

References

[1] K. Ozawa, Y. Nakao, T. Mochiku, Z. Cheng, L. Wang, H. Iwai, Y. Tsuchiya, H. Fujii and N. Igawa, J. Electrochem. Soc. **159**, A304 (2012).
[2] Y. Nakao, K. Ozawa, Y. Menoto, F. Uesugi, H. Fujii and T. Mochiku, J. Ceram. Soc. Jpn. **123**, 589 (2015).
[3] R. Oishi, M. Yonemura, Y. Nishimaki, S. Torii, A. Hoshikawa, T. Ishigaki, T. Morishima, K. Mori and T. Kamiyama, Nucl. Instrum. Meth. Phys. Res. A **600**, 94–96 (2009).
[4] R. Oishi-Tomiyasu, M. Yonemura, T. Morishima, A. Hoshikawa, S. Torii, T. Ishigaki and T. Kamiyama, J. Appl. Cryst. **45**, 299 (2012).

Novel Atomic Imaging Technique for Light Elements: White Neutron Holography on BL10

1. Introduction

For most of the functional materials, or strongly correlated electron systems, the properties can be controlled by doping foreign elements. From the viewpoint of structural physics, it is obvious that changes of atomic structures around dopants (Fig. 1), called *local atomic structures*, must play an important role in transforming their properties. Recently, atomic resolution holography (ARH) has been developing rapidly in Japan as a direct probe of local atomic structures using fluorescent X-rays and photoelectrons [1]. ARH has the following important advantages:

1: ARH can visualise three dimensional (3D) atomic structures around particular atoms (dopants), that is, ARH has element selectivity.

2: ARH can observe atoms up to 20 Å from the dopants.

3: For visualisation, ARH does not need any models because it can record the change of phases. Consequently, atomic images can be obtained directly by Fourier transform.

X-ray fluorescence and photoelectron holography have already provided plenty of results for investigations of novel functional materials, such as dilute magnetic semiconductors, relaxor ferroelectric materials, topological insulators, and so on.

Neutron holography was firstly proposed by Cser et al., and realised by Sur et al. in the Chalk River research reactor [3, 4]. In Japan, the first neutron holography experiment was conducted by the authors group in JRR-3 [4]. However, the accuracy of the atomic images obtained in the reactor facilities were not sufficient because only one wavelength could be used for experiments. In principle, atomic images obtained by data using one wavelength include many artifacts, which lowers significantly the accuracy. In 2017, the authors group succeeded in enhancing the accuracy of atomic images drastically by using white neutrons on BL10 in the MLF [5]. One can obtain holography data with 130 different wavelengths at once. The authors group has already succeeded in visualising local atomic structures in typical scintillator crystal, 2at% Eu doped CaF_2 [5], 0.26at% B doped Si [6], thermoelectric materials, 0.75at% B doped Mg_2Si [7], and so on. The principle and experimental specifics are reported elsewhere in detail [6].

2. Recent results

In the typical strongly correlated electrons systema RB_6 (R: rare earth), characteristic phonon softening was observed, which results from motions of R in the B cage shown in Fig. 2. On the other hand, when Sm is doped in RB_6 (R: Yb, La), Sm becomes divalent in LaB_6, and trivalent in YbB_6. Since the difference of ion radii of Sm^{2+} and Sm^{3+} is ten times larger than that of the lattice constants, the motions of Sm in YbB_6 and LaB_6 must be different. To detect the local behaviour of doped Sm, the authors observed local atomic structures around Sm in 2at% Sm doped RB_6: (R: Yb, La) on BL10.

Figure 3 shows a local atomic structure in 2at% Sm YbB_6 in a (100) plane including Sm. Yb around doped Sm are clearly visualised up to 14 Å from Sm. From the estimations of widths of R around Sm, we found that Sm in YbB_6 fluctuates with a mean displacement, $\sigma = 0.25(4)$ Å, while that of LaB_6 is at most $\sigma = 0.15$ Å; this is due to the

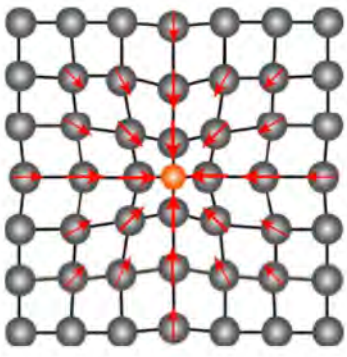

Figure 1. Local atomic structures around a dopant (orange).

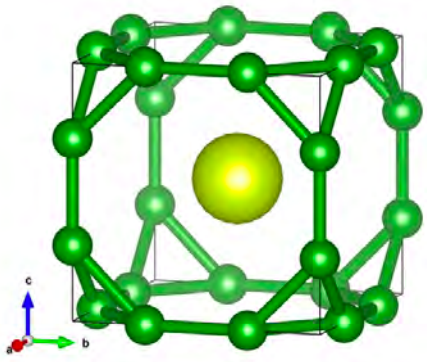

Figure 2. Crystal structure of RB_6 (R: rare earth). Central Yellow and green spheres are R and B, respectively.

difference in the ion radius. On the other hand, we confirmed that the fluctuations of Yb around Sm are negligible. We successfully visualised B images around Sm as well. Figure 4 indicates the distance dependence of the intensity of atomic images of B. The dashed line is the theoretical result. As shown in Fig. 4, the intensity of the second nearest neighbour (NN) and more distant B are consistent with the theoretical values, while that of the first NN B is reduced by 28%. This reduction of intensity can be explained if the first NN B is fluctuated with σ = 0.28 Å. These results mean that Sm doping causes fluctuation of only the first NN B, while Yb and the other B are not affected because of strong covalent bonding of the B cages. This is the first observation of local structures and local behaviour of dopants and atoms around the dopants in rare earth borides.

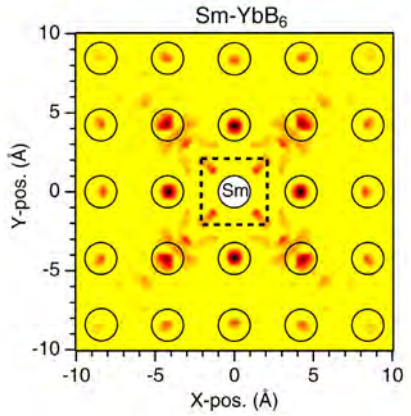

Figure 3. Local atomic structures of Yb in 2at% Sm doped YbB_6[8]. The circles and dashed square are expected positions of Yb, and the unit cell. (Reprinted with permission)

3. Summary

The authors group has succeeded in realising investigations of local structures/behaviour of light elements on BL10. Since light elements play important roles in functional materials, white neutron holography will be an indispensable probe for materials science. Note that white neutron holography can be realised only in J-PARC at the moment; thus, the authors believe that this method will provide a new direction to J-PARC.

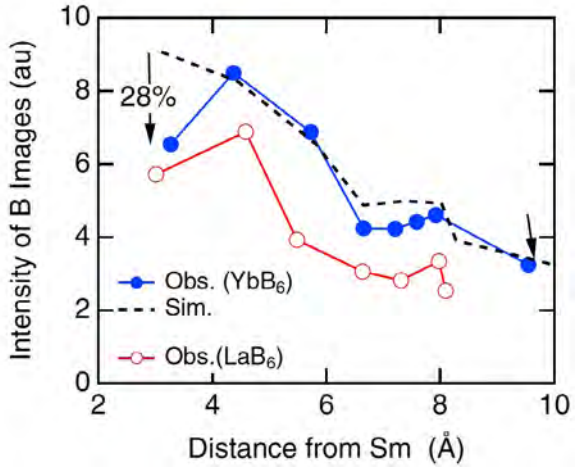

Figure 4. Distance dependence of atomic images of B in Sm doped RB_6 (R: Yb, La) [8]. (Reprinted with permission)

References

[1] K. Hayashi and P. Korecki, J. Phys. Soc. Jpn., **87**, 061003(2018).
[2] L. Cser, et al., Europhys. Lett. **54**,747 (2001).
[3] B. Sur, et al., Nature, **414**, 525(2001).
[4] K. Hayashi et al., Jpn. J. Appl. Phys. **47**, 2291(2008).
[5] K. Hayashi et al., Sci. Adv. **3**, e1700294(2017).
[6] K. Ohoyama and K. Hayashi, Phys. Status Solidi B, **255**, 1800143 (2018).
[7] K. Hayashi et al., AIP Advances **10**, 035115 (2020).
[8] S. Uechi et al., Phys. Rev. B, **102**, 054104 (2020).

K. Ohoyama[1] and K. Hayashi[2]
[1]*Graduate school of Science and Engineering, Ibaraki University;* [2]*Graduate School of Engineering, Nagoya Institute of Technology*

Experimental Evidence for the Existence of a Second Partially-Ordered Phase of Ice VI

1. Introduction

To date, more than 20 crystalline and amorphous phases of ice have been reported [1]. This extraordinary polymorphism makes ice unique with its universality and has inspired many studies within broad disciplines of sciences. The structural variety of ice arises from the geometric flexibility of hydrogen bonds and hydrogen order-disorder phase transition [2]. A prominent unsolved question [3] concerning the structural diversity induced by hydrogen ordering is whether a hydrogen-disordered phase of ice transforms into only one hydrogen-ordered phase. Since hydrogen-ordering causes significant changes in the physical property of ice, such as electric conductivity and dielectricity, the hitherto undiscovered variety of ice polymorphism would be a key point to find or control the functionality of ice. We reported recently a second hydrogen-ordered phase for ice VI, ice XIX, unambiguously demonstrated by in-situ dielectric and neutron diffraction measurements under high pressure [4]. Although theoretical studies report a possibility of existence of multiple hydrogen ordering for ice VI, no experimental studies have found evidence of multiplicity mainly due to technical difficulties of detecting hydrogen ordering of ice VI under high pressure.

2. Experiments

Comprehensive observation of hydrogen ordering of ice VI was first conducted by dielectric experiments in a stable pressure range of ice VI, 0.88–2.2 GPa. Ice VI was initially obtained at room temperature and its dielectric properties were determined in both cooling and heating runs in the temperature range 100–150K, using a newly developed pressure cell (Fig.1a). Based on a phase diagram of ice VI and its hydrogen-ordered phases clarified by the dielectric measurement, neutron diffraction experiments were conducted in a pressure range, where ice XIX appears, using a pressure-temperature controlling 'Mito system' ([5], Fig.1b). Both cooling and heating runs were conducted at each pressure in the temperature range 80–150K. The neutron diffraction experiments were conducted at beamline PLANET in the MLF of J-PARC.

3. Results and discussion

Phase transitions from ice VI to its hydrogen-ordered phases were observed at around 120–130K, along with sudden weakening/slowing down of the dielectric response of ice VI with decreasing temperature (Fig. 2a). Based on the slope of the obtained phase boundary (Fig. 2b), i.e. d*T*/d*P*, between ice VI and its

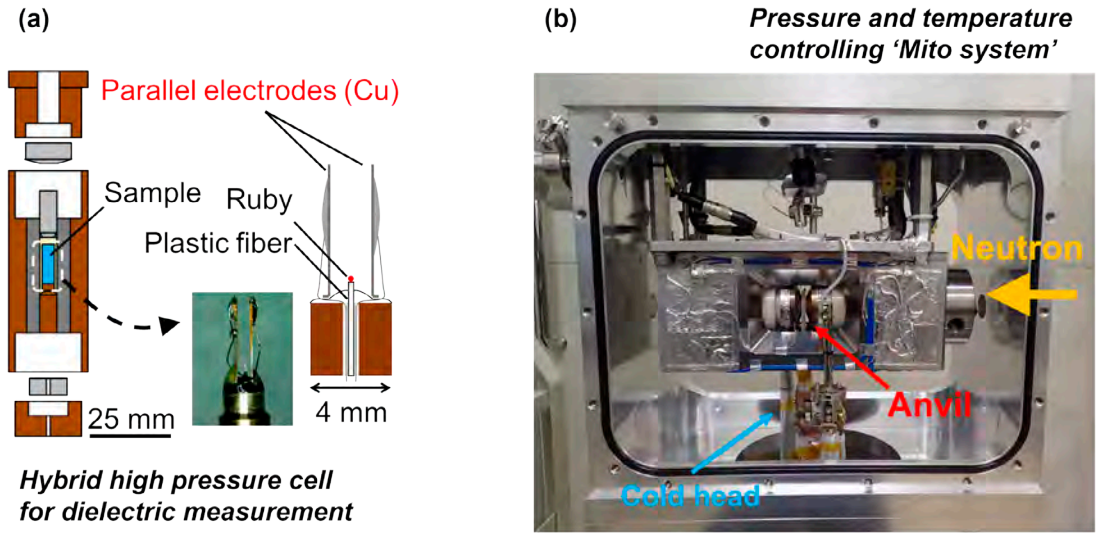

Figure 1. (a) Schematic drawings of hybrid high pressure cell for dielectric measurement using piston cylinder. (b) Pressure and temperature controlling system ('Mito system') for neutron scattering measurement.

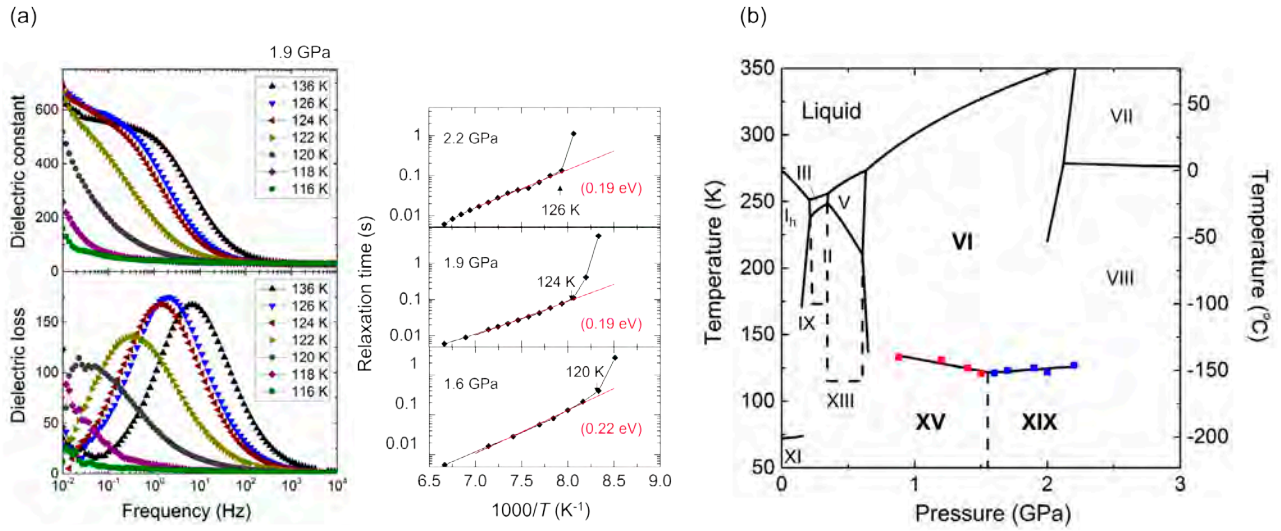

Figure 2. (a) Temperature dependence of dielectric constant and loss of ice VI and ice XIX obtained at 1.9 GPa (left). Pressure changes of temperature dependence of relaxation time of ice VI and ice XIX (right). (b) Phase diagram of ice obtained in this study.

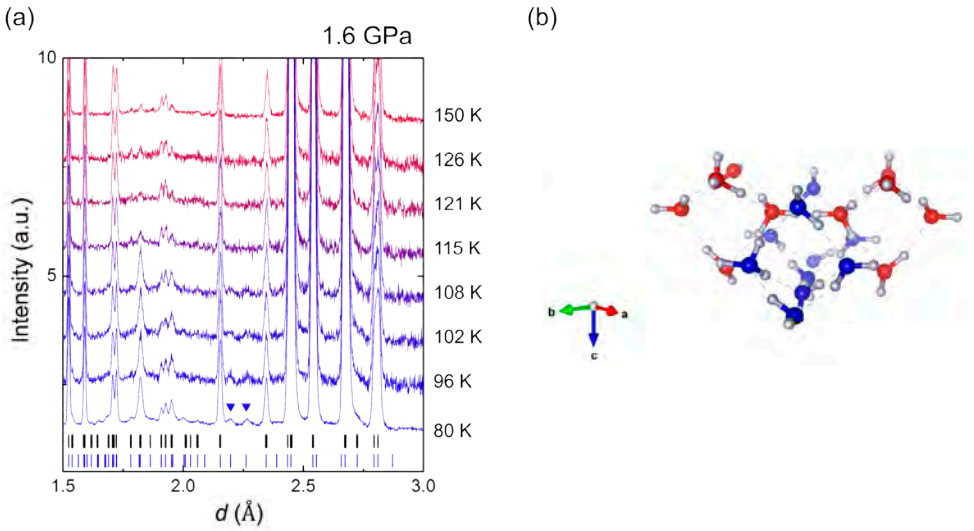

Figure 3. (a) Temperature changes of neutron diffraction patterns of ice VI and ice XIX obtained at 1.6 GPa. The blue and black ticks represent all the peak positions expected from the unit cells of ice XIX and ice XV, respectively. Blue triangles indicate new peaks at 2.20 Å and 2.26 Å, which do not appear from the unit cell of ice XV. (b) Structure models of ice XIX based on the *Pcc*2 model.

hydrogen-ordered phases changes from negative to positive at 1.5–1.6 GPa with increasing pressure. From the Clausius–Clapeyron relationship, this sign change for d*T*/d*P* strongly indicates that ice VI has two different hydrogen-ordered phases with opposite signs for Δ*V*. Since the currently known hydrogen ordering from ice VI to ice XV shows a positive volume change (observed at the lower pressure, 0.4 GPa, [6]), the hydrogen-ordered phase in the higher-pressure region is the new phase. A transition from ice VI to ice XIX was also confirmed in the neutron diffraction experiments at 1.6 and 2.2 GPa, as the appearance of new peaks due to symmetry lowering (Fig. 3a). Some of the new peaks, e.g. those at 2.20 Å and 2.26 Å (indicated by blue triangles in Fig. 3a), cannot be assigned to the unit cell of ice XV; instead, they can be assigned to an expanded $\sqrt{2} \times \sqrt{2} \times 1$ cell with respect to

the unit cell of ice VI (the unit cell of ice XV has a 1×1×1 cell with respect to that of ice VI). This is unambiguous evidence that ice XIX is a new hydrogen-ordered phase of ice VI. The Rietveld method was applied for structure analysis of ice XIX considering the group–subgroup relationship between ice VI and XIX and reflection conditions obtained in the neutron experiments. As a result, $P\bar{4}$ and *Pcc*2 structural models are the most plausible for the space group of ice XIX. Considering the suggested space group of ice XV, $P\bar{1}$ [7] or *Pmmn* [6], centrosymmetry of hydrogen configurations is the most significant difference in hydrogen configuration between ice XIX and ice XV. In particular, *Pcc*2 suggests that a pyroelectric structure, as well as ice XI and its polar direction, is along the *c* axis. In addition, the $P\bar{4}$ and *Pcc*2 structural models include deuterium (hydrogen) atoms whose site occupancy is 50%; in other words, the models show that ice XIX is partially ordered state as the *Pmmn* structure model by Komatsu et al [6] suggested for ice XV. The space groups ($P\bar{4}$ and *Pcc*2) indicate a possibility of the existence of another fully hydrogen-ordered phase of ice VI instead of the partially hydrogen-ordered ice XIX considering the third law of thermodynamics.

4. Future plans

We plan to verify the existence of the fully hydrogen-ordered phase of ice VI by applying high pressure and high electric field (HP-HE) neutron diffraction technique [8]. An electric field may induce the fully hydrogen-ordered phase considering the non-centrosymmety of ice XIX. The HP-HE neutron diffraction technique has recently been developed by our group to observe unique structure changes of materials induced in the frontier region. We hope that the newly discovered diversity of ice polymorphism would spread further in the *P-E* phase diagram with intriguing physical properties.

References

[1] M. Millot et al., Nature, **569** 251 (2019).
[2] E. Whalley, D. W. Davidson and J. Heath, Chem. Phys., **45** 3976 (1966).
[3] C. G. Salzmann, J. Chem. Phys., **150** 60901 (2019).
[4] R. Yamane et al., Nat. Commun., **12** 1129 (2021).
[5] K. Komatsu et al., High Press. Res., **33** 208 (2013).
[6] K. Komatsu et al., Sci. Rep., **6** 28920 (2016).
[7] C. G. Salzmann, P. G. Radaelli, E. Mayer and J. L. Finney, Phys. Rev. Lett., **103** 105701 (2009).
[8] R. Yamane et al., Phys. Rev. B, **99** 174201 (2019).

R. Yamane[1,#], K. Komatsu[1], J. Gouchi[2], Y. Uwatoko[2], S. Machida[3], T. Hattori[4], H. Ito[1], and H. Kagi[1]
[1]*Geochemical Research Center, Graduate School of Science, The University of Tokyo;* [2]*The Institute for Solid State Physics, The University of Tokyo;* [3]*Neutron Science and Technology Center, CROSS;* [4]*Neutron Science Section, Materials and Life Science Division, J-PARC Center;*
[#]*Present affiliation: Institute for Materials Research, Tohoku University*

Quantum Spin Liquid State in a Square-Kagome Antiferromagnet

1. Introduction

New insight into the spin behavior in an exotic state of matter puts us closer to the next-generation spintronic devices. The quantum spin liquid (QSL) state is an exotic state of a magnet where the spin of electrons, which generally exhibits order at low temperatures, remains disordered. Observation of a QSL state is one of the most important goals in condensed-matter physics. However, the QSL state in two-dimensional (2D) systems has not been clearly observed in real materials owing to the presence of site-mixing disorder or deviations from ideal models. The lack of a suitable model material exhibiting the QSL hinders observations of the QSL state in the 2D spin-1/2 systems.

Square-kagome lattice (SKL) (see Fig. 1(a)) magnet is known as the highly frustrated 2D system. There is a possibility that the QSL ground states are realized in the antiferromagnetic $S = 1/2$ Heisenberg model on SKL [1]. However, the lack of a model compound for the SKL system has obstructed a deeper understanding of its spin state. Motivated by the present status on the study of the SKL system, we searched for compounds with the SKL containing Cu^{2+} spins and synthesized successfully the first compound of a SKL antiferromagnet, $KCu_6AlBiO_4(SO_4)_5Cl$ [2].

2. Experimental details

Single phase polycrystalline $KCu_6AlBiO_4(SO_4)_5Cl$ was synthesized by the solid-state reaction in which high-purity $KAl(SO_4)_2$, $CuCl_2$, $CuSO_4$, CuO, and Bi_2O_3 powders were mixed in a molar ratio of 2 : 1 : 6 : 5 : 1, followed by heating at 600°C for three days and slow cooling in air. The μSR experiments were performed using the spin-polarized pulsed surface-muon (μ^+) beam at the D1 beamline of the Materials and Life Science Experimental Facility (MLF) of the Japan Proton Accelerator Research Complex (J-PARC). The spectra were collected in the temperature range from 58 mK to 300 K using a dilution refrigerator and ^{4}He cryostat. The high-energy INS experiment was performed on the HRC, installed at the BL12 beamline in the MLF at J-PARC [3]. A GM-type closed cycle cryostat was used to achieve 5 K. The energy of incident neutrons was $E_i = 45.95$ meV, which yielded an energy resolution of $E_i = 1$ meV at the elastic position. The data collected by HRC were analyzed using the software suite HANA [4]. The INS spectrum in a wide momentum-energy range were measured using the cold-neutron disk chopper spectrometer AMATERAS installed in the MLF at J-PARC [5]. The sample was cooled to 0.3 K using a ^{3}He refrigerator. The scattering data were collected with a set of incident neutron energies, $E_i = 1.69$, 3.14 and 15.16 meV. The data collected by AMATERAS

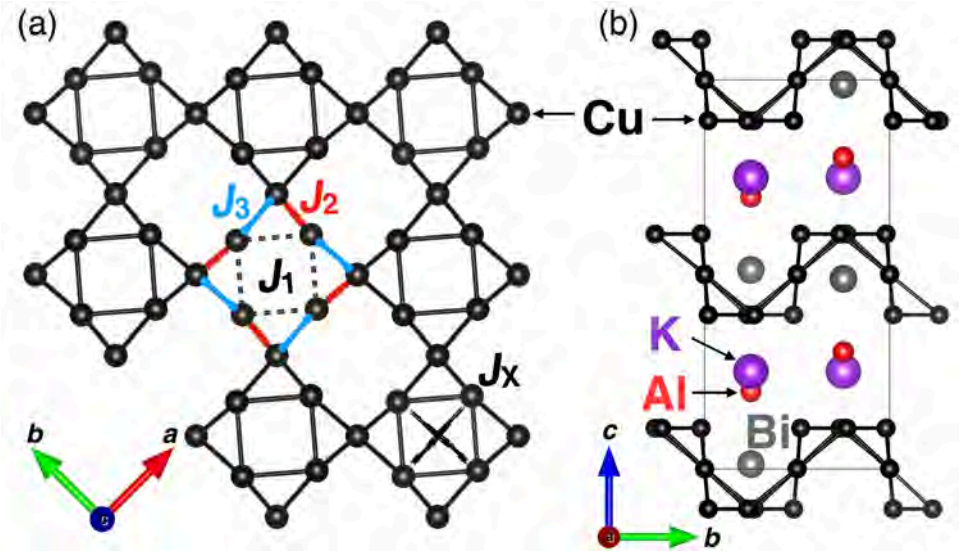

Figure 1. (a) Crystal structure of $KCu_6AlBiO_4(SO_4)_5Cl$. Square- kagome lattice consisting of the Cu^{2+} ions with nearest- neighbor exchange couplings $J1$, $J2$, $J3$ and next-nearest- neighbor exchange coupling JX. (b) Crystal structure of $KCu_6AlBiO_4(SO_4)_5Cl$ featuring a large inter-layer spacing.

were analyzed using the software suite UTSUSEMI [6].

3. Results and discussion

The synthesis of $KCu_6AlBiO_4(SO_4)_5Cl$ was conceived following the identification of the naturally occurring mineral atlasovite $KCu_6FeBiO_4(SO_4)_5Cl$ [7]. As shown Fig. 1(a), the SKL in the crystal structure of $KCu_6AlBiO_4(SO_4)_5Cl$ comprises the Cu^{2+} ions. In each SK unit, the square is enclosed by four scalene triangles. From this crystal structure, it is recognized that $KCu_6AlBiO_4(SO_4)_5Cl$ has three types of first neighbor interactions, J_1, J_2 and J_3, as shown in Fig. 1(a). One prominent and important feature of the present structure is the occupancy of nonmagnetic atoms in the interlayer space of the unit cell (Fig. 1(b)), which elongate the inter-layer spacing. Furthermore, the Cu^{2+} ions and nonmagnetic ions have different valence numbers in $KCu_6AlBiO_4(SO_4)_5C$, avoiding site mixing. Therefore, the crystal perfectness and high two-dimensionality of $KCu_6AlBiO_4(SO_4)_5Cl$ are ideal for studying the intrinsic magnetism on frustrated 2D magnets.

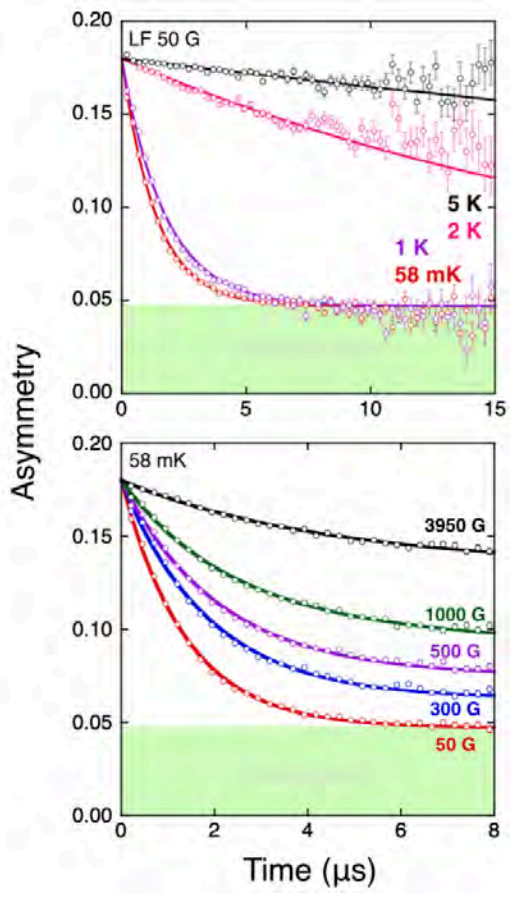

Figure 2. (a) LF-μSR spectra at representative temperatures. (b) LF-μSR spectra measured at 58 mK under several fields. The thick lines behind the data points are the fitted curve

To determine the magnetic parameters of $KCu_6AlBiO_4(SO_4)_5Cl$, we calculated the magnetic susceptibility, the magnetization curve at zero temperature. We succeeded in reproducing the magnetic susceptibility and magnetization curve of $KCu_6AlBiO_4(SO_4)_5Cl$ with the J_1-J_2-J_3 SKL model with J_1 = 135 K, J_2 = 162 K, J_3 = 115 K and g = 2.11 (for detail see [2]).

To confirm the absence of spin ordering caused by quantum fluctuations, we performed muon spin relaxation (μSR) experiments using the spin-polarized pulsed surface-muon (μ^+) beam at the D1 beamline of the J-PARC MLF. Figure 2(a) shows the weak longitudinal-field (LF) (= 50 G) μSR spectra at various temperatures. The weak LF was applied to quench the depolarization due to random local fields from nuclear magnetic moments. The spectra are well fitted by the exponential function

$$a(t) = a_1 e^{-\lambda t} + a_{BG}$$

where a_1 (= 0.133) is an intrinsic initial asymmetry, a_{BG} (= 0.047) is a constant background, λ is the muon spin relaxation rate. The weak LF signals at the lowest temperature (58 mK) decrease continuously without oscillations up to 15 μs, as shown in Fig. 2(a). The relaxation rates λ at 58 mK is 0.759 μs^{-1}. If this spectrum is due to static magnetism, the internal field can be estimated as λ/γ_μ (γ_μ is the muon gyromagnetic ratio), and thus it should be less than 10 G. However, as shown in Fig. 2(b), the relaxation is clearly observed, even in the LF at 3950 G, which is evidence for the quantum fluctuation of Cu^{2+} electron spins without spin ordering/freezing.

To grasp the whole picture of the spin excitation, we performed inelastic neutron scattering (INS) experiments using the high-resolution chopper spectrometer (HRC) and cold-neutron disk chopper spectrometer (AMATERAS) installed in the MLF at J-PARC. As shown in Fig. 3(a), flat signals at around E = 10 and 7 meV were observed at 5K. The signal due to magnetic excitation is generally enhanced at low-Q values, whereas phonon excitation is dominant at high-Q. The signals at around 10 and 7 meV increase with decreasing the Q, indicating that it comes from magnetic excitation. As shown in Fig. 3(b), streak-like excitation at Q = 0.8, 1.25, and 1.58 $Å^{-1}$ is clearly visible down to the elastic line, and its intensity increases continuously without signature of energy gap at least within the instrumental resolution. These INS data are consistent with a gapless continuum of spinon excitations. Judging from the findings above, the flat signals at 10 and 7 meV probably indicate a van Hove singularity of spinon continuum edges at this energy level.

4. Future plans

Our experimental results strongly suggest the formation of a gapless QSL in $KCu_6AlBiO_4(SO_4)_5Cl$ at very low temperature close to the ground state; however, they are inconsistent with the theoretical studies based on the J_1-J_2-J_3 SKL Heisenberg model. We calculated the dynamical spin structure factor $S(\boldsymbol{q}, \omega)$ in the SKL model with various values of the parameters, but we could not reproduce the INS experimental results. In the inelastic neutron-scattering experiment, in the low-energy region, the strongest intensity was registered at around $Q = 0.8$ Å^{-1} as shown Fig. 3(a), while in the dynamical DMRG method, it was around $Q = 1.3$ Å^{-1} [2]. Therefore, in order to realize the QSL state in the SKL, we must impose an additional condition, such as longer-range exchange interactions. Further experimental and theoretical studies would reveal the conditions, inducing the QSL state in SKL antiferromagnets.

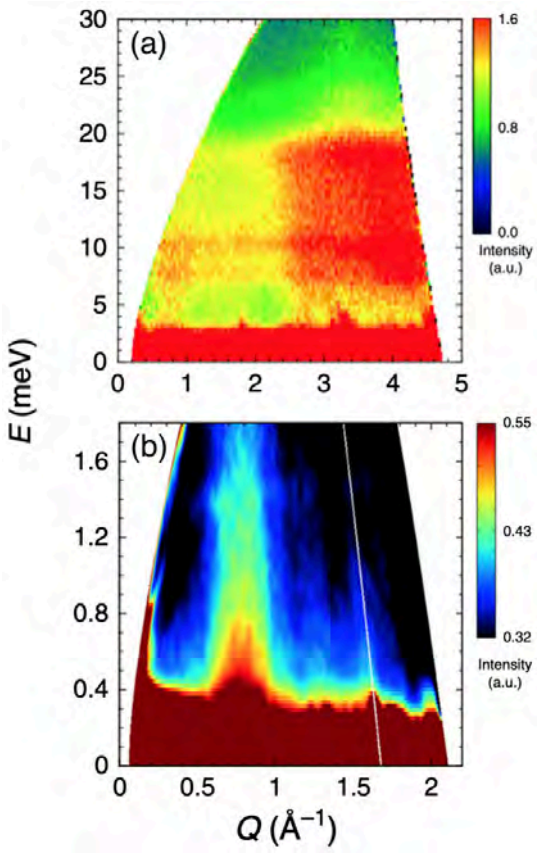

Figure 3. (a) INS spectra at 5 K observed using HRC with an incident neutron energy of 45.95 meV. (b) INS spectra at 0.3 K observed using AMATERAS with incident neutron energy of 3.14 meV.

References

[1] K. Morita et al., J. Phys. Soc. Jpn. **87**, 043704 (2018).
[2] M. Fujihala et al., Nat. Commun. **11**, 3429 (2020).
[3] S. Itoh et al., Nucl. Instr. Meth. Phys. Res. A **631**, 90 (2011).
[4] D. Kawana et al., J. Phys.: Conf. Ser. **1021**, 012014 (2018).
[5] K. Nakajima et al., J. Phys. Soc. Jpn. **80**, SB028 (2011).
[6] Y. Inamura et al., J. Phys. Soc. Jpn. **82**, SA031 (2013).
[7] V. Popova et al., Zap. Vses. Mineral. Obshch. **116**, 358 (1987).

M. Fujihala[1], K. Morita[2], R. Mole[3], S. Mitsuda[1], T. Tohyama[2], S. Yano[4], D. Yu[3], S. Sota[5], T. Kuwai[6], A. Koda[7,8], H. Okabe[7,8], H. Lee[7,8], S. Itoh[9,10], T. Hawai[9,10], T. Masuda[10,11], H. Sagayama[10], A. Matsuo[11], K. Kindo[11], S. Ohira-Kawamura[12], and K. Nakajima[12]

[1]*Department of Physics, Tokyo University of Science;* [2]*Department of Applied Physics, Tokyo University of Science;* [3]*Australian Nuclear Science and Technology Organisation;* [4]*National Synchrotron Radiation Research Center;* [5]*Computational Materials Science Research Team, RIKEN Center for Computational Science;* [6]*Graduate School of Science and Engineering, University of Toyama;* [7]*Muon Science Section, Materials and Life Science Division, J-PARC Center;* [8]*Institute of Materials Structure Science, KEK;* [9]*Neutron Science Section, Materials and Life Science Division, J-PARC Center;* [10]*Institute of Materials Structure Science, KEK;* [11]*The Institute for Solid State Physics, The University of Tokyo;* [12]*Neutron Science Section, Materials and Life Science Division, J-PARC Center*

Neutron Scattering Study on Half-Heusler ZrNiSn

1. Introduction

As a typical energy material, the thermoelectric (TE) material can be used to generate electricity based on the Seebeck effect when a thermal gradient exists or to transfer heat against temperature gradient based on the Peltier effect when an electric current is applied. The energy conversion efficiency for thermoelectric materials is limited by the Carnot's theorem and depends heavily on the materials' performance. Practical application of thermoelectric techniques requires to improve further the performance of thermoelectric materials, which is quantified by the thermoelectric figure of merit, $zT = \alpha^2\sigma T/(\kappa_{ele} + \kappa_{lat})$, where α, σ, T, κ_{ele} and κ_{lat} are the Seebeck coefficient, the electric conductivity, the absolute temperature, the electronic thermal conductivity and the lattice thermal conductivity, respectively. Hence, good TE materials should be 'Phonon Glass Electron Crystal', which means good electrical transport properties (assessed by the power factor, $\alpha^2\sigma$) and a low thermal conductivity. However, the relationship between the carrier concentration and mobility is still a mystery in this area.

2. Experiments

In FY2020, we applied superHRPD and HRC to measure the temperature- and composition-dependence of $ZrNiSn_{1-x}Sb_x$, respectively. Two series of compounds had been synthesized with/without hot pressed.

3. Study the lattice and phonons by neutron scattering

Half-Heusler (HH) material is a typical TE system to study both carrier concentration and mobility effects with the formula of ABX (A and B: transition metal elements, X: sp-valent elements such as Sn, Sb ect.). Figures 1(a) and 1(b) present the crystal lattice and the mobility versus concentration of ZrNiSn-based HH TE compounds at room temperature, respectively [1, 2]. Our recent work demonstrated a comprehensive understanding of both electronic and thermal transport properties in the ZrNiSn-based HH TE compounds. By combinations of inelastic neutron scattering, neutron diffraction, bulk measurements and first-principles calculations, we studied both polycrystalline and single-crystalline Sb-doped ZrNiSn and revealed that the electron-phonon interaction was beyond the expected acoustic phonon scattering, Figs. 2(a)–(d). Specifically, the ionized impurity, the grain boundary, and the polar optical phonon scatterings were shown to contribute significantly to controlling the electronic transport, Fig. 2(e). On the other side, those three scatterings could be well screened by mobile electron gas and the screening effect caused a non-monotonous dependence of the mobility on carrier concentration. Finally, we established a carrier scattering 'phase diagram' in the space of temperature and carrier concentration for the ZrNiSn-based compounds, Fig. 2(f), which could not only serve as a guide for optimizing the thermoelectric performance of HH thermoelectric materials, but also refresh the method of designing a new TE system [3]. Furthermore, the different effects of grain boundary scattering on electronic and thermal transport properties in lightly and heavily doped $NbFe_{1-x}Ti_xSb$ compounds provide a practical example for the applicability of the 'carrier scattering' phase diagram.

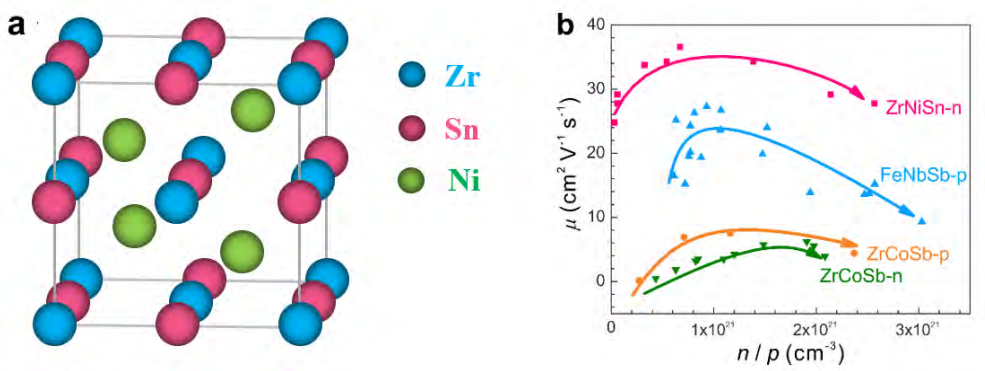

Figure 1. (a) Schematic of the layered crystal structure of ZrNiSn. (b) Room temperature carrier mobility versus carrier concentration n/p of several half-Heusler TE compounds [1].

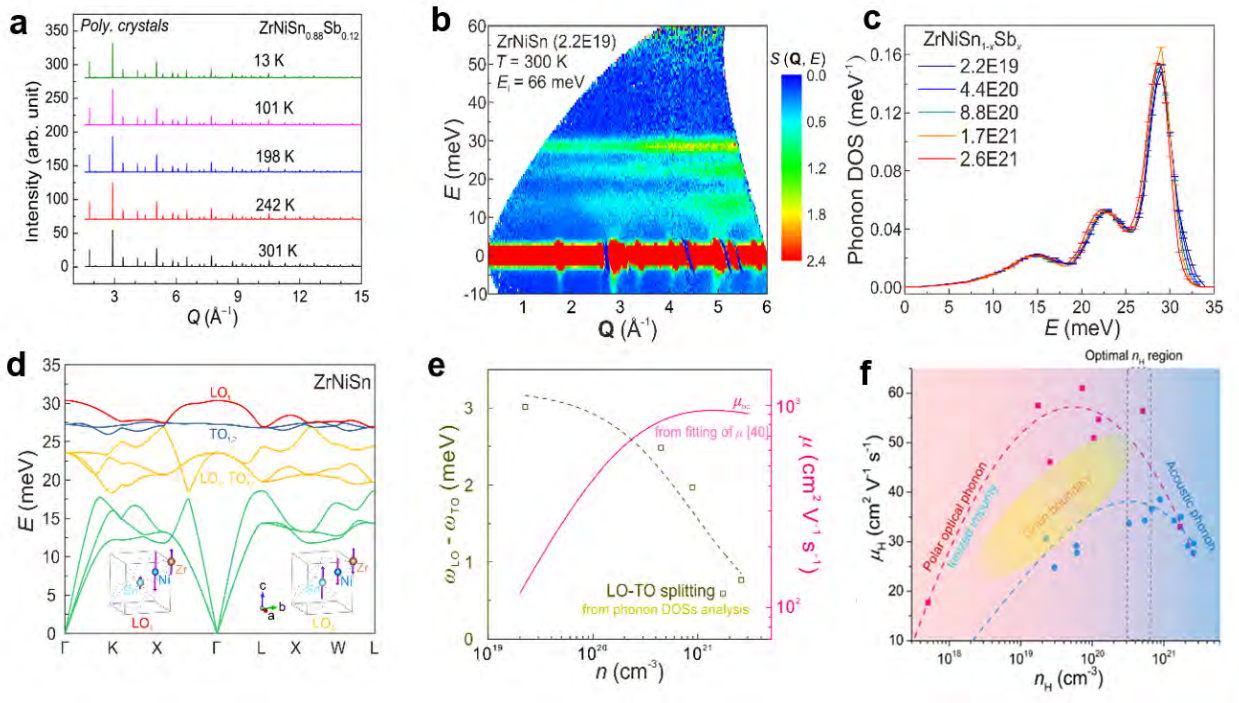

Figure 2. (a) The temperature-dependence of $ZrNiSn_{0.88}Sb_{0.12}$ by neutron diffraction (superHRPD); (b) S(Q,E) of ZrNiSn by inelastic neutron scattering; (c) Carrier concentration dependence of phonon density-of-state; (d) the simulated phonon dispersions of ZrNiSn by first-principles calculations; (e) Phonon density-of-state vs LO-TO splitting; (f) The phase diagram with single- and poly-crystalline data as function of the carrier concentration at 300 K.

4. Future plans

For the neutron diffraction measurement, we found that the atomic ratio of ZrNiSn is not 1 : 1 : 1, and there are more Ni at different atomic site in the system to scatter phonons and conduct electrons, which is regulated by the Sb-doping effect. We will analyze the diffraction data in detail and discuss the extra-Ni effect on the thermoelectricity of Half-Heusler ZrNiSn compound.

References

[1] C. Fu et al., Energy Environ. Sci. **8**, 216-220 (2015).
[2] Qiu Q et al., Adv. Energy Mater. **9**, 1803447 (2019).
[3] Q. Ren et al., Nat. Commun. **11**, 3142. (2020).

Q. Ren[1], C. Fu[2], Q. Qiu[3], S. Dai[4], Z. Liu[1], T. Masuda[5], M. Hagihara[6,7], S. Lee[8], S. Torri[6,7], T. Kamiyama[6,7], L. He[9,10], X. Tong[10,11], C. Felser[2], D. Singh[12], T. Zhu[3], J. Yang[4], and J. Ma[1]

[1]*Shanghai Jiao Tong University;* [2]*Max Planck Institute for Chemical Physics of Solids;* [3]*Zhejiang University;* [4]*Shanghai University;* [5]*Neutron Science Laboratory, Institute for Solid State Physics, University of Tokyo;* [6]*Neutron Science Section, Materials and Life Science Division, J-PARC Center;* [7]*Institute of Materials Structure Science, KEK;* [8]*Sokendai (The Graduate University for Advanced Studies);* [9]*Institute of Physics, Chinese Academy of Sciences;* [10]*Spallation Neutron Source Science Center, China;* [11]*Institute of High Energy Physics, Chinese Academy of Sciences;* [12]*University of Missouri-Columbia*

Multiple Magnetic Bilayers and Unconventional Criticality without Frustration in $BaCuSi_2O_6$

1. Introduction

A foundation stone of statistical physics is the theory of classical and quantum criticality, which states that all physical properties around a quantum phase transition (QPT) obey universal scaling laws dependent only on the dimension of space, *d*, and the dynamical exponent, *z*. The idea that perfectly frustrated competing interactions could lead to an effective reduction of *d* has been both proposed [1–2] and contested [3–4] to explain the physics of $BaCuSi_2O_6$.

This $S = 1/2$ material, known as Han Purple from its use as a pigment in ancient China, presents a three-dimensional (3D) stack of Cu^{2+} bilayers [Fig. 1] with dominant antiferromagnetic (AF) dimerization, significant intra-bilayer interactions, and a geometrically exact offset between adjacent bilayers, but was reported to show 2D scaling exponents around the field-induced QPT [1]. The discovery of inequivalent bilayers in $BaCuSi_2O_6$ [5, 6] raised the question of whether geometric frustration of the inter-bilayer interactions or structural modulation, or both, would be required to explain the apparent dimensional reduction [1]. Intensive investigation [2–4, 6, 7], has not yet resolved this issue, which in fact has far-reaching implications for any layered material.

A recent *ab initio* analysis [8] suggested effectively ferromagnetic (FM) intra-bilayer interactions, which would preclude the aforementioned frustration. Thus an experimental determination of the sign of these interactions is crucial for the understanding of this material.

2. Experimental

We have performed high-resolution inelastic neutron scattering (INS) measurements at 0.3 K on the direct-geometry time-of-flight (TOF) spectrometer AMATERAS in MLF at J-PARC using a single crystal of $BaCuSi_2O_6$, of weight 1.01 g, aligned with (*h* 0 *l*) in the scattering plane. The data were pre-processed and converted to energy-momentum space using the software Utsusemi [9]. Figures 2 (a)–2 (d) collect the TOF intensity data measured on AMATERAS (for incidents neutrons of energy $E_i = 9$ meV) along four high-symmetry directions in $\vec{Q}$ space as functions of energy transfer. Additional data were collected on EIGER at PSI up to larger values in $|\vec{Q}|$.

3. Results and discussion

Our results show clearly the presence of three distinct excitations in large regions of the Brillouin zone [Figs. 2(a), 2(b) and 2(d)]. These must result from three different types of bilayer, and so we label them *A*, *B*, and *C* in ascending order of energy.

We draw attention to the three qualitative features

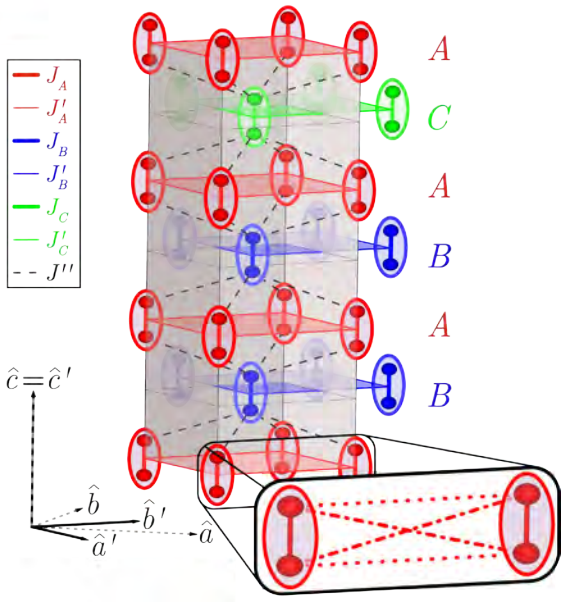

Figure 1. Schematic representation of one unit cell of the minimal magnetic model for $BaCuSi_2O_6$; $\{J_\sigma, J'_\sigma, J''\}$ are Heisenberg interactions. The three distinct bilayer types are labelled *A*, *B*, and *C*. The effective inter-dimer interaction parameters within each bilayer (J'_σ, edges of colored squares) result from four pairwise ionic interactions (inset).

of our data, which all lie beyond the results of Ref. [5].

(i) The minima of strongly dispersive modes in Figs. 2(a) and 2(b), give an unambiguous statement about the intra-bilayer interactions. (ii) Although the inter-bilayer interaction is very weak, making the bands in Fig. 2(c) almost flat, it can be determined from the variation of the intensity with Q_l. (iii) Where this band dispersion becomes Q_l -independent [Fig. 2(d)], the data can be used to establish the relative intensities of the three separate bilayer contributions [inset, Fig. 2(h)], from which we deduce a bilayer ratio of *A*:*B*:*C* = 3:2:1 [10].

Figures 3(a)–3(d) show mode energies and intensities as a function of $\vec{Q}$ along two high-symmetry directions, which were extracted by Gaussian fits to energy transfer cuts obtained from the AMATERAS data [Figs. 2(a) and 2(c)] and energy scans measured on EIGER. The modes *A*, *B*, and *C* could not be resolved individually due to the lower energy resolution on EIGER. Because the double peak structure in intensity of mode *A* along (0 0 Q_l) [Fig. 3(d)] is sensitive to the value of the inter-bilayer interaction parameter *J''*, the mode intensities of *A* and *B*+*C* are ideal to determine this interaction parameter.

A quantitative fit of the complete mode energy and intensity data [Figs. 3(a)–3(d)] using the model shown in Fig. 1, yields the intra-dimer interaction parameters $J_A = 4.275(5)$, $J_B = 4.72(1)$, and $J_C = 4.95(2)$ meV, effective intra-bilayer interactions $J'_A = -0.480(3)$, $J'_B = -0.497(8)$, and $J'_C = -0.57(1)$ meV, and the inter-bilayer interaction $J'' = -0.04(1)$ meV, where $J > 0$ refers to AF interactions and $J < 0$ to FM [10]. These optimal values were used to model the spectra shown in Figs. 2(e)–2(h), which are in excellent agreement with the measured spectra [Figs. 2(a)–2(d)]. In addition, these interactions were used to calculate the mode energies and intensities shown as solid lines in Figs. 3(a)–3(d). The signs and sizes of these interaction parameters are fully consistent with the *ab initio* analysis presented in Ref. [8]. Thus we have confirmed experimentally that the intra-bilayer interactions are effectively FM, which makes frustration of the inter-bilayer interactions impossible.

4. Quantum Monte Carlo (QMC) Simulations

These zero-field parameters have immediate consequences for the field-temperature phase diagram and the field-induced QPT. Figures 3(e)–3(g) show the results of QMC simulations of the six-bilayer (*ABABAC*) model [Fig. 1] using the interaction parameters we determined by INS [10]. The critical properties can be determined from the field-induced triplet densities (ρ_A, ρ_B, and ρ_C), shown in Fig. 3(f) for $T = 100$ mK, whose behavior agrees with nuclear magnetic resonance measurements [6]. From these we deduce that the effective

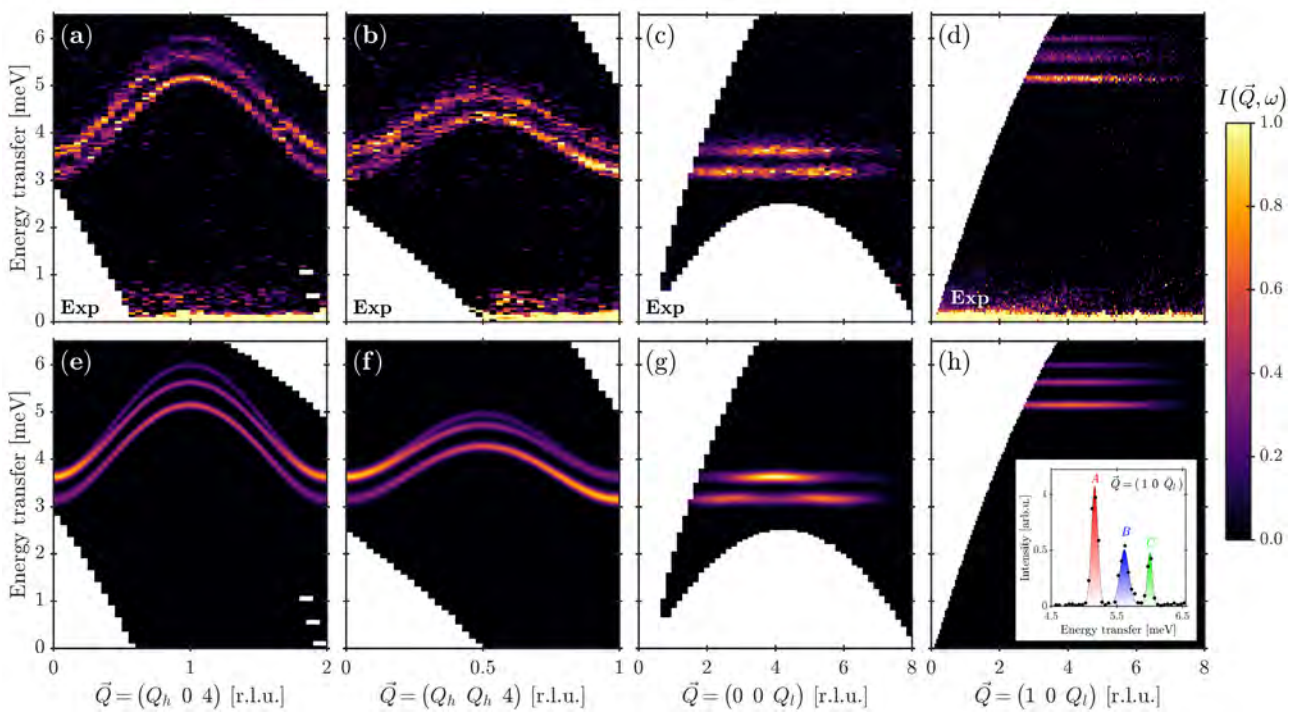

Figure 2. (a)–(d) Intensity, I($\vec{Q}$, ω) measured on AMATERAS for selected high-symmetry directions. (e)–(h) Corresponding spectra calculated with the fitted interaction parameters. The inset in panel (h) shows the intensity, $I(\omega)$, obtained by integrating over the $\vec{Q}$ ranges [0.95, 105] in Q_h, [−0.05, 0.05] in Q_k, and [4, 8] in Q_l, (denoted by $\bar{Q}_l$).

triplet tunneling between the bilayers remains finite at $H = H_{C1}$ and the dispersion is strongly anisotropic but 3D with a critical exponent $\phi = z/d = 2/3$ of a fully 3D QPT. However, the structural modulation introduces a new energy scale $(J'')^2/(J_B - J_A)$ [7]. Temperatures above this energy scale (approximately 0.04 K) may act to decouple the *A* bilayers, leading to an anomalous effective exponent $\phi(H - H_{C1}) \gtrsim 0.72$ [Fig. 3(g)].

5. Conclusion

The appearance of dimensional reduction near the QPT [1] is a consequence not of frustration [4] but only of the inequivalent bilayer units, which causes an anomalous and non-universal scaling regime. With rapidly improving technological capabilities for building atomically layered magnetic materials, this type of knowledge concerning emergent behavior due to layer modulation will be essential to the design of their physical properties.

References

[1] S. E. Sebastian et al., Nature **441**, 617 (2006).
[2] J. Schmalian and C. D. Batista, Phys. Rev. B **77**, 094406 (2008).
[3] M. Maltseva and P. Coleman, Phys. Rev. B **72**, 174415 (2005).
[4] O. Rösch and M. Vojta, Phys. Rev. B **76**, 180401(R); *ibid.* 224408 (2007).
[5] C. Rüegg et al., Phys. Rev. Lett. **98**, 017202 (2007).
[6] S. Krämer et al., Phys. Rev. B **76**, 100406(R) (2007); *ibid.* **87**, 180405(R) (2013).
[7] N. Laflorencie and F. Mila, Phys. Rev. Lett. **102**, 060602 (2009); *ibid.* **107**, 037203 (2011).
[8] V. V. Mazurenko et al., Phys. Rev. Lett. **112**, 107202 (2014).
[9] Y. Inamura et al., J. Phys. Soc. Jpn. **82**, SA031 (2013).
[10] S. Allenspach et al., Phys. Rev. Lett **124**, 177205 (2020).
[11] M. Jaime et al., Phys. Rev. Lett. **93**, 087203 (2004).

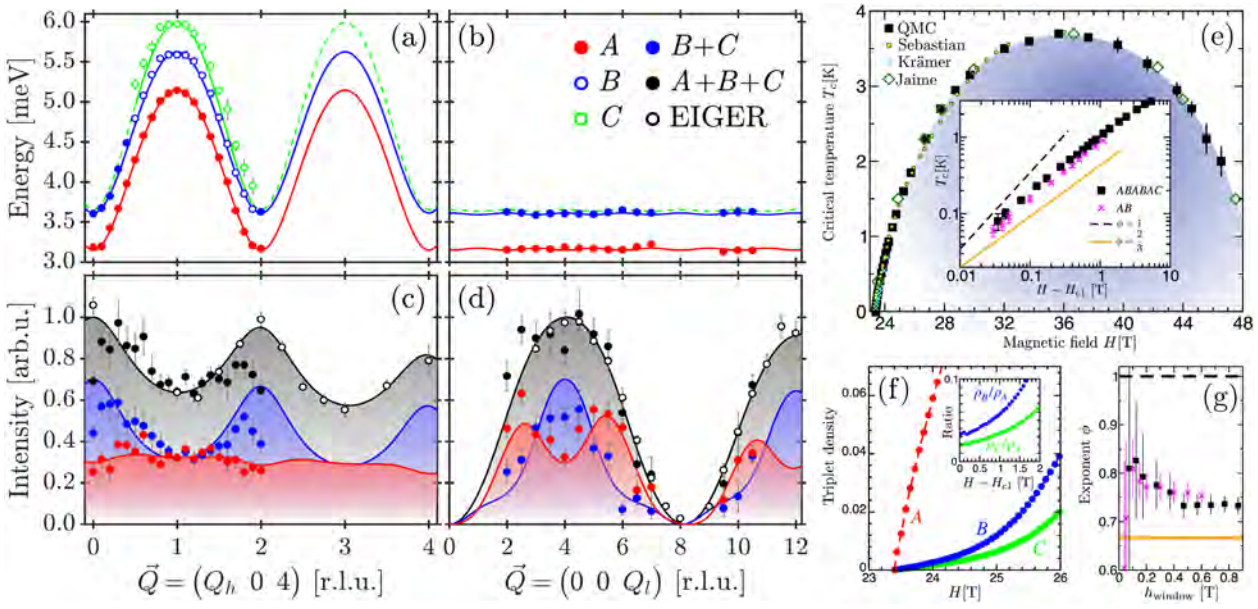

Figure 3. (a-d) Mode energies and intensities. Lines show calculated results; in (a) and (b) the solid blue line represents the mode energy of bilayer *B*, whereas in (c) and (d) it represents the mode intensity of *B*+*C*. The dashed green line denotes the mode energy of bilayer *C* calculated in the range where it was not distinguishable in the experiment. (e-g) QMC results for the *ABABAC* model [Fig. 1]. (e) (H, T) phase diagram of the field-induced ordered regime, compared with experimental data from Refs. [1, 6, 11]. (Inset) Power-law scaling obtained for *ABABAC* and *AB* models and compared with the scaling forms of pure 2D ($\phi = 1$) and 3D ($\phi = 2/3$) criticality. (f) Triplet populations in the three types of bilayer shown as functions of field at $T = 100$ mK. (Inset) Population ratios. (g) Effective exponent, ϕ, extracted from power-law fits of the QMC data [inset (e)] to a window of width h_{window}.

S. Allenspach[1,2], A. Biffin[3], U. Stuhr[3], G. S. Tucker[3,4], S. Ohira-Kawamura[5], M. Kofu[5], D. J. Voneshen[6], M. Boehm[7], B. Normand[1], N. Laflorencie[8], F. Mila[4], and C. Rüegg[1,2]

[1]Neutrons and Muons Research Division, Paul Scherrer Institute; [2]Department of Quantum Matter Physics, University of Geneva; [3]Laboratory for Neutron Scattering and Imaging, Paul Scherrer Institute; [4]Institute of Physics, École Polytechnique Fédérale de Lau-sanne; [5]Neutron Science Section, Materials and Life Science Division, J-PARC Center; [6]ISIS Facility, Rutherford Appleton Laboratory; [7]Institut Laue Langevin; [8]Laboratoire de Physique Théorique, CNRS and Université de Toulouse

Freezable and Unfreezable Hydration Water: Distinct Contribution to Protein Dynamics Revealed by Neutron Scattering

1. Introduction

Water is an indispensable solvent for protein to realize its functions. Especially, water molecules surrounding a protein, i.e. hydration water, play a crucial role for protein dynamics and functioning [1]. Neutron scattering is one of the powerful tools to study the effect of hydration on the protein dynamics, because it can directly monitor the latter by hydrating proteins with D_2O instead of H_2O. It is well known that protein dynamics is activated at ~220 K only when the protein is hydrated, which has been referred to as the protein dynamical transition [2]. This activation occurs after the dynamical coupling between protein and hydration water. However, the details of the coupling have not been fully understood.

A calorimetric study has determined that there are freezable and unfreezable types of hydration water existing on the protein surface [3, 4]. Recently, Yamamoto et al. observed some hydration water freezes when the hydration degree is high [5, 6]. Based on the observation, in this study, we tried to figure out how these freezable and unfreezable types of hydration water contribute to the activation of protein dynamics by using neutron scattering [7]. Freezing was monitored by q-dependent coherent scattering of ice, whereas protein dynamics were evaluated using energy-dependent incoherent scattering.

2. Experimental procedure

In this study, we used hen egg lysozyme with a controlled amount of hydration. To exchange solvent H_2O or exchangeable proton of protein by D_2O or deuterium, the protein powder was dissolved in D_2O, incubated for 12 h, followed by lyophilization. The procedure was repeated three times. This lyophilized sample was defined as the dehydrated state. Then the dehydrated powder was hydrated by D_2O. To change the amount of freezable hydration water, we prepared three different hydrated samples whose h values were 0.30, 0.37, and 0.48, respectively, where the h value indicates the mass ratio of water to protein. Above $h \sim 0.30$, freezable hydration water starts to accumulate on the protein surface [3]. The neutron scattering experiment was conducted using BL14, AMATERAS [8]. Data analyses were performed with the software suite Utsusemi [9].

3. Results

Figure 1 shows q-dependence of elastic scattering of the hydrated sample, where the data in the range of 0 ± 0.05 meV were integrated. The spectra were normalized using integrated values in the range of $0.5 \leq q \leq 1.5$ Å^{-1} at 83 K so that spectra among different hydration levels could be compared per the same amount of protein molecules. At $h = 0.37$ and 0.48, diffraction peaks characteristic to ice Ih of D_2O were clearly observed at around $q = 1.62$, 1.72, and 1.82 Å^{-1} in the low temperature regions, which are fairly identical to those calculated by simulation based on the structure of D_2O ice Ih [10] (indicated by bottom black lines in Fig. 1 in $h = 0.48$). On the other hand, no such diffraction patterns were observed in the sample at $h = 0.30$ or in the dehydrated one at 83 K (Fig. 1(a), gray line shown in $h = 0.30$). These results demonstrate that unfreezable hydration water only exists at $h = 0.30$, whereas freezable water emerges at the higher hydration levels ($h = 0.37$ and 0.48), which is consistent with the previous report in calorimetry where they were termed as uncrystallized and crystallized types of hydration water [3].

We found that the diffraction peaks possess temperature-hysteresis phenomena in the higher hydration levels. The intensity at $q = 1.62$ Å^{-1} is plotted in Fig. 1(b) as a representative of the diffraction peaks to confirm the hysteresis phenomenon. At $h = 0.48$, the diffraction peaks disappear at 273 K during heating from 83 K and re-appear at 243 K during cooling from 293 K. Similar trend was also observed at $h = 0.37$, whereas no such hysteresis occurred at $h = 0.30$. These data demonstrate that freezable hydration water and not unfreezable hydration water do contribute to the hysteresis phenomenon. This phenomenon is caused by supercooling, as mentioned in the calorimetry study [3, 4]. This is the first time to observe the diffraction of freezable hydration water and its temperature hysteresis phenomenon in neutron scattering.

Because the timescale of translational or rotational dynamics drastically changes upon freezing or melting, the protein dynamics would also possess a temperature-hysteresis phenomenon if they conjugate with freezing and melting of hydration water. To monitor how protein dynamics are affected with the temperature-hysteresis phenomenon, quasi-elastic scattering from protein was monitored. The energy resolution (full width at half

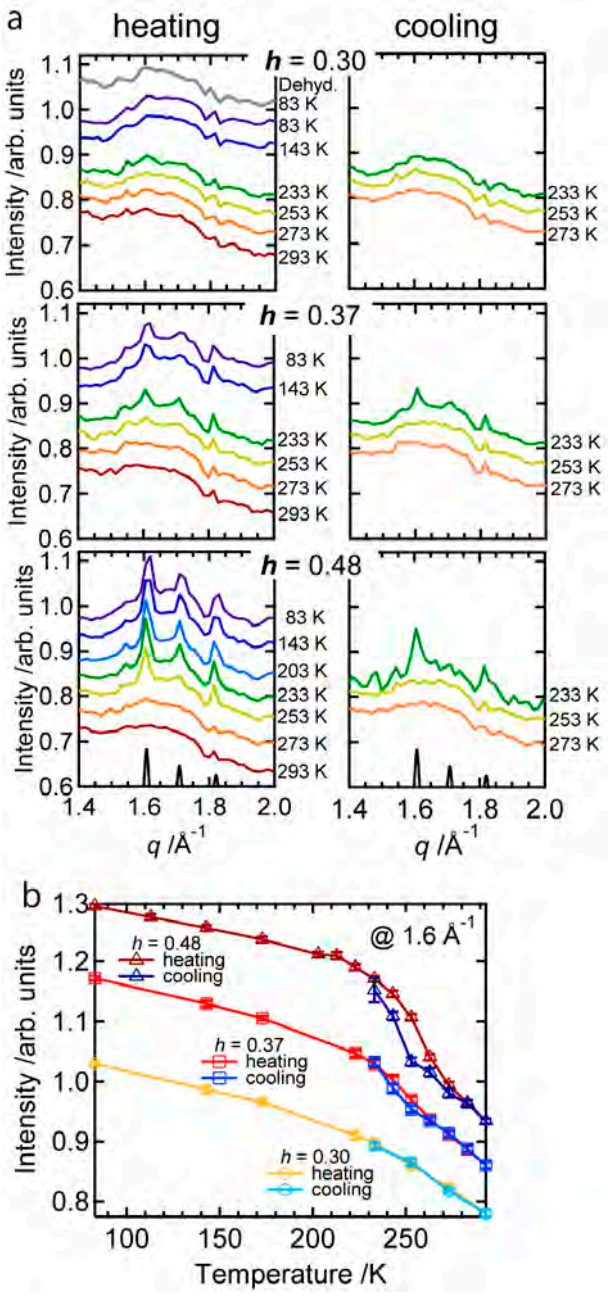

Figure 1. (a) q-dependence of the elastic neutron scattering of a hydrated lysozyme integrated at E = 0 ± 0.05 meV. The left and right panels show scattering profiles obtained in heating and cooling, respectively. The measurement cycle initiated by raising the temperature from 83 to 293 K, followed by decreasing to 233 K. The spectrum of the dehydrated sample (h = 0.12) at 83 K is also shown in the top of the left panel. The black curves in the bottom of both panels indicate a simulated diffraction pattern of D_2O ice Ih based on the crystal structure. (b) Comparison of temperature dependences of the scattering intensities at 1.62 Å^{-1} in the heating and cooling processes, respectively. Offset values are added on data at h = 0.37 and 0.48 for guiding the eyes.

maximum) was 0.1 meV, which corresponded to the resolution time of ~2×10^{-11} s. This means that dynamics faster than 2×10^{-11} s can be detected at this setup. Figure 2(a) and (b) shows the intensity plots of the incoherent-scattering spectra in the elastic ($E = 0 \pm 0.05$ meV) and quasi-elastic ($E = 0.2 \pm 0.05$ meV) regions, respectively, where the spectra were normalized using integrated values in the range of $0.5 \le q \le 1.5$ Å^{-1} at 83 K. In the hydrated states, apparent kinks were observed at around 220 K in comparison with the dehydrated state, both in the elastic and quasi-elastic components. This indicates that the activation of protein dynamics is induced upon hydration, similar to the protein dynamical transition [11].

However, no temperature hysteresis was observed on the elastic and quasi-elastic scattering components at h = 0.37 or 0.48, where apparent temperature hysteresis in the formation of ice is observed (shown in the insets of Fig. 2(a) and (b)). This result clearly demonstrates

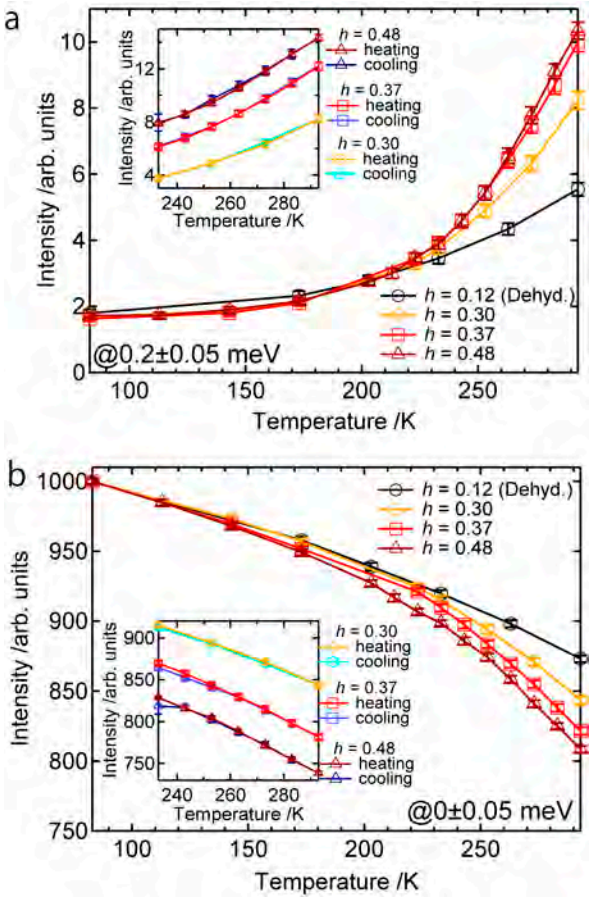

Figure 2. Elastic (a) and quasi-elastic (b) components of the energy-dependent spectra, which were normalized by an integrated value at $0.5 \le q \le 1.5$ Å^{-1} at 83 K. The insets show comparison of the results obtained in the heating and cooling processes where offset values are added on data at h = 0.37 and 0.48 for guiding eyes.

that the protein dynamics are seldom affected by the hysteresis phenomenon. This indicates that freezable hydration water does not affect the protein dynamics, and only unfreezable hydration water contributes to the activation of protein dynamics. We note here that the definition of freezable and unfreezable hydration water is valid as long as their exchanging rate is slower than the time scale of protein dynamics, including the temperature range we studied.

The degree of departure from the dehydrated state in the scattering components at h = 0.37 and 0.48 is larger than at h = 0.30, which is due to an increase in the number of unfreezable hydration water even after freezable hydration water starts to appear [3, 4]. A slightly higher activation of protein dynamics at h = 0.48 than 0.37 would be due to a rearrangement of unfreezable hydration water or its slight increase on the protein surface [2, 12].

4. Discussion

Unfreezable hydration water molecules are those strongly perturbed by protein, and thus they are supposed to directly interact with the protein surface via hydrogen bonds and electrostatic interactions. On the other hand, as our experimental result and previous experiments imply, hydration of freezable water starts to occur once the number of unfreezable hydration water is about to reach a plateau [3, 4]. Therefore, the freezable hydration water molecules could be those interacting with unfreezable hydration water, and not the protein surface. In this case, the dynamics of unfreezable hydration water couple with those of protein due to their strong interaction, so that the unfreezable hydration water and protein behave as if they were one integrated structure. Due to their strong interaction, the freezable hydration water would rather be independent from the unfreezable hydration water or protein, and thus the interaction of freezable hydration water with unfreezable hydration water would be much weaker. In this situation, the dynamics of the freezable hydration water decouple from those of the unfreezable hydration water, which could thus cause the dynamical decoupling of freezable hydration water from protein.

5. Future Plans

Using a different neutron spectrometer, such as BL02, DNA, it would be quite interesting to see if the dynamic decoupling observed in this study is still valid in a slower time scale, such as nanosecond or microsecond, in which proteins would realistically be functioning. Moreover, theoretical studies will help to reach a deeper understanding of the phenomenon.

References

[1] J. A. Rupley and G. Careri, Adv. Protein. Chem. **41**, 37-172 (1991).
[2] J. H. Roh, et al., Biophys. J., **91**, 2573-2588 (2006).
[3] A. Panagopoulou, et al., Food Biophys., **6**, 199-209 (2011).
[4] A. Panagopoulou, et al., BBA-Proteins Proteom., **1814**, 1984-1996 (2011).
[5] N. Yamamoto, et al., J. Phys. Chem. B, **122**, 1367-1377 (2018).
[6] N. Yamamoto, et al., J. Phys. Chem. B, **120**, 4743-4755 (2016).
[7] N. Yamamoto, et al., J. Phys. Chem. Lett., **12**, 2172-2176 (2021).
[8] K. Nakajima, et al., J. Phys. Soc. Jpn., **80**, SB028 (2011).
[9] Y. Inamura, et al., J. Phys. Soc. Jpn., **82**, SA031 (2013).
[10] S. W. Peterson and H. A. Levy, Acta Cryst., **10**, 70-76 (1957).
[11] S. Magazu, et al., J. Phys. Chem. B, **115**, 7736-7743 (2011).
[12] H. Nakagawa and M. Kataoka, J. Phys. Soc. Jpn., **79**, 083801 (2010).

N. Yamamoto[1], M. Kofu[2], K. Nakajima[2], H. Nakagawa[2,3], and N. Shibayama[1]
[1]School of Medicine, Jichi Medical University; [2]Neutron Science Section, Materials and Life Science Division, J-PARC Center; [3]Materials Sciences Research Center, JAEA

Morphological Analysis of Sulfonated Polyphenylene Membranes

1. Introduction

Proton conductive or proton exchange membranes (PEMs) have attracted considerable attention in applications to energy devices, such as fuel cells, batteries, and water electrolyzers. Perfluorosulfonic acid (PFSA) ionomer membranes have been used mostly as state-of-the-art PEMs because of their high proton conductivity, thin membrane flexibility, and dimensional and chemical stabilities [1, 2]. Sulfonated hydrocarbon PEMs which do not contain fluorine atoms are regarded as promising alternatives to PFSA ionomer membranes because of their potential cost effectiveness, wide variety of molecular structures, and environmental compatibility.

In the present study, we have examined the structure of sulfonated polyphenylene (SPP) membranes as emerging hydrocarbon PEMs [3–5]. In particular, the effect of *meta*- and *para*-phenylene sequence on the morphology and properties of the SPP membranes was investigated via NMR, TEM and SANS technique under controlled temperature and humidity conditions.

2. NMR analyses

Three kinds of sulfonated polyphenylenes, SPP-MP, -BP, and -QP (Fig. 1a), were synthesized from dichlorobenzenes, dichlorobiphenyls, and dichloroquinquephenylene, respectively, as hydrophobic comonomers. Figure. 1b shows ^{1}H NMR spectra obtained for the SPP-MP, -BP, and -QP (intensity was normalized by the largest aromatic peak of ***1***). Because of the similar composition (unsubstituted *meta*-phenylene / unsubstituted *para*-phenylene / sulfonated *para*-phenylene ratio), the ^{1}H NMR spectra were very similar. One of the noticeable differences was observed at ca. 7.9 ppm, assignable to the protons ***4*** in the unsubstituted *para*-phenylene connected with the unsubstituted *meta*-phenylene. The signal intensity at ca. 7.9 ppm was in the order SPP-QP > -MP > BP, suggesting this sequence (*i.e.*, the unsubstituted *para*-phenylene - the unsubstituted *meta*-phenylene) was most contained in the SPP-QP. The result is reasonable considering the fact that the unsubstituted *para*-phenylene in SPP-QP is connected solely with the unsubstituted *meta*-phenylene, while all components (unsubstituted *meta*-phenylene, unsubstituted *para*-phenylene, and sulfonated *para*-phenylene) can be connected with each other for SPP-BP and -MP.

Another significant difference was observed in the integral ratio of the three signals at ca. 8.0–8.5 ppm correlated with the protons a in the sulfonated *para*-phenylene (SP). We assigned the three peaks of protons ***a***, as "unsubstituted phenylene - *SP* (***a*$_1$**) - unsubstituted phenylene", "SP - *SP* (***a*$_2$**) - unsubstituted phenylene", and "SP - *SP* (***a*$_3$**) - SP" (Fig. 1c), and defined the integral ratio of (***a*$_1$**/***a*$_1$**+***a*$_2$**+***a*$_3$**) as the randomness of the SP unit or the isolated hydrophilic component (SP) ratio in the backbone for SPP-QP prepared with different polymerization promoters (please note that peaks ***a*$_3$** and **2** were overlapping). The ratio of ***a*$_3$** was calculated using the following equation:

$$a3 = I - NX - 2Y - a1 - a2 \quad (1)$$

where *I* is the total and ***a*$_1$**, ***a*$_2$** and ***a*$_3$** are the integral values estimated from the ^{1}H NMR spectra, N is the number of protons in the hydrophobic components, and X and Y are the compositions of hydrophilic and hydrophobic

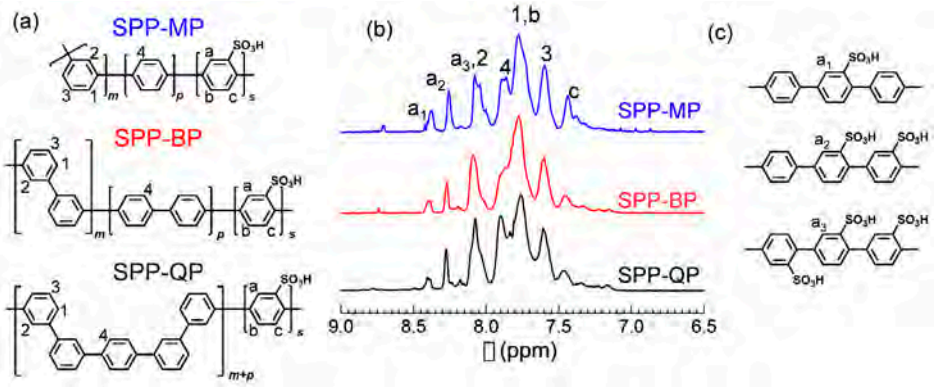

Figure 1. (a) Chemical structures and (b) ^{1}H NMR spectra of SPP-MP, SPP-BP, and SPP-QP. (c) Possible sequences of the sulfophenylene (SP) units.

segments calculated from the titrated ion exchange capacity (IEC) values. The randomness of the SP unit was calculated using the titrated IEC values and was in the order, SPP-MP (51%) > -BP (32%) > -QP (19%), indicating that the hydrophobic components dominated the sequence of the hydrophilic component.

3. TEM images

Transmission electron microscopic (TEM) images were obtained to examine the effect of the sequence (or randomness) of the hydrophilic components on the membrane morphology under dry conditions. Figure 2 shows the cross-sectional TEM images of the SPP-MP, -BP, and -QP membranes stained with Pb^{2+} ions, in which the dark areas represent the hydrophilic clusters composed of lead-stained sulfonic acid groups and bright areas represent the hydrophobic clusters. The membranes showed typical phase-separated morphology based on the hydrophilic/hydrophobic differences in the components, although the interfaces of the domains were not very distinct due to the rigid polyphenylene structure. The size of the clusters was in the order, SPP-MP (ca. 1.8 ± 0.4 nm) = -BP (ca. 1.8 ± 0.3 nm) < -QP (ca. 2.8 ± 0.2 nm) for hydrophilic, and SPP-MP (ca. 1.9 ± 0.4 nm) = -BP (ca. 2.0 ± 0.5 nm) < -QP (ca. 2.7 ± 0.8 nm) for hydrophobic, respectively. The result is reasonable, because the higher randomness should lead to a smaller sequence of the hydrophilic component. As the randomness increased, more isolated SP units must have been included, suppressing the self-aggregation of the components.

4. SANS analyses

To investigate the morphology of the SPP membranes and the structure of the absorbed water molecules, SANS measurements were carried out at 80°C under controlled humidity. Deuterium has a large positive coherent scattering length, while hydrogen has a negative scattering length, and thus, hydrophilic clusters adsorbing D_2O have large contrast in comparison to the hydrophobic clusters. Figure 3 shows SANS patterns of SPP-MP, -BP, and -QP membranes humidified with D_2O. Weak peaks were observed for SPP-BP and -QP membranes, while no peaks were observed for SPP-MP membrane under dry conditions (0% RH). As the humidity increased, the scattering intensity increased in all samples. SANS patterns were more related with the structure of water filling in the membranes. The development of the peak (ca. q = 0.7 nm^{-1}) with humidity was most pronounced for the SPP-QP membrane. From the background-subtracted profiles, the slopes in the Porod

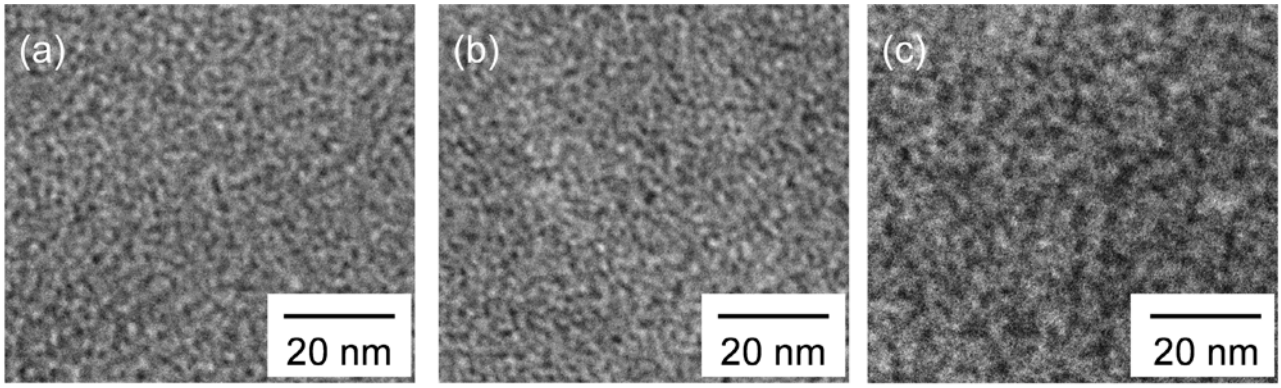

Figure 2. TEM images of (a) SPP-MP, (b) SPP-BP, and (c) SPP-QP membranes.

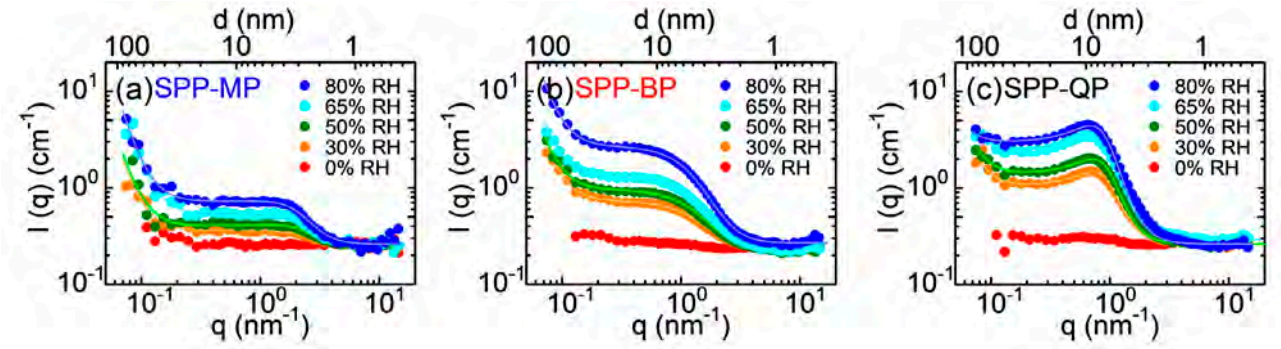

Figure 3. SAXS patterns of (a) SPP-MP, (b) SPP-BP, and (c) SPP-QP membranes humidified with D_2O.

region were roughly estimated to be ca. -1 for SPP-MP, -2 for -BP, and -3 for -QP membranes at 80% RH, suggesting that water clusters were rod-like for -MP, thin disk-like for -BP and more spherical for -QP membranes. At 80% RH, the d values were 3.1 nm, 10.4 nm, and 9.0 nm for SPP-MP, -BP, and -QP membranes, respectively, suggesting that lower randomness of the hydrophilic component led to the formation of more uniform, larger water clusters. Then, the sum of the power law and Teubner - Strey (TS) model was applied to the curves for more quantitative analysis. The curve fitting was performed using the following equation,

$$I(q) = \frac{A}{q^n} + \frac{B(8D^4\pi)}{\xi[16\pi^4+8D^2\pi^2(\xi^{-2}-q^2)+D^4(\xi^2+q^2)]} + C \quad (2)$$

where *A*, *B* and *C* are constants of each component. The ξ and D terms are the domain size and interdomain distance, respectively. Figures 4a and b show the humidity dependence of the ξ and D values. It is noted that both ξ and D values showed only minor dependence on the humidity. The ξ value of SPP-QP (ca. 2.45 nm at 80% RH) was much larger than those of SPP-BP (ca. 0.88 nm at 80% RH) and SPP-MP (ca. 0.67 nm at 80% RH). This result is reasonable, because the smaller randomness of the SP unit must have led to larger water-containing hydrophilic clusters. The D value was not correlated well with the randomness and was higher for SPP-BP and -QP (ca. 7.9 nm) than for SPP-MP (ca. 3.8 nm). In Figure 4c ξ/D is plotted: it represents the connectivity of the water clusters as a function of the humidity. The ξ/D values were in the order SPP-QP > -MP > -BP, suggesting that the hydrophilic clusters were more interconnected for the SPP-QP membrane, while those in the SPP-BP membrane were rather isolated. The connectivity was not dependent on the humidity but was nearly constant in the humidity range from 30 to 80% RH. Although the existence of dead-end channels has not been well-supported by the SANS analyses, relatively small ξ/D values are indicative of dead-end and/or isolated channels.

5. Conclusions

In the SPP membranes, the sequence of the hydrophilic component (or randomness) had a great impact on the morphology. SPP-QP, with smaller randomness of the sulfophenylene units, contained more uniform, larger water clusters with higher interconnectivity. Increasing the humidity led to an increase in the number of water clusters but did not change their size, interdomain distance, or interconnectivity. The interconnectivity was highly correlated with some important membrane properties (proton conductivity and mechanical properties), which are not included in this report but have been covered in detail in our previous publication [5].

References

[1] M. A. Hickner et al., Chem. Rev., **104** 4587 (2004).
[2] M. M. Whistna et al., Proc. Natl. Acad. Sci. USA, **116** 4899 (2019).
[3] J. Miyake et al., Sci. Adv., **3** eaao0476 (2017).
[4] K. Shiino et al., Chem. Commun., **55** 7073 (2019).
[5] K. Shiino et al., ACS Appl. Polym. Mater., **2** 5558 (2020).

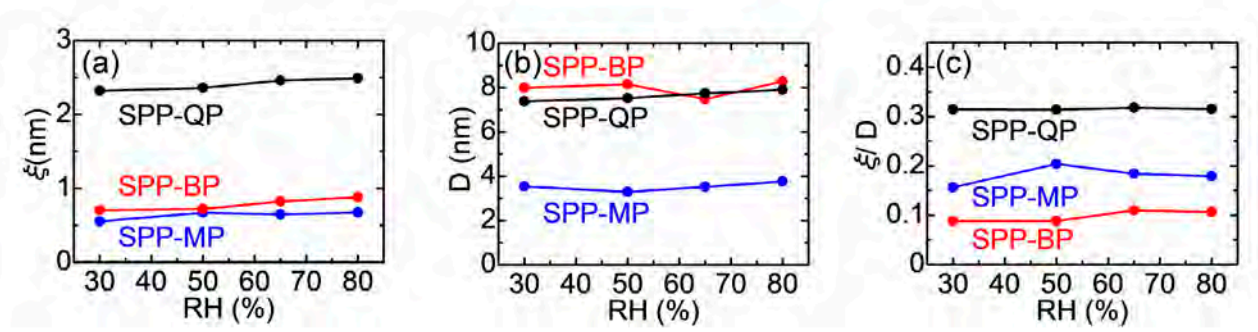

Figure 4. Humidity dependence of (a) domain size (ξ), (b) interdomain distance (D), and (c) ξ/D values of SPP-MP, SPP-BP and SPP-QP membranes calculated from the SANS patterns in Figure 3.

K. Miyatake[1,2,3], K. Shiino[1], J. Miyake[1], T. Otomo[4,5], T. Yamada[6], H. Arima[6], K. Hiroi[4], and S. Takata[4]

[1]*Clean Energy Research Center, University of Yamanashi;* [2]*Fuel Cell Nanomaterials Center, University of Yamanashi;* [3]*Department of Applied Chemistry, Waseda University;* [4]*Neutron Science Section, Materials and Life Science Division, J-PARC Center;* [5]*Institute of Materials Structure Science, KEK;* [6]*Neutron Science and Technology Center, CROSS*

Magnetoelectric Responses in the Chiral Polar Magnet Ni_2InSbO_6

1. Introduction

The space-inversion breaking in magnetic matter gives rise to the antisymmetric exchange interaction between neighboring magnetic moments. The antisymmetric interaction may compete with the conventional exchange, which often results in noncollinear magnetic structures. Such a noncollinear magnetic structure may induce the magneto-electric coupling in insulating magnets and the anomalous transport in itinerant magnets.

Corundum-type sesquioxide compounds are one of the most common mineral family on earth. While the corundum structure is centrosymmetric, the cation sites are not on the inversion center or on the reflection mirror. Therefore, some cation order may break the space inversion and/or mirror reflection. The cation-ordered corundum oxide compounds have hence been considered as a good playground for exploring a large magneto-electric coupling. Ni_3TeO_6 was reported to exhibit a large change in electric polarization (~3 mC/m^2) across the magnetic transition temperature [1].

Ni_2InSbO_6 was first synthesized and confirmed to be isostructural with Ni_3TeO_6 by S. A. Ivanov *et al.* [2]. Ni, In, and Sb atoms are ordered in the corundum-based structure, as shown in Fig. 1. A half of the magnetic Ni ions and the same number of In ions are arranged to form a little buckled Ni-In sheets of ordered honeycomb (like hexagonal boron nitride) perpendicular to the c axis (in this report, we use the hexagonal setting). The Ni-In sheets alternate with Ni-Sb sheets of a similar ordered honeycomb. Each Ni ion occupies a distorted octahedron site formed by six oxygen atoms. The NiO_6 octahedron is connected with other six NiO_6 octahedra on neighboring sheets by sharing corners and with three InO_6 or SbO_6 octahedra in the same sheet by sharing edges. A theoretical study on Ni_3TeO_6 proposed dominant antiferromagnetic exchange interaction between neighboring Ni layers, which should stabilize the layered antiferromagnetic order [3]. On the other hand, the chiral polar crystal structure may favor noncollinear magnetic order. The previous powder neutron diffraction study proposed helimagnetic order of screw or cycloid type with a 15-nm modulation along the *b* axis [2]. The long-wavelength modulation is attributable to the antisymmetric exchange interaction originating from the inversion breaking [4].

Here we carry out a neutron diffraction study by using single crystals to pin down the magnetic structure and to reveal the magnetic-field effect. We also measure the magnetization and magnetoelectric effect.

2. Methods

Single crystals of Ni_2InSbO_6 were grown by the chemical vapor transport method [5]. The crystals had a large *c* plane. Low-field magnetization was measured as a function of magnetic field and temperature by using a commercial magnetometer (MPMS-XL, Quantum Design). Electric polarization along the c axis was measured on a homochiral domain with an area of 0.74 mm^2 by integrating the displacement current, measured by using an electrometer (6517A, Keithley). The dielectric

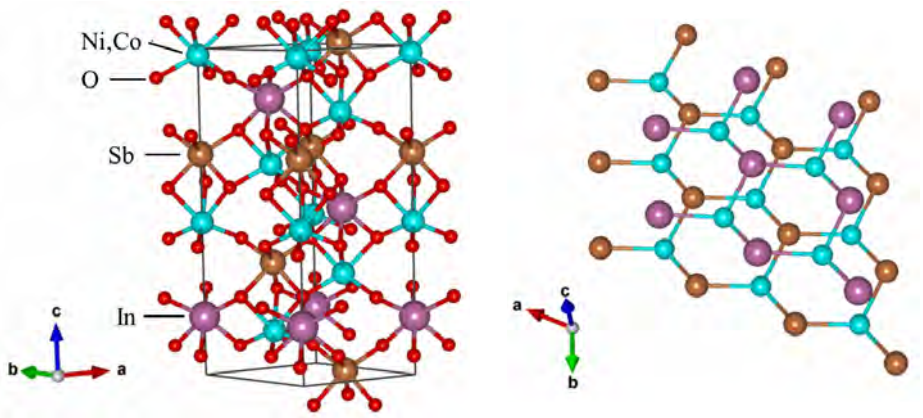

Figure 1. Crystal structure of Ni_2InSbO_6. Oxygen atoms are omitted.in the right panel.

constant along the c axis was measured on a thin crystal using an LCR meter (E4980A, Agilent). Pulsed-magnetic-field measurements of the magnetization and electric polarization were performed at the Institute for Solid State Physics, the University of Tokyo.

A neutron scattering measurement was performed by using the time-of-flight diffractometer TAIKAN on BL15 [6]. A single crystal of Ni_2InSbO_6 was mounted in a refrigerator equipped with a superconducting magnet.

3. Results and discussions

Temperature dependence of magnetization at 0.1 T shows the presence of a magnetic transition at 77 K. Electric permittivity also shows a peak at the magnetic transition temperature, implying some coupling between the magnetism and electricity in this compound. Electric polarization gradually changes by about 2 mC/m^2 across the transition.

Figure 2 shows neutron diffraction patterns in the reciprocal (h k 3) plane around a fundamental Bragg peak (003). Ring-like satellite is observed in the pattern (top panel) collected at 60K after zero-field cooling. The radius of the ring agrees with the previously reported magnetic modulation period [2]. On the other hand, the ring implies that the modulation axis would not be clamped to the b^* or equivalent axis but can vary in the c plane. It is here noteworthy that a hexagonal unit cell contains three pairs of Ni-In and Ni-Sb sheets. The magnetic satellite peaks strongly suggest that the Ni moments on each sheet are gradually modulated in the sheet and that the sheets are antiferromagnetically stacked along the c axis.

We also measured the diffraction pattern after cooling the crystal in a magnetic field of 6 T applied along the a^* axis. The ring was merged into two broad spots along the magnetic field. This result may be explained by assuming the screw-type magnetic order.

Figure 3 shows the magnetization and electric polarization at various temperatures measured by using a pulsed magnet. When the magnetic field is applied along the sheet in the helimagnetic phase, a clear metamagnetic transition is observed. The magnetization curve is convex below the metamagnetic transition and almost linear in the high-field phase. The typical screw magnetic order is changed to a conical structure and the cone axis is reduced to zero with the increase of the magnetic field parallel to the screw axis. The observed magnetization is not consistent with the scenario. The linear magnetization curve with a non-zero magnetization extrapolated to zero field is explained by assuming

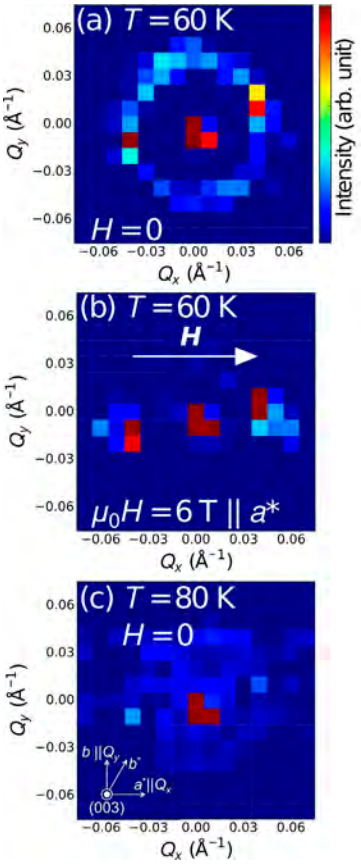

Figure 2. Neutron diffraction patterns in the reciprocal (h k 3) plane around a fundamental Bragg peak (003). (a) Pattern in the absence of the magnetic field after zero-field cooling. (b) Pattern in a magnetic field of 6 T applied along the a* axis after cooling the crystal in the field. (c) Pattern at 0 T and 80K.

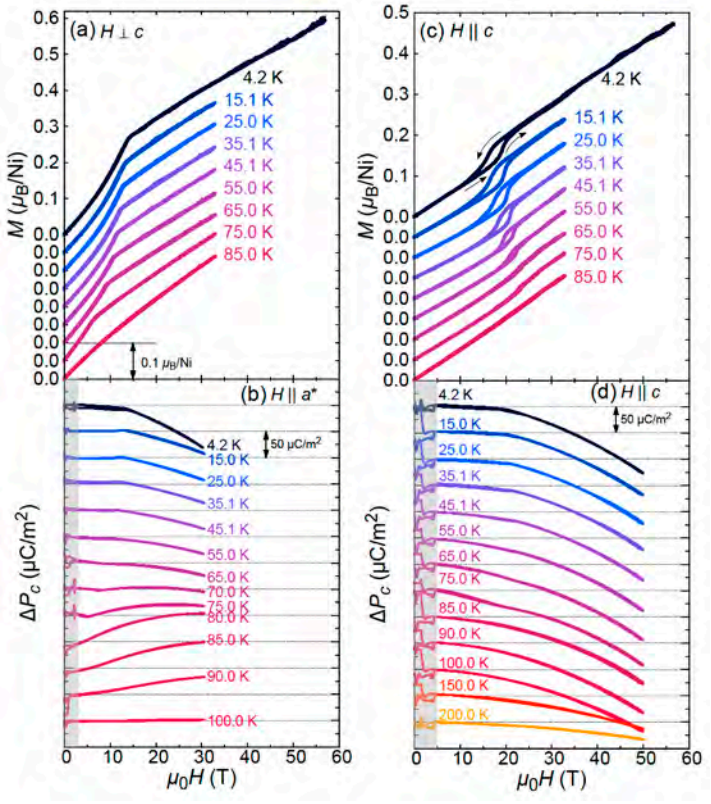

Figure 3. Magnetic field dependence of magnetization and electric polarization at various temperatures. The electric polarization is measured parallel to the c axis. Pulsed magnetic field is applied (a, b) perpendicular to the c axis and (c, d) parallel to the c axis. Low-field parts of polarization measurements are affected by the noise of starting pulsed magnetic field.

the existence of canted layered antiferromagnetic structure in the high-field phase.

A magnetic field along the *c* axis induces a first-order metamagnetic transition accompanied by a clear hysteresis. The magnetic structure remains unrevealed yet.

4. Conclusion

Neutron diffraction of Ni_2InSbO_6 indicates the screw type helimagnetic structure based on the layered antiferromagnetism. The application of a magnetic field induces a magnetic transition accompanied by a fairly large magnetoelectric effect.

References

[1] Y. S. Oh, S. Artyukhin, J. J. Yang, V. Zapf, J. W. Kim, D. Vanderbilt, and S.-W. Cheong, Nat. Commun., **5** 1 (2014).
[2] S. A. Ivanov, R. Mathieu, P. Nordblad, R. Tellgren, C. Ritter, E. Politova, G. Kaleva, A. Mosunov, S. Stefanovich, and M. Weil, Chem. Mater., **25** 935 (2013).
[3] F. Wu, E. Kan, C. Tian, and M.-H. Whangbo, Inorganic Chem., **49** 7545 (2010).
[4] I. E. Dzyaloshinskii, Sov. Phys. JETP, **19** 960 (1964).
[5] Y. Araki, T. Sato, Y. Fujima, N. Abe, M. Tokunaga, S. Kimura, D. Morikawa, V. Ukleev, Y. Yamasaki, C. Tabata, H. Nakao, Y. Murakami, H. Sagayama, K. Ohishi, Y. Tokunaga, and T. Arima, Phys. Rev. B, **102** 054409 (2020).
[6] https://mlfinfo.jp/ja/bl15/

T. Arima[1], Y. Araki[1], T. Sato[1], Y. Fujima[1], N. Abe[1], H. Sagayama[2], M. Tokunaga[3], K. Ohishi[4], and Y. Tokunaga[1]
[1]*Department of Advanced Materials Science, University of Tokyo;* [2]*Institute of Materials Structure Science, KEK;* [3]*Institute for Solid State Physics, University of Tokyo;* [4]*Neutron Science and Technology Center, CROSS*

Water Distribution in Nafion® Thin Films on Hydrophilic and Hydrophobic Carbon Substrates

1. Introduction

Polymer electrolyte membrane fuel cells (PEMFCs) have attracted considerable attention during the past two decades as clean and sustainable energy conversion devices. Hydrogen fuel cells emit only water and not carbon dioxide, which can cause global warming at the point of operation. Traditionally, a critical part of a PEMFC is the catalyst layer (CL), which is composed of Pt nanoparticles on carbon supports (Pt/C) and perfluorosulfonic acid ionomers, such as Nafion. Since protons and oxygen must be transferred through the Nafion, the transport properties limit the power generation performance. During normal operation, a polymer electrolyte membrane (PEM) experiences a range of humidity conditions. These conditions can influence both the water content and the connectivity of the hydrophilic clusters of the PEM, which control the proton conductivity [1].

In this study, we performed H_2O and D_2O double contrast neutron reflectivity (NR) measurements to investigate the water uptake properties of Nafion thin films in CLs, focusing on the effects of hydrophilicity on the carbon surface as well as the humidity conditions. For this purpose, we prepared hydrophobic and hydrophilic carbon surfaces using ultraviolet (UV) irradiation. In the NR experiments conducted on these films, 80% relative humidity (RH) water vapor and bulk water were used to determine the effects of the humidity conditions. Based on the double contrast NR data, we evaluated the volume occupancies of water and Nafion in the thin films as functions of the distance from the substrate.

2. Experimental

We prepared ~25-nm-thick Nafion films by spin coating Nafion solutions on the hydrophobic and hydrophilic carbon films. The Nafion solution (D2020) underwent further dilution to a concentration of 1.0 wt% using 1-propanol. Finally, we annealed the obtained films for 2 h at 140°C in a vacuum oven to mimic PEMFCs formed by hot-pressing more closely.

We performed the NR measurements using the SOFIA reflectometer at the Materials and Life Science Experimental Facility (MLF) at J-PARC, Japan. The obtained reflectivity data were analyzed using the Motofit macro package of Igor Pro. Notably, the NR experiments were performed with two scattering contrasts on the same system using H_2O and D_2O (double contrast measurements). This method enabled quantitative evaluation of the amount of water penetrating the Nafion thin films.

3. Results and discussion

Figures 1(a) shows the NR curves and the fitting results for Nafion thin films on the hydrophobic carbon in 80% RH H_2O and D_2O vapor. The fit between the calculated and observed NR curves is good for both the H_2O and D_2O contrasts. Then, we evaluated the corresponding SLDs based on the fitting results, as shown in Fig. 1(b). To examine the distribution of water in the Nafion thin films quantitatively, we directly evaluated the amount of water in the films in both water vapor and bulk water. Then, we evaluated the distributions of water and Nafion in the thin film along the depth direction from the SLD profiles in Fig. 2.

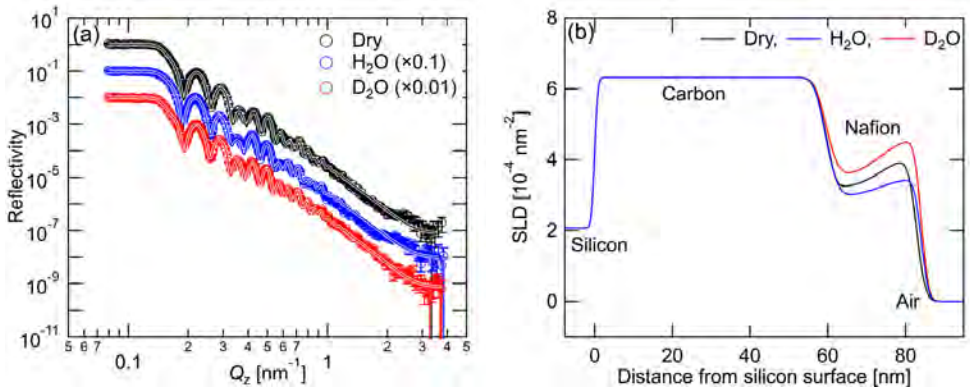

Figure 1. (a) NR curves and fitting results (solid curves) for the Nafion thin film on hydrophobic carbon in dry nitrogen (black), 80% RH H_2O vapor (blue), and 80% RH D_2O vapor (red). (b) SLD profiles of the Nafion thin films on hydrophobic carbon in dry nitrogen (black), 80% RH H_2O vapor (blue), and 80% RH D_2O vapor (red). Adapted with permission from [7]. Copyright 2020 American Chemical Society.

Figures 2 present the volume occupancy evaluated for water and Nafion in the Nafion thin films on hydrophobic(a) and hydrophilic(b) carbon in 80% RH water vapor. Figures 2 show that the Nafion density is higher at the air than in the middle of the thin films on hydrophobic and hydrophilic carbon. This tendency must be due to the crystallization of Nafion near the surface. This may be because heterogeneous nucleation more easily occurs in material interface than in bulk. On the other hand, the Nafion density is higher at the carbon interface than in the middle only on hydrophilic carbon. This characteristic likely occurs because of the charged side chains in Nafion accumulated near the hydrophilic carbon surface due to the hydrophilic nature of carbon. In addition, a water-rich layer exists near the hydrophilic carbon surface, closer than the dense Nafion layer.

Using the H_2O and D_2O double contrast, we evaluated the depth profiles of water and Nafion in the thin films quantitatively. However, these measurements indicated other problems. Summing the volume occupancies of Nafion and water in Figures 2(a) and 2(b) yielded less consistency in the thin films, and ~0.80 was obtained in a case in which the occupancy was particularly small when calculated using the bulk values of density from the literature [2]. We considered two feasible physical scenarios. One is the existence of excess free volume or voids in the Nafion thin film. Another possibility is as follows. Exposure of a Nafion thin film to water vapor or immersion in bulk water means that an exchange of water occurs between the inside and outside. However, this scenario assumes the existence of water in the film that cannot be exchanged with outside water. The former and latter are referred to as exchanged water (EW) and residual water (RW), respectively. Further, we assumed that the introduction of RW occurred in the film during the spin-coating process or the first immersion into water. As mentioned in the experimental part, the Nafion thin films were thermally annealed. Then, we expected that voids or the residual water could be removed, but they were not. One of the possible reasons is that the paths to the voids from the outside were collapsed during the thermal annealing, resulting in the isolated voids or the residual water region. To evaluate the distributions of RW and EW, we applied the volume conservation law in this experiment.

Figure 3 presents the volume occupancies of Nafion, RW, and EW, for the thin films on hydrophobic carbon in (a) 80% RH water vapor as functions of the distance from the carbon surface. This figure elucidates the distributions of RW in the thin films. It is clear that the RW filled the open volume, according to volume conservation. The amounts of RW in the films in water vapor and bulk water is less than that in the dry film. This observation indicates that some of the RW was exchanged with the water molecules from outside. The RW near the air interface was exchanged more than that near the carbon interface and was more enhanced in bulk water. As mentioned before, we considered that the residual water was isolated due to the collapse of the paths to the outside, and the present observation suggested that the collapse occurred more frequently near the carbon surface than near the air surface.

Figure 3(b) presents the results of the same analyses for the Nafion thin films on hydrophilic carbon film in 80% RH water. The RW distribution is mainly in the central part of the Nafion film for hydrophilic carbon, whereas the EW is evenly distributed across the film and shows higher volume occupancy near the hydrophilic carbon interface. This distribution is due to the hydrophilic nature of the carbon surface. In any case, the EW distribution is essentially the same as in the first analysis without considering the RW; hence, the discussions of

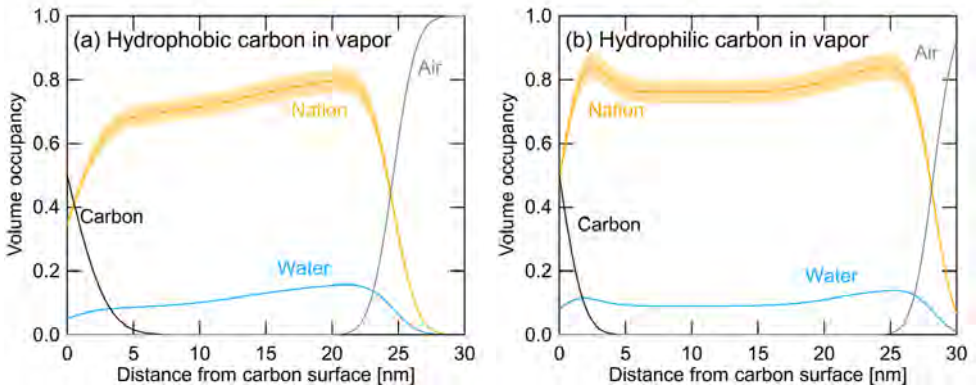

Figure 2. Volume occupancies of Nafion and water in films on hydrophobic (a) and hydrophilic (b) carbon in 80% RH water vapor as functions of the distance from the carbon surface. Adapted with permission from [7]. Copyright 2020 American Chemical Society.

the water and Nafion distributions in regard to Figs. 2 remain valid.

The first and second physical scenarios suggest that some voids were present and there was RW, which was not exchanged with outside water. Both possibilities imply the existence of areas (voids or RW areas) isolated from the outside water, which probably indicates that such isolated areas have no paths connecting to the outside. On the other hand, EW, which is mainly located near charged side chains as a cluster [3], can move in the Nafion thin film. In this case, the RW in the Nafion film cannot contribute to proton transfer in the PEMFC operation. In other words, the wetting ratio (ratio of the water fraction to the Nafion fraction) is not directly related to the proton transfer. This point is crucial to note regarding the efficiency improvement of PEMFC.

Finally, Figures 4 schematically illustrate the concept of voids or RW in Nafion thin films. The key point is the presence of some isolated regions (voids or RW areas) and portions that are connected to the outside (EW areas) in the Nafion film. The Nafion and water distributions along the depth direction are also involved.

This is the first report on the depth profile of the water distribution in Nafion thin films on hydrophobic and hydrophilic carbon in water vapor and bulk water. This depth profile information is crucial for the development of properties in PEMFCs such as proton conductivity [4], flooding [5], and discharge of water [6].

References

[1] B. R. Frieberg et al., ACS Appl. Mater. Interfaces **8**, 33240 (2016).
[2] A. Kusoglu et al., Chem. Rev. **117**, 987 (2017).
[3] T. Mashio et al., J. Phys. Chem. C **114**, 13739 (2010).
[4] M. Bass et al., Macromolecules **44**, 2893 (2011).
[5] D. K. Paul et al., Macromolecules **46**, 3461 (2013).
[6] R. P. Dowd et al., J. Electrochem. Soc. **164**, F138 (2017).
[7] K. Ito et al., Langmuir **36**, 12830 (2020).

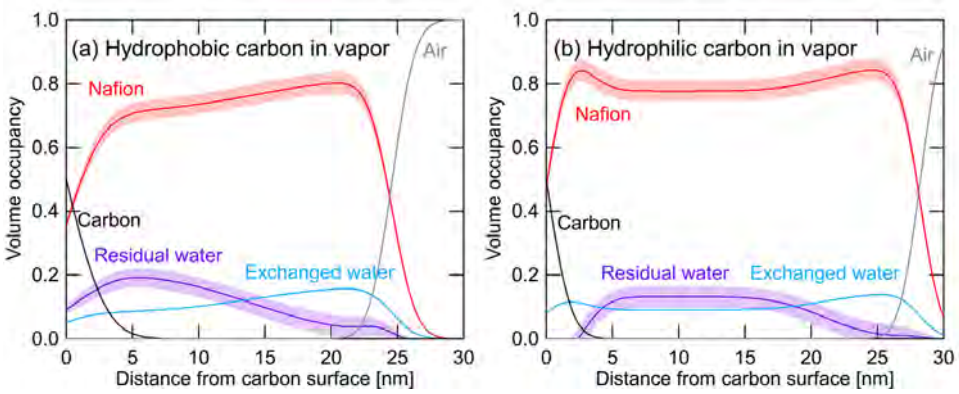

Figure 3. Volume occupancies of Nafion, EW, and RW in the Nafion thin films on hydrophobic (a) and hydrophilic (b) carbon as functions of the distance from the carbon surface in 80% RH water vapor. Adapted with permission from [7]. Copyright 2020 American Chemical Society.

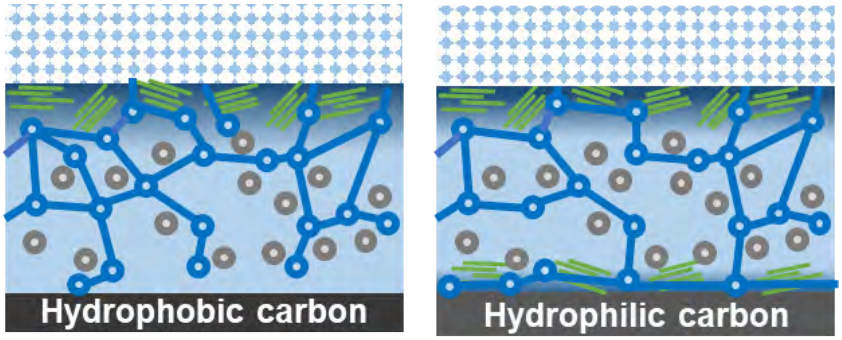

Figure 4. Schematic illustrations of inner structures of Nafion thin films on hydrophobic and hydrophilic carbon in 80% RH water vapor. Nafion crystals or dense region (green lines), residual water (or voids) isolated from the outside (gray circles), and exchanged water penetrating from outside (blue circles). The blue lines show the connecting paths between the exchanged water clusters. Adapted with permission from [7]. Copyright 2020 American Chemical Society.

K. Ito[1], M. Harada[2], N. L. Yamada[1,3], K. Kudo[2], H. Aoki[1,3], and T. Kanaya[1,3]

[1]Neutron Science Section, Materials and Life Science Division, J-PARC Center; [2]Toyota Central R&D Labs., Inc.; [3]Institute of Materials Structure Science, KEK

Interfacial Cross-Link Inhomogeneity of a Phenolic Resin on a Silica Surface as Revealed by XRR and NR Measurements

1. Introduction

Transportation vehicles, such as automobiles, aircrafts, and trains, are required to further reduce fuel consumption because of global warming gas emission regulations. One of the most effective ways to reduce fuel consumption is to reduce vehicle weight via replacement of metals with resins. A glass fiber-reinforced phenolic resin has been widely used as a metal replacement material, especially in mechanical parts, such as in transmissions, pulleys, and pump impellers, where particularly excellent strength and rigidity are required. However, a decrease in the interfacial adhesion between the resin and glass fiber causes undesirable interfacial delamination that causes cracks in the glass fiber-reinforced resin. Therefore, understanding the interfacial resin structure on the silica surface at a nanometer level is important for improving the adhesion and for achieving long-term reliability of the glass fiber reinforcement.

In this study, to determine the interfacial structure of a phenolic resin on a glass surface, the structure of hexamethylenetetramine (HMTA)-cured phenolic resin nanofilms prepared on a silicon wafer with a native silica layer on its surface was investigated by complementary X-ray and neutron reflectometry (XRR and NR, respectively) analyses [1]. As a contrast-variation technique, the structural analyses were performed in the dry and water-absorbed wet states. The water absorption can change structural contrast in terms of mass density via swelling. Additionally, using deuterated water with the coherent neutron scattering length density (SLD) of 6.36×10^{-4} nm^{-2} can increase the SLD of the resin via the D_2O absorption and can allow H-to-D exchange reactions of hydroxyl groups on phenolic rings to proceed, which considerably changes the structural contrast in the NR analyses.

2. Experimental

Phenolic resin nanofilms were prepared via spin coating using 1.5, 1.2, and 0.9 wt% ethanol solutions of a 1.0/0.12 (wt/wt) mixture of novolac resin and HMTA. The ethanol solution was deposited onto an ethanol-cleaned wafer with a diameter and thickness of 50 and 2 mm, respectively, and then spun at 2000 rpm for 15 s. The spin-coated wafer was heated at 100°C for 2 min on a hotplate to remove the remaining solvent and then cured at 180°C for 8 h in an oven under atmospheric conditions. The water-absorbed wet samples were prepared by immersing the dry samples in water at room temperature for 3 h after the reflectivity measurements in which H_2O and D_2O were used for the XRR and NR analyses, respectively. Samples PR-1.5, PR-1.2, and PR-0.9 were prepared from 1.5, 1.2, and 0.9 wt% solutions, respectively.

XRR measurements were performed on an Ultima IV X-ray diffractometer (Rigaku Corporation) using X-rays with a wavelength (λ) of 0.154 nm from a CuKα spectral line excited at 40 kV and 40 mA.

NR measurements were performed on a time-of-flight neutron reflectometer, SHARAKU, installed at the BL17 beamline at the MLF, J-PARC, using a 25-Hz pulsed neutron beam at an accelerator operating power of 0.5 MW. The reflected neutrons with a λ band of 0.22–0.88 nm were measured using a ^{3}He gas tube neutron detector at three reflection angles of 0.3, 0.7, and 1.6°.

The measurements of the dry and wet samples were performed under low and high humidity conditions, respectively, to avoid structural changes during the measurements due to moisture absorption or drying of the resin: XRR and NR measurements were conducted at 21–25°C and 21–28% RH under atmospheric conditions for the dry samples and at 28–30°C and 81–85% RH for the wet samples. The NR measurement was conducted under a D_2O vapor-containing nitrogen atmosphere using a beamline-specific humidity-controlled sample cell [2].

3. Results and discussion

Figure. 1 shows the XRR profiles of PR-1.5. The reflection profiles exhibited a clear interference pattern over a wide q range, which is called Kiessig fringes, indicating that the specimen exhibited a flat and smooth surface. Both XRR profiles of dry and wet samples were successfully reproduced by a structural model with a single-resin layer on the native silica. The water absorption of the phenolic resin layer resulted in an increase in t from 41.6 to 44.0 nm and a decrease in ρ_m from 1.40 to 1.39 g cm^{-3}, thereby indicating that the amount of absorbed water was 5.0 wt% based on the dry resin.

Figure. 2 shows the NR profiles of PR-1.5. Both the

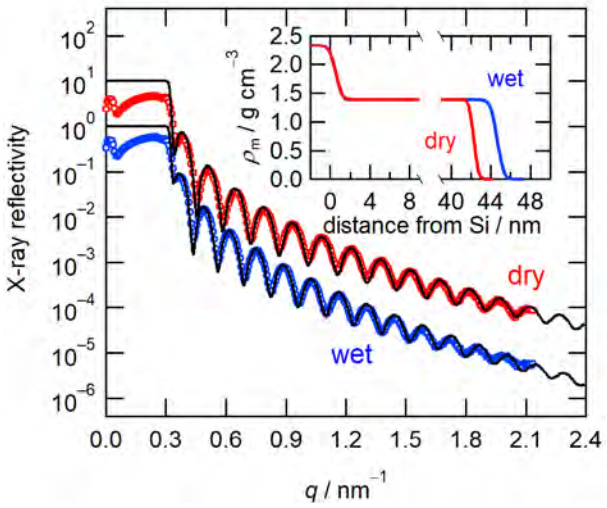

Figure 1. XRR profiles of PR-1.5 in dry and wet states. The profile in the dry state is vertically shifted by a factor of 10 for clarity. The solid lines represent the fitting curves. (Inset) Mass density profiles of PR-1.5 in the dry and wet states. Reprinted (adapted) with permission from [1]. Copyright 2020, American Chemical Society.

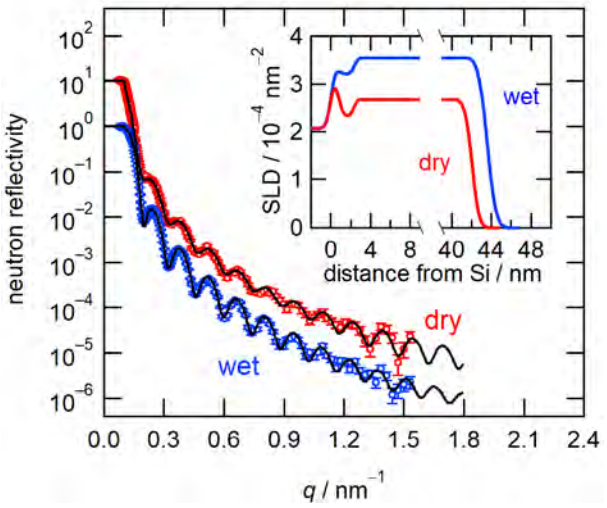

Figure 2. NR profiles of PR-1.5 in dry and wet states. The profile in the dry state is vertically shifted by a factor of 10 for clarity. The solid lines represent the fitting curves. (Inset) SLD profiles of PR-1.5 in the dry and wet states. Reprinted (adapted) with permission from [1]. Copyright 2020, American Chemical Society.

interference fringes of the XRR and NR profiles decayed with increasing q, whereas the NR profiles have a feature in which the logarithmic-scale fringe amplitude recovered at $q > 0.12$ nm^{-1}. The NR profile analysis was performed in the observed q range of 0.075–1.5 nm^{-1}, in which structural parameters of the silicon and silica layers were fixed to those obtained from the XRR analysis as a constraint for the fitting procedure. The structural model with a single-resin layer on the native silica that was applied in the XRR analysis was first investigated; however, the fitting analysis failed and the aforementioned feature of interference fringes of the NR profile was not reproduced with the model. However, a structural model containing a low-SLD resin layer with a thickness of 1–2 nm between the bulk phenolic resin and native silica produced good fitting results both for dry and wet samples as shown in Fig. 3. This result indicates that there was an interfacial layer between the bulk phenolic resin and native silica in terms of SLD, and the interfacial layer had the same mass density and a lower SLD compared with the bulk resin layer. According to the theoretical SLD values [1], the bulk layer of the dry sample with the SLD of 2.68×10^{-4} nm^{-2} was well characterized as a HMTA-cured phenolic resin, where the theoretical SLD was 2.65×10^{-4} nm^{-2}, and the increase in the SLD to 3.54×10^{-4} nm^{-2} by D_2O absorption can be explained by ≈5 wt% D_2O absorption and the progress of the H-to-D exchange of hydroxyl groups. The interfacial layer on the native silica exhibited an SLD of 2.31×10^{-4} nm^{-2} and t of 1.6 nm in the dry state. The SLD value suggests that the interfacial layer had a structure similar to the novolac resin, where the theoretical SLD was 2.34×10^{-4} nm^{-2}. Thus, an increase in the SLD to 3.20×10^{-4} nm^{-2} by D_2O absorption can be similarly explained as for the bulk resin layer. The thickness of the interfacial layer corresponds to a few repeating units of the novolac resin. These results suggest that the low-SLD interfacial layer was regarded as a novolac resin adsorption layer on the native silica.

The formation of the adsorption layer could be driven by a strong hydrogen-bonding interaction between the novolac resin and the silica surface [40]. The presence of a low-SLD interfacial layer on the silica surface indicates that the novolac resin adsorption layer was first formed before curing via the strong hydrogen-bonding interaction between the resin and silica surface. The preferential formation of the novolac resin adsorption layer caused a low HMTA concentration in the layer compared with that in the bulk resin layer, which resulted in the presence of the low-SLD layer after curing. There was no distinct difference in mass densities between the novolac and HMTA-cured resins, which resulted in the absence of the interfacial structure in the XRR profiles.

When the low-SLD interfacial layer owing to the novolac resin adsorption onto the silica surface is a general

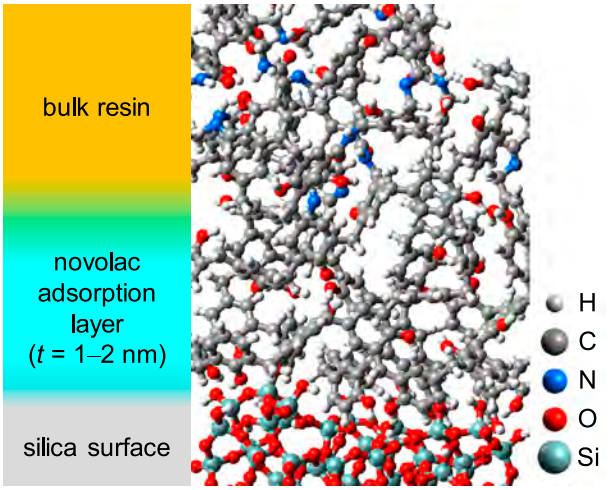

Figure 3. Interfacial structure of a HMTA-cured phenolic resin on silica surface. Reprinted (adapted) with permission from [1]. Copyright 2020, American Chemical Society.

structural feature of the HMTA-cured phenolic resin, the thickness of the interfacial layer, 1–2 nm, will not be significantly affected by the thickness of the bulk resin layer as illustrated in Fig. 3. This conjecture was verified by additional dry-state NR analyses with PR-1.2 and PR-0.9, in which their bulk-layer thicknesses were 30 and 20 nm, respectively, and interfacial-layer thicknesses were both 1.3 nm.

4. Summary

The interfacial structure of a HMTA-cured phenolic resin on silica surface was investigated by complementary use of XRR and NR. The contrast-variation technique was applied using D_2O for the NR analysis in which the SLD largely changed because of D_2O absorption of the dry phenolic resin and H-to-D exchange of phenolic hydroxyl groups. The XRR profile indicated no clear interfacial structure in terms of the mass density, whereas the NR profile indicated the presence of an interfacial nanolayer on the native silica surface in terms of the SLD. The thickness of the interfacial layer was 1–2 nm, which was independent of the thickness of the bulk resin layer. The formation of the interfacial layer on the silica surface could be driven by preferential adsorption of the novolac resin on the silica surface via strong hydrogen bonding between phenolic units in the novolac resin and silanol and silyl ether groups on the silica surface, which resulted in interfacial cross-link inhomogeneity of the phenolic resin on the silica surface in the thickness direction.

5. Future plans

This interfacial structure may correspond to a "weak boundary layer (WBL)" for phenolic resin–silica composites in which the WBL considerably affects the interfacial adhesive strength [3]. Further elucidation of the adsorption nanolayer via XRR and NR analyses and characterization of the interfacial structure–property relation of phenolic resin–silica composites are our future tasks.

References

[1] A. Izumi et al., Macromolecules, **53** 4082 (2020).
[2] S. Ohira-Kawamura et al., Neutron News, **30** 11 (2019).
[3] J. J. Bikerman, Ind. Eng. Chem., **59** 40 (1967).

A. Izumi[1], Y. Shudo[1], M. Shibayama[2], T. Yoshida[2], N. Miayata[2], T. Miyazaki[2], and H. Aoki[3,4]
[1]*Corporate Engineering Center, Sumitomo Bakelite Co., Ltd.;* [2]*Neutron Science and Technology Center, CROSS;* [3]*Neutron Science Section, Materials and Life Science Division, J-PARC Center;* [4]*Neutron Science Section, Materials and Life Science Division, J-PARC Center Institute of Materials Structure Science, KEK*

Garnet-Type High Li-ion Conductivity Single Crystal as Solid Electrolyte for All-solid-state Li Battery

1. Introduction

The all-solid-state lithium battery, which is one of the next-generation secondary batteries, is expected to be a secondary battery that has both high safety and high energy density because it does not use an organic electrolyte. To this realization, research and development is currently being carried out at research institutes and companies around the world. The all-solid-state Li battery includes an oxide-based all-solid-state Li battery that uses an oxide as a solid electrolyte and a sulfide-based all-solid-state Li battery that uses a sulfide. It has been reported that sulfide-based solid electrolytes have high ionic conductivity and high moldability, and it is easy to make an all-solid-state lithium battery, but hydrogen sulfide becomes toxic when it reacts with water. Therefore, there is a drawback in safety. On the other hand, oxide-based solid electrolytes provide excellent safety, but their lithium-ion conductivity is about an order of magnitude lower, and there is a problem with moldability, making it difficult to improve the relative density of the sintered body. Therefore, our research team started to grow a large single crystal in order to produce a solid electrolyte with a relative density of 100%. The target substance is a garnet-type solid electrolyte that has a relatively high lithium-ion conductivity among oxide-based solid electrolytes. If a large single crystal is successfully grown, accurate bulk lithium-ion conductivity can be measured, making it more attractive as a member. In addition, detailed crystal structure analysis using single crystal neutron diffraction, which has not been performed so far, can be performed [1, 2]. In this report, we report on the lager single crystal growth of garnet-type solid electrolyte and crystal structure analysis using single crystal X-ray and neutron diffraction data.

2. Single crystal growth of garnet-type solid electrolyte by melting method

Our team had previously used the flux method to grow garnet-type solid electrolytes. However, the flux method did not make the size usable as a member, and because of repeated studies, we tried to grow a garnet-type solid electrolyte single crystal by the floating zone method (FZ method) in an optical image furnace (Crystal system, Inc., Japan) equipped with four 1 kW halogen lamps. The FZ method is one of the melting methods. There are two reasons for choosing the FZ method. One is a single crystal growing method that does not use a crucible, so that impurities can be avoided. Another point is that the volatile component (lithium) can be controlled because the molten part is local. In single crystal growth, considering the volatilization of lithium, lithium carbonate was charged 1.2 times in molar ratio, and single crystals of garnet-type solid electrolytes $Li_{6.5}La_3Zr_{1.5}Nb_{0.5}O_{12}$ (LLZNb05) and $Li_{6.5}La_3Zr_{1.5}Ta_{0.5}O_{12}$ (LLZTa05) were grown. As a typical single crystal, Figure. 1 shows a photograph of the single crystal of LLZNb05. A single crystal with a diameter of about 8 mm and a length of about 40 mm was grown by the FZ method. The orientations of the as-grown single crystals were measured using monochromatized Cu $K\alpha 1$ radiation (40 kV, 30 mA) at 295K on a two-axis X-ray diffractometer (Rigaku SmartLab, Japan) equipped with a charge-coupled device detector and a Johansson's Ge (111) curved crystal. The X-ray diffraction pattern of the LLZNb05 single-crystal plate collected with a biaxial diffractometer indicated that crystal growth occurred in the <332> direction.

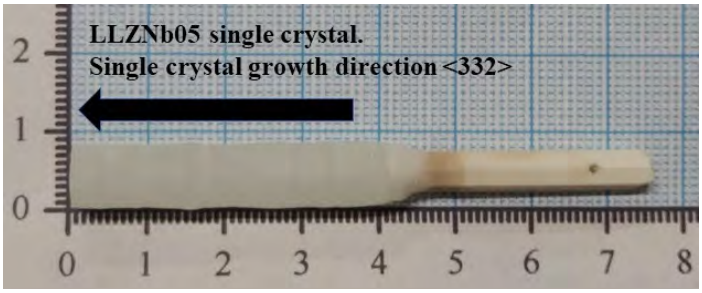

Figure 1. As-grown LLZNb05 single crystal rod by the FZ method.

3. Crystal structure analysis by X-ray and neutron diffraction using single crystal

In order to analyze their crystal structures, small transparent crystals were processed into 0.2 mm (φ) spheres for single-crystal X-ray diffraction (XRD) and 0.5 mm (φ) spheres for single-crystal neutron diffraction measurements. For structural refinement, the XRD intensities of the LLZNb05 and LLZTa05 single crystals were recorded on a 2D diffractometer (Rigaku R-AXIS RAPID-II, Japan) equipped with an imaging plate detector, a graphite monochromator, and a Mo *K*α radiation source (50 kV, 30 mA) at 295K. The neutron diffraction intensities of the LLZNb05 and LLZTa05 single crystals were measured using a time-of-flight neutron diffractometer equipped with a 2D detector (BL18 SENJU; J-PARC, Japan, proposal No. 2015A0147 and 2016A0235) [3] using a poisoned decoupled hydrogen moderator (100 kW) at 295K. Structural refinement was performed using the Jana2006 program [4].

The structure in LLZNb05 and LLZTa05 comprised of LaO_8 and (Zr, Nb, or Ta)O_6 polyhedra was refined using the single-crystal XRD data and the reported garnet-type atomic coordinates. The Li sites in LLZNb05 LLZTa05 were determined from the single-crystal XRD and neutron diffraction data using a differential Fourier synthesis map. The reliability values of the single-crystal XRD data obtained from LLZNb05 were $R = 4.25\%$ and wR = 5.82%. R and wR of the single-crystal neutron diffraction were 7.09% and 7.94%, respectively. The R and wR values of the single-crystal XRD data from LLZTa05 were 3.32% and 4.45%, respectively. The reliability values of the single-crystal neutron diffraction data were $R = 8.82\%$ and w$R = 7.45\%$. Even when the XRD and neutron diffraction data were used complementarily for refinement, it was difficult to determine the occupancy ratios of Zr and Nb or Ta. We, therefore, refined the crystal structure using fixed values obtained from the ICP-AES analysis. The LLZNb05 and LLZTa05 crystal lattice parameter (a) was refined by the least-squares method using the single-crystal XRD data. In LLZNb05, $a = 12.9130(8)$ Å, whereas $a = 12.9455(6)$ Å in LLZTa05. Figure 2 shows the refined crystal structure of LLZNb05. A similar crystal structure was constructed for LLZTa05. Based on these structural refinements, we determined the chemical composition of LLZTa05 to be $Li_{6.32}La_3Zr_{1.5}Ta_{0.5}O_{12}$. The chemical composition of LLZNb05 was $Li_{6.49}La_3Zr_{1.5}Nb_{0.5}O_{12}$. Li ions occupied two interstitial sites in the framework structure. Li1 and Li2 ions were located in distorted tetrahedral and octahedral 96*h* sites, respectively. In the $(La_3Zr_{1.5}Ta_{0.5}O_{12})^{6.5-}$ and $(La_3Zr_{1.5}Nb_{0.5}O_{12})^{6.5-}$ garnet solid electrolyte framework structures, Li+ occupied the A-sites formed by (Zr, Nb, or Ta)O_6 and the C-sites formed by LaO_8. The 96*h* sites were split from the 24*d* sites, where Li ions formed tetrahedrons. However, other 96*h* sites were split from the 48*g* sites, where Li ions formed octahedrons. The conductivity of Li-ion

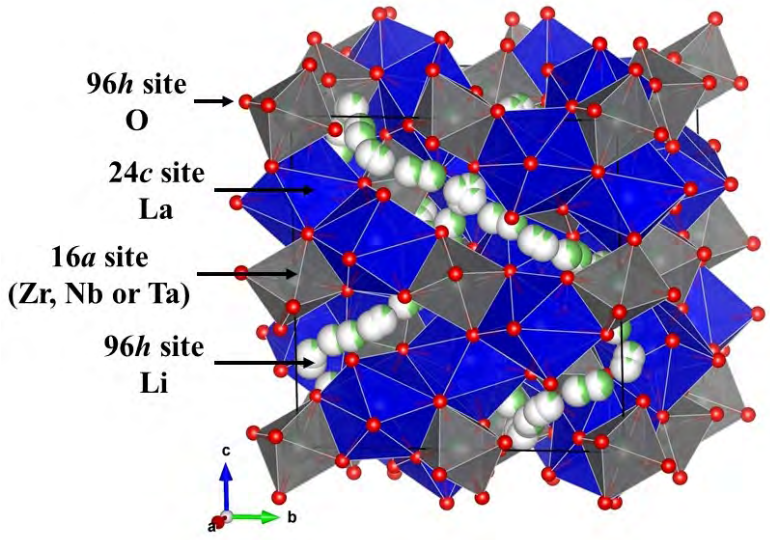

Figure 2. Crystal structure of LLZNb05 (LLZTa05) by X-ray and neutron diffraction data refinement using a single crystal.

seems to have been improved by splitting because the distance between Li sites was shortened. Our results suggested that the arrangement of Li ions in the garnet structure differed from the previously reported arrangement. In previous studies, Li ions in a crystal structure within the $Ia\bar{3}d$ space group were reported to occupy the tetrahedral 24*d* and distorted octahedral 96*h* sites [5, 6]. Thus, the Li-Li distances in our structures were shorter than those reported previously. A short Li-Li distance, disordering of Li sites, and partial occupation by Li atoms are thought to be key for Li-ion diffusion in the garnet structure. Accordingly, we speculated that Li ions might have diffused more rapidly in our single crystals than they did in the reported polycrystalline samples [5, 7, 8].

4. Future plans

We will continue to explore the growth of garnet-type solid electrolyte single crystals with higher lithium-ion conductivity. Furthermore, we aim to elucidate the Li-ion conduction phenomenon in solids by combining garnet-type solid electrolyte single crystals and single crystal neutron diffraction. In addition, we will conduct research and development to realize an all-solid-state lithium battery that uses a garnet-type solid electrolyte single crystal as a member.

References

[1] K. Kataoka, H. Nagata and J. Akimoto, Sci. Rep., **8** 9965 (2018).
[2] K. Kataoka and J. Akimoto, ChemElectroChem, **5** 2551 (2018).
[3] T. Ohhara et al., J. Appl. Crystallogr., **49** 120 (2016).
[4] V. Petricek, M. Dusek, L. Z. Palatinus, Kristallografiya, **229** 345 (2014).
[5] N. Hamao, K. Kataoka, N. Kijima, J. Akimoto, J. Ceram. Soc. Jpn., **124**, 678 (2016).
[6] J. Awaka, A. Takashima, K. Kataoka, N. Kijima, Y. Idemoto, J. Akimoto, Chem. Lett., **40** 60 (2011).
[7] H. Yamada, T. Ito, R. H. Basappa, Electrochim. Acta, **220** 648 (2016).
[8] K. Hayamizu, Y. Matsuda, M. Matsui, N. Imanishi, Solid State Nucl. Mag., **70** 21 (2015).

K. Kataoka
Energy Conversion and Storage Material Team, Advanced Coating Technology Research Center, National Institute of Advanced Industrial Science and Technology (AIST)

In-situ Neutron Diffraction Analysis on Low Temperature Deformation Behavior in Low Alloy Steel

1. Introduction

Transformation-induced plasticity (TRIP) results in improvement of strength and ductility in low alloy steel due to the transformation of metastable retained austenite (γ) to martensite (α′) (deformation induced martensitic transformation: DIMT) [1]. The behavior of TRIP strongly depends on the mechanical stability of γ. Sugimoto et al. [2] reported that a low alloy steel containing metastable γ showed excellent total elongation at 423 K as the γ was in a suitable stable condition. On the other hand, there are few reports on the stability of γ and the DIMT at low temperatures. In our previous study [3], we investigated the tensile properties and changes of the phase fraction of γ in a low alloy steel at low temperatures using the electron back scattered diffraction (EBSD) method. The tensile strength of the steel increased without decreasing the total elongation as the deformation temperature decreased from 293 K to 193 K, which was accompanied by a high work-hardening rate in the initial stage of deformation. Then, we suggested that γ with the DIMT contributed to the high work-hardening rate, but there was no direct proof showing evolution of the stresses of γ and α′ during deformation. In addition, a reason why the steel showed the excellent elongation at low temperature was also not clear yet because the counting loss of γ with a small grain size occurred in the EBSD measurement. Hence, an accurate observation of the DIMT behavior of γ at low temperatures is necessary.

In-situ neutron diffraction during tensile deformation represents an effective method for the simultaneous evaluation of the deformation and DIMT behavior. In this study, the changes of phase fractions and phase stresses of constituent phases (bainitic ferrite matrix, γ, and α′) in a low alloy steel during tensile loading below room temperature were evaluated using in-situ neutron diffraction, and the role of γ in the deformation and DIMT is discussed.

2. Experimental procedure

Fe-0.31C-1.74Si-1.49Mn (in mass%) was used in the present study. The steel consists of bainitic ferrite (α matrix) and γ. Plate type specimens with a thickness of 2.5 mm were prepared. In-situ neutron diffraction measurement during a tensile test at low temperature was carried out at TAKUMI. The test temperatures were 293 K, 233 K, 193 K, and 134 K, which were controlled by liquid nitrogen cooling system equipment. The tensile test was done by a step-increasing load control with 300 s holding time in the elastic region and by a continuous crosshead speed control with the initial strain rate of 1.3×10^{-5} s^{-1} in the plastic region. The measurements were performed up to the ultimate tensile strengths. Peak separation between α and α′ was conducted by assuming that the c/a ratio of α′ was constant during the whole deformation and could be simplified by a single-broad BCC peak [4]. The phase fractions of γ were obtained by Rietveld refinement using a software called Z-Rietveld. The lattice constants were obtained by Pawley refinement using the same software. Since α′ was not found in the specimen before loading, the stress-free lattice constant of α′ ($a_{\alpha',0}$) was evaluated by using a stress equilibrium approach. That is, the sum of phase stresses -weighted by their phase fractions must be equal to the applied true stress in a loaded state. The $a_{\alpha',0}$ value for each test temperature was determined independently.

3. Results and discussion

Figure 1(a) shows the nominal stress-nominal strain curves at various test temperatures. The steel exhibited good balance of tensile strength and homogeneous elongation at 233 K, 193 K, and 134 K. The changes of the phase fraction of γ during tensile deformation at various test temperature are shown in Fig. 1(b). The phase fraction of γ before deformation at low temperatures slightly decreased (~1%) during cooling. The martensitic transformation occurred mostly after macroscopic yielding at each test temperature. At 293 K, the phase fraction of γ decreased linearly with the increase in the applied true strain, and this trend was kept until the end of deformation. The phase fraction of γ decreased at a higher rate by lowering the test temperature, in which the rate became smaller at the latter part of deformation.

The phase strains for all constituent phases were evaluated and converted to the phase stresses. By weighting the phase stress with the phase fraction of each constituent phase, a contributed stress to the strength (contributed stress) of each constituent phase can be evaluated. Figure 2 shows the contributed stresses of α matrix, γ, and α′ as a function of the applied true strain during a tensile test at 293 K and 134 K.

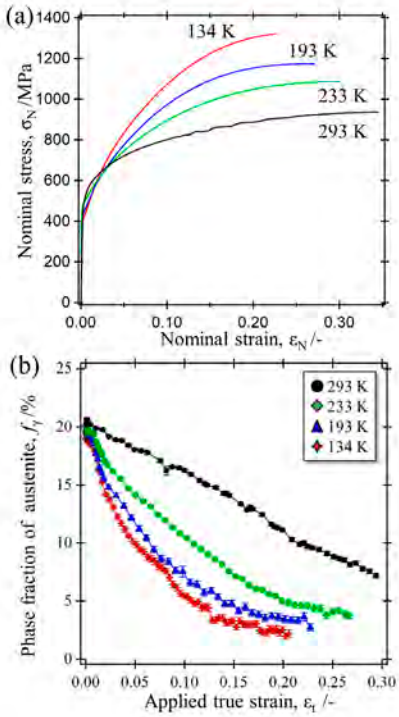

Figure 1. (a) Nominal stress – nominal strain curves and (b) phase fraction of retained austenite as a function of the true strain at various test temperatures. Adapted from Ref. [5].

The contributed stress of the α matrix is higher than the other phases at the early stage of deformation due to its large phase fraction. It increases with deformation due to its work hardening. The contributed stress of α′ is very low at the early stage of deformation due to its small phase fraction. The contributed stress of α′ is enhanced with deformation and becomes much higher than the contributed stress of α, due to the increase in the phase fraction and the work hardening of α′. The contributed stresses of α matrix and α′ are enhanced also by decreasing the test temperature. The contributed stress of γ, however, decreases by progressing of deformation, particularly at low temperature. The main reason may be due to the decrease of the phase fraction of γ as a result of continuous DIMT with the progress of deformation.

We conclude that the role of γ in the low alloy steel used in this study at low temperature deformation, does not contribute directly to the stress but it improves the elongation through the TRIP effect and increases the work hardening rate by promoting the DIMT.

Acknowledgement

This study was financially supported by JSPS KAKENHI Grant Number 15H05767 and 19K15279. The neutron diffraction measurements were performed in the MLF of J-PARC with the proposal of 2016P0200.

References

[1] I. Tamura, Metal Sci., **16** 245 (1982).
[2] K. Sugimoto et al., Metall. Mater. Trans. A, **23** 3085 (1992).
[3] T. Yamashita et al., ISIJ Int., **58** 1155 (2018).
[4] S. Harjo et al., Sci. Rep., **7** 15149 (2017).
[5] T. Yamashita et al., Scripta Mater. **177** 6 (2020).

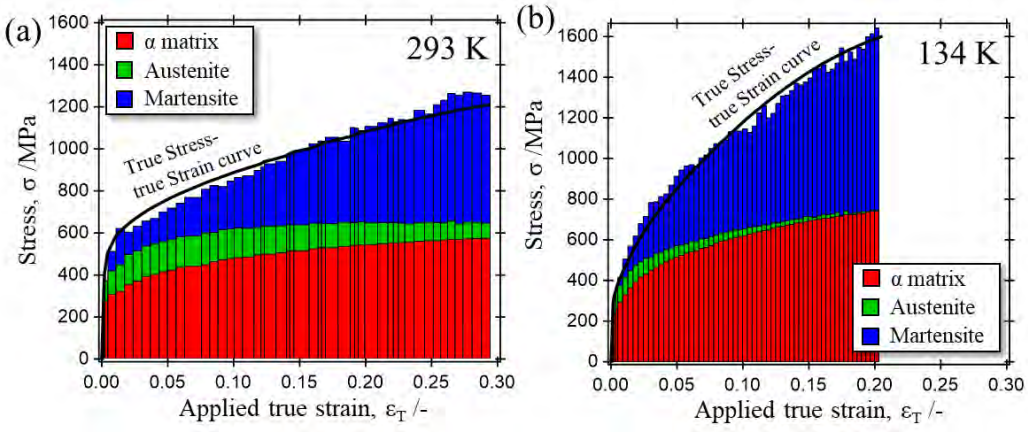

Figure 2. The changes of fraction weighted phase stresses of each consisting phases during the tensile test at (a) 293 K and (b) 134 K. Adapted from Ref. [5].

T. Yamashita[1], S. Morooka[2], S. Harjo[2], T. Kawasaki[2], N. Koga[3], and O. Umezawa[4]

[1]*Joining and Welding Research Institute, Osaka University;* [2]*Neutron Science Section, Materials and Life Science Division, J-PARC Center;* [3]*Faculty of Mechanical Engineering, Kanazawa University;* [4]*Faculty of Engineering, Yokohama National University*

In-plane Low Thermal Expansion of NiTi Via Controlled Cross Rolling

1. Introduction

Recently, efforts were devoted to develop polycrystalline shape memory alloys (SMAs) with macroscopic low thermal expansion (TE) along a certain direction to further enhance the functionality of the materials [1–5]. Among the different routes reported, microstructure control via uniaxial rolling has attracted the attention. Without altering the intrinsic TEs of the constituent crystals, such route aims to achieve low TE of polycrystalline SMAs via tuning the microstructural parameters such as grain size, phase compositions and textures [2, 3, 5]. One limitation of unidirectionally rolled SMAs is that the TE is highly anisotropic in the rolling plane and the low TE is only achieved along a specific direction, while large positive and negative TEs still exist along other directions, which dramatically limits real applications. It is desirable to reduce such TE anisotropy and even to achieve in-plane low TE of SMAs.

Here, we find that via controlled cross rolling, the in-plane coefficients of thermal expansion (CTE) of a NiTi SMA sheet can be lowered to near-zero within a very narrow range over a large temperature window of 223 K. The mechanism for the achieved in-plane low TE is identified via neutron diffraction and theoretical calculation.

2. Results and Discussions

We processed a solution-treated NiTi sheet through cross rolling with 30% total thickness reduction and a three-step rolling path (RD-15%, TD-10% and RD-5%). The in-plane TE behaviors of the sample (hereafter called CroR-15%-10%-5% NiTi) are presented in Fig. 1(a), showing in-plane CTEs within the range of -2.7×10^{-6} K^{-1} to $+3.0 \times 110^{-6}$ K^{-1} over the temperature range of 77 K to 300 K. Such in-plane CTEs are smaller than the values of the reported SMAs and are comparable to that of the commercial FeNi Invar alloy (Fig. 1(b)). the strain *vs* temperature curves of all the samples are nonlinear and exhibit a small hysteresis loop over a large temperature span, indicating that a continuous and reversible formation of B19′ martensite takes place in cooling and contributes to the observed macroscopic TE.

We observed the microstructure of the CroR-15%-10%-5% sample using TEM at room temperature. As shown in Fig. 2(a), the microstructure is characterized by triple-cross bands of 100 ~ 200 nm wide and several microns long (Fig. 2(a1)). Inside the bands, we observed nanocrystals of 10 ~ 100 nm in size (Fig. 2(a3)). The electron diffraction patterns in Fig. 2(a2) show the presense of the B19′ phase at room temperature, which reaches 50% of volume fraction as quantified by neutron diffraction. Such rolling-induced residual B19′ phase indicates the existence of large residual stress in the nanostructure, which can reach 400 MPa as estimated from the critical stress for B2 → B19′ phase transformation [6, 7].

We performed *in-situ* neutron diffraction using iMATERIA on the CroR-15%-10%-5% NiTi at temperatures from 2.3 K to 300 K (Fig. 2(b)). The results show that upon the cooling and heating over a large temperature span, a small fraction (12 vol%) of reversible B2 ⇔ B19′ transformation takes place (Fig. 2(b1)). Such overall

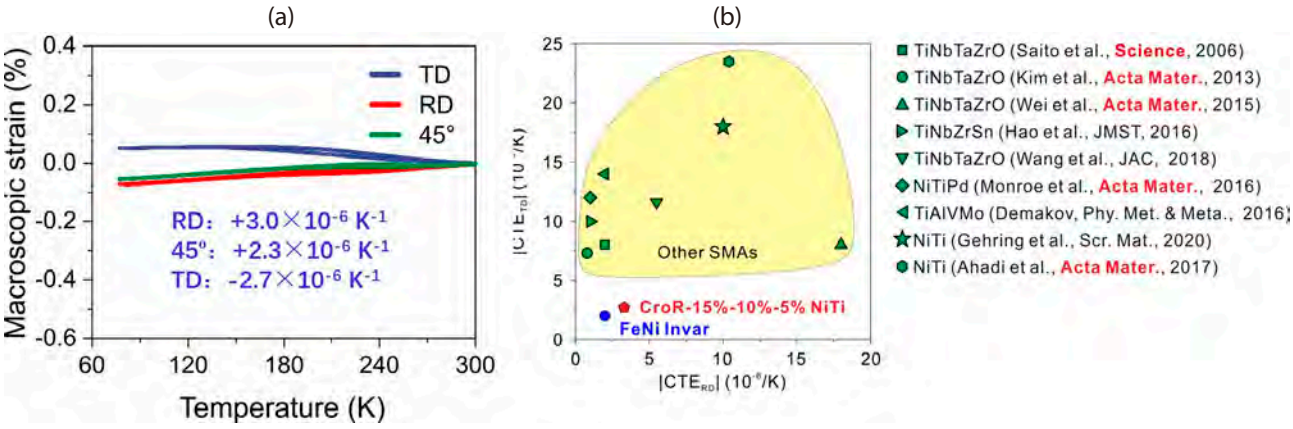

Figure 1. (a) Measured in-plane TE of the CroR-15%-10%-5% NiTi sheet. (b) Comparison of the CTEs of the CroR-15%-10%-5% NiTi with those of other reported SMAs and commercial FeNi Invar alloy.

continuous phase transformation is caused by the nanoscale grain size inhomogeneity and the presence of the residual stress [6, 8–10]. At 300 K, the B19′ phase has {102}⟨*UVW*⟩ fiber texture (Fig. 2(b2)), indicating its nearly random orientation in the rolling plane. During cooling, the orientation densities on the entire fiber increase homogeneously, meaning that the thermally induced B19′ variants also have {102}⟨*UVW*⟩ fiber texture. Such in-plane randomly oriented variant formation is probably due to the weak direction sensitivity of residual stress.

During heating and cooling, both the TEs of the textured B2 and B19′ aggregates and the reversible B2 ⇔ B19′ transformation will contribute to the macroscopic overall TE. To identify the governing mechanism for the overall in-plane low TE, we quantified each contribution using a theoretical model based on Reuss approximation [11] together with the data measured by neutron diffraction (including lattice-level TEs, temperature-dependent volume fractions and textures of the B2 and B19′ phases). The calculated TE behaviors are compared with the measured ones in Fig. 3. Overall, the model calculations agree fairly well with the measurements (Fig. 3(d)). Moreover, the calculation reveals that the B2 ⇔ B19′ phase transformation produces negative TE along both the RD and TD through the reversible formation-vanishing of the {102}⟨*UVW*⟩ fiber-textured B19′ variants (Fig. 3(a)). Such in-plane negative TE compensates the positive TEs of the B2 aggregate (Fig. 3(c)) and B19′ aggregate (Fig. 3(b)), leading to the overall in-plane low TE.

3. Conclusions

In summary, we show that via three-step cross-rolling with 30% total thickness reduction and the 15%-10%-5% rolling path, the in-plane CTEs of the NiTi are reduced down to a very narrow range of -2.7×10^{-6} K^{-1} to $+3.0 \times 10^{-6}$ K^{-1} over the temperature range from 77 K to 300 K. Such in-plane CTEs are not only significantly smaller than those of other reported SMAs but also close to the value of commercial FeNi Invar alloy ($+2.0 \times 10^{-6}$ K^{-1}). *In situ* neutron diffraction and a rule-of-mixture calculation show that in the cross-rolled nanostructured NiTi, the in-plane positive TEs of textured B2 and B19′ aggregates are compensated by the in-plane negative TE caused by the reversible continuous formation (vanishing) of {102}⟨*UVW*⟩ fiber-textured B19′ variants in cooling (heating), thereby leading to the overall in-plane low TE. Such unusual property represents an important and big step forward to the commercialization of the low thermal expansion SMAs.

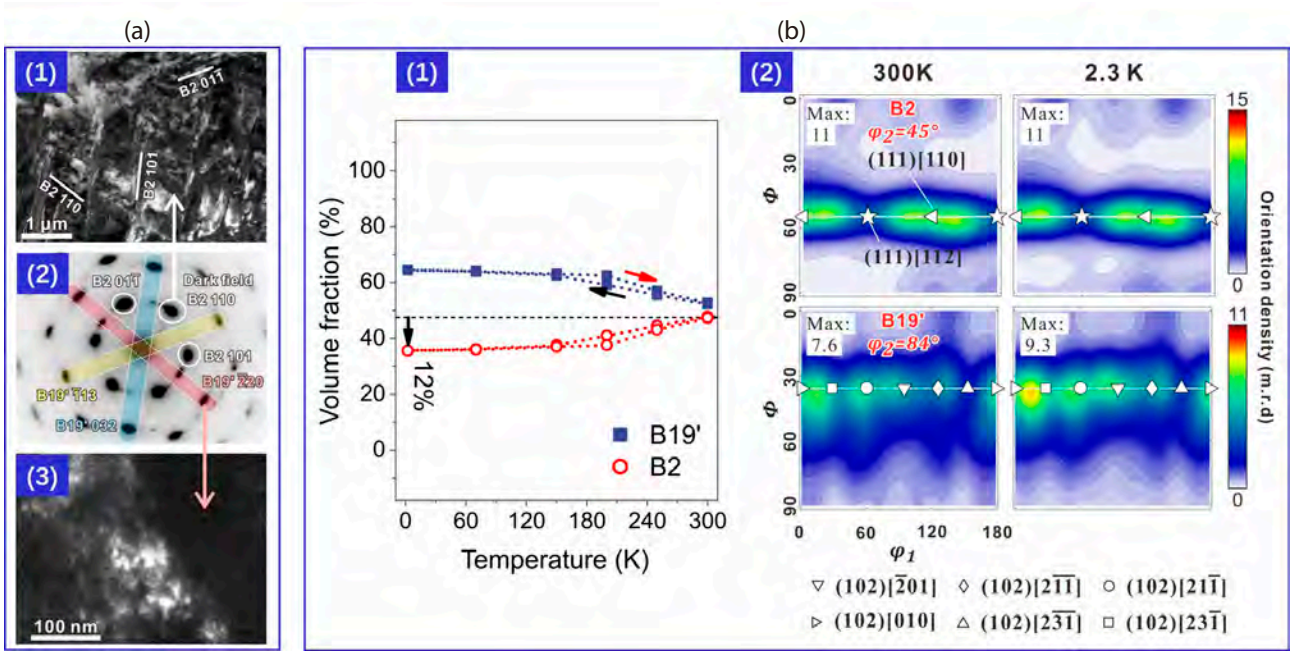

Figure 2. (a) Nanostructure of the CroR-15%-10%-5% NiTi. (b) Thermally-induced nanoscale phase transformation of the CroR-15%-10%-5% NiTi characterized using iMATERIA at temperatures from 2.3 K to 300 K.

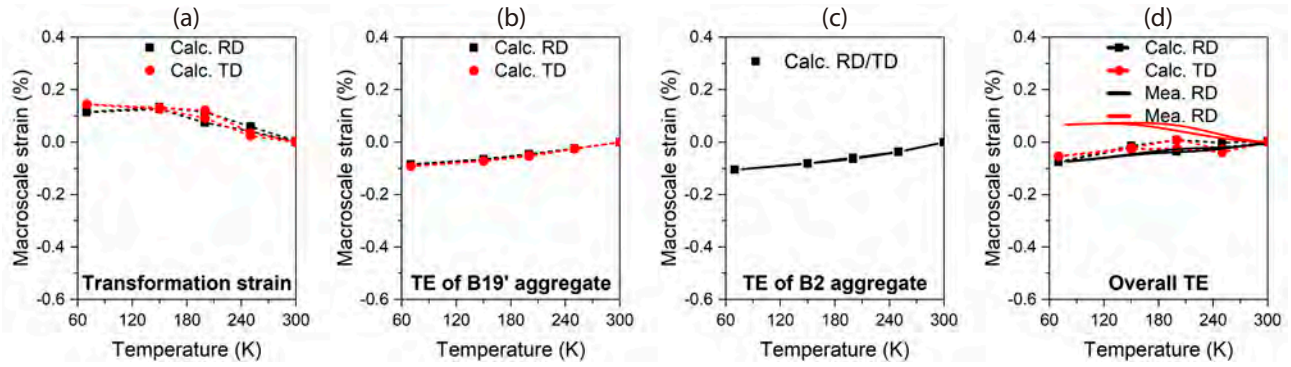

Figure 3. Comparison between the calculated and measured macroscopic TE of the CroR-15%-10%-5% NiTi: (a) Calculated TE from B2 ↔ B19′ phase transformation; (b) Calculated TE of the B19′ aggregate; (c) Calculated TE of the B2 aggregate; (d) calculated and measured overall TE of the sample.

References

[1] T. Saito et al., Science 300(5618) (2003) 464-467.

[2] H. Y. Kim et al., Acta Materialia 61(13) (2013) 4874-4886.

[3] L.S. Wei et al., Acta Materialia 100 (2015) 313-322.

[4] J. A. Monroe et al., Acta Materialia 102 (2016) 333-341.

[5] A. Ahadi et al., Acta Materialia 124 (2017) 79-92.

[6] A. Ahadi et al., Acta Materialia 76 (2014) 186-197.

[7] P. Hua et al., Acta Materialia 185 (2020) 507-517.

[8] T. Waitz et al., Acta Materialia 52(1) (2004) 137-147.

[9] T. Waitz et al., Materials Science and Technology 24(8) (2013) 934-940.

[10] A. Ahadi et al., Applied Physics Letters 103(2) (2013) 021902.

[11] Q. Li, et al., Acta Materialia 204 (2021) 116506.

Qiao Li[1], Zhongzheng Deng[1], Yusuke Onuki[3], and Qingping Sun[1, 2]

[1]Department of Engineering Mechanics, Wuhan University, Wuhan, China; [2]Department of Mechanical and Aerospace Engineering, The Hong Kong University of Science and Technology, Hong Kong, China; [3]Frontier Research Center for Applied Atomic Sciences, Ibaraki University, Shirakata, Tokai, Ibaraki, Japan

Crystal Structural Investigations for Understanding the Hydrogen Storage Properties of $YMgNi_4$-Based Alloys

1. Introduction

Efficient hydrogen storage methods have been considered as key issues for establishing of a hydrogen-based society. At present, gaseous hydrogen, liquid hydrogen and hydrogen storage alloys (metal hydrides) are candidate methods. In particular, the hydrogen storage alloys, in which hydrogen is stored as atomic state, can reach higher volumetric hydrogen densities than gaseous or liquid hydrogen stored as hydrogen molecules [1]. Although Mg or Mg containing intermetallic compounds are promising candidates in hydrogen storage alloys, most of them are thermodynamically stable, which indicates to heat materials up for hydrogen absorption and desorption reactions [2]. By contrast, $REMgNi_4$ based alloys (RE: rare-earth metals) exhibit reversible hydrogen absorption and desorption reactions at room temperature through formation of α-, β-, γ-phase hydrides [3-8]. The γ-phase hydride has the highest hydrogen storage capacities formed at the highest hydrogen pressure. Though Y as RE elements was expected to acquire higher gravimetric hydrogen densities due to the lightest element in the RE elements, the hydrogen absorption reaction of $YMgNi_4$ is halted during the formation of the β-phase hydride [3]. In our recent studies of hydrogen storage properties in $Y_{(2-x)}Mg_xNi_4$ ($0 < x < 2$), the hydrogen absorption and desorption reaction pressure decreased and hydrogen storage capacities increased with the decrease of the Mg amounts [9]. In the study, $Y_{1.06}Mg_{0.94}Ni_{4.00}$ had the highest hydrogen storage capacities in $Y_{(2-x)}Mg_xNi_4$.

Hence, we attempted neutron diffraction experiments under D_2 pressure combined with synchrotron X-ray diffraction experiments to understand the hydrogen absorption reaction of $Y_{1.06}Mg_{0.94}Ni_{4.00}$ viewed from the atomic arrangements.

2. Experiment

$Y_{1.06}Mg_{0.94}Ni_4$ were prepared from powder mixtures of YNi_2 and $MgNi_2$ at molar ratios of 1.2 : 0.8 [9].

Crystal structures of as-synthesized and hydrogen (deuterium) absorbed samples were investigated by synchrotron radiation powder X-ray diffraction (SR-PXD) and powder neutron diffraction (PND) performed on the BL-8A at the PF, and the NOVA at the J–PARC, respectively. For the SR-PXD, the samples were placed in a Lindemann glass capillary with an outside diameter of 0.3 mm and thickness of 0.01 mm. The measurement was conducted in an Ar atmosphere, and the data were collected at room temperature. For the PND, the samples were placed in a V sample container with an outside diameter of 10.80 mm and thickness of 1.5 mm. The samples were heat-treated at 423 K in a vacuum for 3 h to initiate the hydrogen absorption reaction. Following heat treatment, the PND data were collected at 323K under vacuum and deuterium gas pressure.

3. Results

Figure 1 shows Rietveld refinement fits of the PND patterns of $Y_{1.06}Mg_{0.94}Ni_{4.00}$ under vacuum, D_2 pressure of 3 MPa and vacuum at 323 K. The Bragg peaks under vacuum and D_2 pressure of 3 MPa were indexed by an FCC unit cell and an orthorhombic unit cell, which were finally refined to become a = 7.04108(08) Å and Z = 4 in F-43 m (No. 216), and a = 5.0407(1) Å, b = 5.4162(2) Å, c = 7.3035(2) Å and Z = 2 in $Pmn2_1$ (No. 31) in $Y_{1.06}Mg_{0.94}Ni_{4.00}D_{3.86}$, respectively. The deuterided phase corresponds to the β-phase hydride.

Crystal structures and atomic arrangements around D atoms during the absorption reaction of $Y_{1.06}Mg_{0.94}Ni_{4.00}$ are illustrated in Fig. 1. The D atoms were located in four crystallographically different sites, D1, D2, D3, and D4. The D1 and D2 atoms were located inside the triangular bipyramids and coordinated by two Y, one Mg, and two Ni atoms. The D3 atoms were positioned inside of the tetrahedron and coordinated by one Y and three Ni atoms. Although the positions of D1, D2, and D3 were analogous to those previously reported for the β-phase hydrides of $REMgNi_4$, small amounts of D4 atoms, which were located inside the tetrahedron and coordinated by one Y and three Ni atoms, were identified in our crystal structural investigations.

The crystal structure model of $Y_{1.06}Mg_{0.94}Ni_{4.00}D_{3.86}$ containing the D4 atoms exhibited better reproducibility of the experimentally observed PND pattern than the crystal structure model without the D4 atoms. Although the better Rietveld refinement fits of the PND for $Y_{1.06}Mg_{0.94}Ni_{4.00}D_{3.86}$ with D4 atoms were obtained, the interatomic distances between the D4 and the D2 (1.62 Å) or the D3 (1.87 Å) atoms were shorter than a criterion reported by Switendick [10] in which the minimum interatomic D–D distance were described to be 2.1 Å. Shorter interatomic D–D distances than the

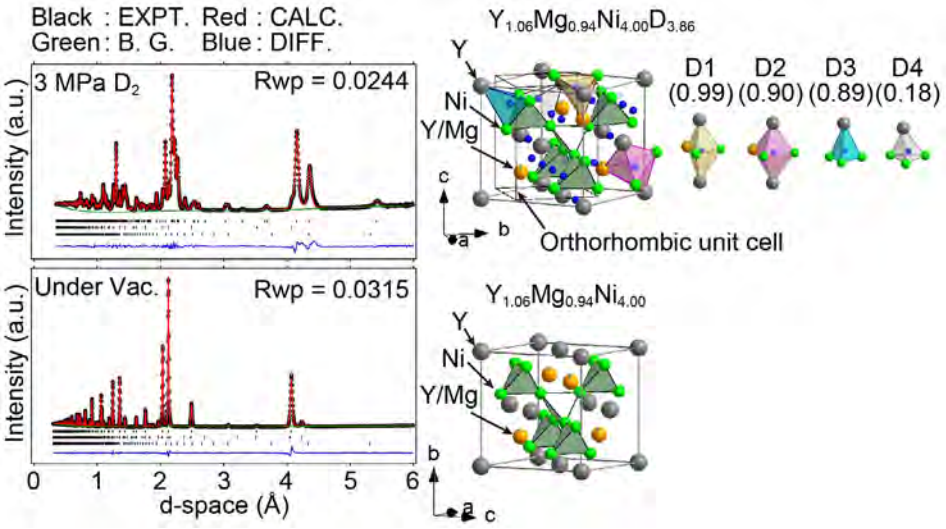

Figure 1. The Rietveld refinement fits of (left) $Y_{1.06}Mg_{0.94}Ni_{4.00}$ (under vacuum) and $Y_{1.06}Mg_{0.94}Ni_{4.00}D_{3.86}$ (under D_2 pressure of 3MPa), and (right) their crystal structures. The Y, Mg, Ni and D atoms are represented by the grey, orange, green and blue circles, respectively. In the atomic arrangements around D atoms, the D atomic sites in the triangular bipyramid and tetrahedra are represented by pink (D1), yellow (D2), cyan (D3) and green (D4) polyhedra. Parentheses indicate occupancies at each D atomic site.

criterion have been often reported for intermetallic compounds [11]. Recently, the shortest H–H interatomic distances with 1.5–1.6 Å in ZrV_2 ($ZrV_2H_{3.7}$), were reported by Borgschulte et al. who investigated the H atomic positions in $ZrV_2H_{3.7}$ by inelastic neutron scattering combined with theoretical calculations [12]. In this study, $Y_{1.06}Mg_{0.94}Ni_{4.00}$ adopted similar arrangements with ZrV_2. Notably, the local atomic arrangements of the D4 atoms in $Y_{1.06}Mg_{0.94}Ni_{4.00}D_{3.86}$ corresponded to some D atomic positions in the γ-phase hydride, which are obtained in higher H_2 pressure than β-phase hydrides. Considering on similarities to $ZrV_2H_{3.7}$ and the γ-phase hydride of $REMgNi_4$ and better Rietveld fits with D4 atoms, we propose the presence of the D4 atoms in the crystal structure of the β-phase hydride, $Y_{1.06}Mg_{0.94}Ni_{4.00}D_{3.86}$.

4. Future plans

We will study hydrogen vibrational properties during the hydrogen absorption reactions using inelastic neutron scattering for further understanding of hydrogen in $YMgNi_4$-based alloys. Based on the results, we will propose room temperature operated hydrogen storage materials, which have higher gravimetric and volumetric hydrogen densities than applicably used hydrogen storage alloy $LaNi_5$-based AB_5 alloys.

Acknowledgements

This research was supported by JST SICORP (JPMJSC 1802) and MEXT/JSPS KAKENHI (JP18H05513, JP18H05518, 19K05051).

References

[1] A. Züttel, Mater. Today, **6** 24 (2003).
[2] J. -C. Crivello et al., Appl. Phys. A, **122** 97 (2016).
[3] K. Aono et al., J. Alloys Compd. **309** L1 (2000).
[4] L. Guénée et al., J. Alloys Compd. **348** 129 (2003).
[5] N. Terashita and E. Akiba, Mater. Trans. **47** 1890 (2006).
[6] K. Sakaki et al., J. Phys. Chem. C **116** 19156 (2012).
[7] K. Sakaki et al., Inorg. Chem. **52** 7010 (2013).
[8] V. V. Shtender et al., J. Alloys Compd. **603** 7 (2014).
[9] T. Sato et al., ACS Omega **5** 31192 (2020).
[10] A. C. Switendick, Z. Phys. Chem. **117** 89 (1979).
[11] V. A. Yartys et al., J. Alloys Compd. **330-332** 132 (2002).
[12] A. Borgschulte et al., Proc. Natl. Acad. Sci. USA **117** 4021 (2020).

T. Sato[1], T. Mochizuki[2], K. Ikeda[3], T. Honda[3], T. Otomo[3], H. Sagayama[3], H. Yang[4, 5], W. Luo[4, 5], L. Lombardo[4, 5], A. Züttel[4, 5], S. Takagi[2], T. Kono[2], and S. Orimo[2, 6]

[1]*Shibaura Institute of Technology;* [2]*Institute for Materials Research, Tohoku University;* [3]*Institute of Materials Structure Science, KEK;* [4]*Institute of Chemical Sciences and Engineering, Basic Science Faculty, EPFL Valais/Wallis;* [5]*Empa Materials Science and Technology;* [6]*Advanced Institute for Materials Research (WPI-AIMR), Tohoku University*

Identifying Water/ice in Simulated Fuel Cell for Vehicle by Pulsed Neutron Imaging

1. Introduction

Polymer electrolyte fuel cells (PEFCs) are electrochemical devices that convert the chemical energy stored within hydrogen into electricity, with water as the only by-product. PEFCs are expected to be an efficient and clean powertrain for automobiles. Toyota launched the world's first mass-produced fuel cell electric vehicle (FCEV), the MIRAI, in 2014 [1].

FCEVs have to be operated under various environmental conditions, including sub-zero start-up operations. If produced water in the FC stack freezes, ice formation in the cell could prevent the transfer of the hydrogen and oxygen gases [2–7]. Therefore, the liquid water and/or ice distribution in the FC is important. Energy-resolved neutron radiography has been a vitally effective methodology to identify liquid water and ice [8–10]. In the latest research, water and/or ice in gas diffusion layers and flow channels of PEFC were measured using this method [10].

In this work, energy-resolved neutron imaging with large view area was employed to visualize the distribution of liquid water and ice in a simulated environment of an automotive FC at the RADEN beamline, which is the dedicated instrument for energy-resolved neutron imaging [11–14] in the Materials and Life Science Experimental Facility (MLF) of the Japan Proton Accelerator Research Complex (J-PARC).

2. Experimental and data processing

The experimental setup and the sample are shown in Fig. 1 and Fig. 2 [15]. A CCD camera system [16] was employed, and energy-selected images using the wavelength-definition chopper were recorded. The field of view of the CCD camera was 300 mm × 300 mm. The energy ranges were 20 – 100 meV (first energy range, E_1, in which the neutron cross section of liquid water is almost equal to that of ice.) and 0.9 – 2.0 meV (second energy range, E_2, in which neutron cross section of liquid water is larger than that of ice).

The sample size was 4 mm × 96 mm × 256 mm to simulate the flow channels of automotive FC. Glass and stainless-steel capillaries, both water-filled and empty, were mounted in the case made from Al alloy (A2017). Titanium (Ti) plate sealed in an Al foil bag with water was also mounted. Thermocouples were installed around the Al case. The sample case was sandwiched by two cooling pads, in which Fluorinert© (FC-770) flowed as the refrigerant. The sample with cooling pads was placed in a polycarbonate chamber with Al windows, and dried air was continually flowed through the chamber to avoid condensation of water vapor.

Time-lapse observations were performed while

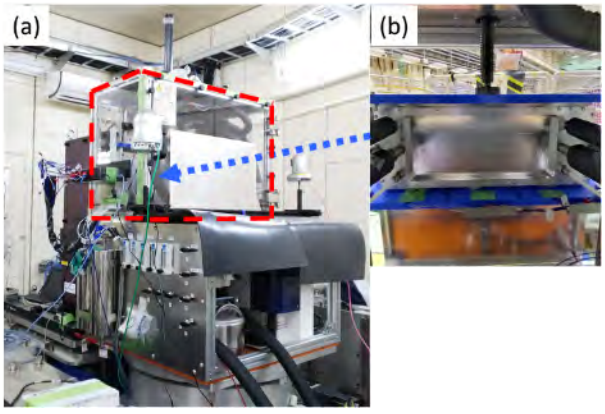

Figure 1. Setup of the experiment. (a) thermal insulation chamber, highlighted by the red dashed line, with Al windows. (b) cooling pads sandwiching the Al sample case, and Fluorinert is flowed inside [15].

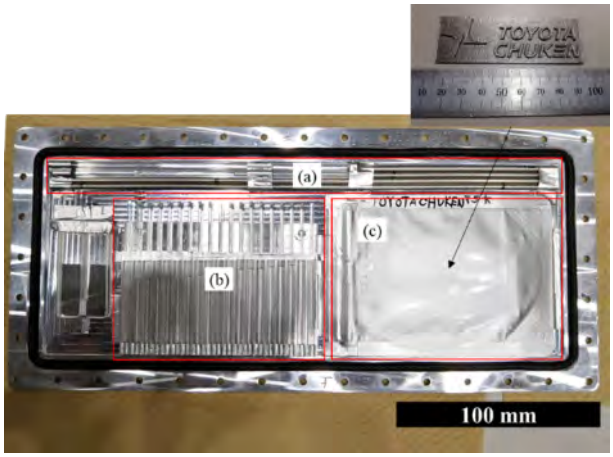

Figure 2. Sample contents in the Al alloy case. The samples consist of (a) long stainless-steel and glass capillaries (inner diameter of 2.0 mm), (b) short glass capillaries (inner diameter of 1.15 mm), and (c) an additively manufactured Ti plate with the raised logo of Toyota Central R&D Labs., Inc. (TOYOTA CHUKEN). The plate thickness ranges from 0.9 to 1.9 mm [15].

alternately changing the neutron energy range (E_1 and E_2). Measuring temperature was, at first, –30°C, and then was gradually heated up to 17°C. Since the MIRAI guarantees its operation at –30°C, the evaluation of FCs under such a cold environment is necessary.

Two parameters were used in data processing. The one concerns the amount and the phase recognition of H_2O, and is calculated from the neutron transmission at the higher neutron energy range (above a few tens meV, which is E_1 in this report) as follows:

$$\ln[1/T_{H_2O}(E,x,y)] = \rho(x,y)d(x,y)\sigma'(E,x,y) \quad (1)$$

where $T_{H_2O}(E,x,y)$ is the transmission for neutron energy E at the position (x,y), $\rho(x,y)$ is the molecular number density, $d(x,y)$ is the projected number of molecules. $T_{H_2O}(E,x,y)$ is calculated from the radiograph of the sample as a numerator and the blank image as the denominator. $\sigma'(E,x,y)$ is the cross section including possible contributions due to scattered neutrons from the neighboring capillary. Eq.1 depends only on the amount of H_2O, irrespective of its state. The other parameter for the phase recognition is obtained by consideration of the neutron cross section at the lower neutron energy range below a few meV, which is E_2. Here we define another new parameter, α, which is the normalized cross section calculated from two transmission images taken at different energies, cancelling the uncertainty of σ and d, as follows:

$$\alpha(x,y) = \frac{\sigma'(E_2,x,y)}{\sigma'(E_1,x,y)} = \frac{\ln[T_{H_2O}(E_2,x,y)]}{\ln[T_{H_2O}(E_1,x,y)]} \quad (2)$$

For the following visualizations, we normalized the parameter $\alpha(E)$ as β. The value was between 0 and 1, corresponding to ice and water states, respectively.

$$\beta(x,y) = \frac{\alpha(x,y) - \alpha(x,y)_{\mathrm{ice}}}{\alpha(x,y)_{\mathrm{water}} - \alpha(x,y)_{\mathrm{ice}}} \quad (3)$$

We also introduced the additional parameters α' and β', defined below, which are used as alternatives to α and β when blank images are not available.

$$\alpha' = \frac{\ln[T_{\mathrm{sample}}(E_2)]}{\ln[T_{\mathrm{sample}}(E_1)]} \quad (4)$$

$$\beta' = \frac{\alpha' - \alpha'_{\mathrm{ice}}}{\alpha'_{\mathrm{water}} - \alpha'_{\mathrm{ice}}} \quad (5)$$

3. Results and discussion

Figure 3 show a neutron radiograph of the sample and images of β'during the thawing process for water/ice identification. Note that the base value, α'_{ice} and α'_{water}, used for the calculation of β', were taken at –12°C and 17°C, respectively. The hues of these images changed in correspondence with the volume change of H_2O in the capillaries arising from the phase transition from ice to

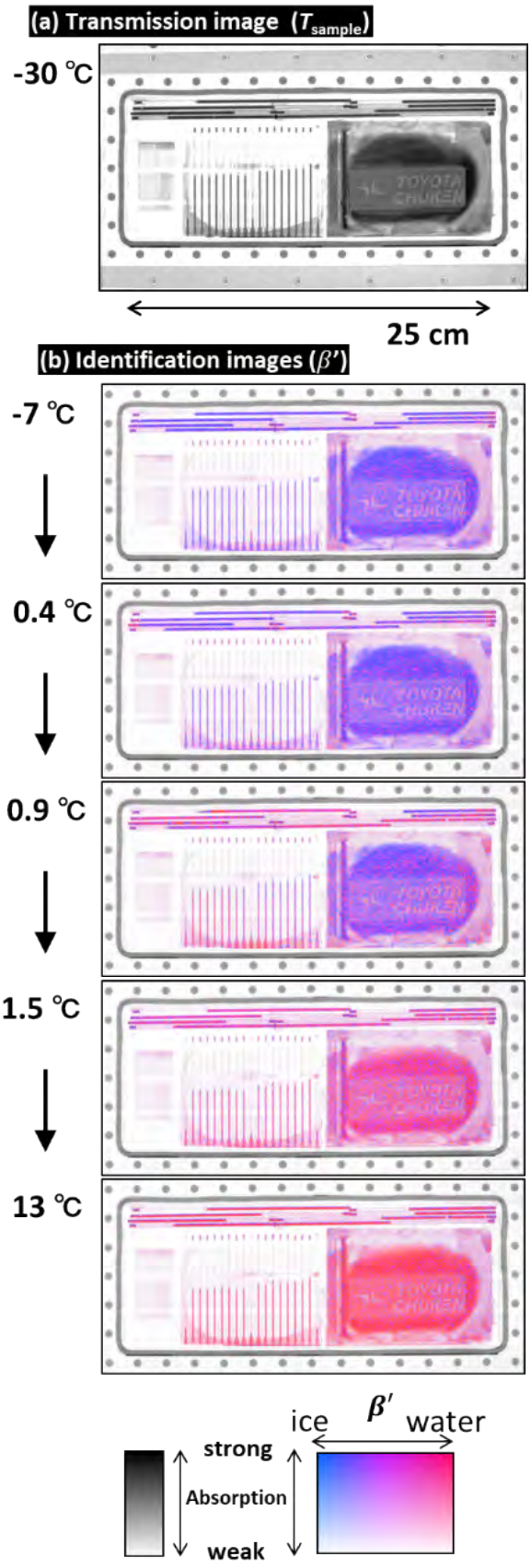

Figure 3. (a) Transmission image at –30°C and (b) water/ice identification images during the thawing process are shown. The temperatures show the average of the measured values by the thermocouples around the sample case [15].

liquid. The β' images showed that that the thawing of ice in the capillaries did not happen simultaneously at the temperature close to 0°C. Additionally, inhomogeneous thawing seemed to had happened in this setup.

Thus, visualization of ice and liquid water distributions with a large field of view was confirmed according to the analysis method introduced in this experiment, and recognition of the state of water in the large size system (full-scale of automotive FC) was successfully performed.

By utilizing the difference of the energy-dependent neutron cross section of ice and water states, we were able to distinguish with a large field of view the phase of H_2O in a metal-cell. However, it did not cancel correctly the contribution of objects other than H_2O, because blank images are not available. In the case of an actual FC, it is possible to measure and extract the water information free from the interference of the surroundings, since FCs in a dry condition can be easily measured. We expect to be able to clarify the freezing-thawing behavior of H_2O in-side the automotive FC by using the identification by the energy-dependent imaging with pulsed neutrons.

List of symbols and units

T	Transmission.
T_{H_2O}	Transmission of only H_2O.
T_{sample}	Transmission of sample.
σ	neutron cross section [m^2].
σ'	Value equivalent to neutron cross section [m^2].
ρ	number density of H_2O molecule [m^{-3}].
d	Thickness of H_2O [m].
α	Identification term.
α'	α including background.
β	Identification term.
β'	β including background.

References

[1] N. Konno, S. Mizun et al., SAE Int. J. Alt. Power., 2015, 4, 123–129.
[2] G. S. Hwang et al., Electrochim. Acta, 2013, 95, 29–37.
[3] S. Kim, et al., J. Power Sources, 2008, 179, 140–146.
[4] Y. Ishikawa et al., J. Power Sources, 2008, 179, 547–552.
[5] Y. Tabe et al., J. Power Sources, 2012, 208, 366–373.
[6] I. Mayrhuber et al., Chem. Electro. Chem, 2015, 2, 1551–1559.
[7] L. Li, S. Wang et al., Int. J. Hydrogen Energy, 2019, 44, 12033–12042.
[8] J. Biesdorf et al., Phys. Rev. Lett., 2014, 112, 248301.
[9] M. Siegwart et al., Rev. Sci. Instrum., 2019, 90, 103705.
[10] M. Siegwart et al., J. Electrochem. Soc., 2020, 167, 064510.
[11] K. Mochiki et al., J. Instrum., 2018, 13, C01038.
[12] Y. Kiyanagi et al., Phys. Procedia, 2013, 43, 92–99.
[13] T. Shinohara et al., J. Phys.: Conf. Ser., 2016, 746, 012007.
[14] T. Shinohara et al., J. RADEN, Rev. Sci. Instrum., 2020, 91, 043302.
[15] Y. Higuchi et al., Phys. Chem. Chem. Phys., 2021, 23, 1062–1071.
[16] Y. Matsumoto et al., Phys. Procedia, 2017, 88, 162–166.

Y. Higuchi[1], D. Setoyama[1], K. Isegawa[2], Y. Tsuchikawa[2], Y. Matsumoto[3], J. D. Parker[3], T. Shinohara[2], and Y. Nagai[1]

[1]Materials Analysis & Evaluation Research-Domain, Toyota Central R&D Labs., Inc.; [2]Neutron Science Section, Materials and Life Science Division, J-PARC Center; [3] Neutron Science and Technology Center, CROSS.

Polarization Analysis for Small-Angle Neutron Scattering with ^{3}He Spin Filter

1. Introduction

Small-angle neutron scattering (SANS) is a powerful technique to study microscopic structures of soft matters such as polymers, collides, biomolecules and so on. In the SANS experiment, incoherent scattering, which does not contain structural information, is a main source of background to determine structures of a sample. If the size of the scatterers containing hydrogen atoms, which has very large incoherent scattering cross section, is less than several nanometers, the coherent and incoherent scattering intensities tend to compete in a Q region of typically Q > 0.1 Å. Therefore, accurate separation of the coherent scattering from the incoherent scattering is necessary in such cases. Since a neutron spin polarity flips with a probability of 2/3 in the incoherent scattering but not in the coherent scattering, the coherent and incoherent scattering intensities can be separated by the polarization analysis with a polarized neutron beam.

^{3}He spin filter is a neutron polarization device in which polarized ^{3}He gas is encapsulated into a special glass cell. It can polarize a neutron beam in a broad energy range with a large solid angle, and therefore, it is suitable as a polarization analysis apparatus of BL15 TAIKAN, which is a small- and wide-angle neutron scattering instrument at MLF [1].

This paper reports on our new experimental setup for the polarization analyzed SANS using ^{3}He spin filter at TAIKAN and its first result of the demonstration study.

2. Development of polarization analysis system

The ^{3}He spin filter based on a spin exchange optical method has been developed in J-PARC for various neutron scattering experiments [2]. We fabricated a ^{3}He spin filter with a diameter of 60 mm and thickness of 40 mm for the SANS experiment using a gas filling station at J-PARC. The ^{3}He gas pressure was 1.5 atm, which is optimized to neutrons around 3 Å. The ^{3}He spin filter was polarized by a fiber laser system with a power of 110 W and then transported to the neutron beam line. Since the ^{3}He polarization decays by an inhomogeneous magnetic field at the beamline, a Helmholtz coil with a diameter of 60 cm was developed to apply a homogenic magnetic field to the ^{3}He spin filter (Fig. 1). It equips a motorized sample changer on which six samples can be mounted simultaneously. The ^{3}He spin filter was placed 10 mm behind the sample to cover a wide solid angle, which corresponds to a scattering angle of 0–24°. Note that the scattering angles covered by middle-angle (MA) and small-angle (SA) detector banks at TAIKAN were 11.5–25.0° and 0.20–12.5°, respectively.

3. Experiment and results

Some types of colloidal particle dispersion samples were measured in this study. The incident neutron beam was polarized by magnetic supper mirrors installed at the upstream-optics section of TAIKAN. A measurement time of 2 hours was required for each sample. The ^{3}He spin polarity was fixed, and the neutron spin polarity was flipped every hour using a spin flipper placed just behind the polarizer. Since the ^{3}He polarization varies due to a polarization relaxation, it was periodically determined during the experiment by measuring the neutron transmission of the ^{3}He spin filter measured without the sample. The ^{3}He polarization at the start time of the experiment and the relaxation time were 71% and 170 h, respectively. They are sufficient for continuous use for approximately 2 days, thus reaching the typical duration

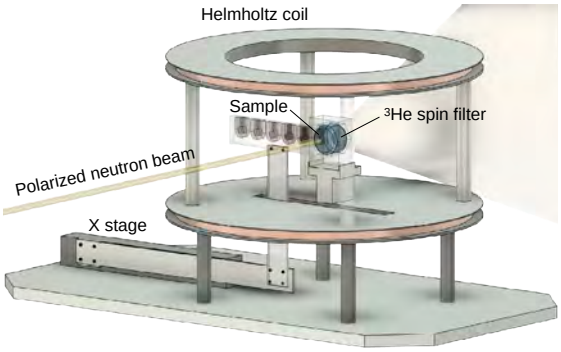

Figure 1. The polarization analysis system with the ^{3}He spin filter for the SANS experiment.

required for a complete set of SANS experiments.

In the experiment, we measured scattering intensities when polarized neutron spins and that of ^{3}He are parallel and anti-parallel for each sample. By correcting these scattering intensities with the ^{3}He polarization degree, transmission of ^{3}He cell and the sample, the spin-flip and spin-non-flip intensities I_{sf}, I_{nsf} were obtained. The coherent and incoherent scattering intensities I_{coh}, I_{inc} are given as

$$I_{nsf} = (1 - p)\, I_{inc} + I_{coh} \quad (1)$$

$$I_{sf} = p\, I_{inc}. \quad (2)$$

Since the spin flip probability of the incoherent scattering p is deviated from 2/3 depending on a composition of the sample because of the multiplicity of neutron scattering event in the sample, the value of p was estimated using a Monte-Carlo simulation by considering the elemental composition of the sample. The experimental results are shown in Fig 2. We can see that the scattering intensity was accurately separated to the coherent and incoherent components. The incoherent component from the SA detector bank is almost constant with Q as expected, whereas that from the MA detector bank is Q-dependent and is not consistent with that of SA even at the same Q. However, the coherent components show good agreement with the SA and MA detector banks in the overlapping Q region. Note that the difference in the inelastic scattering component, which is contained in the incoherent component in the SA and MA detector banks, is likely to contribute to the discrepancy in the scattering intensity, which is known as the Placzek effect [3]. This result shows that a contribution of the inelastic scattering can be isolated as well as the incoherent component from the coherent component by using the polarization analysis method. We successfully demonstrated the polarization analysis with the ^{3}He spin filter at the SANS experiment, and these results provided substantial progress in SANS data analysis at TAIKAN. The details of the experimental setup, corrections, and results are described in Ref. [4].

4. Future plans

The polarization analysis in the higher Q region is also worth studying because the influence of inelastic scattering event becomes more pronounced at the higher Q region. We are planning to perform a polarization analysis experiment with a high-angle and backward detector banks at TAIKAN in the near future. The polarization analysis method reported in this work is anticipated to be used frequently, not only in SANS experiments but also throughout neutron scattering experiments at J-PARC.

References

[1] S. Takata et al., JPS Conf. Proc., **8** 036020 (2015).
[2] T. Okudaira et al., Nucl. Inst. and Meth. Phys. Res. A, **977** 164301 (2020).
[3] G. Placzek, Phys. Rev., **86** 377–388 (1952).
[4] T. Okudaira et al., J. Appl. Cryst., **54** 548–556 (2021).

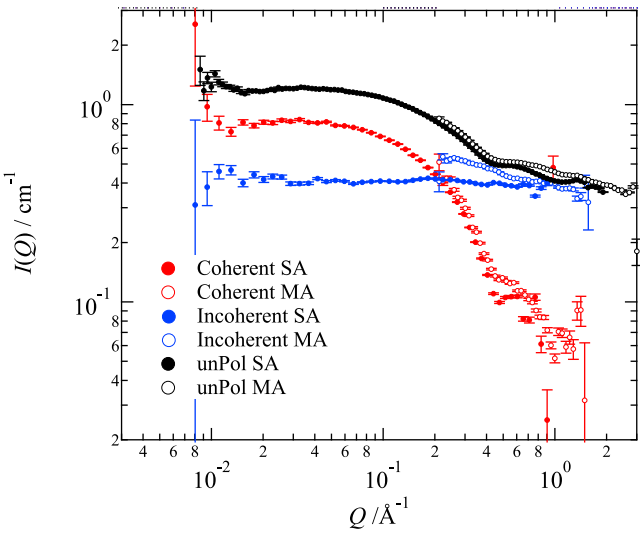

Figure 2. SANS profiles obtained for the colloidal particle dispersions of $PtCl_6(BEHU{\cdot}H)_2$ complexes. Coherent scattering intensity (red close and open circles) and incoherent scattering component (blue close and open circles) are plotted as a result of the polarization analysis. SANS profiles obtained using an unpolarized incident neutron beam are indicated by black closed and open circles. The abbreviations SA and MA denote the small-angle and middle-angle detector banks, respectively.

T. Okudaira[1,2], Y. Ueda[3,4], K. Hiroi[5], R. Motokawa[2], Y. Inamura[5], S. Takata[5], T. Oku[2,6], J. Suzuki[7], H. Endo[5,8], and H. Iwase[7]
[1]Department of Physics, Nagoya University; [2]Technology Development Section, Materials and Life Science Division, J-PARC Center; [3]Materials Sciences Research Center, Japan Atomic Energy Agency; [4]Advanced Science Research Center, Japan Atomic Energy Agency; [5]Neutron Science Section, Materials and Life Science Division, J-PARC Center; [6]Graduate School of Science and Engineering, Ibaraki University; [7]Neutron Science and Technology Center, CROSS; [8]Institute of Materials Structure Science, KEK

A Novel Challenge of Nondestructive Analysis for Medical Inheritances: Identification of OGATA Koan's Sealed Medicine by Muonic X-ray Analysis

1. Introduction

OGATA Koan (1810–1863) was a physician and the director of Tekijuku, and he contributed to Western medicine in the late Edo period. Two of his medicine chests are preserved at Osaka University. The medicine chest which was used in his last years (the second chest) contained 22 glass bottles and 6 wooden cylinders. These bottles and cylinders contained formulated medicines; however, about half of them were sealed tightly and could not be opened after having been kept in storage for a long time. It is necessary to reveal the physical properties of both the containers and their contents for their proper preservation. However, destructive analysis is not allowed, because they are historically precious inheritances. To analyze these medicines sealed in the glass bottles, we focused on muonic X-ray analysis, which has high transmittance that would realize the analysis of contents through the glass. We applied this groundbreaking method on medical inheritances for the first time and tried to analyze the chemical components of both the containers and their contents.

Before the analysis of Koan's inheritance, we performed a preliminary experiment to examine the analytical method using the historical medicinal specimen preserved at the Osaka University. Second, we applied that method on the bottles stored in the second chest (Fig. 1) [1].

2. Experimental

First, we applied X-ray fluorescence (XRF) to identify the component of the glass of the bottles stored in the second chest. Thereafter, we moved on to the muonic X-ray analysis.

Figure 1. OGATA Koan's second medicine chest.

The muonic X-ray analysis was conducted at the D2 area in the Material and Life Science Facility, J-PARC. We constructed the muonic X-ray analysis setup according to the previous method [2, 3]. The muon beam was collimated to a diameter of 30 mm. Muonic X-rays emitted from the sample were recorded by two high-purity germanium semiconductor detectors (ORTEC, GMX20). Before the long-time analysis, muon irradiations with incident muon momenta of 40–60 MeV/*c* were conducted, and an optimum incident muon momentum was determined to stop the muon in the medication of the bottle efficiently. The durations of muon irradiations with optimum incident muon condition were 7 h for the preliminary study and 12 h for Koan's inheritance. The elemental composition at the muon stopping position for each measurement was determined from the intensities of muonic X-rays for constituent elements by correcting the detection efficiencies of the germanium detectors.

3. Results and discussion

For the preliminary study, we selected the sealed glass bottle with tablets containing mercuric chloride ($HgCl_2$) from the specimen stored at Osaka University. By the muonic X-ray analysis, the peaks of Hg and Cl were detected at the 55 MeV/*c* incident muon condition and those muons were estimated to stop at the tablets. This result showed that the muonic X-ray measurement can analyze the medicinal inheritances sealed in a glass bottle.

Then we chose the sealed glass bottle with the label "甘" from the second chest for muonic X-ray analysis. Its height was 62.5 mm and the base was a rectangle with each side of 19.0 mm × 18.0 mm, then a white powder was left in the bottle at a depth of about 13 mm. By the historical investigation and the appearance of the content of the bottle, the sign "甘" was inferred to represent "甘汞" which means calomel or mercurous chloride (Hg_2Cl_2).

Muonic X-ray analysis was performed for the bottle, and we attained the spectrum shown in Fig. 2. The peaks of Hg, Cl, Pb, Si, and O were detected at 55 MeV/*c*

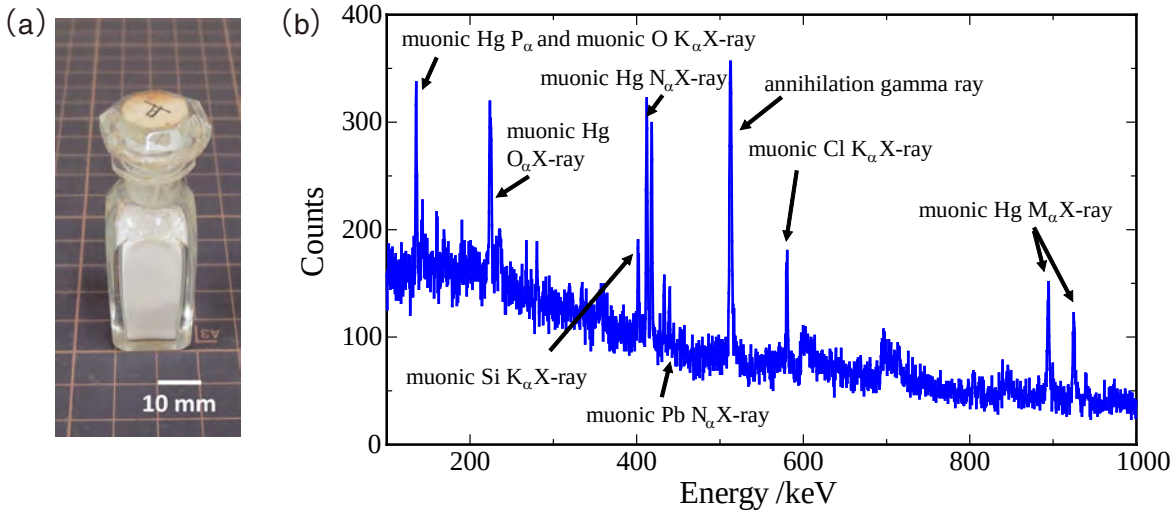

Figure 2. OGATA Koan's glass bottle used for the analysis (a) and muonic X-ray spectrum from its measurement (b). Muonic X-rays from Hg and Cl were originated from the contents of the bottle. Small muonic X-ray peaks from Pb, Si and O came from the muon stop in the bottle.

incident muon momentum condition. The significant peaks, Hg and Cl were assigned as the main components of the medication. The rest of the smaller peaks, Pb, Si, and O seemed to originate from the bottle. In this study, the beam diameter was larger than the bottle and the muons should have also stopped in the glass. These detected elements correspond with the result of XRF, which have suggested the glass to be lead potash glass.

The intensity ratio of muonic Hg to Cl X-rays was about three times higher than that from the analysis by the sample of the preliminary study. We concluded that the content of the glass bottled specimen "甘" is not $HgCl_2$ but Hg_2Cl_2. The result from the muonic X-ray analysis was consistent with the historical and pharmacognostical investigation. Through these studies, we demonstrated that the muonic X-ray can be used for a novel nondestructive analysis of medical inheritances.

4. Future plans

In this study, we applied the muonic X-ray analysis on the medical inheritances and succeeded in analyzing the content sealed in a glass bottle. This would be an epoch-making method for cultural properties which would allow the nondestructive analysis of both container and contents even if it is completely sealed. Presently, most of the targets of the muonic X-ray analysis are inorganic materials. On the other hand, it has been revealed that the muon capture processes are different with structures of muon capturing molecules [4]. This suggests the possibility for application of muonic X-ray analysis on organic materials, and such advances will expand its further application on cultural properties.

Acknowledgments

The muon experiment at the Materials and Life Science Experimental Facility of the J-PARC was performed under a user program (Proposal No. 2019B0314 and 2014MS01). This work was supported by Grant-in-Aid for Scientific Research (A) (No. 17H00832) and Grant-in-Aid for Scientific Research (C) (No. 18K01102) from the Japan Society for the Promotion of Science.

References

[1] K. Shimada-Takaura et al., J. Nat. Med., **75** 532 (2021).
[2] K. Ninomiya et al., Bull. Chem. Soc. Jpn., **85** 228 (2012).
[3] K. Ninomiya, Hamon, **25** 13 (2015).
[4] K. Ninomiya et al., J. Radioanal. Nucl. Chem., **319** 767 (2019).

Kyoko Takahashi[1,2], Kayoko Shimada-Takaura[1], Kazuhiko Ninomiya[3], Akira Sato[3], Naomi Ueda[4], Motonobu Tampo[5], Soshi Takeshita[5], Izumi Umegaki[6], and Yasuhiro Miyake[5]

[1]The Museum of Osaka University; [2]Tekijuku Commemoration Center; [3]Graduate School of Science, Osaka University; [4]Gangoji Institute for Research of Cultural Property; [5]High Energy Accelerator Research Organization; [6]Toyota Central Research & Development Laboratories., Inc.

Detection of Metallic Li Deposition on an Anode of a Li-ion Battery Using Muonic X-rays

1. Introduction

In recent years, the applications of the lithium (Li)-ion batteries have expanded making them an indispensable part of our lives. Recently, the reuse of used Li-ion batteries is being considered, and in order to reuse them safely and efficiently, it is necessary to observe the inside of Li-ion batteries in a non-destructive manner. In a used battery, Li is sometimes reduced and deposited as metal on its electrode, depending on the operating conditions of the battery. The metallic Li is known to lead to short-circuits between electrodes, thermal reactions with the electrolyte, and reduced capacity. Once deposited, metallic Li does not easily return to ions, so it is important to evaluate the amount of the metallic Li deposition before reusing Li-ion batteries.

In the elemental analysis with fluorescent x-rays, in general, Li can be detected only at the surface of a sample because their energy for Li is below 0.5 eV. There are some non-destructive analysis techniques to detect Li: Auger Electron Spectroscopy, Rutherford Backscattering Spectroscopy and Electron Probe Micro Analyzer (EPMA). However, the applications of these techniques are also limited to the surface of a sample.

On the other hand, elemental analysis with muonic x-ray is a candidate for a non-destructive analytical technique. This is because a muon can penetrate a sample deeply depending on its momentum. The energy of muonic x-rays, which is generated when a negative muon is captured by a nuclear to form a muonic atom in the sample, is about 200 times higher than that of fluorescent x-rays. In the case of Li, it is 18.7 keV. Since the energy is intrinsic to an element, the latter is determined by detecting muonic x-rays. Then, the muonic x-rays of Li can pass through the housing of a Li-ion battery to be detected by a Ge semiconductor detector.

2. Experimental

A highly sensitive detection system for muonic x-rays of Li in Li-ion batteries has been developed at MUSE, MLF, J-PARC. In addition, a low-momentum, high-intensity negative muon beam is required to measure samples with a layered structure of several tens of μm thick electrodes, such as Li-ion batteries.

We prepared two samples, which were composed of a fully charged (C_6Li) graphite anode and metallic Li deposition. They were wrapped in a laminated sheet. The location of the deposition was set at 45 μm (Sample A) and at 135 μm (Sample B) from the surface of the samples [Fig. 1(b)].

3. Results and consideration

We obtained energy spectra including some peaks corresponding to the elements of main components for Sample A, that is, C and Li. The peak at 18.7 keV was assigned as Kα signal for Li. Figure 1 shows the depth dependence of the intensity of the peak (I_{CLi}). The intensity of the muonic x-rays of Li is normalized by that of the C-Kα signal represented as I_{CLi}, because the signal of

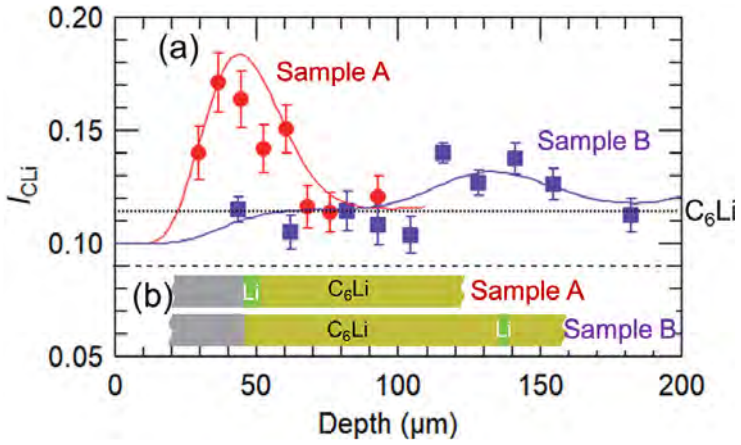

Figure 1. The depth dependence of I_{CLi} for samples with metallic Li deposition located at 45 (Sample A) and 135 μm (Sample B) in the depth from the surface.

Li-Kα cannot be distinguished from the one of C-Lβ with the resolution of Ge semiconductor detectors. Assuming the ratio of signals between C-Kα and C-Lβ is constant, any deviation of the ratio represents the existence of Li.

As the depth increases, I_{CLi} increases up to 0.17 and decreases down to 0.115 at 70 μm. Above 70 μm, the composition is C_6Li and I_{CLi} is 0.115. This broad increment is considered to be corresponding to the existence of Li at 45 μm [Fig.1(b)], since the distribution of muons is rather wide at several tens of μm. It was the first time to apply successfully nondestructive detection of metallic Li deposited on a graphite anode. We concluded that detection of metallic Li can be achieved due to the high contrast between metallic Li and Li in an anode (Fig. 2). Such high contrast between metallic Li and C_6Li comes from the fact that the capture rate of negative muons differs between metallic Li and Li ions in C_6Li, and the detection sensitivity per Li atom for both differs by about 50 : 1.

Furthermore, we obtained the depth dependence of I_{CLi} for Sample B, in which metallic Li was deposited at 135 μm in the depth [Fig.1(a)]. The increase of I_{CLi} between 105 to 180 μm, represented the existence of metallic Li deposition. Since the location of metallic Li deposition in a Li-ion battery will be similar to this situation, this result implies the possibility to detect metallic Li deposition in a Li-ion battery.

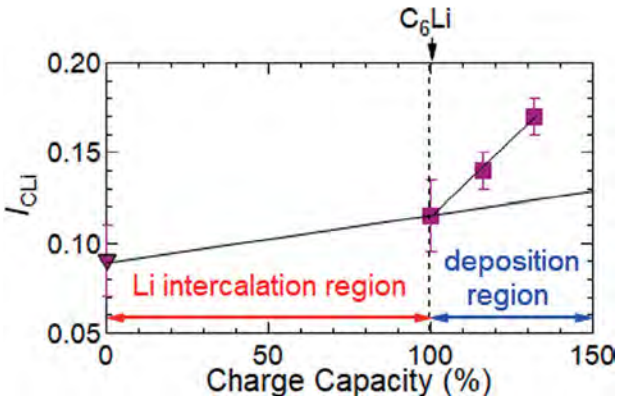

Figure 2. The relationship between I_{CLi} and the charge capacity.

It is noted that, in this study, the electrode with metallic Li deposition was obtained and wrapped in a laminated sheet for this experiment, while batteries commercially available also possess containers and electrolytes inside. Although it is necessary to consider the change in the stopping range due to the electrolyte, this effect is not significant. In addition, since a 0.5 mm-thick aluminum housing allows muonic x-rays to pass through, this technique can be applied to a Li-ion battery with an aluminum housing as well as a laminated Li-ion battery. It is hoped that this research will lead to further improvements in the safety of Li-ion batteries, which will promote eco-friendly reuse of Li-ion batteries in near future.

Further information can be obtained from [1].

4. Future plans

Future enhancement of muon intensity and improvement of the detectors may enable in-situ analysis. It is also desirable to obtain an image of the metallic Li deposition on the electrode in a non-destructive way in order to control the metallic Li deposition. We will expand this technique to an imaging technique providing elemental mapping for Li in a non-destructive way.

Reference

[1] I. Umegaki, Y. Higuchi, Y. Kondo, K. Ninomiya, S. Takeshita, M. Tampo, H. Nakano, H. Oka, J. Sugiyama, M. K. Kubo, and Y. Miyake, Analytical Chemistry, **92** 12, 8194-8200 (2020).

I. Umegaki[1,2], M. Tampo[1,2], S. Takeshita[1,2], Y. Miyake[1,2], and K. Shimomura[1,2]

[1] *Muon Science Section, Materials and Life Science Division, J-PARC Center;* [2]*Institute of Materials Structure Science, KEK*

Neutron Source

Neutron Source Section

1. Overview of the beam operation

In fiscal year 2020, the neutron source section started the beam operation with beam power of 500 kW, but it was forced to stop it from April 20 to May 15 due to the coronavirus pandemic. After the beam operation was resumed, the beam power was raised to 600 kW on May 18 and the stable operation continued. Thus, for the first time, an operation with over 600 kW for the long-term user program was achieved. At the end of the beam operation before the summer outage, a high-power operation was maintained for 36.5 hours at 930 kW from June 25 to 27, much longer than the 10.5 hours achieved in 2019. This made it possible to obtain significant operation data, which normally would require long time to reach a stable value. Also, the validity of the system design with regard to the ultimate power goal was reconfirmed. After the summer outage, the beam operation for the user program started on December 1 after three weeks delay from the original schedule. The neutron source continued its stable operation at 600 kW after the summer outage period and the average operational efficiency in fiscal year 2020 reached 91%.

2. Mercury target system

A notable achievement was the successful operation of the new-type target vessel, target #11, in which the coupling-free structure between the inner mercury and the surrounding outer water shroud removes the structural cause of generating high thermal stress on the target. This was one of the major milestones to achieve stable and long-term operation at 1 MW.

There was also an important outcome in the pitting damage mitigation technology of the target vessel to achieve a stable 1 MW operation. As shown in the middle of Fig. 1, injection of micro-bubbles of helium gas into the mercury flow in the target vessel was used to reduce the intensity of the pressure waves which caused pitting damages. In addition to that, the narrow channel has been made by adding an inner wall at the forefront wall of the target vessel to mitigate the pitting damage by a steep velocity gradient of rapid mercury flow. Specimens were cut out from the forefront wall of target vessel #11 with a hole-saw drilling machine. The bottom picture in Fig. 1 shows that the pitting damages on both the narrow channel side and the bulk side of the inner wall specimen are very small, even after the long run of the 600 kW operation. These results demonstrated the excellent effect of the present technology for

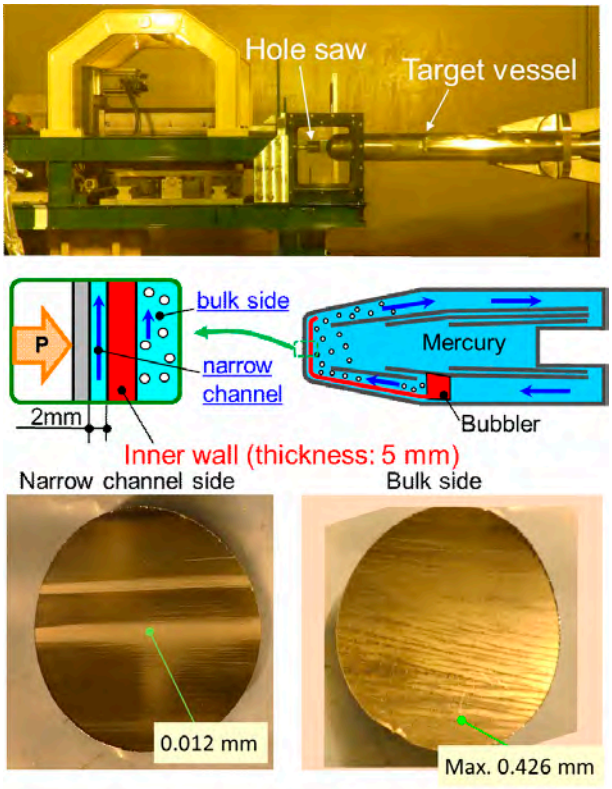

Figure 1. Cutting machine (top) and structure of the target vessel (middle) and the surfaces of an inner wall specimen (bottom)

pitting damage mitigation and are promising for further power ramp-up.

Target vessel #11 was replaced with a new target vessel but misalignment of the coolant pipe position led again to a target replacement with another spare target, which caused a delay in the maintenance schedule. To prevent a recurrence of this failure, the fabrication and inspection procedure for the target vessel was improved.

3. Cryogenic hydrogen system

The cryogenic hydrogen system, which supplies liquid hydrogen to three moderators, was designed to suppress the temperature rise of liquid hydrogen, caused by the nuclear heating at the moderators, to be below 3 K at a 1 MW beam operation. The dependency of the temperature rise on the flow rate of liquid hydrogen, which corresponds to the rotation speed of the hydrogen circulation pumps, were measured during the 1 MW beam test, and it was shown that the temperature rise at the coupled moderator was 2.7 K with the flow rate of 82 g/s at 915 kW beam power. This result demonstrated

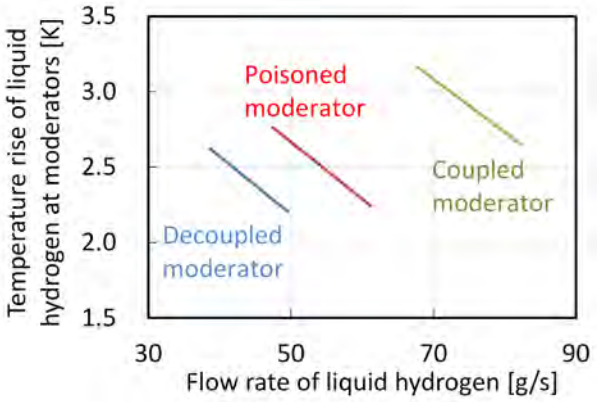

Figure 2. Temperature rise of liquid hydrogen at each moderator at 915 kW beam operation.

the capability of the cryogenic hydrogen system to achieve the design goal, but the rotation speed of the hydrogen circulation pumps had to be increased from the rated value of 40,000 rpm to 47,000 rpm to achieve the result. It is necessary to verify the stability of the hydrogen circulation pump at high revolutions for a long-term operation.

4. Replacement of a proton beam window and maintenance of the general control system

During the summer outage, replacement of the proton beam window was carried out after a 3 year operation since the last replacement in 2017. Because the used proton beam window is a highly radioactive component irradiated within a relatively short period of time, in a situation similar to that of the used target vessel, it will be transported to the RAM (Radio Activated Materials) building in near future.

The general control system (GCS) of the MLF has been modified according to the annual upgrade of the target systems, user apparatuses, etc. and instruments of subsystems comprised in GCS have been replaced based on their sustainable maintenance plans. In 2020, modification of GCS was carried out to increase user apparatuses of muon S2 and H1 lines, and instruments of the 3 NBT control LAN were replaced with next generation models. In addition, operation tests on the personal protection system were carried out successfully based on the periodical inspection that is conducted once every 5 years by the Nuclear Safety Technology Center.

5. Fabrication of a decoupler for a spare moderator

The lifetime of the moderators and the reflector is 6 years under the 1 MW beam operation and fabrication of spares for those components is going on. The neutron absorber, made of Au-In-Cd alloy and called decoupler, is the important part mounted in the moderators and the reflector for realizing high neutronic performance of the neutron source and is manufactured in-house. In 2020, we introduced a small NC milling machine to form the precise shape of the decoupler parts. Since cadmium is a toxic material, the milling machine was installed in a fume hood and special care had to be taken to secure the chemical safety. The finished decoupler was sent to the vendor and mounted in the new moderator.

Figure 3. NC milling machine (Left) and upper part of the decoupler (Right).

6. International collaboration

As one of the international collaborations, technical workshop with SNS (Spallation Neutron Source) of Oak Ridge National Laboratory was held in March 2021 and substantial amounts of information were exchanged, including R&D for the pitting damage mitigation technology, material fatigue experiments, and the cryogenic moderator system operation.

K. Haga
Neutron Source Section, Materials and Life Science Division, J-PARC Center

Target Diagnostic System by Sound Measurement

1. Introduction

In the mercury target for the J-PARC pulsed neutron source, cavitation erosion caused by the proton beam-induced-pressure waves degrades the structural integrity of the target vessel. So far, the cavitation erosion is the dominant factor to determine the lifetime of the vessel, since the thickness of the beam window is designed to be 3 mm to reduce the thermal stress. To reduce the cavitation erosion, a technique of gas microbubble injection into the flowing mercury, which mitigates the pressure waves that induce cavitation, was developed, and applied to the target system [1].

The radiation resistance of the sensors is required to remotely diagnose the operational status of the target vessel, including the effect of the gas microbubble injection on pressure wave mitigation in the high-radiation dose environment. At the J-PARC, the target diagnostic system consists of a laser Doppler vibrometer (LDV), which has been installed to enable non-contact and remote-control measurements [2]. A microphone has also been installed as a backup of the LDV system for unexpected troubles [3]. The recent troubles affecting the LDV system were the drop of a retro-reflective mirror for target No. 9, and misalignment of the optical axis for target No. 11.

Here, the applicability of the sound measurement of the alternative method of the LDV diagnostic system for the target vessel was evaluated through investigating correlation between the operational conditions (the proton beam power and the gas flow rate for injecting gas microbubbles) and the sound signals.

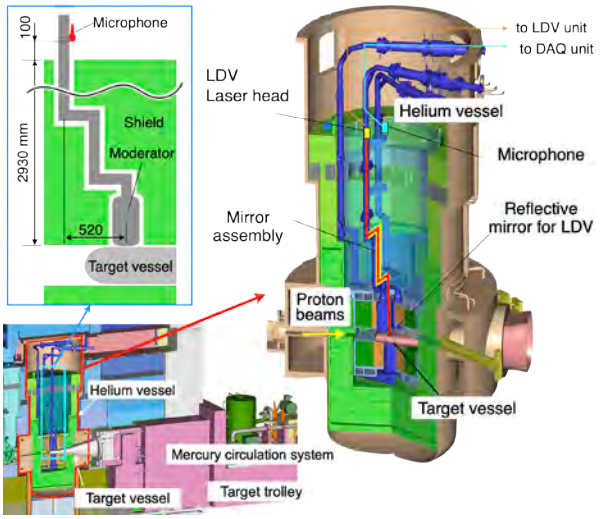

Figure 1. Schematic view of the target diagnostic system installed in the helium vessel.

2. Target diagnostic system

Figure 1 shows a schematic view of the helium vessel installed at the J-PARC. The front end of the target vessel is inserted into the helium vessel during the operation. The helium gas microbubbles are injected into the mercury through a microbubble generator that was installed in the target vessel [1].

A laser head of the LDV system was placed on an iron shield in the helium vessel approximately 3 m from the target vessel. A He-Ne laser was irradiated to the retro-reflective mirror on the target vessel by a path through the narrow gap between the iron shield and the piping of the poisoned moderator using a mirror assembly. The microphone was also placed on the iron shield in the helium vessel aiming to detect the sound propagated from the gap between the shield and the piping of the decoupled moderator as shown in the upper left of Fig. 1. Dynamic microphone with flat frequency response from 150 Hz to 1 kHz was used for the sound measurement since the back-electret microphone commonly used for the sound measurement is drastically damaged by the radiation environment.

3. Sound measurement

Sound signal was recorded with the sampling rate of 100 kHz. Figure 2 shows the time responses of the sound signals with and without gas microbubble injection for a single-shot beam injection at equivalent beam power of 300 kW . The ratio of the injected gas flow rate to the mercury, known as the void fraction, was approximately 10^{-3}. It should be noted that the time 0 denotes the timing of the proton beam injection in mercury, and the sound signal was arbitrarily unit-normalized at the peak value of the averaged signal due to the lack of calibration.

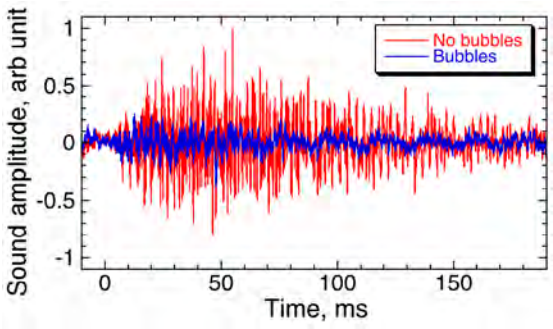

Figure 2. Time histories of a sound signal with and without gas microbubble injection at 300 kW/pulse.

The attenuation time of the sound was longer than 40 ms regardless of conditions. Therefore, echo of the sound signal was superimposed under the 25-Hz operation. The difference between those recorded with and without injection of gas microbubbles before approximately 15 ms, was hardly noticeable. In contrast, after 15 ms, it was confirmed that the sound amplitude was clearly reduced by injecting gas microbubbles. The peak amplitude of sound with injection of gas microbubble was approximately 0.4 of that without injection of gas microbubbles. It is thought that the sound source before 15 ms originated from the water shroud.

The relationship between the peak amplitude of the sound signal and the proton beam power with and without gas microbubble injection under the condition of a 25-Hz operation is summarized in Fig. 3. It can be seen that the peak amplitude is well correlated with the beam power and is clearly reduced by gas microbubble injection regardless of the beam power even at a 25-Hz operation. Details are not shown here, the sound amplitude changes depending on the gas flow rate for the microbubble injection [3]. To understand the effect of gas microbubbles on pressure wave mitigation during operation, we defined the bubble effect as a ratio of the equivalent beam power under gas injection to the actual operational beam power. Equivalent beam power denotes the beam power whose peak sound amplitude with gas microbubble injection corresponds to the one without gas microbubbles as shown in Fig. 3.

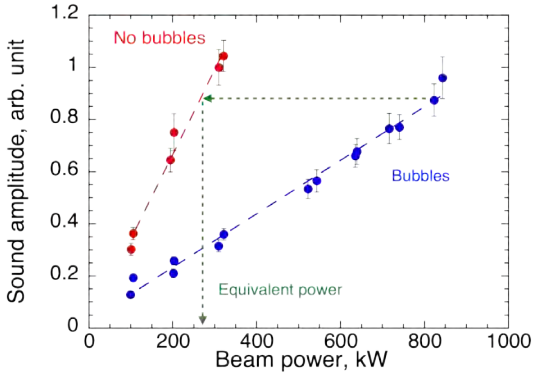

Figure 3. Relationship between the peak amplitude of the sound signal and the proton beam power with and without injection of gas microbubbles.

Figure 4 shows the time histories of the beam power and the bubble effect for target vessels Nos. 11 (fabrication number) and 10. For target No. 11, an averaged bubble effect is almost constant regardless of the beam power, although the individual bubble effect varies widely due to the unstable gas flow rate for the microbubble injection. In contrast, for target No. 10, the variation of the bubble effect is clearly lower than that of No. 11, and the overall bubble effect (0.30) is lower than that of No. 11 (0.43). It is because the indirect path to eliminate the gas flow fluctuation in the target trolley was applied. Due to the low variance for the bubble effect by adopting an indirect path, we understood that the bubble effect changes depending on the gas and mercury temperature immediately after the recovery of the beam operation from the beam trip.

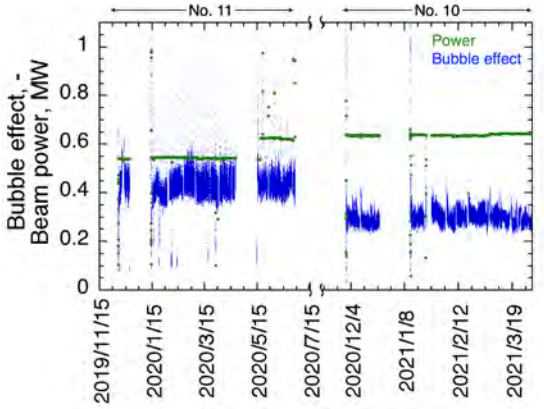

Figure 4. Time histories of the bubble effect and beam power for targets Nos. 11 and 10 during the 25-Hz operation.

4. Summary

It was revealed that the sound measurement has the potential to diagnose both the beam power dependency and the status of the gas microbubble injection. Sound measurement is applicable to the alternative method of the LDV diagnostic system for the mercury target vessel installed in the high-radiation dose environment.

References

[1] H. Kogawa et al., J. Nucl. Sci. Technol., **54** 773 (2017).
[2] M. Teshigawara et al., J. Nucl. Mater., **398** 238 (2010).
[3] T. Naoe et al., Nucl. Inst. and Meth. Phys. Res. A, **982** 164566 (2020).

T. Naoe, H. Kogawa, T. Wakui, M. Teshigawara, and K. Haga
Neutron Source Section, Materials and Life Science Division, J-PARC Center

Experimaital Characterization of High-Energy Neutrons at NOBORU (BL10)

1. Introduction

In the spallation neutron source at J-PARC, neutrons with high energy ranging up to 3 GeV are generated by spallation reactions in a mercury target with a 3 GeV proton incident. Although the source is primarily designed to provide slow neutrons and to shield high-energy neutrons from the mercury target, it could be possible to extract high-energy neutrons through beam holes in the primary shield structure. We have already provided a neutron spectrum of each beam line obtained by calculation of a model based on the engineering design of the source. The problems associated with high-energy neutrons above 1 MeV are identified as follows:

(1) High-energy neutrons could potentially become background elements in the experiment data because they have stronger penetration capability compared to low-energy neutrons. Simulation results of the early stage show that the high-energy neutron intensity for neutron energies above 1 MeV ranges from 10^5 to 10^6 n/cm^2/s at the sample position in BL10 (14 m).

(2) As high-energy neutrons ranging from 1 MeV to a few hundred MeV are requested for irradiation tests to detect the soft-error and hard-error resistance of semiconductor devices with respect to cosmic rays, obtaining precise neutron spectral intensity is imperative.

(3) It is necessary to construct a complex model for the simulation of high-energy neutrons extracted through the beam lines. Additionally, calculating neutron spectral intensity is time consuming. It is basically required to experimentally validate the simulated neutron spectral intensity used in the design, which was provided to the users.

Therefore, this research aims to measure the high-energy neutron spectrum at NOBORU (BL10), particularly above 1 MeV along the extracted neutron beam at the J-PARC pulsed neutron source. The foil activation method is selected with different threshold energies ranging from 0.3 MeV to 80 MeV [1]. The foil activation method is the conventional technique to make it possible to determine the absolute neutron flux value. The result is compared with the simulation using the PHITS code [2], the JENDL-3.2 nuclear data [3, 4], and the JENDL dosimetry file [1]. In this manuscript, the measurement results with/without a filter and a slit, and a comparison with calculations were mentioned. The details have already been reported in Ref [5].

2. Experiment

2.1. Foil irradiation for activation

Table 1 shows a list of threshold reactions applied in this experiment. Threshold energies of activation reactions ranged from 0.3 MeV to 63.1 MeV, which corresponded to those of the ^{115}In(n, n')^{115m}In and the ^{209}Bi(n, 8n)^{202}Bi reactions, respectively. A sample foil was on an aluminum plate of 0.1 mm in thickness and positioned at 13.4 m from the moderator surface along the neutron beam axis and was irradiated for the required time. The sizes of the foils were 20 mm × 20 mm × 2 mm for Al, 15 mm × 15 mm × 1 mm for In, 20 mm × 20 mm × 1 mm for Nb and 20 mm × 20 mm × 3 mm for Bi. The opening and closing times of the neutron beam shutter corresponded to the start and stop time of irradiation. Irradiation times for the cases were about 8 hours for about 500 kW operation.

2.2. Radioactivity measurement

The γ-rays from the radioactive materials produced

Table 1. Reactions with high-energy neutrons and their threshold energies.

Reaction	Threshold energy (MeV)
^{115}In(n, n')^{115m}In	0.3
^{27}Al(n, α)^{24}Na	3.2
^{93}Nb(n, 2n)^{92m}Nb	8.9
^{209}Bi(n, 4n)^{206}Bi	22.6
^{209}Bi(n, 6n)^{204}Bi	38.0
^{209}Bi(n, 8n)^{202}Bi	63.1

were measured using a high-purity germanium detector (GEM20P4-70, ORTEC®). The detector efficiency for the full-energy peak of γ-ray was calibrated using standard γ-ray sources Europium-152 (^{152}Eu).

3. Calculation and experiment results of the effect of the boron carbide slit and lead filter

The B_4C slit of NOBORU, which consists of couples of plates of 5 mm in thickness sintered B_4C, are normally used to form incident thermal and cold neutron neutrons. The B_4C slit, by full closing, also eliminated thermal and cold neutrons extracted from the moderator and reduced unnecessary radioactivity associated with the reactions of the slow neutrons in the sample. In this study, the B_4C slit was used as a filter by full closing. The purpose of the Pb filter was to attenuate γ-rays from the moderator. Three irradiations were performed with and without the slit and the filter to examine the effect on neutron spectral intensity at the sample position. The irradiation cases were (1) No filter case, (2) B_4C slit (thickness: 10 mm) case, and (3) B_4C slit (thickness: 10 mm) and Pb filter (thickness: 25 mm) case.

Figure 1 shows the calculation results with/without the B_4C slit and the Pb filter at 13.4 m in NOBORU. Figure 2 shows the comparison of the calculations with the measurements. Although there were materials of the slit and the filter reducing neutrons slightly, the reaction rates of Case 2 and Case 3 were nearly identical to those of Case 1 because of the transparency of high-energy neutrons for media such as B_4C and Pb.

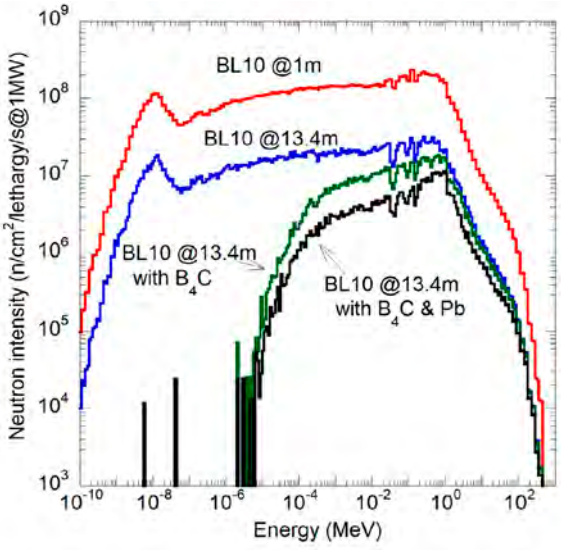

Figure 1. Calculated neutron spectral intensity at BL10.

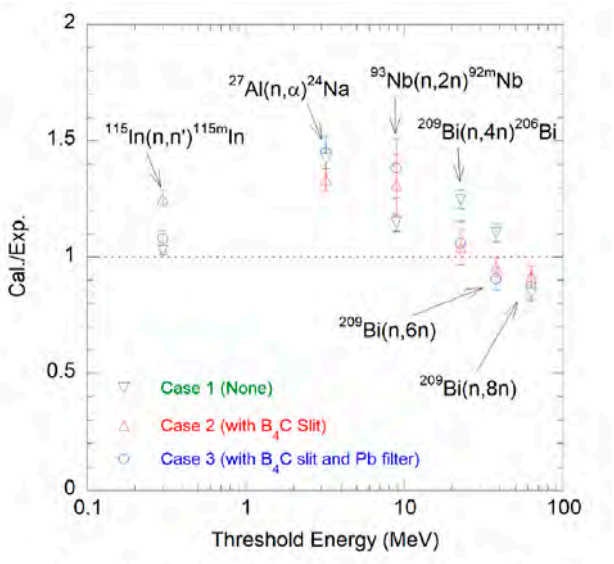

Figure 2. Calculation/Experiment ratio as a function of the threshold energy.

4. Summary

This is the first study to experimentally confirm the adequacy of calculation results of the high-energy neutron flux spectrum using the foil activation method at the J-PARC spallation neutron source facility. Reaction rates for the threshold reaction tended to decrease with the increase in reaction threshold energy in the range of 0.9 – 1.3.

Acknowledgments

We would like to thank Y. Kasugai for his guidance and R. Kikuchi for his support in the experiment. The neutron experiment at the Materials and Life Science Experimental Facility of J-PARC was performed under user programs (Proposal No. 2015P0801, 2016I0010, 2017I0010 and 2018I0010).

References

[1] F. Maekawa, et al., in: Proc. ISRD-10, American Society for Testing and Materials, 2001, p. 417.
[2] T. Sato, et al., J. Nucl. Sci. Technol. **55** (2018) 684.
[3] T. Nakagawa, et al., J. Nucl. Sci. Technol. **32** (1995) 1259.
[4] K. Shibata, et al., J. Nucl. Sci. Technol. **34** (1997) 1171.
[5] M. Harada, et al., Nucl. Instr. Meth. A 1000 (2021) 165252.

M. Harada[1], M. Teshigawara[1], M. Ooi[1], K. Oikawa[2], H. Takada[1], and Y. Ikeda[3]
[1]Neutron Source Section, Materials and Life Science Division, J-PARC Center; [2]Neutron Science Section, Materials and Life Science Division, J-PARC Center; [3]J-PARC Center

Proton Beam Transport for High-Intensity Beam

1. Introduction

Cavitation erosion of the target-vessel material is a significant concern in the high-power operation at the MLF and is a life-limiting factor of the mercury target vessel. After operating the beam at high power without the helium bubbler to mitigate the cavity erosion, significant pitting erosion of the mercury target caused by pressure waves was observed in a spent target vessel at the MLF and the SNS in Oakridge National Laboratory (ORNL). To minimize the damage on the target vessel, reducing the peak beam current density on the target is crucial. Beam scanning is commonly used to decrease the time-averaged peak current density at many facilities. To obtain a flat beam profile, beam scanning with pulse magnets to create a flat time-averaged profile is generally employed. In the case of a short-duration beam impinging on a liquid-metal target, scanning the beam with a deflecting magnetic field does not mitigate the pitting damage caused by the beam because this damage is proportional to about the fourth power of the peak density.

Using linear optics (i.e., quadrupole magnets) for beam transport, the peak current density can be reduced by expanding the beam at the target. However, beam expansion increases heat near the target, where the shielding is located. Therefore, the peak current density is limited by the heat induced near the target, the allowable limit of which is possibly lower than 1 W/cc. At the MLF, the minimum peak current density is expected to be 9 μA/cm^2, resulting in a thermal-energy density of 14 J/cc/pulse at the target. Owing to the low repetition rate of 25 Hz at the MLF, which is 60 Hz in the case of SNS, the beam power of one shot and the peak heat density in mercury at the MLF for a 1 MW beam is about twice as high as that in the present 1.4 MW SNS beam. Therefore, to mitigate the pitting erosion, a beam-flattening system for peak-density reduction is urgently required at the MLF.

2. Study on nonlinear optics using octupole magnet

The octupole magnet has a cubic function of the magnetic field along the transverse direction, which introduces nonlinearity in the beam optics. By the cubic function, the particles located at the beam periphery are deflected toward its center, which flattens the beam distribution. To obtain a flat distribution in both the horizontal and vertical directions, two octupole magnets are required. Using a simplified model dealing with the beam as a simple filament distribution in the phase, called filament model, the required parameters were known to obtain flat beam distribution at the target. However, the filament model was found not to predict the beam shape and the beam loss correctly by the exact solution of the beam transport equation. We proceeded with a detailed study on the nonlinear optics and found that the beam shape can be characterized by only two parameters [1], which are the octupole magnetic field of K^*_8 related to the beam width at the octupole magnet and the cotangent of the phase advance of ϕ between the octupole magnet and the target.

With the nonlinear focusing, the shape of the beam can be manipulated to fit the aperture at the target as well. Due to the reduction of the intensity at the tail, it is possible to reduce the peak current density by an expansion of the beamwidth. As a typical case, we discussed a target with an aperture of 2.5 times beamwidth of 1σ by linear optics. Figure 1 shows the integral intensity of the beam located outside of $\pm$2.5 σ in a single plane for various K^*_8 and $cot\ \Phi$. Due to the nonlinear optics, the integral intensity can be reduced about 7 magnitudes lower than linear optics with $K^*_8 = 1.5$ and $cot\ \phi = 8$, respectively. Note that the integral beam intensity for the same area with the linear optics is 1.2×10^{-2}. The integral intensity located outside of 2.5 σ becomes smaller for the case of $K^*_8 \geq 0.5$ and $cot\ \phi \geq 3$ due to nonlinear convergence. The solid black line shown in Fig. 1 indicates a guide curve to achieve the lowest intensity under the minimization of K^*_8. For the same K^*_8 compared to the filament model result shown in the solid red line, a slightly larger $cot\ \phi$ was found to be optimal. The solid black line in Fig. 1 can sustain beam convergence with minimized beam loss downstream of the octupole magnet. On the

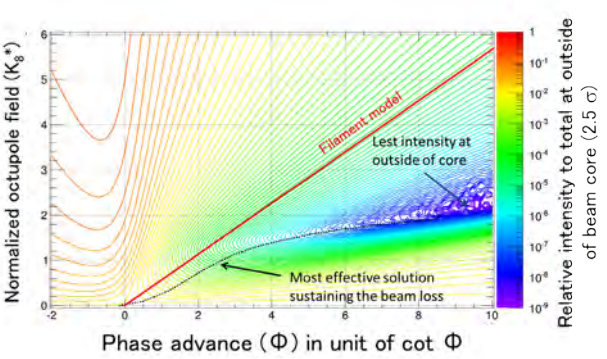

Figure 1. Beam intensity using the nonlinear optics with an octupole magnet at the outside of the beamwidth for 2.5 σ given by linear optics.

contrary, at the phase advance of $cot\ \phi = -1$, the beam shape is spread as an increase of the octupole magnetic field K^*_8. This spread shape is a side effect of nonlinear optics, introducing beam loss. To suppress the beam loss to less than the allowable value (1 W/m) while obtaining a reasonable flatness, the optimal parameter was chosen as $cot\ \phi = 3$ and $K^*_8 = 1$, which was applied in the actual beam operation.

3. Nonlinear beam optics using octupole magnets at the MLF

Based on the optics design, two pieces of the octupole magnet shown in Fig. 2 were fabricated for horizontal and vertical nonlinear focus on the target. We designed the octupole magnets with OPERA-3D code. The designed magnetic field gradient is ~900 T/m^3, and the magnet has a bore diameter of 0.3 m and a length of 0.6 m in the direction of the pole. To obtain a significant degree of freedom for beam turning, the octupole magnet was powered using bipolar power supplies.

At J-PARC, a 3 GeV proton beam with a beam power of 1 MW and a repetition rate of 25 Hz is extracted from the RCS. The 3 GeV proton beam is delivered via a beam-transport channel called 3NBT in J-PARC. The 3 GeV proton beam extracted from the RCS is well described by a simple Gaussian. With linear beam optics, the beam shape remains Gaussian. Two octupole magnets were placed upstream of the muon production target to obtain a flat beam shape at the target.

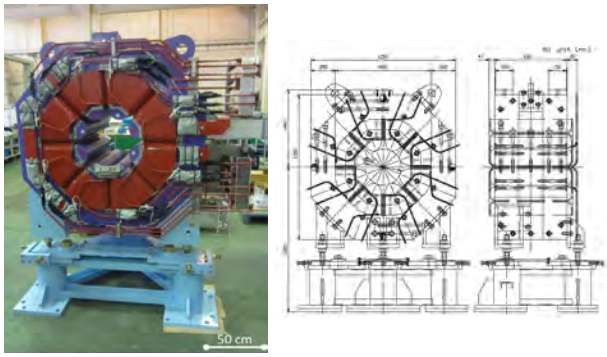

Figure 2. Fabricated octupole magnet placed at 3NBT.

4. Beam profile at the target

The beam profile for the 1-MW beam was observed at 1.8 m upstream of the target using linear and nonlinear optics (i.e., without and with excitation by the octupole magnet), respectively. The results of the beam profile of the experiment and the calculation are compared in Fig. 3. The calculation shows a good agreement with the experiment, which proves that the beam can be controlled as intended. During beam operation with 1 MW, the beam loss was confirmed to be enough smaller than the allowable one along the beam transport line.

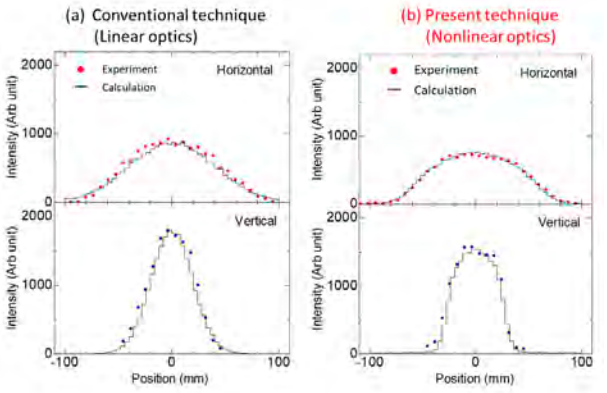

Figure 3. Comparison of the experiment and the calculation of the beam profile at 1.8 m upstream of mercury target. The left and right panels show a conventional technique based on linear optics, and the right one presents a technique based on nonlinear optics, respectively.

5. Summary

Thanks to the present beam flattening system, a beam for neutron and muon production with the power of 600 kW had been steadily delivered by 3NBT in Japanese Fiscal Year (JFY) 2020. At the end of June 2020, we successfully delivered a proton beam of 920 kW for 3 days. The present work is expected to contribute to stable beam operation of future high-intensity accelerator facilities, such as the ADS. Among other works related to beam transport, a technical award was received from the Japanese Society for Neutron Science in September 2020.

Reference

[1] S. Meigo, et al., M. Ooi, and H. Fujimori, Phys. Rev. Accel. Beam **23**, 02802 (2020).

S. Meigo[1], Y. Yamaguchi[1], M. Ooi[1], and H. Fujimori[2]
[1]Neutron Source Section, Materials and Life Science Division, J-PARC Center, JAEA; [2]Muon Science Section, Materials and Life Science Division, J-PARC Center, Institute of Materials Structure Science, KEK

Neutron Science

Neutron Science Section

1. Introduction

The Neutron Science Section (NSS) has worked hard to expand the neutron scientific and experimental activities on neutrons in the Materials and Life Science Experimental Facility (MLF). In 2020, the COVID-19 pandemic prevented researchers from travel, which affected the user facilities, such as J-PARC. Most of the users from abroad had to cancel their scheduled MLF experiments. The situation was more serious for students who were about to earn their degrees. The NSS took notice of the difficult situation and proceeded to deal with it. Some of the experiments were carried out by the instrument group as a representative, as mentioned below.

We renewed the NSS. The Leader and Sub-Leaders of the Neutron Science Section were replaced in April 2020: K. Nakajima by Y. Kawakita as the section leader. S. Itoh and Y. Kawakita by T. Yokoo and M. Nakamura as the sub-leaders, respectively. The new NSS started with a new management under the COVID situation.

2. Proposal round in 2020

A state of emergency was officially announced by the Government of Japan on April 14, which caused the cancelation of the MLF beam operation from April 20 to May 14. After the accessibility to the MLF resumed on May 15, it was gradually extended from in-house use and mail-in experiments to all users' access on June 19. Since it was expected that the available beamtime would be significantly decreased in the period of 2020B due to the existence of many experiments carried over from 2020A, 2020B and 2021A were jointly called. Among 384 neutron general proposals, 200 were approved to be conducted by July 2021. The beamlines available for the Fast-Track Proposal (FTP) were timely added in the fall, so that 7 beamlines - BL08, BL11, BL16, BL17, BL18, BL21 and BL22, are available for FTP. The long-term proposal (LTP) was not called for the 2021 round, because all approved LTPs showed certain delay in the experimental plan and therefore a half-year elongation of the approved term was accepted. A new category, "one-year proposal", was introduced to BL11 PLANET aiming at promotion of research projects that include technology development in collaboration with the instrument group.

Under the pandemic situation, many of the user experiments were carried out by the instrument group, as shown in Fig. 1, instead of the users, because the latter were unable to travel. For some of the beamlines popular among foreign researchers, this rate exceeded 50% of the conducted experiments. Developments of remote access and automation of the instrument were closed up in priority. The government also supported our activities by an additional budget (PRISM) of 55 million JY prompting collaboration among industry, government and academia.

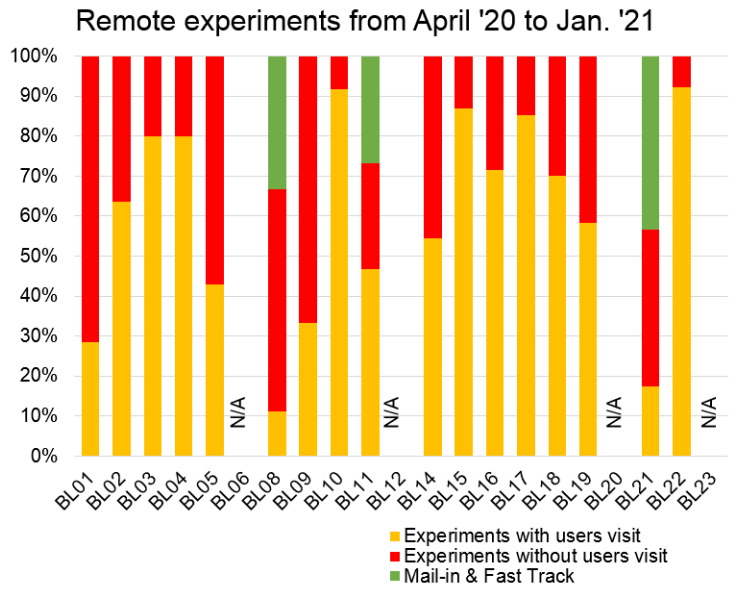

Figure 1. Rate of the remote experiments among the conducted experiments.

3. Instrumentation up to date

The new beamline instrument, POLANO (BL23) started as a part of the user program in 2019. POLANO is a polarization inelastic spectrometer, currently operating in an unpolarized-mode only for the user program. Unfortunately, all proposed experiments were canceled because of COVID-19. For the future polarization experiment, spin exchange optical pumping (SEOP) polarizer system, and several magnets for the guide field were almost ready to start commissioning. Vin Rose (BL06) is a neutron spin echo (NSE) spectrometer consisting of two different types of NSE instruments, namely, a modulated intensity by zero effort (MIEZE) type instrument and a neutron resonance spin echo (NRSE) type instrument. The user program was served by MIEZE with a 4 Kelvin GM cryostat and an electromagnet generating a field of up to 0.6 Tesla.

4. Award

SuperHRPD (BL08) group (S. Torii, K. Oikawa, M. Hagihala, C. Kwanghee, T. Kamiyama) received the Technical Award by the 20th Annual Meeting of the Japanese Society for Neutron Science for the achievement of "Development of the World's Highest Resolution TOF Type Powder Neutron Diffractometer, SuperHRPD".

5. Scientific outcome

The research activities in neutron science at the MLF resulted in more than 190 papers and 12 press releases. Representative papers are listed in the references [1–9]. Neutron Diffraction study using TAKUMI revealed the mechanism for strengthening cast iron (see Fig. 2), which is widely used in the casing of hydraulic equipment for construction machinery and various parts of automobiles [2]. The developed research method in this study will be applied to elucidate the excellent deformation mechanism of advanced metal materials.

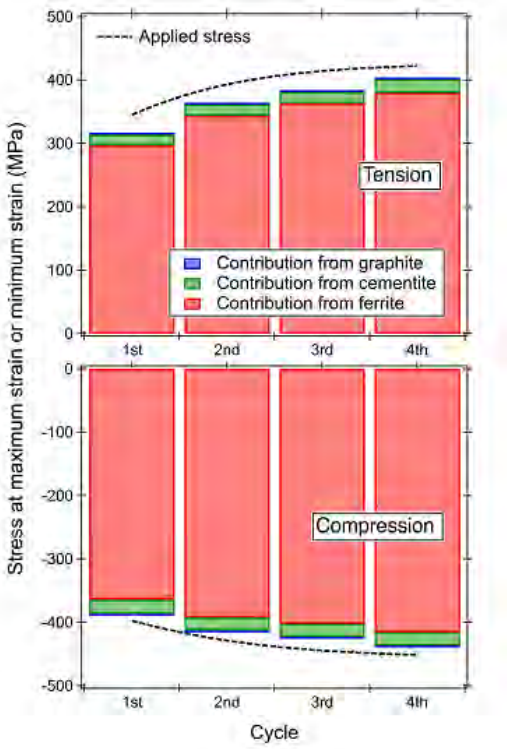

Figure 2. Contribution to the strength of each constituent phase at maximum and minimum macroscopic strains.

References

[1] V. Sonnenschein et al., Rev. Sci. Instrum., **91** 033318 (2020).
[2] S. Harjo et al., Acta Mater., **196** 584 (2020).
[3] N. L. Yamada et al., J. Appl. Crystallogr., **53** 1462 (2020).
[4] T. Yamamoto et al., Nat. Commun., **11** 5923 (2020).
[5] K. Hirota et al., Prog. Theor. Exp. Phys., **2020** 123C02 (2020).
[6] M. Yashima et al., Nat. Commun., **12** 556 (2021).
[7] R. Yamane et al., Nat. Commun., **12** 1129 (2021).
[8] Y. Kosugi et al., Adv. Funct. Mater., **31** 2009476 (2021).
[9] L. Kong et al., Adv. Funct. Mater., **31** 2009131 (2021).

Y. Kawakita[1], T. Yokoo[1,2], and M. Nakamura[1]
[1]Neutron Science Section, Materials and Life Science Division, J-PARC Center; [2]Institute of Materials Structure Science, KEK

BL01: 4D-Space Access Neutron Spectrometer 4SEASONS

1. Use trends

4SEASONS is a direct-geometry time-of-flight neutron spectrometer for thermal neutrons, and one of the Public Beamlines in the MLF [1]. The momentum-energy region for this spectrometer occupies the middle of the momentum-energy space covered by all the MLF spectrometers [2]. In 2020, 21 General Use (short-term) proposals and 1 Instrument Group Use proposal were approved for 4SEASONS. Due to the COVID-19 pandemic, some of the proposals in 2019 were carried out in 2020, and a part of the proposals in 2020 were postponed for 2021. Conversely, 5 reserved (short-term) proposals were given beam-time to compensate for the vacancy. The user group of 4SEASONS includes a large number of international users, and 77% of the General Use proposals were submitted by the latter. Some of the users' experiments, for which the research group had difficulties to visit the MLF due to the pandemic, were carried out by the instrument group instead of the research group. 66% of the submitted proposals were in the field of magnetism, while the rest of them targeted phonons and other atomic vibrations. As for the outcomes from using the instrument, 11 peer-reviewed papers were published in 2020. 10 were papers about material science, while 1 paper was related to the instrumentation.

2. Instrument upgrade

Vacuum system: The vacuum system for the sample scattering chamber of 4SEASONS consists of a screw pump (Leybold SP630), a turbo-molecular pump (Leybold MAG W2200), and a cryopump (Polycold PFC-1100HC). The combination of these pumps evacuates the chamber to reach enough high vacuum for operating the cryostats (typically 10^{-3}–10^{-4} Pa). However, these pumps have been used since the first day of the operation of the instrument and have become unstable or were at the end of their designed lifetime. To solve the problems with aging, in 2020, we replaced the screw pump with a new one (Kashiyama SDE603X), switched the turbo-molecular-pump to the spare one, and overhauled the cryopump.

Sample environment: We have been using a low-temperature sample stick with Si diode sensors for low-temperature experiments below room temperature and a high-temperature sample stick with Rh-Fe sensors for experiments below 600 K in combination with a top-loading closed-cycle refrigerator. However, the low-temperature stick caused vacuum leak due to aging of an O-ring seal. Then, we developed a new low-temperature sample stick to replace the old one (Fig. 1). In addition, we developed a new high-temperature sample stick with Si diode sensors, which can warm up the sample up to 500 K. It is under commissioning and will be available next year.

Beam optics: 4SEASONS has a 45 × 45 mm^2 rectangular beam collimator just upstream of the sample to define the beam size in combination with a four-quadrant beam slit. In 2020, we replaced this collimator with a rotary optics switching device. This device developed by the Technology Development Section of the MLF can hold four optical devices at maximum and switch them by rotation (Fig. 2). Now it holds a simple rectangular collimator of the same dimension as before, but we plan to add other optics, such as Soller-type beam collimator and converging beam guide.

Detector: 4SEASONS increased the ^{3}He detectors gradually and completed the installation in 2019. The pulse height distribution of the detected signal depends on the circuit parameter of the preamplifier, and it can differ between detectors due to the difference in the circuit parameters. We recently found that preamplifiers after a certain period of time display largely different circuit parameters from the older preamplifiers, which

Figure 1. The old (left) and new (right) low-temperature sample sticks.

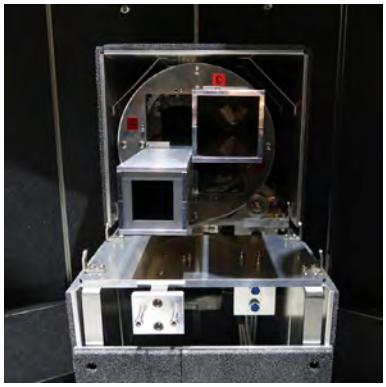

Figure 2. The rotary optics switching device being installed in the vacuum scattering chamber of 4SEASONS.

caused significant difference in the pulse height distribution. In 2020, we repaired the electric circuits of the problematic preamplifiers to mitigate this pulse height problem.

Chopper: As reported in the 2019 annual report, 4SEASONS has been operating with a renovated T0 chopper since 2019, which can now run at 100 Hz at maximum. However, there was no control software for this new chopper, and the chopper was operated locally on the controller. In 2020, the Technology Development Section developed a device driver for the device control software framework IROHA2 [3]. By installing this driver, we now operate the T0 chopper remotely on the web similarly to the other neutron devices at 4SEASONS.

Acknowledgements

We thank K. Inoue and W. Kambara for their support and advice. The instrumentation works described here were supported by the engineers of the Neutron Science Section and the Technology Development Section of the MLF.

References

[1] R. Kajimoto et al., J. Phys. Soc. Jpn. **80**, SB025 (2011).
[2] H. Seto et al., Biochim. Biophys. Acta, Gen. Subj. **1861**, 3651 (2017); K. Nakajima et al., Quantum Beam Sci. **1**, 9 (2017); R. Kajimoto et al., Physica B **562**, 148 (2019).
[3] T. Nakatani et al., JPS Conf. Proc. **8**, 036013 (2015).

R. Kajimoto[1], M. Nakamura[1], K. Kamazawa[2], Y. Inamura[1], K. Iida[2], K. Ikeuchi[2], and M. Ishikado[2]
[1]*Neutron Science Section, Materials and Life Science Division, J-PARC Center;* [2]*Neutron Science and Technology Center, CROSS*

Current Status of BL02 DNA in 2020

1. Introduction

DNA is a TOF backscattering spectrometer designed to elucidate atomic and molecular dynamics [1]. DNA can provide micro-eV energy resolution measurements over a broad energy range of -500 μeV < E < 1500 μeV, thanks to the near-backscattering geometry of the instrument and its pulse-shaping options. DNA has two types of analyzers Si111 and Si311 which allow to access momentum transfer range from 0.08 to 1.86 $Å^{-1}$, and from 1.79 to 3.39 $Å^{-1}$, respectively.

The hot topic for 2020 is the participation of Dr. Tamatsukuri in the BL02 team (Fig. 1). His current research interest is in the field of low-energy dynamics of conducting ions or spins in recently-developed functional materials, such as hydride conductors and anionic electron systems (electrides).

The number of peer-reviewed papers from DNA was 8 in 2020, almost at the average yearly amount since 2017. BL02 was also used for one master thesis and one doctoral thesis.

2. User Program in the periods 2020A and 2020B-2021A

In 2020, 20 (2020A) and 33 (2020B-2021A) General Proposals (GP) were submitted to BL02. 5 GPs, and 13 GPs (including 1 New User Promotion (NUP)) were approved for 2020A and 2020B, respectively. The portion of approved beamtime from all requested beamtime was 25% for 2020A and 38% for 2020B. The competition rate was high: 5.0 and 2.75 for 2020A and 2020B, respectively. Additionally, 3 and 2 reserved proposals were conducted in 2020A and 2020B.

Due to the pandemic situation, users, especially from foreign countries, could not come to J-PARC. Three experiments with simple setup were conducted by the BL02 staff without the users. Unfortunately, one experiment requiring careful sample handling was canceled.

One project conducted as a Long Term Proposal (hereafter LTP) in the General Proposal Program has been accomplished in 2020A. Instead, one LTP adopted from 2020B. In total, 4 LTP's ran at BL02.

3. Beamline activities

Additional Si311 analyzer mirrors were installed at scattering angle (2θ) of $-90° < 2\theta < -54°$. Now, Si311 analyzers cover momentum transfer from 1.79 to 3.39 $Å^{-1}$, which overlaps Q-region of Si111 $0.08 < Q < 1.98$ $Å^{-1}$. However, some spurious peaks from the aluminum wall of the BL02 cryostat exist for Si311 analyzers. We plan to suppress those scatterings by oscillatory radial collimators, which will be installed during the beam shutdown in 2021.

The impact of COVID-19 is accelerating the developments for remote or smart experiments. In BL02, we are promoting the Internet of Things (IoT) of the equipment involved in BL02. The equipment in BL02 can be categorized as follows: (a) sample environment devices, (b) devices, such as a vacuum pump, which need to work properly under the BL02 operation, and (c) utilities (electricity, water, gas, and compressed air). As (a) and (b) are often electrically controlled, they are potentially easy to introduce IoT, but (c) is often not.

For (a), we have developed a device for the automatic control of the atmosphere in the inner vacuum chamber (IVC), naming DNA IVC control equipment (DICE) [2]. DICE facilitates the control of the amount of gas in the IVC by sequentially operating solenoid-valves

Figure 1. A photograph of the BL02 regular meeting held by Zoom. Clockwise from top left: Y. Kawakita, M. Matsuura, H. Nakagawa, T. Tominaga, T. Yamada, and H. Tamatsukuri.

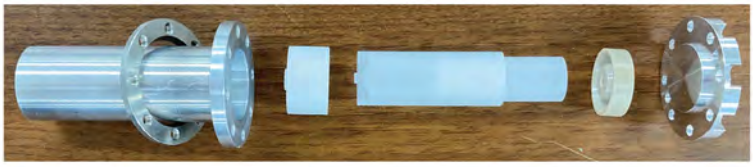

Figure 2. A photograph of the single crystal sapphire cell within the Al cell.

and a gate-valve, to flash the IVC, to set the helium gas pressure and to set the high vacuum continuously. An automatic sample changer (PEACE), which elevates up and down in the IVC [2], has now extended the controlled sample temperature range of 10–320K. We are also developing an automatic sample changer capable of loading 20 cells.

For (b), we have developed a remote-turbomolecular pump (rTMP), which enables remotely the start/stop of the TMP operation and the monitoring of the vacuum gauge. A pressure regulator with a digital pressure gauge was developed to monitor the residual pressure of the helium gas cylinder introduced to the IVC.

The developed IoT devices are linked to the operating system of neutron scattering measurements by the IROHA2 software [3], which can integrate the devices status. With these smart devices, we automated successfully various operations and management that have been done manually or visually.

To maintain the stability of the beam monitor, we developed a gas replacement system and freshened the converter gas. The intensity of the monitors was restored by the refreshment. In addition, we found that the TOF spectrum was shifted when the beam monitor was measured at the sample position. We speculate that the shift consists of the inaccurate position of the beam monitor and the neutron wavelength dependent TOF-offset. To overcome this issue, we also plan to develop a new monitor, which can be used at the sample position.

Since 2019, we have been developing a special sample stick which can apply electric field at 300°C with the help of Dr. Kazuhiro Mori in Kyoto University. To see the dynamics of Li ions under an electric field, we measured the electric field dependence of QENS in a $Li_7P_3S_{11}$ metastable crystal. We successfully observed the enhancement of QENS in a wide energy range, indicating the activation of the Li Ion movement.

In addition, we have developed a single crystal sapphire cell (Fig. 2) which is utilized for aqueous samples, such as biological solution samples, as an alternate option to avoid unfavorable corrosion of the Al cell.

Almost all these beamline activities were published in JPS Conf. Proc. Vol.33 in March 2021 [4].

Software

Advanced Computing Environment (ACE) managed by the MLF computing team was installed to replace the data storage system. The instrument control software, IROHA2 [3], was updated to improve the stability. The data reduction software, Utsusemi, was also updated to be compatible with Python 3.

4. Future plans

We will proceed with the further installation of Si311 analyzer mirrors and replacement of damaged Si111 analyzer mirrors. We are developing a compact furnace that can heat up to 1000°C Radial collimators will be installed in 2021 to reduce the scattering from sample environments, such as the BL02 GM-cryostat and the compact furnace.

References

[1] Kaoru SHIBATA et. al., JPS Conference Proceedings, 8 (2015), 036022.
[2] T. Tominaga et al., JPS Conf. Proc. 33, 11095 (2021).
[3] T. Nakatani et al., Proceedings of NOBUGS 2016, P17-19 (2016).
[4] The proceedings of J-PARC Symposium 2019, https://journals.jps.jp/doi/book/10.7566/J-PARC2019

Y. Kawakita[1], M. Matsuura[2], T. Yamada[2], T. Tominaga[2], H. Tamatsukuri[1], and H. Nakagawa[1,3]
[1]Neutron Science Section, Materials and Life Science Division, J-PARC Center; [2]Neutron Science and Technology Center, CROSS; [3]Materials Sciences Research Center, JAEA

Current Status of iBIX in 2020

1. Introduction

The complementary use of both neutron diffraction data and X-ray diffraction data is one of the powerful methods to obtain the structure information of all atoms in the protein samples because the neutron diffraction data include more information about hydrogen (deuterium) atoms, and the X-ray diffraction data include more information about non-hydrogen atoms (such as C, O, N, and S). This is particularly important, because understanding the enzyme chemistry of proteins at the atomic level requires the visualization of hydrogen atoms on active sites and water molecules. The IBARAKI biological crystal diffractometer called iBIX is a high-performance time-of-flight single crystal neutron diffractometer to elucidate the hydrogen, protonation and hydration structures of organic compound and biological macromolecules in various life processes [1, 2]. In 2019, the iBIX diffractometer, equipped with 34 detectors, was available for user experiments on organic compound, biological macromolecules and polymer samples, supported by the Frontier Research Center of Applied Atomic Sciences, Ibaraki University. The specifications of iBIX are shown in Table 1.

2. Current status

In 2020, J-PARC was operated regularly at an accelerator power of 600 kW. We were able to collect a full data set of biological macromolecules for neutron structure analysis with around 2.0 Å resolution in about 7 days by using iBIX at the accelerator power of 600 kW. The maximum unit cell size was 135 × 135 × 135 $Å^3$. The typical crystal volume of the sample measured by iBIX was around 1.0 mm^3. If the accelerator power reaches 1 MW, the total measurement time will be reduced to nearly half of the previously necessary time, or the sample size can be reduced to nearly half size with the same measurement time.

In 2020, 12 test measurements for a proposal of an innovative research project of the Ibaraki Neutron Beamline (2020A: 4, 2020B: 8), 1 test measurement for a proposal of the MLF general use, and 5 test measurements for a proposal of a leading research project of the Ibaraki Neutron Beamline (2020A: 2, 2020B: 3) were performed using iBIX. Also, 8 proposals involving full data collection for neutron structure analysis moved forward.

Due to the effects of COVID-19 and a trouble with the accelerator, the total amount of beam time for user experiments was reduced in both 2020A and B. If the accidents did not happen, 1 or 2 more protein samples could have been provided for full data collection.

Table 1. Specifications of iBIX.

Moderator	Coupled
Range of wavelength of incident neutron (Å)	0.7 ~ 4.0 (1st frame) 4.0 ~ 8.0 (2nd frame)
Neutron intensity ($n/s/mm^2$) (@1 MW)	0.7×10^6
L_1 (m)	40
L_2 (mm)	491
Solid angle of detectors (% for 4π str)	22.0
Detector covered region (deg.)	15.5 ~168.5
Detector size (mm^2)	133 × 133
Detector's pixel size (mm^2)	0.52 × 0.52
No. of detectors	34
Sample environment	Gas flow type cooling system by N_2 gas (~100K)
	Heating system for polymer sample (~600K)
	Tensile loading system for polymer sample (~200 N, ~90 mm, 1~1000 mm/sec)

3. Development

The current data acquisition (DAQ) system was installed in FY2013. The maintenance contract of all components of DAQ system expired in the end of FY2019. The DAQ system should have a faster data reading and writing function and a higher capacity storage than the previous one because iBIX will need to collect the diffraction data in the 1 MW operation of the accelerator in the near future. A part of the DAQ system (storage, KVM drawer, uninterruptible power supply and network switch) was updated at the end of FY2019 and the large-scale parallel access storage of the MLF advanced computational environment (MLF-ACE) was connected to the iBIX DAQ system as the main data storage for diffraction experiments by iBIX. In FY2020, 4 DAQ computers were replaced with new ones and connected to the iBIX DAQ system and the large-scale parallel access storage of MLF-ACE (Fig. 1). By the end of December 2020, we completed their installation and at the same time, the system became available for user experiments.

4. Future plans

It has been over 10 years since the iBIX instrument was installed on the beam line, so some components already need replacement due to age deterioration. One

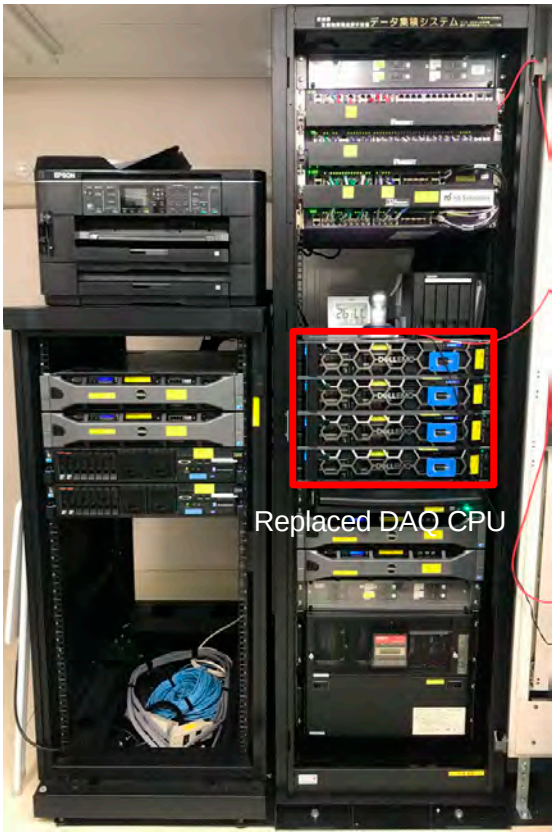

Figure 1. New data acquisition system for iBIX.

of them is the temperature control system of the experimental hatch. Temperature control of the experimental hatch is important to constantly maintain the detector sensitivity because the photomultiplier tube of our scintillator detectors is very sensitive to temperature changes. Next year, we will replace the water-cooled type air-conditioning package of the temperature control system.

In the near future, the accelerator power of J-PARC will increase to about 1 MW. iBIX should be available regularly for full data-set measurement of samples with a volume of less than 1 mm^3. We will continue to develop the data reduction software and the beam line instruments to improve the measurement efficiency and the accuracy of intensity data obtained from small samples.

References

[1] I. Tanaka, K. Kusaka, T. Hosoya, N. Niimura, T. Ohhara, K. Kurihara, T. Yamada, Y. Ohnishi, K. Tomoyori and T. Yokoyama, Acta Cryst., D**66** 1194 (2010).

[2] K. Kusaka, T. Hosoya, T. Yamada, K. Tomoyori, T. Ohhara, M. Katagiri, K. Kurihara, I. Tanaka and N. Niimura, J. Synchrotron Rad., **20** 994 (2013).

K. Kusaka, T. Yamada, N. Yano, T. Hosoya, and I. Tanaka
Frontier Research Center for Applied Atomic Sciences, Ibaraki University

Neutron Filtering System for keV Neutron Capture Cross Section Measurement at BL04: ANNRI

1. Introduction

Ever since the J-PARC accelerator was switched to double-bunch mode, neutron capture cross section measurements using keV neutrons have become impractical. In the keV region, the 0.6 μs time difference between neutron generating events, i.e., spallation reactions, is not negligible as it is within the same order of magnitude compared to the neutron time-of-flight (TOF), which is lower than 30 μs for $E_n > 5$ keV neutrons. Thus, the double-bunch mode introduces serious ambiguities for keV-neutron induced reactions due to the dichotomy between the two neutron-generating events since it is not possible to separate the contribution from each proton pulse. As an example of the difference in energy, neutron events detected with a TOF of 6.4 μs have a nominal value of 100 keV but can also have the value of 120 keV if they were induced by neutrons generated by the delayed proton shot.

The neutron filtering technique was applied to the BL04 of the MLF to bypass the double-bunch structure of the neutron beam. The incident neutron flux was tailored into sharp quasi-monoenergetic peaks by means of using filter material with the attribute of a sharp minimum in the neutron total cross section. Neutrons with the energy of the minimum are able to pass through the filter materials whereas the remaining majority of neutrons with different energies are stopped. ^{nat}Fe and ^{nat}Si were employed in order to mold the incident neutron flux into sharp peaks with average energy of 24 keV for ^{nat}Fe and 54 and 144 keV for ^{nat}Si as shown in Fig 1.

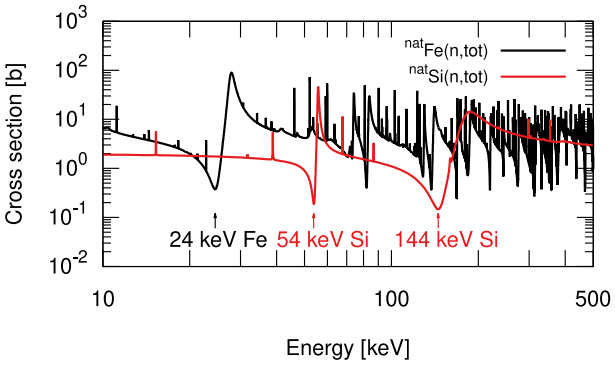

Figure 1. Neutron total cross section of ^{nat}Fe and ^{nat}Si from JENDL-4.0.

2. Experiment and simulation

The filter materials were introduced into the rotary collimator of the BL04 before the experimental areas with filter configurations consisting of 20 cm of ^{nat}Fe and 20 cm of ^{nat}Si. The exact position of the neutron filter is displayed in the schematic of the BL04 in Fig. 2.

The performance of the neutron filtering system was tested through neutron capture experiments employing the NaI(Tl) spectrometer in the BL04. The time distribution of the filtered neutron flux was determined from the $^{-10}$B(n, αγ)^{7}Li reaction using a 90.4% enriched boron sample, because this reaction solely emits one γ-ray with the energy of 478 keV and, hence, it is rather easy to identify this reaction from the detected events. At the same time, simulations using the Monte-Carlo code PHITS [1] were performed to derive the neutron energy distribution within the filtered neutron peaks. In TOF neutron capture cross section experiments, the neutron energy distribution is directly derived from the experimentally measured time distribution, however, due to the double-bunch structure, the energy distribution cannot be reliably determined for keV neutrons from experimental analysis. Simulations with the PHITS code are able to accurately reproduce the time distribution of the incident filtered neutron beam as presented in Fig. 3. Thus, since the PHITS code is able to simultaneously calculate the time and energy distribution for the present

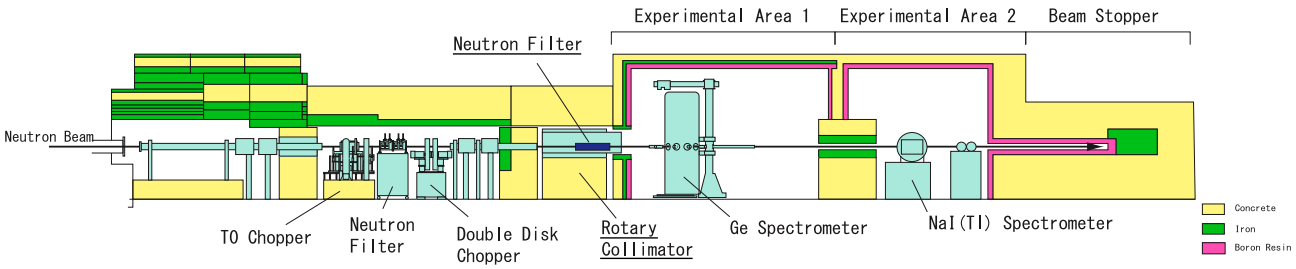

Figure 2. Schematic of the BL04 of the MLF. The neutron filter material, namely ^{nat}Fe and ^{nat}Si, was introduced in the rotary collimator.

experimental setup, the neutron energy distribution can be precisely derived from the PHITS simulations based on the good agreement of the time distribution results. The neutron energy distribution at each of the three filtered peaks was derived by gating the events from 5.4 to 6.4 μs and from 8.6 to 9.8 μs for the Si filter and from 12.6 to 15.0 μs for the Fe filter. The centroid energy at each filtered peak as well as the standard deviation is shown in Table 1. The averaged value for the highest energy filtered peak for Si was determined as 127.7 keV, much lower than the expected value around 144 keV. The reason for this is the amount of ^{27}Al included in the BL04 which has a large neutron scattering cross section at around 145 keV and shifts the filtered peak to a lower averaged neutron energy.

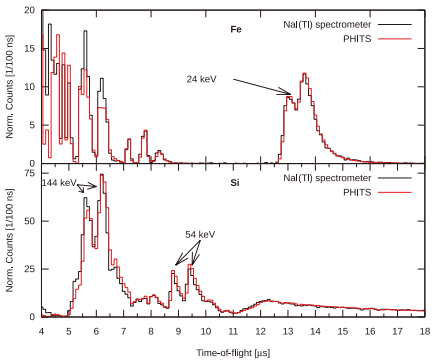

Figure 3. Experimental TOF spectrum measured with the NaI(Tl) spectrometer (black) compared with PHITS results (red) for the filter array consisting of 20 cm of Fe (up) and 20 cm of Si (down).

Table 1. Summary of the averaged neutron energy for the three neutron filtered peaks.

Filter Material	TOF gate [μs]	Av. energy [keV]	Std. dev. [keV]
Fe	12.6–15.0	23.5	1.4
Si	8.6–9.8	51.5	3.9
	5.4–6.4	127.7	12.5

3. Performance in neutron capture cross section measurements

The effectiveness of the neutron filtering technique was evaluated by means of neutron capture cross section measurements of the cross section standard ^{197}Au. An extensive amount of experimental data is available for the ^{197}Au(n, γ) ^{198}Au reaction and, hence, it is commonly used as standard value in order to evaluate the capabilities of detection systems. In the present study, the prowess of the neutron filtering system involving the use of ^{nat}Fe and ^{nat}Si was evaluated by determining the ^{197}Au(n, γ) ^{198}Au at the averaged neutron energies of the three filtered peaks of 23.5 keV for Fe; and 51.5 and 127.7 keV for Si. As shown in Fig. 4, the present results agree within uncertainties with the evaluated data from both JENDL-4.0 [2] and the IAEA Standard [3] libraries.

4. Conclusions

A neutron filtering system has been instituted in the BL04 of the MLF in order to circumvent the double-bunch structure of the neutron beam. Sharp well-defined quasi-monoenergetic peaks are tailored by the neutron filtering system through the use of ^{nat}Fe and ^{nat}Si as filter materials with averaged neutron energies of 23.5 keV for ^{nat}Fe; and 51.5 and 127.7 keV for ^{nat}Si. The performance of the neutron filtering system in neutron capture cross section measurements was analyzed by means of the standard 197Au(n, γ) ^{198}Au reaction. The present results using the neutron filtering system provide agreement within uncertainties with both the JENDL-4.0 and the IAEA Standard evaluated nuclear data libraries. Thus, proving to be a suitable solution for neutron capture cross section measurements in the keV region. Further information about the neutron filtering system can be found in Ref. [4].

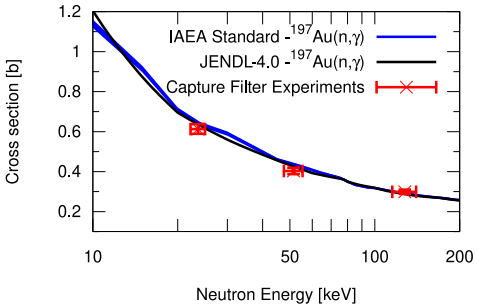

Figure 4. Averaged neutron capture cross section results for ^{197}Au using the filter arrangements of 20 cm of Si (51.5 and 127.7 keV) and 20 cm of Fe (23.5 keV) compared with the evaluated data from JENDL-4.0 and the IAEA standard data library. The standard deviation is represented as the x-axis bars.

References

[1] T. Sato et al., J. Nucl. Sci. Technol., **55** 684 (2018).
[2] K. Shibata et al., J. Nucl. Sci. Technol., **48** 1 (2011).
[3] A. D. Carlson et al., Nucl. Data Sheets, **148** 143 (2018).
[4] G. Rovira et al., Nucl. Inst. Meth. A, **1003** 165318 (2021).

G, Rovira[1], A. Kimura[1], S. Nakamura[1], S. Endo[1], O. Iwamoto[1], N. Iwamoto[1], T. Katabuchi[2], Y. Kodama[2], H. Nakano[2], J-I. Hori[3], Y. Shibahara[3], and K. Terada[3]

[1]Nuclear Science and Engineering Directorate, Japan Atomic Energy Agency.; [2]Laboratory for Zero Carbon Energy, Tokyo Institute of Technology.; [3]Institute for Integrated Radiation and Nuclear Science, Kyoto University

Status of Fundamental Physics Beamline BL05 (NOP) in 2020

1. Introduction

"Neutron Optics and Physics (NOP/ BL05)" at the MLF in J-PARC is a beamline for studies in the field of fundamental physics. The beamline is divided at the upstream into three branches, the so-called Polarized, Unpolarized, and Low-Divergence branches, used in different experiments in a parallel way [1–2].

A neutron lifetime measurement is conducted at the Polarized beam branch with a spin flip chopper. Pulsed ultra-cold neutrons (UCNs) by a Doppler shifter are available at the Unpolarized beam branch. At the Low-Divergence beam branch, the search for an unknown intermediate force is performed by measuring neutron scattering with rare gases. The beamline is used also for R&D of optical elements and detectors.

2. Measurement of the neutron lifetime

A neutron decays into a proton, an electron, and an antineutrino. The decay lifetime is an important parameter for the unitarity of the CKM matrix and also for the primordial big bang nucleosynthesis [3]. However, recently reported values for the neutron lifetime deviate significantly from the systematic uncertainties. An experiment to measure the neutron lifetime with a pulsed beam is ongoing at BL05 (NOP). The lifetime is measured as a ratio of the electron events of the neutron decay to the ^{3}He(n, p)^{3}H events caused by ^{3}He gas precisely doped in a time projection chamber (TPC). We published our first result of the neutron lifetime as $\tau_n = 898 \pm 10$ (stat.) $^{+15}_{-18}$ (sys.) s [4] (Fig. 1).

Upgrades are in progress. Currently, data corresponding to a statistical uncertainty of 4 s for the neutron lifetime have been obtained. The goal of the experiment is 1 s. In 2020, a spin-flip chopper (SFC) was enlarged, and the intensity was increased by 3.2 times. This will enable us to reach the accuracy of 1 s in about 60 days.

3. Multilayer-type Neutron Interferometer

Neutron interferometry can observe the interaction of the neutron waves with high sensitivity. The sensitivity of multilayer-type neutron interferometers can be improved by using neutrons with longer wavelength and/or making the flight path longer. By using a pulsed neutron beam and the time-of-flight (TOF) method, the number of neutrons available can be greatly increased. Furthermore, the time-dependent systematic uncertainty can be suppressed because the interference fringes are repeated on the TOF of the pulse repetition.

A multilayer-type neutron interferometer was demonstrated with pulsed neutron at J-PARC MLF BL05 (NOP). The geometrical optics of the Jamin interferometer was constructed using a "beam splitting etalon" [5, 6], which is a high-precision assembly of multilayer neutron mirrors on a quartz substrate. The anti-correlated moderations between the forward (O) beam and deviated

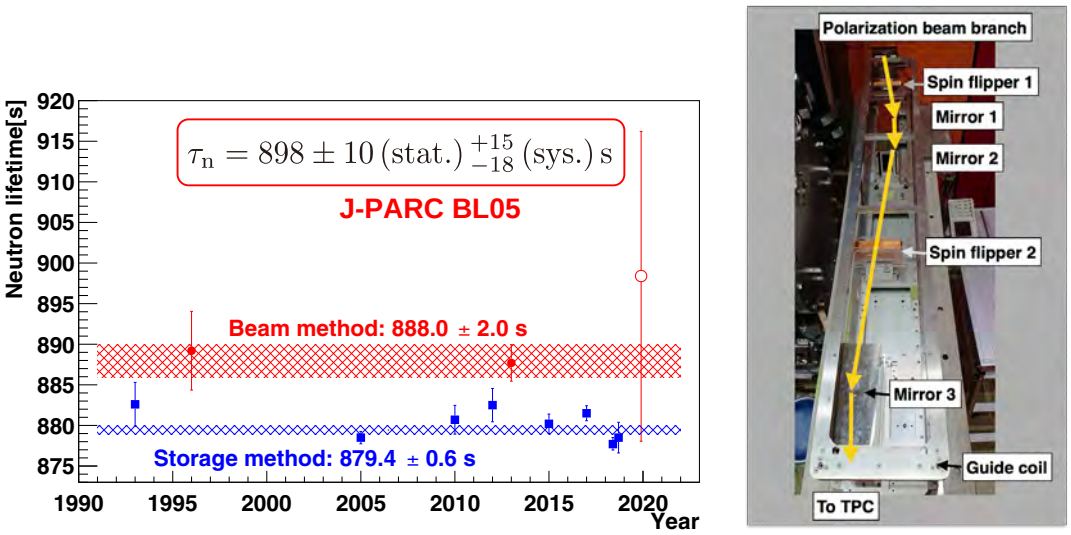

Figure 1. (Left) The results of the neutron lifetime obtained from previous experiments by the bottle (blue) methods, the beam (red), and by the present experiment [4]. The new SFC installed at the Polarization branch of BL05.

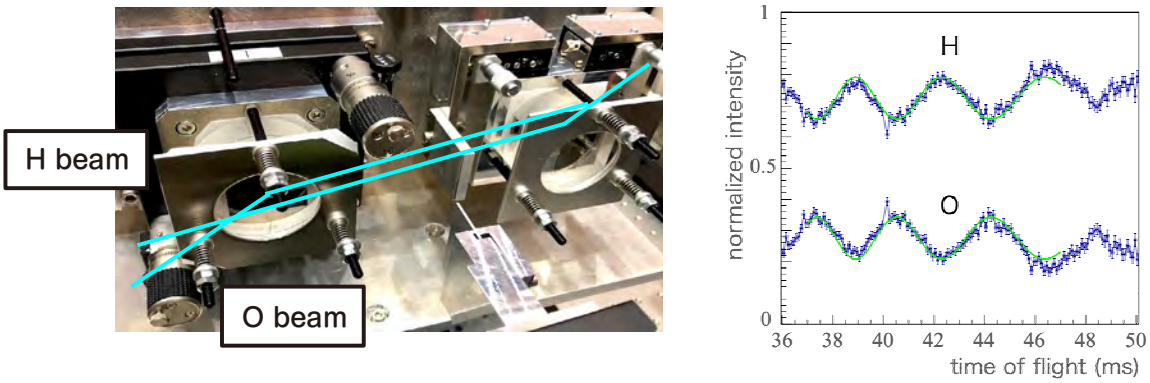

Figure 2. (Left) The setup of the multilayer-type neutron interferometer. A neutron wave function is divided into the two paths at the first half-mirror and recombined at the second half-mirror. (Right) TOF spectrum of the H beam and O beam at the detector position. The anti-correlated moderations between the two were clearly observed [7].

(H) beam on the TOF were clearly observed (Fig. 2) [7].

In the future, we plan to expand the available wavelength range and improve the experimental environment to develop an interferometer for high-precision experiments. We aim to apply the high-precision measurement of scattering length of various nuclei as basic data to basic physics experiments, such as the search for unknown interactions.

References

[1] K. Mishima et al., "Design of neutron beamline for fundamental physics at J-PARC BL05", *Nucl. Instruments Methods Phys. Res. Sect. A*, vol. 600, no. 1 (2009) 342–345.

[2] K. Mishima, "J-PARC Neutron fundamental physics beamline (BL05/NOP)," *Hamon Neutron Netw. news*, vol. 25, no. 2 (2015) 156–160.

[3] P.A. Zyla et al. (Particle Data Group), Prog. Theor. Exp. Phys. 2020, 083C01 (2020) and 2021 update.

[4] K. Hirota et al., "Neutron lifetime measurement with pulsed cold neutrons", Prog. Theor. Exp. Phys. (2020) 123C02.

[5] M. Kitaguchi, et al., Phys, Rev. A 67, 033609 (2003).

[6] Y. Seki, et al., J. Phys. Soc. Jpn. 79, 124201 (2010).

[7] M. Kitaguchi et al., "Multilayer-type neutron interferometer", The 20th Annual Meeting of the Japan Society for Neutron Science (2020).

K. Mishima[1,2] on behalf of NOP collaboration

[1]*Neutron Science Section, Materials and Life Science Division, J-PARC Center;* [2]*Institute of Materials Structure Science, KEK*

BL06: Commissioning Status of Village of Neutron Resonance Spin Echo Spectrometers (VIN ROSE)

1. Introduction

NSE is a variety of inelastic and quasi-elastic neutron scattering methods with fine energy resolution [1]. Because the energy resolution of the energy transfer measurement is not limited by the energy spectrum of the incoming neutrons in the NSE technique, a moderately (10−15% FWHM) mono-chromatic neutron beam can be acceptable. In addition, the intermediate scattering function can be directly derived by NSE, so that the method is suitable for investigating slow relaxation dynamics in condensed matter, and high-intensity and high-energy-resolution NSE spectrometers have been developed and realized [2].

At BL06, two types of resonance neutron spin echo (NSE) spectrometers, which are a modulated intensity by zero effort (MIEZE) instrument and a neutron resonance spin echo (NRSE) instrument, have been under construction in collaboration between Kyoto University and The High Energy Accelerator Research Organization (KEK) since 2011.

The NSE spectrometers are equipped with neutron resonance spin flippers (RSFs), which enable us to replace large magnetic precession fields with low guide fields, therefore downsizing and adjacence of the two spectrometers have become possible [3].

In this report, the status of the MIEZE and NRSE spectrometers at BL06 in FY2020 is summarized.

2. Commissioning status at BL06 in FY2020

The user program has started partially with the MIEZE spectrometer since the 2017B proposal round. At the NRSE spectrometer, used for fine-energy resolution, commissioning of devices, such as two-dimensional ellipsoidal neutron-focusing mirrors [2], is still necessary and has been intensively conducted.

The main scientific highlights of BL06 achieved in FY2020 are (i) The quantitative understandings of time-of-flight (TOF) MIEZE [3] and (ii) slow dynamics of magnetic skyrmions in MgSi studied by MIEZE [4], which are described in the following sections in detail.

3. The characteristics of TOF MIEZE

In this study, the features of MIEZE by using pulsed beams, which are based on the quantum-state manipulation of the neutron spin and energy, were comprehensively examined. A formulation of the MIEZE combined with the TOF method (TOF MIEZE) was established by considering the characteristics of the pulsed neutron beams. Moreover, a parameter, namely, the detuning parameter, was introduced as a measure of the magnitude of detuning from the optimized instrumental state, known as the spin-echo condition. The phase and frequency shifts of the neutron intensity signals resulting from the TOF MIEZE under various configurations were investigated systematically, and the detuning parameter was found to be equal to the derivative of phase with respect to the TOF, whose zero-point corresponds to the spin-echo condition. The theoretical predictions on phase and frequency shifts by the established formulation were well validated by the experiments at BL06. The further detailed description of this result is given in [3] and another article in this annual report.

4. Dynamics of crystallization of magnetic skyrmions in MgSi

The dynamics of crystallization of magnetic skyrmions were investigated by means of the MIEZE method. The magnetic skyrmions are nanometric vortexlike spin objects, which can be regarded as topological defects in a ferromagnetic spin arrangement, and thus behave like particles [5]. It was found that the skyrmions aggregate into small skyrmion-lattice (SkL) domains with orientational disorder on the transition from the paramagnetic phase to the SkL phase. These domains are nearly static dynamically and coexist with chiral spin fluctuations with a characteristic relaxation time of 10^{-9} [s] near the transition temperature. As the temperature is further decreased, the SkL domains merge into the long-range-ordered SkL, see the ref. [4].

This experiment could be made possible by the MIEZE method, as rather strong magnetic field (~0.2 T) parallel to the beam direction at the sample position is necessary to realize the skyrmion phase, while such a strong magnetic field is typically impossible for NSE with the conventional Mezei type spectrometers. The maximum 0.6 T electromagnet and 4 K GM cryostat have been available as sample environments of BL06 since FY2021, see Fig. 1.

5. Summary

In this report, the current status of BL06 VIN ROSE in FY2020 was summarized. The two scientific

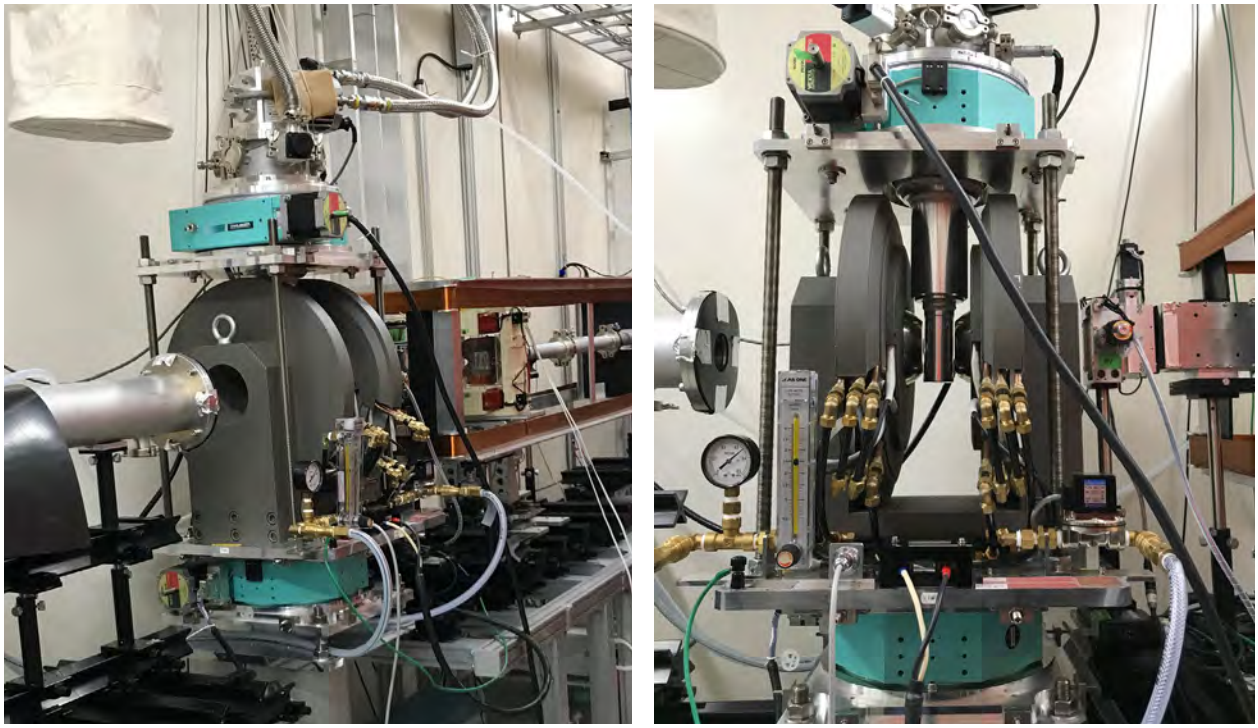

Figure 1. Pictures of the 4 K GM cryostat and the max. 0.6 T electromagnet for the MIEZE spectrometer. Left: the overall view at the sample position. Right: the side view of the magnet and the cryostat.

achievements were introduced, i.e., the characteristics of TOF MIEZE were elucidated both theoretically and experimentally, which was only possible with BL06. Then, the achievement was immediately fed into the study of the dynamics of crystallization of magnetic skyrmions to evaluate the spin echo data very quantitatively. Both results have been already published in refs. [3] and [4].

References

[1] F. Mezei ed., Neutron Spin Echo, Lecture Notes in Physics, (Springer, Berlin) **128**, (1982).

[2] T. Hosobata, M. Hino, H. Yoshinaga, T. Kawai, H. Endo, Y. Yamagata, N. L. Yamada, S. Takeda, *JPS Conf. Proc.* **22**, 011010 (2018).

[3] T. Oda, M. Hino, H. Endo, H. Seto, Y. Kawabata, *Phys. Rev. Appl*. **14**, 054032 (2020).

[4] T. Nakajima, T. Oda, M. Hino, H. Endo, K. Ohishi, K. Kakurai, A. Kikkawa, Y. Taguchi, Y. Tokura, T. Arima, *Phys. Rev. Res*. **2**, 043393 (2020).

[5] S. Mühlbauer, B. Binz, F. Jonietz, C. Pfleiderer, A. Rosch, A. Neubauer, R. Georgii, and P. Böni, *Science* **323**, 915 (2009).

H. Endo[1,2], M. Hino[3], T. Oda[4], N. L. Yamada[1,2], H. Seto[1,2], and Y. Kawabata[3]

[1]Neutron Science Division, Institute of Materials Structure Science, KEK; [2]Neutron Science Section, Materials and Life Science Division, J-PARC Center; [3]Institute for Integrated Radiation and Nuclear Science, Kyoto University; [4]The Institute for Solid State Physics, The University of Tokyo

BL08: Commissioning of a New Cryofurnace

1. Introduction

The Super High Resolution Powder Diffractometer (SuperHRPD [1, 2]) is a TOF-type neutron diffractometer with the highest resolution in the world. It is one of the J-PARC MLF beamlines that has been open for General Use Proposals since the end of 2008 and has been in operation for more than 10 years. The sample environments of SuperHRPD includes an auto sample changer for room temperature measurements, a 4 K-cryostat, a top-loading cryostat, a 1 K-cryostat, a vanadium high temperature furnace and a 14 T magnet. Of these, the auto sample changer and the top-loading cryostat had been used at the KENS facility of KEK for more than 20 years and needed to be upgraded to improve the efficiency of the measurements. In addition, there was a growing demand from users for a consistent measurement environment from low to high temperatures across room temperature, but we had to replace the sample environment above and below room temperature. Therefore, we decided to introduce a cryofurnace that can measure consistently from low to high temperatures.

2. Specification of the cryofurnace

The design specifications of our cryofurnace are shown in Table 1.

Figure 1 shows the drawing and external view of the cryofurnace. The Gifford-McMahon cryocooler and compressor used in this cryofurnace are RDE-418D4 and F-50L manufactured by Sumitomo Heavy Industries, Ltd [3]. Silicon diodes and platinum resistance thermometers are used for the temperature sensor, and Model 336 manufactured by Lake Shore Cryotronics, Inc [4] is used for the temperature control. Figure 2 shows the off-beam cooling test data. The temperature of the sample sensor was below 4.2 K in 5 hours as per the specification, and the lowest temperature reached was ~3.5 K.

Table 1. Specifications of the cryofurnace

Minimum temperature	4.2 K
Maximum temperature	800 K
Time to reach minimum temperature from RT	~5 hours
Temperature rise time	
4 K to 300 K	~2 hours
300 K to 800 K	~2 hours

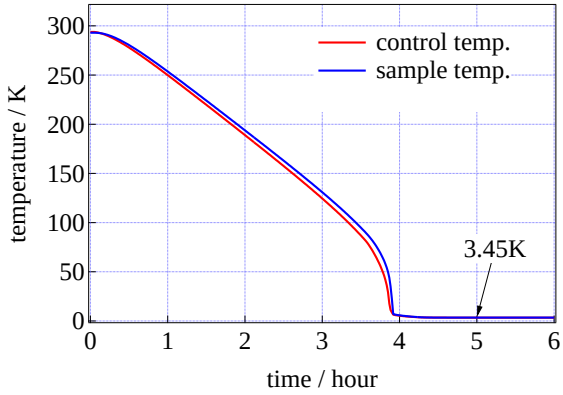

Figure 2. Off-beam cooling test data. The control temp. and sample temp. are the temperatures of the sensors located at the sample chamber and the sample mounting attachment of the sample stick, respectively. The tempera-ture reached ~3.5 K after 5 hours of cooling.

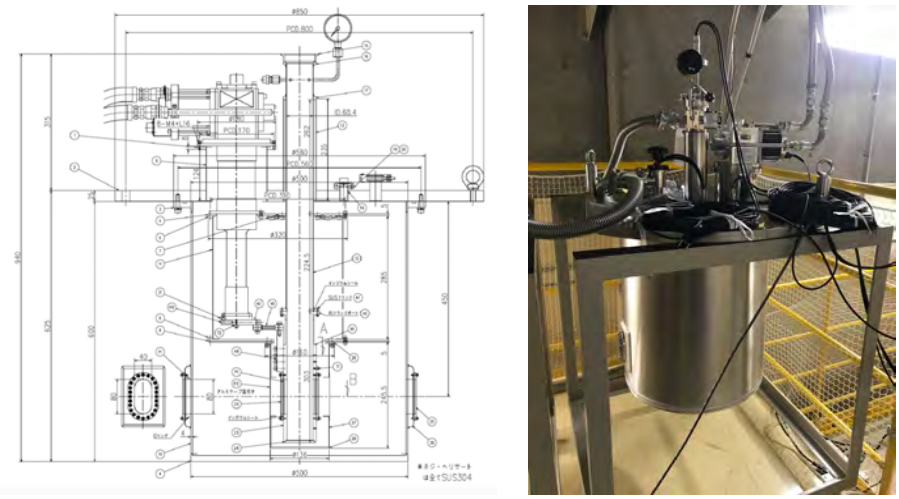

Figure 1. Drawings and external view of the cryofurnace.

3. On-beam commissioning

In this cryofurnace, the sensor located at the sample mounting attachment of sample stick is used to record the temperature near the sample, but the actual sample temperature is expected to be somewhat different due to the distance from this sensor. In order to verify this difference, we first performed the on-beam commissioning using a sample with a structural phase transition at low temperature. Figure 3 shows the temperature dependence of the magnetic peak intensity of $Co_2(OD)_3Br$. The magnetic transition was reported to occur at $T_{N1} = 6.2$ K and $T_{N2} = 4.8$ K [5], and this sample was suitable for verification near the lowest temperature. For reference, the data of the existing 4 K cryostat are also shown. For the low temperature measurement, the data were almost the same as the magnetic peak appearance temperature of the 4 K cryostat. By adjusting the pressure of the exchange gas, it is expected that the difference between the sample temperature and the sensor near the sample can be reduced.

The measurements at high temperatures were validated using the structural phase transition of Na_2CO_3 [6]. Figure 4 shows the temperature dependence of the crystal structure parameters. Since the transition temperature of the reference material is ~750 K, we found a temperature difference of about 2%. In the high temperature measurement, there is a concern about the temperature gradient of the sample because it is heated in a vacuum atmosphere. Currently, we are installing an additional sensor closer to the sample to improve the temperature accuracy, including the optimum value of PID control for the high temperature side.

4. Summary

As one of the new sample environments for SuperHRPD, a cryofurnace has been introduced. Commissioning of the first stage has been completed and it is being used for user experiments. We are planning to improve the temperature accuracy further by continuing the detailed commissioning.

References

[1] S. Torii et. al., J. Phys. Soc. Jpn. SB020 SB020-1-4 (2011).

[2] S. Torii et al., J. Phys.: Conf. Ser. 502 012052 (2014).

[3] https://www.shi.co.jp/products/precision/cold/index.html

[4] https://www.lakeshore.com/products/categories/temperature-products/cryogenic-temperature-controllers

[5] M. Hagihala et. al., Phys. Rev. B, 82, 214424 (2010).

[6] I. P. Swainson et al., J. Phys.: Condens. Matter, 7, 4395 (1995).

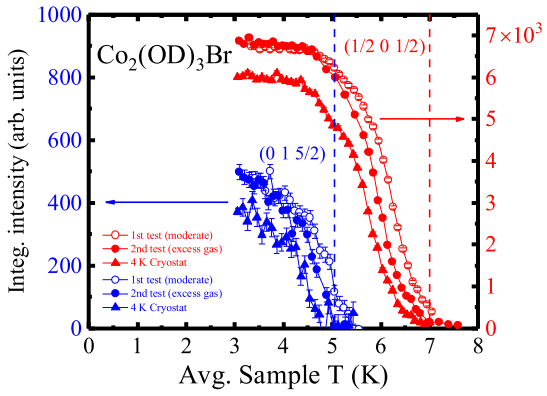

Figure 3. The temperature dependence of the magnetic peak intensity of $Co_2(OD)_3Br$. The data of a bottom-loading 4 K cryostat is also plotted for reference. The temperature at which the magnetic peak occurs was found to be comparable to that of the existing cryostat. In the case of "moderate", the sample chamber was filled with He gas at 0.01 MPa at room temperature. For "excess gas", the gas was filled at 0.05 MPa.

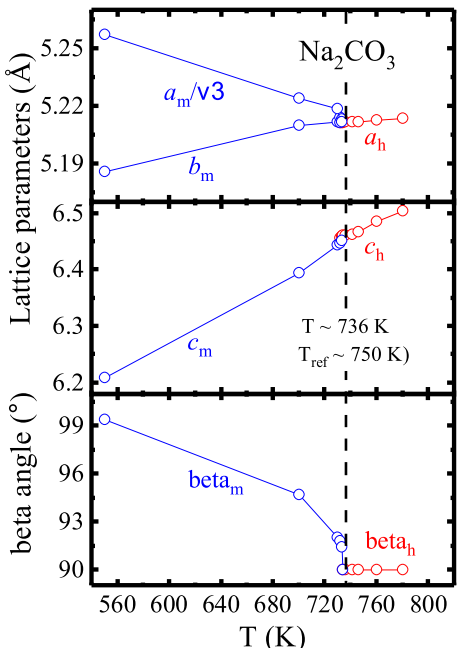

Figure 4. The temperature dependence of the crystal structure parameters of Na_2CO_3.

S. Torii[1,2], M. Hagihala[1,2], K. Cho[2], and T. Kamiyama[1,2]

[1]*Neutron Science Section, Materials and Life Science Division, J-PARC Center;* [2]*Institute of Materials Structure Science, KEK*

Current Status of BL09 (SPICA)

1. Introduction

Special Environment Powder Diffractometer (SPICA) installed at BL09 is a time-of-flight neutron powder diffractometer [1]. It has been designed and dedicated to studies for the next generation rechargeable battery [2-6]. Now it is also open for General Use Proposals, and 5 proposals (including 2 Long-Term Proposals) were accepted in the 2020A and 2020B+2021A terms.

The rechargeable battery is a key component of mobile devices and electric vehicles, and there are strong demands for developing such batteries with higher performance. Observation of the electrochemical reactions in operating batteries, as well as basic structural studies of each of the component materials are essential in the development of the next generation rechargeable battery. BL09 is equipped with ^{3}He detector banks for TOF neutron powder diffraction and nGEM/μPIC detector instruments for neutron imaging experiments. Together with its off-line electrochemical evaluation instruments and chemistry laboratory, BL09 provides an ideal environment for the study of batteries using neutrons.

2. Cryostat and cryofurnace

In FY2020, the temperature control of both the cryostat and cryofurnace was automated. A new IROHA2 device server software was developed to enable automatic temperature dependent measurements. Users can run programmed measurements, including stepwise temperature control and/or constant-rate temperature scanning. This reduced significantly the manpower required for temperature dependent measurements using these instruments.

Sample exchange procedures in a top-loading cryostat or cryofurnace are easier than those in bottom loading ones. Still, there are series of operations for exchanging samples, which require time and careful attention. In FY2020, the software was modified to enable the automation of valve operations for the cryostat and cryofurnace. Further steps will be taken to partly automate the sample exchange procedures, which will reduce the time for sample exchange procedures for these instruments.

The maximum temperature at the sample position for the top-loading cryofurnace at BL09 was about 600 K. There are, however, growing demands for experiments at higher temperatures at BL09. Therefore, a sample rod was newly designed and manufactured to increase the maximum sample temperature, as shown in Fig. 1. The temperature at the sample position was calibrated, and the maximum sample temperature is now 700 K, which is about 100 K higher than that for the previous one. Modification of the sample rod is underway to increase further the maximum sample temperature.

3. Vanadium furnace

A vanadium furnace is being developed to enable measurements at temperatures up to 1000 K. The furnace is designed to perform neutron powder diffraction measurements from room temperature up to 1000 K, under vacuum for gas flow. Samples will be heated by the radiant heat from the surrounding vanadium heater. In FY2020, we designed and manufactured the sample rod for the vanadium furnace.

4. General-purpose sample stage

Operando diffraction measurements of commercially available 18650-type lithium-ion batteries can be done at BL09 by using the sample stage specifically

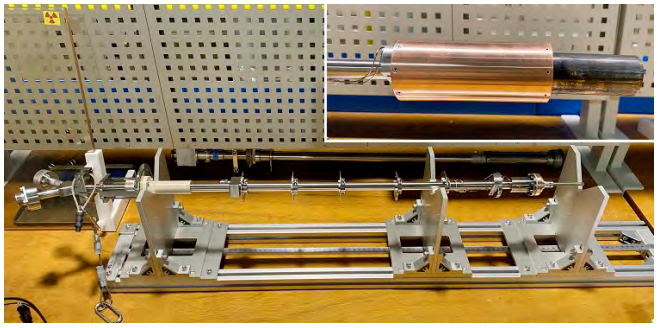

Figure 1. New sample rod for the top-loading cryofurnace in BL09. The inset shows the radiation shields installed around the sample and the heater.

designed for such type of battery. For other kinds of battery samples, a 5-axis goniometer is available, although it requires a crane operation for sample exchange. Therefore, it is desirable to develop a sample stage suitable for various kinds of battery samples, that does not require a crane operation for sample exchange. Such a sample stage can also be useful for samples with shape not suitable for an automatic sample changer. In FS2020, we manufactured a general-purpose sample stage for measurements at room temperature, which consists of a sample rod connected to a JIS 200A flange, as shown in Fig. 2. Further modifications will be made to enable operando measurements for rechargeable battery samples.

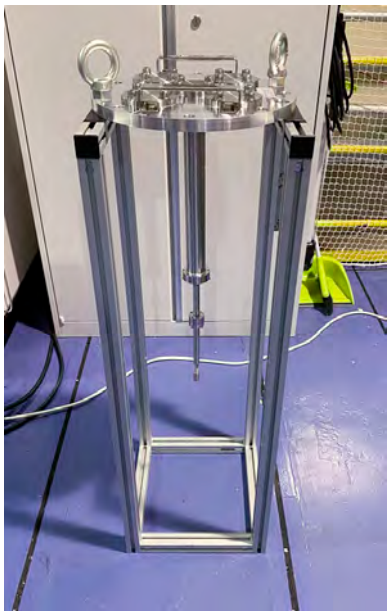

Figure 2. General-purpose sample stage in BL09.

5. Future plans

We will continue to work on the partial automation of the sample exchange procedures for the cryostat and cryofurnace, and on the increase of the maximum sample temperature of the cryofurnace. The development of the vanadium furnace will also be continued, as well as the modification of the general-purpose sample stage.

6. Acknowledgements

We would like to thank Mr. Shioya, Mr. Namba, Mr. Nanjo and Mr. Tanino for the technical support in operating SPICA. This work was supported by the Research and Development Initiative for Scientific Innovation of New Generation Batteries 2 (RISING2) project of the New Energy and Industrial Technology Development Organization (NEDO).

References

[1] M. Yonemura, et. al., J. Phys. Conf. Ser., **502**(1) Article# 012053 (2014).
[2] S. Shiotani, et. al., J. Power Sources., **325**, 404-409 (2016).
[3] S. Taminato, et. al., Scientific Reports., **6**, Article# 28843 (2016).
[4] T. Matsunaga, et. al., Chem. Mater., **28**(12), 4143-4150 (2016).
[5] K. Kino, et. al., Solid State Ionics., **288**, 257-261 (2016).
[6] T. Matsunaga, et. al., J. Phys. Chem. Lett., **7**, 2063-2067 (2016).

T. Saito[1,2,3] and T. Kamiyama[1,2,3]
[1]Institute of Materials Structure Science, KEK; [2]Neutron Science Section, Materials and Life Science Division, J-PARC Center; [3]Department of Materials Structure Science, School of High Energy Accelerator Science, The Graduate University for Advanced Studies, SOKENDAI

BL10: NOBORU

1. Introduction

In FY 2020, fifteen general-use proposals and three project-use proposals were carried out at NOBORU. Three general-use proposals and one long-term proposal were postponed due to an entry restriction for foreigners because of the COVID-19 status.

This year, several experiments were proposed to scan a large sample in two dimensions using prompt γ-ray activation analysis (PGAA). For this purpose, we introduced an electrically cooled high-purity germanium (HPGe) detector and its DAQ system to work in the IROHA2 environment. This system enables automatic measurement of prompt γ-rays that require more than a week of continuous scanning. In the following sections, we briefly describe the measurement system.

2. Development of scanning PGAA system

Figure 1 shows a schematic diagram of the constructed prompt γ-ray automatic measurement system. An electrically cooled HPGe detector manufactured by CANBERRA has been used. The signals from the HPGe detector and a timing signal of 3NBT-CT trigger are connected to the measurement module, APV8008, manufactured by TechnoAP. The event data generated by the APV module is recorded on the measurement PC by a DAQ-Middleware component called GathererAPV. The large sample is mounted on an XY stage manufactured by KOHZU or SIGMAKOKI. The X and Y stages are controlled by Tsuji Electronics' stepper motor controller (PM16C-04XDL), which is widely used in DAQ-Middleware of the MLF, and its drive control is automated by the IROHA2 facade. The obtained event data are converted to a photon energy spectra or photon-energy vs. TOF map by using Python-based CLI program or GUI program "Utsusemi for APV".

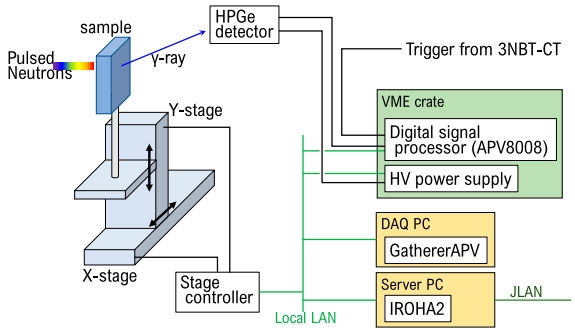

Figure 1. Schematic of the PGAA measurement system.

3. Experiment

Figure 2 shows an example of experimental setting for the scanning PGAA system at NOBORU. The aperture of the incident beam collimator is made of boron polyethylene and/or stainless steel, and the diameter is selected from 2 to 10 mm depending on the target gauge volume. For a PGAA measurement at NOBORU, a number of lead blocks need to be assembled on the experimental table to shield the γ-rays from the environmental background. To reduce this time and effort, we fabricated a mounting frame for the HPGe detector, which can be uniquely positioned using the screw holes in the experimental table, thus greatly reducing the set-up time, and improving the experimental reproducibility. In addition, a pinhole in the front of the lead shield of the detector, through which only the target part of the sample is restricted to be visible, enables easy and accurate alignment of the sample at the intersection of the beam axis and the detector axis.

For the two-dimensional PGAA measurement of a sample, a total of 17 × 57 auto-controlled mesh measurements were performed over an area of 27 mm × 87 mm, and the boron distribution was obtained with a spatial resolution of about 3 mm. The scanning system of the stage also functioned as a sample changer. About 30 coin-sized boride samples were measured for 1 to 2 hours each to perform automated experiments of PGAA, and the results were reported [1].

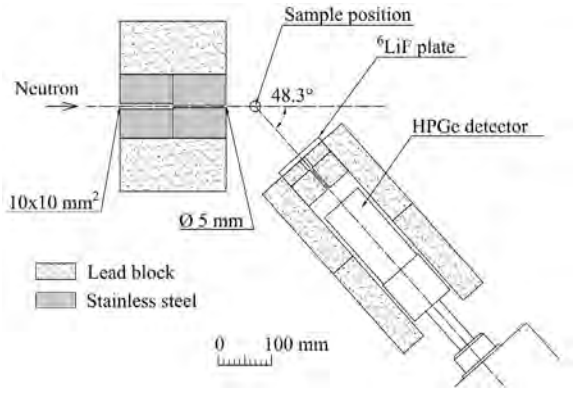

Figure 2. Experimental setting for the scanning PGAA system.

Reference

[1] Y. Tsuchikawa et al., Nucl. Inst. and Meth. Phys. Res. A, **991** 164964 (2021).

Y. Tsuchikawa, T. Kai, and K. Oikawa
Neutron Science Section, Materials and Life Science Division, J-PARC Center

Development of Piston Cylinder Cells for Diffraction, QENS, and SANS at High Pressures

1. Introduction

Piston cylinder cells have been widely used in in-situ and ex-situ high-pressure experiments due to their simple structure, compactness, and extraordinarily large sample volume (~cm^3). The last characteristic satisfies the requirements for neutron scattering experiments in which the sample signal is generally weak; thus, many piston cylinder cells have been developed and applied to various neutron scattering studies. The compactness also makes it possible to attach the cells to a cryostat, which enables experiments under multi-extreme conditions. In the last few years, we have been developing piston cylinder cells for various types of neutron scattering, such as diffraction, INS, QENS, SANS. In this report, we summarize the recent developments.

2. Piston cylinders and their performance

We used five piston cylinder cells made of different materials or with different diameter, which were invented by Uwatoko [1] and our group [2] (Table 1). Their performance in high-pressure generation and neutron transparency was evaluated at PLANET prior to the application to various types of neutron scattering.

Figure 1 shows the pressure generation performance. A Pb chunk was put in the sample container made of Al or Teflon, together with water or Fluorinert (3M, FC72), and compressed with a hydraulic press (Riken CDM-10PA). Pressure was determined by the lattice parameter of Pb on the basis of the equation of state. The results showed that the maximum available pressure increased in the order from NA700 monobloc, SCNM439–NA700 hybrid, CuBe monobloc, and NiCrAl–CuBe hybrid cells. The pressure generation efficiency compared to the ideal one without friction was 63–83% and 87–88% for cells with outer / inner diameter of 30 mm / 8 mm and 25 mm / 6 mm, respectively.

Table 1. Various cells tested and their nomenclature.

Cells*	Outer /Inner diameter
NA700 monobloc (30/8)	30 mm / 8mm
SNCM439–NA700 hybrid (30/8)	30 mm / 8mm
CuBe monobloc (30/8)	30 mm / 8mm
CuBe monobloc (25/6)	25 mm / 6mm
NiCrAl–CuBe hybrid (25/6)	25 mm / 6mm

*Numbers in the parenthesis represents outer and inner diameters of the cylinder.

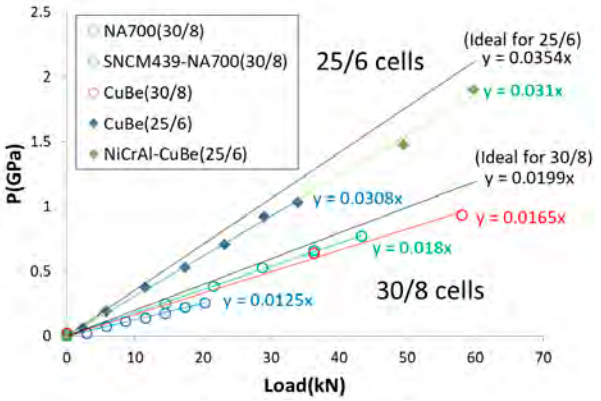

Figure 1. Pressure-generation performance of various cells. The ideal performance without friction is also shown by black lines.

Figure 2 shows the wavelength-dependent neutron transparency. The transmission increases in the order from CuBe (30/8), NiCrAl–CuBe (25/6), CuBe (25/6), SNCM439–NA700 (30/8) and NA700 (30/8). The CuBe material was found to have strong attenuation. The transmission of the SNCM439–NA700 (30/8) hybrid cylinder at 5.10 Å (3.14 meV in energy), which is the wavelength of the incident beam employed in the QENS experiment shown later, was four times larger than that for the CuBe cells, indicating that the hybrid cylinder is efficient in the experiments where the intensity at large wavelength is important, such as QENS, SANS.

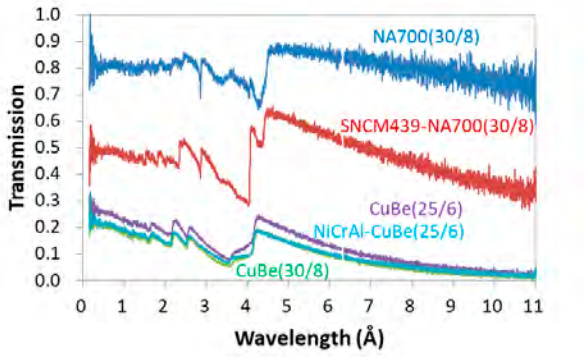

Figure 2. Neutron transmission of various cells.

3. Application to diffraction at low temperatures

In the PLANET, the lowest temperature at which neutron diffraction experiments were possible was limited to 77 K. To extend it toward a lower temperature region, the CuBe monobloc cell (30/8) was attached to the 4 K-GM refrigerator (Iwatani, Cryo Mini HE-01). Figure 3

shows the temperature dependence of the diffraction pattern of Ho_2Fe_{17} at 0.85–0.95 GPa. Upon decreasing the temperature, the magnetic peaks significantly shifted while maintaining the positions of nuclear peaks. The data quality was not degraded even with the NiCrAl–CuBe hybrid cell; thus, the experiments at pressures of up to 2 GPa and temperatures down to 7 K became possible.

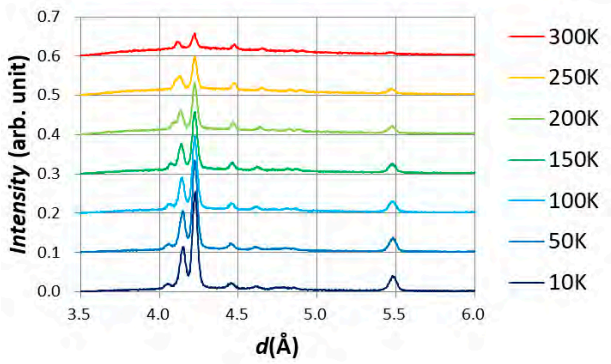

Figure 3. Temperature dependence of the diffraction patterns of Ho_2Fe_{17} at 0.85–0.95 GPa (courtesy of Yili).

4. Application to QENS at AMATERAS

The incoherent scattering from water was measured at 0.8 GPa and 300 K with the SNCM439–NA700 hybrid (30/8) cell at AMATERAS. An Al rod slightly thinner than the inner diameter of the Al container was inserted into the container, and Milli-Q water was introduced into the gap to avoid multiple scattering of water. This assembly was compressed and clamped at the target load, and then attached to a top loading stick. The $S(Q,E)$ map with an incident energy of 3.14 meV (Fig. 4) showed the

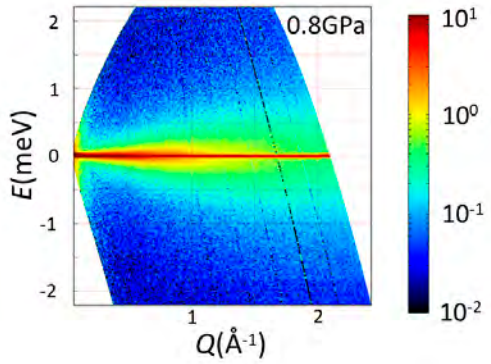

Figure 4. S(Q,E) map of water at 0.8 GPa taken with SNCM439–NA700 hybrid cells at high pressures.

marked incoherent scattering from water, which was almost the same as that taken without cells [3]. By employing the hybrid cylinder, the investigation of water over a whole pressure region where water is stable (up to 1 GPa at 300 K) became possible. However, additional details revealed that the hybrid cell generated an unwanted scattering near $(Q,E) = (0,0)$ due to the magnetic scattering. Therefore, the combination of nonmagnetic materials would be preferable in a study in which the intensity near $(Q,E) = (0,0)$ is important.

5. Application to SANS at TAIKAN

Scattering from $CrNb_3S_6$ was measured at 1.2 GPa and 3–150 K with a CuBe monobloc (30/8) cell at TAIKAN. 16 single crystals were glued on both sides of a thin Al plate in the same crystal orientation. It was inserted into a sample container filled with Fluorinert and compressed to the target load. The piston cylinder cell was attached to a 4K-GM refrigerator. Figure 5 shows the $I(Q_X,Q_Y)$ map obtained at 3 K. The magnetic peaks were clearly observed at both sides of the direct beam. On the other hand, these peaks were not observed due to a high background from the cell when the NiCrAl–CuBe hybrid cell was used.

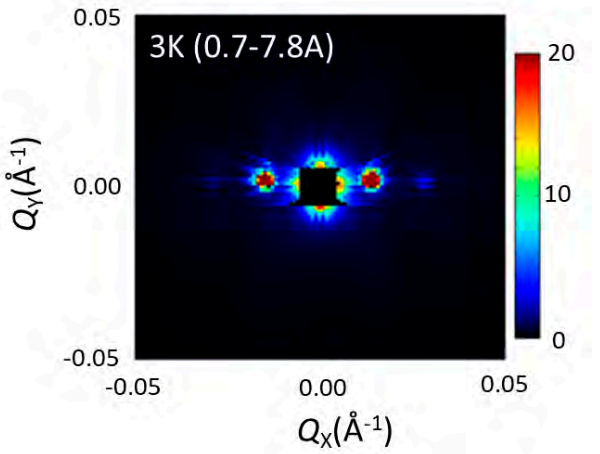

Figure 5. $I(Q_X,Q_Y)$ map of single crystal $CrNb_3S_6$ obtained at 1.2 GPa and 3 K.

References

[1] Y. Uwatoko et al., J. Phys. Condens. Matter, **14** 11291 (2002).
[2] T. Hattori et al., (submitted).
[3] T. Kikuchi et al., Phys. Rev. E, **87** 062314 (2013).

T. Hattori[1], J. Abe[2], S. Kawamura-Ohira[1], K. Ohishi[2], and Y. Kousaka[3]
[1]Neutron Science Section, Materials and Life Science Division, J-PARC Center; [2]Neutron Science and Technology Center, CROSS; [3]Department of Physics and Electronics, Osaka Prefecture University

High Resolution Chopper Spectrometer HRC

1. Introduction

The High Resolution Chopper Spectrometer (HRC) is being operated at BL12 in the MLF under the S type project of IMSS, KEK and the IRT project of ISSP, the University of Tokyo, in order to study the dynamics in condensed matter, especially in a wide range of correlated electron systems. Activities of the HRC in FY2020 are summarized in this report.

2. Web application for INS experiments

We developed a simulation program in the form of Web application using JavaScript for inelastic neutron scattering (INS) experiments using a single crystal sample on the HRC [1, 2]. The users can simulate INS experiments on the Web browser without installing any special software on their personal computers. This program consists of Neutron Laue diffraction pattern simulator, Flux/resolution simulator and Accessible Q-E range simulator, and is useful for planning experiments and educating students.

In the first step of INS experiments using a single crystal sample, the crystal orientation is found by observing the Laue spots using a white neutron beam. In the Laue diffraction pattern simulator, the Laue spots on the detector map of the HRC are simulated from the crystal structure with the lattice constants and displayed. The observed Laue pattern, which is generated on the data visualization program HANA, is transferred to the simulator and is compared with the simulation. Figure 1 shows the comparison between the observation and the simulation of the Laue pattern of $Ba_2MnGe_2O_7$ with tetragonal crystal structure. The simulation agrees well with the observation, and the crystal orientation can be defined on the coordinate system of the spectrometer. The crystal axis ω is defined as an angle between the principal crystal axis and the incident beam direction.

Then, the INS experiments started with operating the Fermi chopper. In order to observe the excitations on the desired 4-dimensional Q-E space limited by the detector configuration of the HRC, the incident neutron energy Ei and the crystal angle ω should be selected. In many cases for 3-dimensional systems, the ω rotation is required to observe enough Q-E space. Figure 2 shows an accessible reciprocal lattice space with Ei = 40 meV and with a certain range of ω, where $a^* = b^* = 1.5$ Å^{-1}, in the Accessible Q-E range simulator. By moving the slide bar in the upper part of the figure, accessible Q space can be found as a function of the energy transfer.

The multi-Ei method can be performed on the HRC, similarly to the other chopper spectrometers at the MLF. To realize the multi-Ei method, it is important to know the neutron flux, the resolution, and the accessible Q-E space for the Ei's. These pieces of information can be consistently obtained by the combined use of the Flux/resolution simulator and the Accessible Q-E range simulator.

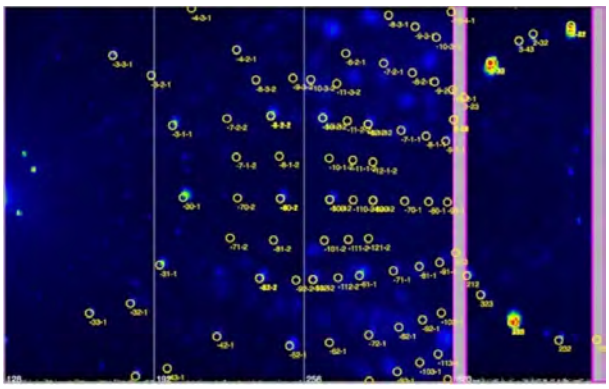

Figure 1. Typical Laue pattern of a single crystal sample measured on HRC and a comparison with a simulation.

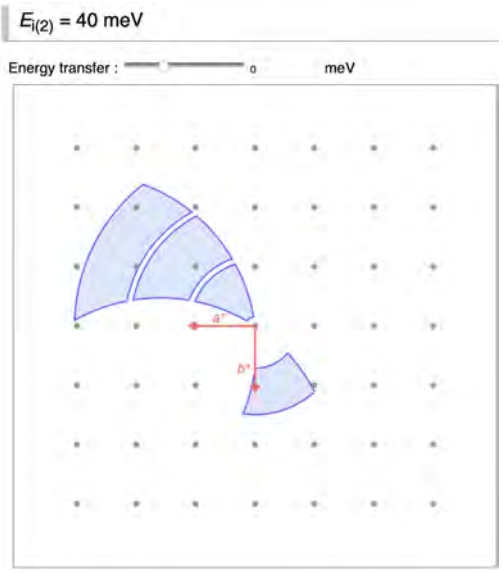

Figure 2. Accessible Q-E range for Ei = 40 meV. Shaded area and gray dots show the accessible area and the reciprocal lattice points, respectively.

3. Other instrumentations

As we reported last year, we performed a maintenance work for T0#2 (the second machine of the T0 chopper). T0#1 was operated until June 2020, then, we replaced it with the restored T0#2. At the same time, the optical fibers, which transfer the rotational signal of the T0 chopper, were renewed.

In January 2019, some failures occurred in the start-up of the HRC. Due to a lower voltage of the battery in the PLC (programmable logic controller) of the Fermi chopper controller, the Fermi chopper became out of control and a touch-down occurred in the magnetic levitation system of the rotor. Therefore, this Fermi chopper was replaced with a spare one. This year, to repair the damaged Fermi chopper, the damaged touch-down bearing was replaced with a new one. However, a stable rotation was not realized due to rotor balance loss. Further work is required.

In the vacuum system of the scattering chamber, 2 sets of the dry pumps with the mechanical booster pumps are used for the rough exhaust and the dryer is used for generating dry air for breaking the vacuum. We performed regular maintenance for these systems. Also, we performed maintenance for the backing pump (dry pump) of the turbo molecular pump for the Fermi choppers, because there was a strange noise.

The neutron choppers are provided by two companies: companies A and B are responsible for the mechanical engineering and the electrical control, respectively. In company B, the organization was changed and the development work for the electrical control was terminated. Company B provided KEK with a complete set of the information of the control system of the neutron choppers. Company A tried to establish a way to develop the electrical control system based on the information, and successfully manufactured a circuit board for the Fermi chopper control.

The 1 K refrigerator on the HRC is a ^{3}He gas circulation type one, where the lowest temperature was 0.6 K in the best case. Recently, the lowest temperature unstably reached 2 K, and the volume of the ^{3}He gas decreased. We added ^{3}He gas, but the situation did not improve. An overhaul is required.

4. Scientific results

Several publications came up as results from the general user program: magnetic correlation in $YBaCo_4O_7$ with kagome and triangular lattices [3], establishing the carrier scattering phase diagram for ZrNiSn-based half-Heusler thermoelectric materials [4], gapless spin liquid in a square-kagome lattice antiferromagnet [5], noncoplanar ferrimagnetism and local crystalline-electric-field anisotropy in the quasicrystal approximant $Au_{70}Si_{17}Tb_{13}$ [6], and spin-waves in 2D honeycomb lattice XXZ-type van der Waals antiferromagnet $CoPS_3$ [7]. A crystal growth technique contributing to the experiments on the HRC has been reported: floating zone furnace equipped with a high-power laser of 1 kW composed of five smart beams [8].

References

[1] https://sites.google.com/view/hrc-web-tools/
[2] T. Nakajima and D. Kawana, Hamon **31** 128 (2021).
[3] M. Soda et al., Phys. Rev. B **101** 214444 (2020).
[4] Q. Ren et al., Nat. Commun. **11** 3142 (2020).
[5] M. Fujihala et al., Nat. Commun. **11** 3429 (2020).
[6] T. Hiroto et al., J. Phys.: Condens. Matter **32** 415802 (2020).
[7] C. Kim et al., Phys. Rev. B **102** 184429 (2020).
[8] Y. Kaneko and Y. Tokura J. Crystal Growth **533** 125435 (2020).

S. Itoh[1,2], T. Masuda[3,2], T. Yokoo[1,2], T. Nakajima[3], S. Asai[3], H. Saito[3], D. Ueta[1,2], D. Kawana[3], R. Sugiura[3], T. Asami[3], Y. Ihata[4], and H. Tanino[1,2]
[1]Neutron Science Section, Materials and Life Science Division, J-PARC Center; [2]Institute of Materials Structure Science, KEK; [3]The Institute for Solid State Physics, The University of Tokyo; [4]Technology Development Section, Materials and Life Science Division, J-PARC Center

BL14 AMATERAS

1. Introduction

AMATERAS is a cold-neutron disk-chopper spectrometer for studies of the dynamical properties in atomic, molecular and magnetic systems from cold to sub-thermal energy range with high efficiency and flexible resolution [1, 2]. In FY2020, due to the global spread of the coronavirus infection, travels from foreign countries have been restricted all year long. Because of that, we experienced an unusual situation when many users' experiments were remotely carried out by the beamline staff or postponed to FY2021. During a short break of the beam operation, we upgraded the evacuation system for the vacuum scattering chamber.

2. User program, outreach activities and outcomes

The numbers of general proposals (short-term) submitted to the 2020A and 2020B+2021A periods were 25 (accepted: 8, reserved: 16, not approved: 1) and 35 (accepted: 7, reserved: 27, not approved: 1), respectively. Note that more than 70% of the approved proposals were from foreign users. In FY2020, the users and beamline staff members were seriously affected by the spread of the coronavirus infection. The foreign users could not visit the MLF for their experiments all year long, and even the domestic users could not enter the experimental hall in April and May. As a result, many users' experiments were postponed to FY2021 or carried out remotely by the beamline staff members in the absence of the users. Experiments of 16 general proposals and two JAEA project research proposals were carried out, and 10 of them were done remotely. As of the research fields of the 15 approved general proposals, one involved liquid and non-crystalline systems, one - the energy materials, and the other 13 dealt with magnetism and strongly correlated electron systems, which was the same trend as in the previous periods.

In FY2020, 13 refereed papers related to works at AMATERAS were published, and two students received their degrees. Dr. Kazuki Iida (CROSS) won the JSNS Young Researcher Prize for the study of magnetic fluctuations in novel superconductors by using a pulsed neutron source, which included works at AMATERAS [3]. Moreover, an article written by Dr. Nobuyuki Kurita and Prof. Hidekazu Tanaka (Tokyo Institute of Technology) to "Hamon", related to the study of magnetism in the frustrated quantum spin system conducted at AMATERAS, was selected as a JSNS President Choice [4].

AMATERAS was supposed to accept a guest researcher from the AONSA Young Research Fellowship organized by Asia-Oceania Neutron Scattering Association. However, his stay has been postponed due to the COVID-19 pandemic and presently, there is no concrete plan about his visit.

3. Instrument-related upgrades

In FY2020, we upgraded the evacuation system of the vacuum scattering chamber of AMATERAS during a short break of the beam operation from the end of December 2020 to the beginning of January 2021. The vacuum scattering chamber originally accommodated a cryopump, which consists of three sets of the coldhead and compressor, to achieve high vacuum. However, in recent years, we had often encountered some troubles with this cryopump. Therefore, last fiscal year, we purchased a new cryopump and a gate valve to achieve a more effective operation of the system. The new gate valve, a huge elbow and the new cryopump (ULVAC) were fitted to the bottom of the vacuum scattering chamber as shown in Fig. 1. Its control system was also partly modified and then we carried out a test operation. Although the cooling power of the new cryopump is lower than the original one, we could achieve a vacuum level high enough to perform practical experiments. The cooling time to the lowest temperature was reduced by half an hour than before. Furthermore, the newly introduced gate valve enabled us to change the sample environment without warming up the cryopump. Consequently, we are now able to reduce the time for changing the samples by more than five hours in the maximum case. The upgrade of the evacuation system is expected to bring about an effective beam-time operation. We are planning to modify the vent port and then automate the system next year.

We have also slightly improved the design of our bottom-loading closed-cycle refrigerator: we made the radiation shield thinner and added a room-temperature shield made of aluminum foil. With these modifications, the cooling speed was effectively improved and now it takes two hours to reach the lowest temperature (~3 K). Gradual warming in the long-time operation at the lowest temperature was successfully prevented by the new room-temperature shield.

References

[1] K. Nakajima et al., J. Phys. Soc. Jpn. **80**, SB028 (2011).
[2] K. Nakajima, RADIOISOTOPES **66**, 101 (2017).
[3] K. Iida et al., J. Phys. Soc. Jpn. **89**, 053702 (2020).
[4] N. Kurita and H. Tanaka, Hamon. **30**, 130 (2020).

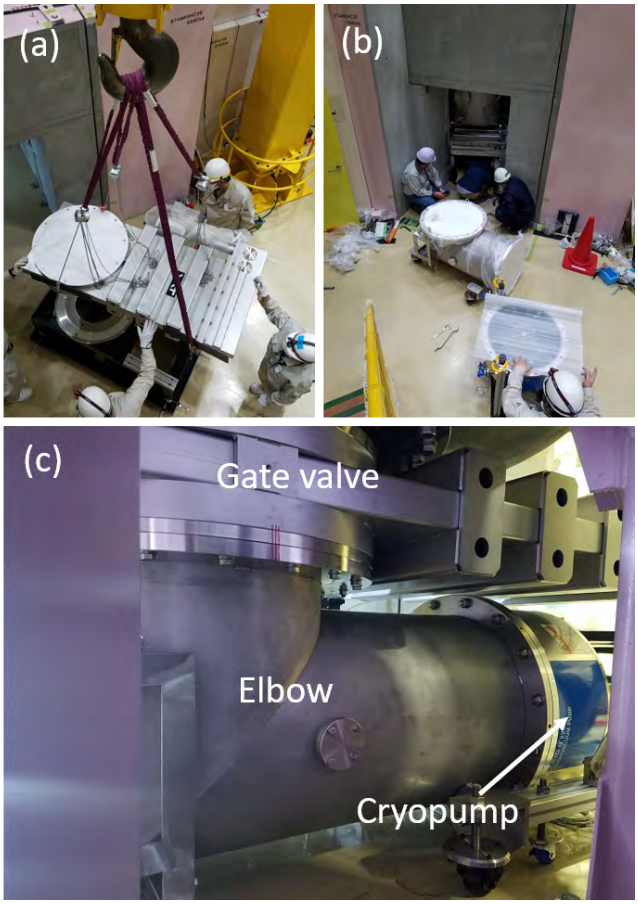

Figure 1. (a) Gate valve, (b) elbow and cryopump newly introduced to the vacuum scattering chamber of AMATERAS. (c) The new components fitted on the bottom of the vacuum scattering chamber.

S. Ohira-Kawamura[1], M. Kofu[1], N. Murai[1], Y. Inamura[1], D. Wakai[2], and K. Nakajima[3]
[1]Neutron Science Section, Materials and Life Science Division, J-PARC Center; [2]NAT Corporation; [3]Materials and Life Science Division, J-PARC Center (Present: Material Science Research Center)

Upgrading TAIKAN

1. Introduction

The small and wide angle neutron scattering instrument TAIKAN (BL15) has been developed and upgraded at J-PARC to analyze precisely and efficiently the microstructures or hierarchical structures of substances in various scientific fields with a 1 MW spallation neutron source [1]. In FY2020, it was upgraded further to perform efficient wide-*q* measurement and tensile test measurement.

2. Upgrading for efficient wide-*q* measurement

The detector system of TAIKAN is composed of 5 detector banks: small-, middle-, high-, ultra-small-angle, and backward detector banks. On the high-angle detector bank, 80 ^{3}He PSD tubes were additionally installed. The measurement efficiency of the high-angle detector bank increased by 25%. The number of ^{3}He tubes then increased to 912, 720, 400, and 80 for the small-, middle-, high-angle, and backward detector banks, respectively, and reached 2,112 in total. The installation ratios of the ^{3}He tubes became 100, 100, 76, and 100% for the small-, middle-, high-angle, and backward detector banks, respectively, and became 94% as an overall average. Figure 1 shows the lower section of the high-angle detector bank after installing the ^{3}He tubes.

Furthermore, for more efficient measurement, the detector with a gas pressure of 6 atm was replaced with one with a gas pressure of 20 atm. Also, 32 detectors in the center of the small-angle detector bank and 80 detectors in the backward detector bank were replaced.

3. Upgrading for tensile test measurement

A tensile testing machine with a load cell was developed for the study of soft matter (Fig. 2). A sample is mounted in a gas chamber. The standard size of the sample is 65 mm long and 40 mm wide. The maximum stroke is 500 mm. The maximum tensile force is 500 N. The head speed is 0.01 to 50 mm/min. The temperature of the sample can be controlled between RT and 80°C. This machine can be combined with a humidity control system, and the sample atmosphere can be any mixture of light and heavy water vapor.

4. Future prospects

The installation of high-angle detectors and the replacement of low gas pressure detectors with high gas pressure detectors further improved the efficiency of the wide-*q* measurement. The development of the tensile testing machine has provided an experimental environment for advancing the study of nanoscale mechanical deformation behavior of soft matter. Such upgrades are expected to contribute to the nanoscale study of non-equilibrium states, a need that emerged recently.

Reference

[1] S. Takata, J. Suzuki, T. Shinohara, T. Oku, T. Tominaga, K. Ohishi, H. Iwase, T. Nakatani, Y. Inamura, T. Ito, K. Suzuya, K. Aizawa, M. Arai, T. Otomo and M. Sugiyama, JPS Conf. Proc., **8** 036020 (2015).

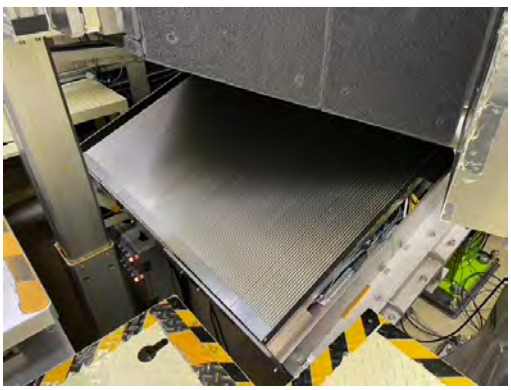

Figure 1. The lower section of the high-angle detector bank.

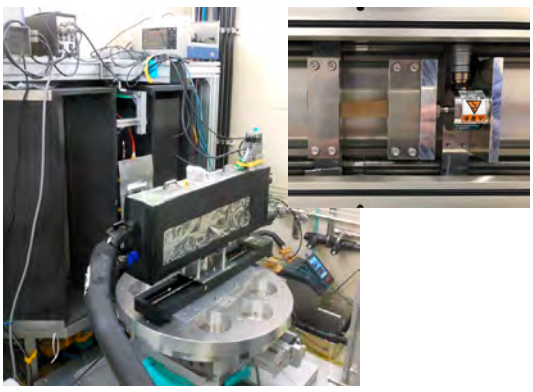

Figure 2. The tensile testing machine with a load cell for the study of soft matter.

J. Suzuki[1], S. Takata[2], K. Ohishi[1], H. Iwase[1], Y. Kawamura[1], K. Hiroi[2], T. Morikawa[1], and M. Sahara[1]
[1]Neutron Science and Technology Center, CROSS; [2]Neutron Science Section, Materials and Life Science Division, J-PARC Center

Detector Replacement of Neutron Reflectometer at BL16 SOFIA

1. Introduction

Neutron reflectometry (NR) is very useful for investigations of structures of surfaces and buried interfaces composed of soft materials. SOFIA is a horizontal-type neutron reflectometer constructed at Beamline 16 (BL16) of the Materials and Life Science Experimental Facility (MLF) of the Japan Proton Accelerator Research Complex (J-PARC) [1, 2]. Due to the high-flux beam of J-PARC, less than one hour is needed for taking a full *Q*-range data and only a few seconds for a limited *Q*-range data in the case of a sample with 3 inches (76 mm) in diameter; even though the beam power is still one-third of the planned value, 1 MW. However, several hours are still needed for a small sample, such as 10 mm × 10 mm, which is a typical size of a sample for X-ray reflectometry.

For further upgrade of the SOFIA reflectometer, we have developed an elliptical focusing mirror to illuminate a sample with a neutron beam with a large beam divergence. So far, we developed focusing super-mirrors [3, 4, 5]. The latest mirror is capable of focusing neutrons with a width of 0.13 mm in full width at half maximum (FWHM). This mirror has already been installed in the SOFIA and opened for users as reported last year.

Furthermore, we have a plan to realize a multi-incident neutron reflectometry (MI-NR) at the SOFIA by applying focusing mirrors, in which neutrons are transported by two different paths and converged at a sample position with different incident angles. As the difference in the incident angle is 2.3° and the distance from the sample to detector is 2 m, the beam positions of the two paths are 81 mm apart from each other at the detector position. This difference is, however, too large to detect with the detector called RPMT (resistance division photomultiplier tube; Hamamatsu Photonics K. K.) [6] used in the SOFIA, whose detection area is approximately 80 mm in diameter. In addition, the RPMT detector was discontinued. Hence, we have evaluated a new detector utilizing a flat-panel multi-anode-type photomultiplier tube (FRP) with the detection area of 48 × 48 mm^2 as a replacement for RPMT [7] and replaced the old RPMT detector with the new FRP detector.

2. Assembly

The FRP system consists of a multi-anode-type photomultiplier tube, H12700 (Hamamatsu Photonics K. K.), a resister array E14340 (Hamamatsu Photonics K. K.) installed behind the PMT, and a ZnS (Ag)/^{6}LiF scintillator (Scintacor, Ltd.) fixed on the H12700 with a gap of 4 mm. The thickness of the scintillator was 0.45 mm, which is more than that used with the old RPMT detector, 0.3 mm (OHYO KOKEN KOGYO Co., Ltd.). The high voltage of -920 V was applied and output analog signals through an amplifier were processed by the NeuNET as the RPMT detector.

3. Evaluations

The position of a neutron event converted to photons by the scintillator is detected by a charge division method. Generally, the detection position shows a good linearity at the center but is gradually distorted at the edge. Hence, distortion correction is required to use the neutron signals at the edge of the detector. To correlate the read beam position and the actual position on the detector, the neutrons with the beam size of 0.1 × 2 mm^2 were illuminated on the detector with a checkerboard pattern at a distance of 2 mm, by moving a sample position. Figure 1 shows the result of the mesh scan. As mentioned before, the signals around the center presented a good linearity with 22 channel/mm (the full scale was 1000 channels), whereas the change in the channel

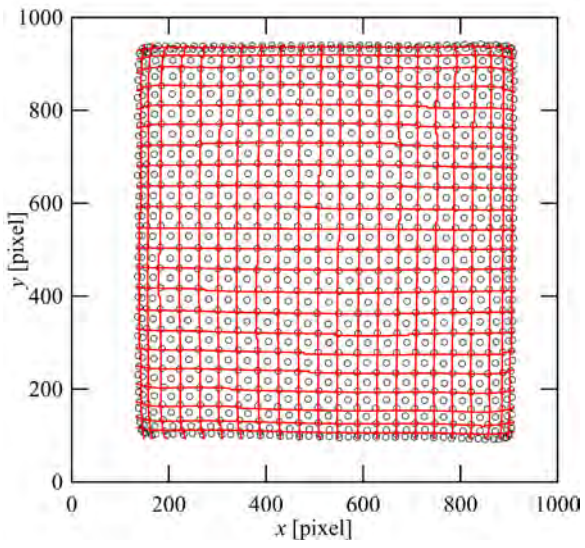

Figure 1. Result of the mesh scan for distortion correction. Symbols indicate the detection positions of a collimated beam with changing the detector position and lines indicate the contour lines of the 2D-fitting result with a 10th degree polynomial function every 2 mm.

becomes smaller at the edge. The position dependence was two dimensionally fitted with a 10th degree polynomial function. This result was used for to make a correction map to convert the detection position to the actual position. With the map, the spatial resolution of the detector was evaluated to be approximately 0.6 mm around the center.

Next, the counting efficiency of neutrons was evaluated. Figure 2 shows the comparison of counting rates taken with old and new detectors depending on the neutron wavelength with the same slit condition. Because of the use of a thicker scintillator, the counting rate doubles for the thermal neutrons (approximately 20% to 40% in comparison with ^{3}He tube detector). This indicates that the accumulation time can be cut in half when taking the data with the same statistics. Though the gain through the thicker scintillator is less for neutrons with a longer wavelength, this doesn't matter because the counting rate of the reflection neutrons is higher for longer wavelength owing to the higher reflectivity.

Finally, the homogeneity of the efficiency of the neutrons was evaluated. Figure 3 presents an image of incoherent scattering by a polyethylene block. The block was illuminated with an incident angle of 4°, and the detector was placed 2 m apart from the block with a deflection angle of 10°. The uniform incoherent scattering by the hydrogens in the block can reveal the homogeneity of the detection efficiency depending on the detection position. As shown in the figure, the homogeneity was not bad, but there was a periodic change in the efficiency. This comes from the pitch of the multiplier tube: the FRP consists of the 8 × 8 tubes with the size of 6 × 6 mm^2. According to frequency analysis, the standard deviation of the inhomogeneity was 18%.

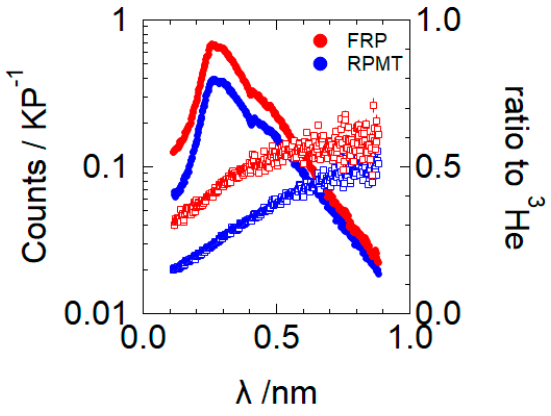

Figure 2. Comparison of the counting rates taken with the old (RPMT) and new (FRP) detectors depending on neutron wavelength with the same slit condition.

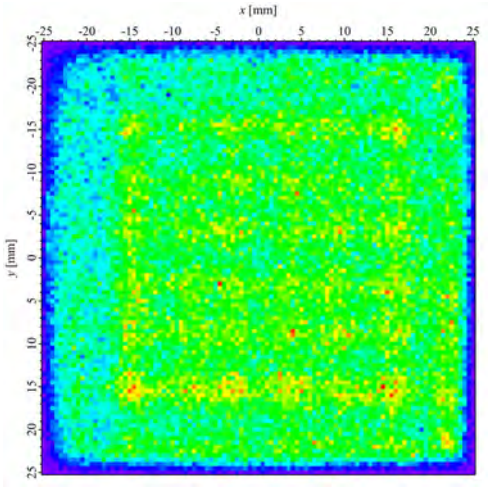

Figure 3. Image of incoherent scattering by a polyethylene block for homogeneity check.

4. Conclusion

As shown above, the new FRP detector performs better than the old RPMT detector. The spatial resolution of the new detector is approximately 0.6 mm at the center, whereas for the old one it is approximately 1 mm. In addition, the counting efficiency of the new detector is approximately 40% to ^{3}He tube, whereas it was 20% for the old one. Because of these good features, we have already replaced the detector before the upgrade for the MI-NR.

References

[1] N. L. Yamada et. al., Euro. Phys. J. Plus, **44** 9424 (2011).
[2] K. Mitamura et. al., Polymer J., **45** 100 (2013).
[3] S. Takeda et. al., Opt. Express, **24** 12478 (2016).
[4] T. Hosobata et. al., Opt. Express, **25** 20012 (2017).
[5] T. Hosobata et. al., Opt. Express, **27** 26807 (2019).
[6] K. Hirota et. al., Phys. Chem. Chem. Phys. **7** 1836 (2005).
[7] S. Satoh, Plasma Fusion Res. **13** 3 (2018).

Norifumi L. Yamada[1,2], Fumiya Nemoto[3], and Setsuo Satoh[1,2]
[1]Neutron Science Section, Materials and Life Science Division, J-PARC Center; [2]Institute of Materials Structure Science, KEK; [3]National Defense Academy

Current Status of SHARAKU: Polarized Neutron Reflectometer

1. Introduction

SHARAKU is a neutron reflectometer with horizontal scattering plane equipped with a polarization neutron option installed at BL17 at Materials and Life Science Facility of J-PARC. It has been used for the structure analysis of the surface and interfaces in thin film samples in research fields such as polymer and magnetic materials. To expand the application of the neutron reflectometry to various research, novel reflectometry techniques [1–3] and sample environments [4, 5] have been developed. In this fiscal year, we developed temperature-controlled water cell system, as an example, for the neutron reflectometry experiment to enable to estimate the structure and dynamics of layer structure of thin film samples.

2. Temperature-controlled water cell system

The temperature-controlled water cell system is one of the sample environment devices that can change the temperature of the sample and liquid from room temperature to 90°C. It consists of two major parts: a cell housing, where the sample is mounted, and a temperature controller.

An overview of the cell housing is shown in Fig. 1. The recommended sample is a silicon wafer with a diameter of 2 inches and a thickness of 3 mm. The liquid reservoir is made of aluminum alloy and has a capacity of about 5 cc. An O-ring (Kalrez 4079) is used to seal the reservoir to the sample. At the top of the reservoir, there are two small holes, one for solution injection and the other for air venting, and the solution is sealed with silicon packing. The housing with the sample and solution is fixed to a copper heater plate.

Neutrons are injected from the side of the substrate, which is visible on the side of the housing, and are reflected at the solid-liquid interface between the liquid reservoir and the substrate. It is then exited from the opposite side of the substrate. During the actual reflectivity measurement, the housing and the heater plate are covered with a cover to prevent the spread of contamination by solvent vapor in case of boiling.

An overview of the temperature controller is shown in Fig. 2. This controller was developed mainly to control the temperature of the housing described above, and is intended for experiments at BL17. However, it can also be used for other sample environment instruments and beamlines. The temperature control is mainly done by UT-55A made by Yokogawa Electric Corporation. Two thermocouples are installed for temperature control. By monitoring these two K-type thermocouples, an interlock mechanism is provided to prevent abnormal operations due to disconnection of the thermocouples or heater wires.

The interlock mechanism can be triggered not only by the functions of the UT-55A as described above, but also by an emergency button installed in the main body of the temperature controller or an emergency button that can be installed outside the experimental hatch with an extension cable. The interlock alarm can also be connected to a patrol light installed in the beamline, making it possible to notify the surroundings of the occurrence of an abnormality.

This temperature controller can be operated by itself, but it can also be controlled externally via ethernet communication. For the external control, we have developed a driver for the IROHA2 system, which is the MLF device control protocol (Fig. 3). This allows the control of

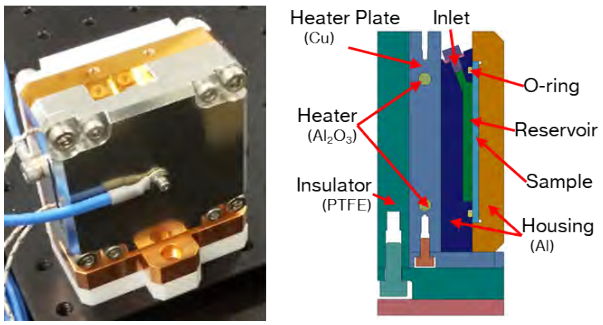

Figure 1. An overview cell housing of the temperature-controlled water cell system.

Figure 2. Photograph of the temperature controller.

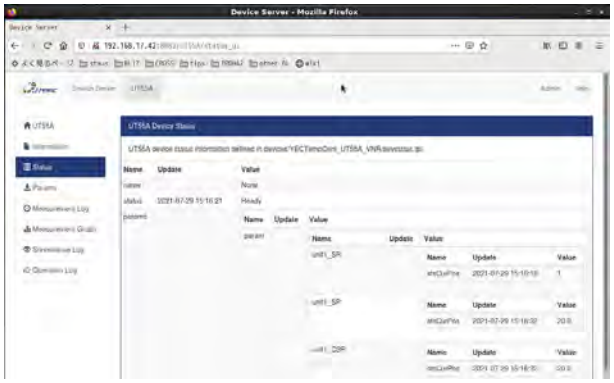

Figure 3. IROHA2 web interface for the temperature controller.

the temperature controller to be incorporated into the conventional reflectivity measurement sequence, and the temperature, sample, and measurement order can be freely changed by external control from the control cabin. This improves greatly the efficiency of the experiment. In addition, the developed driver for IROHA2 can be easily ported to other MLF devices that use IROHA2, which makes a clear contribution to the common use of sample environment equipment.

3. Commissioning and future plans

The system was commissioned in the experimental preparation room at CROSS using water as the solvent, and was confirmed to work reliably in the range from room temperature to 90°C with an appropriate waiting time. Based on these results, the temperature controller passed the MLF safety examination and is now used by many users.

The developed temperature controller is not only for this cell but can also be used for general temperature control experiments. We are planning to apply the controller to a sample environment apparatus that can be heated up to about 200°C in a vacuum atmosphere, and to develop a multi-channel controller that can control multiple temperature controllers simultaneously.

References

[1] K. Sakurai, J. Jiang, M. Mizusawa, T. Ito, K. Akutsu, N. Miyata, Sci. Rep. **9** 571 (2019).

[2] H. Aoki, H. Ogawa, M. Takenaka, Langmuir, **37**, 196 (2021).

[3] T. Kumada, K. Akutsu, K. Ohishi, T. Morikawa, Y. Kawamura, M. Sahara, J. Suzuki, N. Torikai, J. Appl. Crystall. **52** 1054-1060 (2019).

[4] S. Ohira-Kawamura, T. Hattori, S. Harjo, K. Ikeda, N. Miyata, T. Miyazaki, H. Aoki, M. Watanabe, Y. Sakaguchi, T. Oku, Neutron News, **30**, 11 (2019).

[5] H. Arima-Osonoi, N. Miyata, T. Yoshida, S. Kasai, K. Ohuchi, S. Zhang, T. Miyazaki, H. Aoki, Rev. Sci. Instrum., **91**, 104103 (2020).

N. Miyata[1], H. Kira[1], S. Kasai[1], H. Arima-Osonoi[1], T. Miyazaki[1], H. Aoki[2,3], K.Soyama[4], D. Yamazaki[5], K. Akutsu[1], and T. Hanashima[1]

[1]Neutron Science and Technology Center, CROSS; [2]Neutron Science Section, Materials and Life Science Division, J-PARC Center; [3]Institute of Materials Structure Science, KEK; [4]Materials and Life Science Division, J-PARC Center; [5]Neutron Instrumentation Section, Materials and Life Science Division, J-PARC Center

Status of SENJU 2020

1. Introduction

SENJU is a TOF single-crystal neutron diffractometer designed for precise crystal and magnetic structure analyses under multiple extreme environments, such as low-temperature, high-pressure, and magnetic-field, as well as for taking diffraction intensities of small single crystals with a volume of less than 1.0 mm^3 down to 0.1 mm^3 [1]. Since the operation of SENJU started in 2012, our instrument group has carried out continuous commissioning and upgrades.

In 2020, we installed a top-loading cryostat with a φ-axis sample stick for rapid sample exchange and stable ω- and φ-axes rotation. We also installed an auto He gas loading system in the vacuum sample chamber to shorten the sample heating time after low-temperature measurement. In addition, we also report on the purposes of the instrument beam-time for SENJU.

2. Development of a top-loading 2-axes cryostat

The bottom-loading type cryostat is the most frequently used sample environment device in SENJU. SENJU has two bottom-loading 4 K cryostats; one is a GM-type cryostat, and another is a pulse-tube-type cryostat. Both cryostats are equipped with piezo-rotating devices to rotate a sample crystal with two axes, ω and φ, under vacuumed and low-temperature conditions. However, the movement of the piezo-rotator is unstable at low temperature, and the low-temperature measurement uses the bottom-loading cryostat stacks often during the automatic sequential measurement. To overcome this problem and perform users experiments stably, we developed a top-loading type 4 K cryostat system with ω- and φ-axes.

The cryostat system is composed of a main body with the ω-axis and a sample stick with the φ-axis. Figure 1 shows photos of the φ-axis sample stick. A pulse motor for the φ-axis rotation is attached under the vacuum flange, where the temperature is kept at room level. The sample stick has three rotational shafts and two universal joints to transfer the rotation of the motor to the φ-axis at the end of the stick.

In a preliminary cooling test, the bottom temperature of the stick end was 4 K, almost the same as the bottom-loading cryostats. The rotation of the ω- and φ-axes was stable even at the bottom temperature.

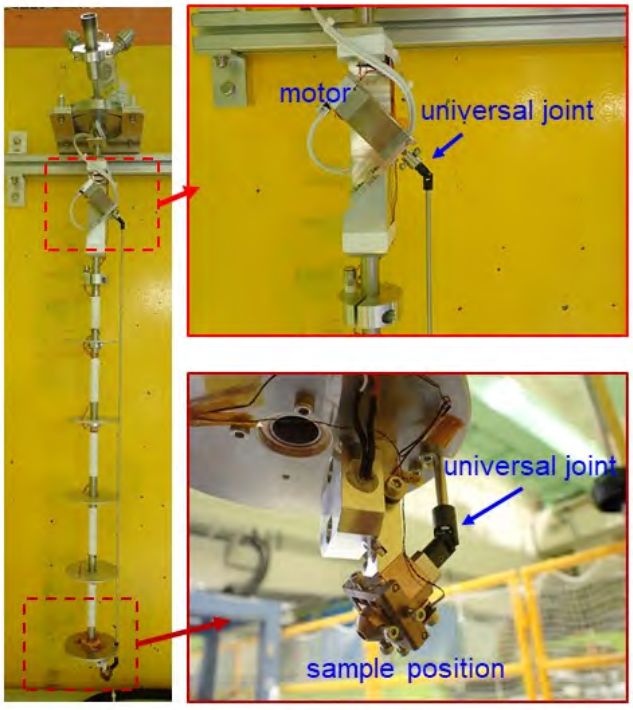

Figure 1. Photos of the φ-axis sample stick for the two-axes top-loading cryostat system.

3. Development of automatic He gas loading system for the vacuum sample chamber

In the low-temperature diffraction measurement at SENJU, a sample crystal is attached at the end of a cryostat and set in a vacuum sample chamber. In the sample heating process, following the low-temperature measurement, a user had to switch off the compressor of the cryostat and vacuum pump and wait for about five hours to heat the sample. The waiting time made the sample changing and user switching period very long. In addition, the compressor/vacuum pump control was not automated. So, when one SENJU user ended the measurement and switched to the following user in the morning, the former user had to come to the SENJU site in the early morning or sometimes at midnight to switch off the compressor and the vacuum pump. However, in the mail-in and alternate measurements during the COVID-19 pandemic, the on-site vacuum control becomes a heavy load for the instrument scientists. To shorten the sample changing and user switching time and to relieve the load of instrument scientists and users, we developed an automatic He gas loading and vacuum control system for the vacuum sample chamber of SENJU.

Figure 2 shows the schematic view of the He gas loading system. There are two magnetic valves between the vacuum sample chamber and a gas canister. The IROHA2 system automatically controls the valves. By opening/closing the two valves sequentially, a small amount of He gas between the valves is loaded in the chamber, and the He gas pressure in the chamber rises to about 1 Pa. The He gas in the chamber acts as a heat medium to heat the sample and the cryostat. The heating time from 4 K to room temperature with the He gas is about three hours. In addition, we developed and installed an automatic switch on/off system for the compressor and the vacuum pump. The IROHA2 controls this system as well.

The use of the automatic He gas loading system and the switch on/off system for the compressor and vacuum pump shortens the sample changing and user switching time. In addition, users/instrument scientists do not need to go to the SENJU site at midnight, even when the following user's experiment starts the next morning.

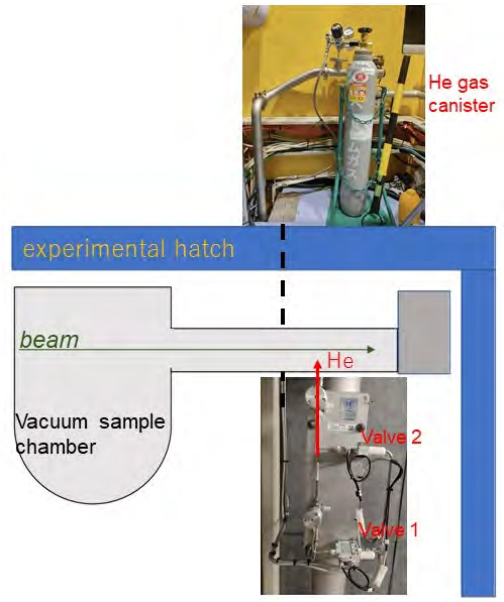

Figure 2. Schematic view of the He gas loading system.

4. Use of the instrument beam time

In 2020, the instrument beam time was used mainly for measurements of standard samples, and a vanadium-nickel alloy for calibration of the detector efficiency.

Reference

[1] T. Ohhara et al., J. Appl. Cryst., 49 120 (2016).

T.Ohhara[1], R. Kiyanagi[1], A. Nakao[2], K. Munakata[2], Y. Ishikawa[2], K. Moriyama[2], I. Tamura[1], and K. Kaneko[1]
[1]Neutron Science Section, Materials and Life Science Division, J-PARC Center; [2]Neutron Science and Technology Center, CROSS

Engineering Materials Diffractometer TAKUMI

1. Introduction

TAKUMI is a pulsed neutron diffractometer dedicated for research in engineering materials sciences, installed at beamline 19 in the MLF of J-PARC. TAKUMI employs careful analysis of the Bragg peaks in a neutron diffraction pattern to reveal important structural details of sample material, such as internal stresses, phase conditions, dislocations, texture, etc. As expressed in the name of instrument (Engineering Materials Diffractometer), TAKUMI covers not only residual stress mapping in engineering components, but also microstructural evolutions during deformations of structural or functional materials at various temperatures, microstructural evolutions during manufacturing (thermomechanical) processes, as well as texture analyses of engineering materials.

2. Activities in 2020

The following upgrades were performed in FY2020:
(1) Development of a new sample chamber for low-temperature deformation test to reduce the time for the sample change and the temperature control. The work on the necessary hardware was completed but the commissioning needs to be continued.
(2) Large tilting stage for strain mapping allowing alignment of large samples (< 150 kg) has been built.
(3) The real-time monitoring software allowing to see the newest diffraction patterns (not summed for the whole exposure time) was completed, and the device control software was upgraded.

Due to the COVID-19 pandemic restrictions, call proposals for the 2020B term were not handled separately, but were processed in the joined term of 2020B + 2021A. Therefore, it was difficult to separate the proposals assigned only to FY2020. Here, we counted the proposals until July 2021 (including the 2021A term). The percentages of the approved general proposals and reserved ones with beamtime allocation were 78% for 2020A and 73% for 2020B + 2021A. 30 general use proposals, 2 long-term proposals and 2 project use proposals were successfully conducted on TAKUMI. Among them, about 40% of general proposals were conducted without the attendance of principal investigators or the collaborators, i.e., they were on-behalf experiments, due to the travel limitations caused by COVID-19. The on-behalf experiment is not a customary type of support provided by J-PARC, but the instrument scientists were encouraged not to stop the scientific research activities. However, 2 general proposals were cancelled, due to difficulties in the handling of samples and devices brought by users.

The statistics on the experimental types and the sample materials of conducted experiments during FY2020 are summarized in Fig. 1. More than half of the beamtime was occupied by *in situ* measurement during loading test, as it happened every year. In particular, the demand for low temperature loading has been increasing in the past few years due to the expanding research on the deformation properties of high entropy alloys. Meanwhile, for high temperature conditions, the

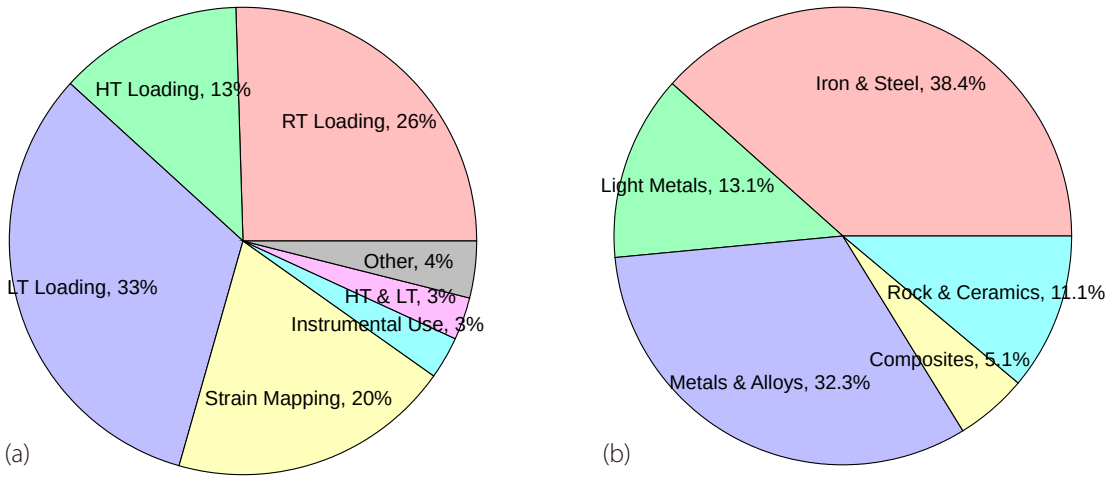

Figure 1. The statistics of the kinds of experiments conducted at TAKUMI (a) and the kinds of materials used in these experiments (b) in FY2020. The percentages show the beamtime use.

requirements for *in situ* measurements during thermo-mechanical controlled processes, which include rapid heating, cooling and deformation, are increasing. The instrument called "thermec-mastor" and the newly developed loading machine equipped with an induction heating system were used for these kinds of experiments. The percentage of beamtime for strain mapping experiments (internal stress analysis of mechanical parts) increased slightly in comparison to the last year statistics (14%). Most of this kind of experiments were proposed by industrial users. Iron- or aluminum-based objects were measured in these experiments. Reflecting the importance of iron and steel as structural materials, the percentage of these materials in all the samples increased slightly to 38%. The percentage of light metals slightly decreased, while that of metals and alloys (Ni-based superalloy, high entropy alloys and other alloys, 32%) was almost unchanged.

3. Achievements

Thanks to the users and the collaborators, 22 reviewed papers and 2 proceedings papers using the data measured at TAKUMI have been published in 2020. In addition, the data were also used in 2 doctoral or master theses. Based on the papers, 2 press releases were launched, and 3 awards were achieved. Some of the highlighted papers are described below:

(a) "**Role of retained austenite in low alloy steel at low temperature monitored by neutron diffraction**", by T. Yamashita et al. [1]. *In situ* neutron diffraction measurements during tensile tests at low temperatures of a low alloy steel containing retained austenite (γ) have been performed to analyze and discuss the role of γ in the steel during deformation at low temperatures.

(b) "**Extremely high dislocation density and deformation pathway of CrMnFeCoNi high entropy alloy at ultralow temperature**", by M. Naeem et al. [2]. The deformation behavior of CrMnFeCoNi high-entropy alloy was investigated by *in situ* neutron diffraction at an ultralow temperature of 15 K, to elucidate the extraordinary strength–ductility combination at ultralow temperature.

(c) "**Neutron diffraction monitoring of ductile cast iron under cyclic tension–compression**", by S. Harjo et al. [3]. To understand work hardening behavior during low-cycle loading, ductile cast iron containing 10.1 vol% spheroidal graphite, 19.6 vol% pearlite, and ferrite matrix was investigated in an *in situ* neutron diffraction study of up to four cycles of tensile–compressive loading with applied strains of ±0.01.

(d) "**Mechanism of improved ductility of 1500 MPa-class ultra-high strength cold-rolled steel sheet produced by rolling and partitioning method**", by Y. Hosoya et al. [4]. *In situ* neutron diffraction during tensile loading was conducted to elucidate the deformation behavior of a newly developed 1500 MPa class stainless steel sheet having an excellent yield strength and total elongation balance.

(e) "**Microstructural features and ductile-brittle transition behavior in hot-rolled lean duplex stainless steels**", by O. Takahashi et al. [5]. The characteristics of the texture and microstructure of lean duplex stainless steels with low Ni content produced through hot rolling followed by annealing were investigated locally with electron backscatter diffraction and globally with neutron diffraction, to elucidate the ductile–brittle transition behavior.

4. Future Plans

In order to enhance the convenience of TAKUMI, several upgrades on the sample environment devices and the software have been scheduled as follows:

(1) Commissioning of a new sample chamber for low-temperature deformation test.

(2) Upgrades of the data reduction software to make it more user-friendly.

References

[1] T. Yamashita et al., Scripta Mater. **177**, 6-10 (2020).
[2] M. Naeem et al., Scripta Mater. **188**, 21-25 (2020).
[3] S. Harjo et al., Acta Mater. **196**, 584-594 (2020).
[4] Y. Hosoya et al., ISIJ Int. **60**, 2097-2106 (2020).
[5] O. Takahashi et al., Quantum Beam Sci. **4**, 16 (2020).

S. Harjo[1], T. Kawasaki[1], W. Gong[1], S. Morooka[1,2], and K. Aizawa[3]
[1]Neutron Science Section, Materials and Life Science Division, J-PARC Center; [2]Materials Sciences Research Center, JAEA; [3]Materials and Life Science Division, J-PARC Center

The Current Status of the Versatile Neutron Diffractometer, iMATERIA

1. Introduction

Ibaraki Prefecture, local government of Japan's area where the J-PARC sites are located, has decided to build a versatile neutron diffractometer (IBARAKI Materials Design Diffractometer, iMATERIA [1]) (Fig. 1) to promote industrial applications for the neutron beam in J-PARC. iMATERIA is planned to be a high-throughput diffractometer that could be used by materials engineers and scientists in their materials development work, including chemical analytical instruments.

The applications of neutron diffraction in materials science are (1) to do structural analyses of newly developed materials, (2) to clarify the correlation between structures and properties (functions), and (3) to clarify the relation between structural changes and improvements of functions, especially for practical materials. A diffractometer with super high resolution is not required to achieve those goals. The match of features like intermediate resolution around $\Delta d/d = 0.15\%$, high intensity and wide d coverage is more important.

This diffractometer is designed to look at a decoupled-poisoned liquid hydrogen moderator (36 mm, off-centered) (BL20), and it has an incident flight path (L1) of 26.5 m, with three wavelength selection disk-choppers and straight neutron guides with a total length of 14.0 m. The instrumental parameters are listed in Table 1. There are four detector banks, including a low-angle and small-angle scattering detector bank. The angular coverage of each detector bank is also shown in Table 1. The rotation speeds for the disk-choppers are the same, with a pulse repetition rate of 25 Hz for the most applications (SF mode). In this case, the diffractometer covers $0.18 < d$ (Å) < 2.5 with $\Delta d/d = 0.16\%$ and covers $2.5 < d$ (Å) < 800 at three detector banks of 90-degree, low-angle and small-angle with gradually changing resolution. When the speed of the wavelength selection disk-choppers is reduced to 12.5 Hz (DF mode), we can access a wider d-range, $0.18 < d$ (Å) < 5 with $\Delta d/d = 0.16\%$, and $5 < d$ (Å) < 800 with gradually changing resolution with doubled measurement time compared to the SF mode.

2. Current status

All of the four banks, high-resolution bank (BS bank), special environment bank (90-degree bank), low-angle bank and small-angle bank, are operational. It takes about 5 minutes (in DF mode) to obtain 'Rietveld-quality' data in the BS bank at 700 kW beam power for about 1 g of standard oxide samples.

Figure 2 shows a typical Rietveld refinement pattern

Table 1. Instrumental parameters of iMATERIA. L2 is the scattered flight path. The d-range (q-range) for each bank is the maximum value for 2-measurement mode.

L1	26.5 m	
Guide length		Total 14 m (3section)
Position of Disk choppers		7.5 m (double)
		11.25 m (single)
		18.75 m (single)
High	2θ	$150^\circ \le 2\theta \le 175$
Resolution	L2	2.0 – 2.3 m
Bank	d-range	$0.09 \le d\ (A^\circ) \le 5.0^\circ$
Special	2θ	$80^\circ \le 2\theta \le 100^\circ$
Environment	L2	1.5 m
Bank	d-range	$0.127 \le d\ (A^\circ) \le 7.2$
Low	2θ	$10^\circ \le 2\theta \le 40^\circ$
Angle	L2	1.2 – 4.5 m
Bank	d-range	$0.37 \le d\ (A^\circ) \le 58$
Small	2θ	$0.7^\circ \le 2\theta \le 5^\circ$
Angle	L2	4.5 m
Bank	q-range	$0.007 \le q\ (A^{\circ -1}) \le 0.6$

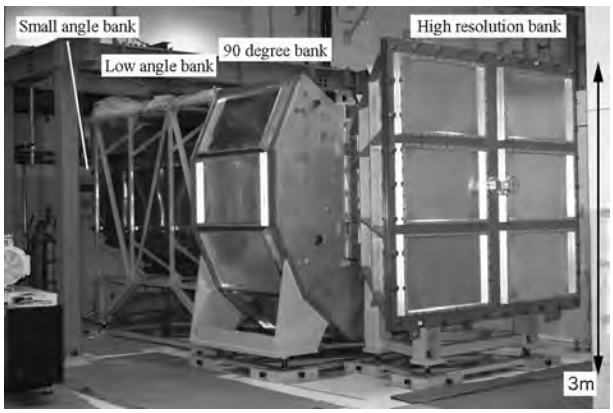

Figure 1. IBARAKI Materials Design Diffractometer, iMATERIA without detector for each bank and instrument shielding. The BS bank, 90-degree bank, and low-angle bank, can be seen from right to left. The small-angle detector bank, which is not shown in the picture, is situated in the low-angle vacuum chamber (left-hand side of the picture).

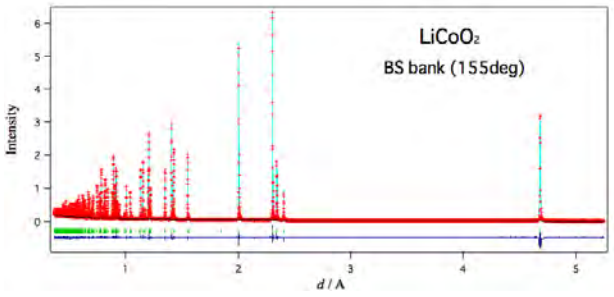

Figure 2. Rietveld refinement pattern for $LiCoO_2$ at the BS bank of iMATERIA.

for $LiCoO_2$ sample, cathode material for lithium-ion battery (LIB), at the BS bank by the multi-bank analysis function of Z-Rietveld software [2]. It takes 20 min in DF mode to collect the available Rietveld data, due to the high neutron absorption cross section for natural Li (σ_s^{Nat} =70 barn).

3. Sample environments

The automatic sample changer is the most important sample environment for high-throughput experiments. Our automatic sample changer [3] consists of a sample storage, elevating system of two lines, two sets of pre-vacuum chambers and a sample sorting system. We can handle more than 600 samples continuously at room temperature (RT) without breaking the vacuum of the sample chamber.

The vanadium-furnace (~900°C), the gas flow furnace (~1000°C), and the 4K and 1K cryostats are ready for experiments.

The rapid heating/quenching furnace with automatic sample changer (RT – 1273 K with heating speed 10 K/s and cooling speed >20 K/s) [4] and the universal deformation testing machine (max loading 50 kN with RT – 1273 K) [5] are available for texture measurements.

The in-operando charge and discharge measurement system for LIB with a sample changer is available in cylindrical, coin and laminated types of batteries. Figure 3 shows a typical in-operando time-dependent diffraction pattern for laminated type LIB under charging process. The changes in the negative electrode active material can be observed around 3.5 Å, and the changes in the positive electrode active material NMC can be observed around 4.8 Å.

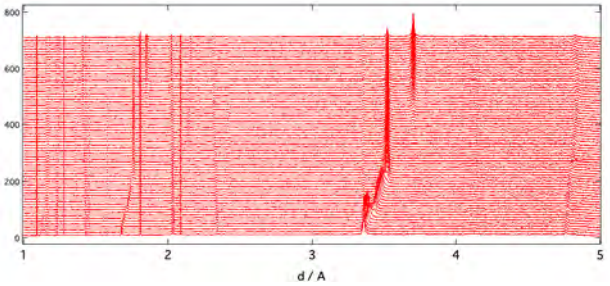

Figure 3. The in-operando time-dependent neutron diffraction patterns for laminated type LIB under charging process at the BS bank. It shows the time division changes of the diffraction patterns for 1 minute every 10 minutes.

References

[1] T. Ishigaki, et al., Nucl. Instr. Meth. Phys. Res. A600 (2009) 189-191.
[2] R. Oishi, et. al., Nucl. Instr. Meth. Phys. Res. A600 (2009) 94-96.
[3] A. Hoshikawa, et al., J. Phys.: Conf. Ser. 251 (2010) 012083.
[4] Y. Onuki, et. al., Metall. Mat. Trans. A. 50 (2019) 4977-4986.
[5] Y. Onuki, et. al., Quantum Beam Sci., 4 (2020) 31.

T. Ishigaki, A. Hoshikawa, T. Matsukawa, and Y. Onuki
Frontier Research Center for Applied Nuclear Sciences, Ibaraki University

Status of the High Intensity Total Diffractometer (BL21, NOVA)

1. Introduction

Total scattering is a powerful technique to analyze disordered structure in materials with atomic Pair Distribution Function (PDF). NOVA was designed to perform total scattering and is the most intense powder diffractometer with reasonable resolution ($\Delta d/d \sim 0.5\%$) in J-PARC. It is easy to adapt NOVA to a very wide area of fields: liquids, glasses, local disordered crystalline materials, magnetic structures, and so on.

2. Polarized Neutron Scattering Experiment

A neutron polarizer with polarized ^{3}He gas, referred to as a ^{3}He spin filter, based on the Spin Exchange Optical Pumping (SEOP) was equipped to perform polarized neutron scattering experiments at NOVA [1]. The polarizer was installed at the upstream of the beamline, and the neutron polarization was held by the magnetic field produced with a guide coil to the sample. The scattered neutrons by the sample were analyzed with two ^{3}He cells located at 20 mm from the sample position in a vacuum chamber. The diffraction patterns of the NaH powder were measured with incident beam of non-spin-flip (++) and spin-flip (–+) scattering (Fig. 1). Bragg peaks of 111 (lattice spacing, d = 2.82 Å), 311 (d = 1.47 Å) and 331 (d = 1.12 Å) were clearly detected only in the case of (++), which showed that the spin flippers work properly [2]. (Peaks of d = 4.8 Å and 5.0 Å are unexpected background.) Difference for baseline corresponds to significant incoherent scattering cross section, including inelastic scattering of hydrogen, which is evaluated to extract coherent scattering term.

3. Reverse Monte Carlo (RMC) modelling

Vanadium hydride is of interest as a possible hydrogen storage material owing to its reversible hydrogen absorption/desorption reactions at room temperature between mono-hydride (hydrogen-to-metal ratio; H/V ~ 1) and di-hydride (H/V ~ 2). Because cyclic hydrogen storage reaction introduces distortion to the metal lattice, the local structure around hydrogen is important. Neutron structure factors of $VD_{0.7}$ and VD_2 were measured on NOVA and their pair distribution functions were analyzed using Reverse Monte Carlo (RMC) modelling method [3]. Partial radial distribution functions (D-D, D-V, V-V) of $VD_{0.7}$ and VD_2 are shown in Fig. 2. The first peak in the D-D partial is in both cases just above 2 Å in compliance with the Switendick criterion [4]. Atomic arrangements of 1×1×1 were derived from projection after modelling by 8×8×8 of $VD_{0.7}$ and VD_2, respectively. Deuterium occupies 8*c* site of *Fm*-3*m* in VD_2 with little displacement, but the occupation around 12*d* site of *Im*-3*m* in $VD_{0.7}$ is dispersed. In the alloy system, the relationship between the hydrogen-metal pair and the hydrogen storage properties would be investigated.

4. Future plans

We will continue with the development of the polarized neutron scattering experiment system to analyze the static structure of aqueous solution and hydrides, and the magnetic structure of strongly correlated electron system. The Reverse Monte Carlo (RMC) modelling will be expanded to local structure analysis of other disordered crystalline materials.

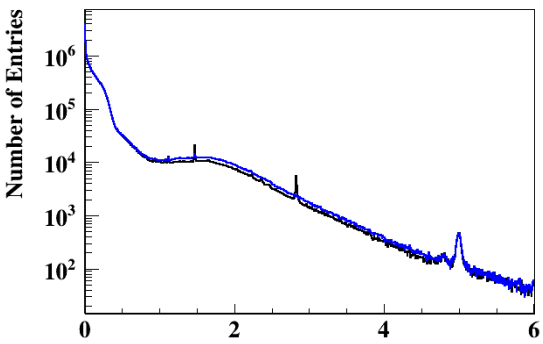

Figure 1. Diffraction patterns of the NaH powder with incident beam of non-spin-flip (++) (black) and spin-flip (–+) (blue) scattering.

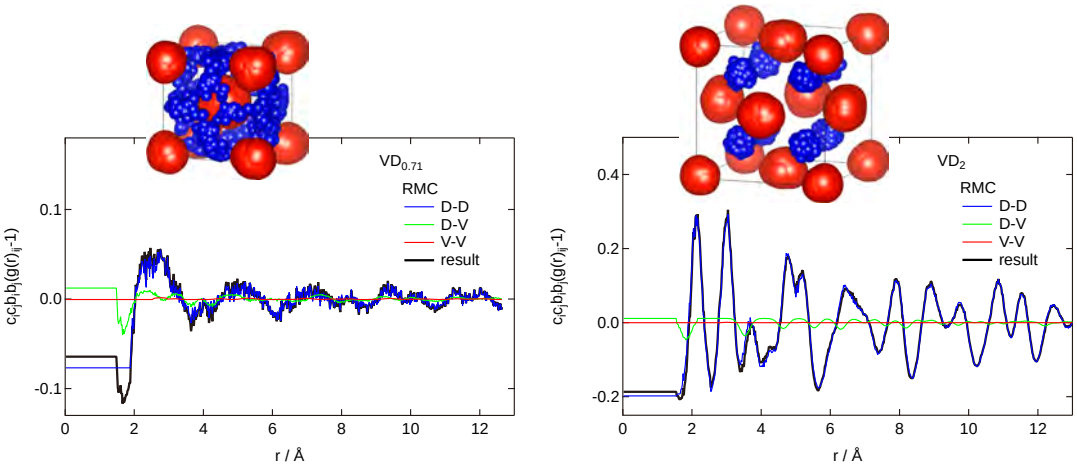

Figure 2. Reverse Monte Carlo (RMC) modelling results of $VD_{0.7}$ and VD_2. Atomic arrangements of 1×1×1 were derived from a projection after modelling by 8×8×8.

Acknowledgements

The polarized neutron scattering experiment system was developed with Dr. Okudaira and Dr. Oku. We would like to thank Mr. Maya for his technical support in operating NOVA. The operation and developments of NOVA was performed under the S1-type program (2019S06) approved by the Neutron Scattering Program Advisory Committee of IMSS, KEK.

References

[1] T. Okudaira et al., Nucl. Instrum. Methods Phys. Res. A, **977** 164301 (2020).
[2] R.M. Moon et al., Phys. Rev., **181** 920 (1969).
[3] M.G. Tucker et al., J. Phys. Condens. Matter, **19** 335218 (2007).
[4] B. Rao and P. Jena, Phys. Rev. B, **31** 6726 (1985).

K. Ikeda[1,2,3], T. Honda[1,2,3], T. Otomo[1,2,3,4], H. Ohshita[1,2], S. Sashida[3], and M. Tsunoda[4]

[1]Institute of Materials Structure Science, KEK; [2]Neutron Science Section, Materials and Life Science Division, J-PARC Center; [3]Department Materials Structure Science, The Graduate University for Advanced Studies; [4]Graduate School of Science and Engineering, Ibaraki University

Current Status of the Energy-Resolved Neutron Imaging System RADEN

1. Introduction

The Energy-resolved neutron imaging system "RADEN", installed at beam line BL22 in the MLF of J-PARC, is a dedicated instrument for wavelength/energy-dependent neutron imaging experiments, which utilizes fully the short-pulsed neutron's nature [1]. A variety of imaging experiments have been conducted at RADEN, such as Bragg-edge imaging, neutron resonance absorption imaging, and polarized pulsed neutron imaging, in addition to the conventional neutron imaging. After the start of the user programs, RADEN has been accepting about 40 user programs every year. In 2020, because of the spread of the COVID-19 virus, many users could not visit J-PARC for the experiments and some of the programs have been conducted by the instrument group members on behalf of them. In addition, RADEN started accepting the Fast Track Proposals for the feasibility check before the regular full proposal. In this report, the results of the technical development conducted at RADEN are described.

2. High-resolution imaging

We introduced a high-spatial resolution imaging system, which is utilized for the high-resolution X-ray imaging, and consists of a scintillator screen, a mirror, optical lenses and an sCMOS camera. This system uses two lenses behind the mirror so as to magnify the object image on the image sensor plane. Three scintillator screens, 10 μm-thick P43, 10 and 100 μm-thick $Gd_3Al_2Ga_3O_{12}$:Ce (GAGG) were tested with this system, and achieved spatial resolution of 10.5 μm by using the 100 μm-thick GAGG scintillator (Fig. 1) [2]. This is a remarkable improvement compared to the former spatial resolution at RADEN, which was 30 μm. Furthermore, the result that a fine spatial resolution could be realized even though the scintillator thickness was 10 times larger than the achievable resolution is thought to originate in the small light scattering inside the scintillator because GAGG is a single crystal. We will continue the development of high-spatial resolution imaging system using a single crystal scintillator screen.

3. Development and deployment of the BμNID

The μNID (μPIC-based Neutron Imaging Detector) [3] is currently one of the main energy-resolved neutron imaging detectors at RADEN. The μNID utilizes a time-projection-chamber with a 400 μm pitch, and a two-dimensional μPIC (Micro-Pixel Chamber) micropattern strip readout. Using ^{3}He for neutron conversion, a fine spatial resolution (0.1 mm) is achieved via three-dimensional tracking of the resulting proton and triton. The μNID also features a 26% detection efficiency for thermal neutrons and an effective global neutron count rate of 1 Mcps.

To improve the rate performance, we developed a variant of the μNID, the BμNID, which replaces the ^{3}He gas converter with a ^{10}B thin film (~1.2 μm thick) deposited on the drift cathode. Compared to ^{3}He, the n-^{10}B reaction produces heavier charged secondaries, namely an alpha particle or Li nucleus, leading to reduced event sizes and better event separation for improved rate performance up to 10 Mcps. The increased rate comes with a trade-off in both spatial resolution (0.3 mm) and detection efficiency (5%) compared to the μNID; however, there are many use-cases requiring only moderate spatial resolution, which benefit greatly from the increased

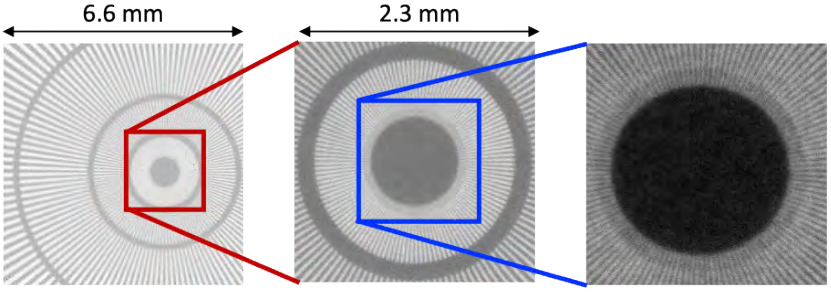

Figure 1. High-resolution image of test pattern using a new imaging equipment [1]. The Siemens star pattern was used to confirm the spatial resolution. The smallest line width of 10 μm could be well recognized in the right image.

Table 1. Performance characteristics of the standard μNID and BμNID.

	μNID	BμNID
Area	10 cm x 10 cm	
Filling gas	CF_4:iC_4H_{10}:^{3}He (45:5:50), 2 atm	CF_4:iC_4H_{10} (90:10), 1.6 atm
Spatial resolution	0.1 mm	0.3 mm
Time resolution	0.25 μs	10 ns
Efficiency@25.3 meV	26%	5%
Effective count rate	1 Mcps	10 Mcps

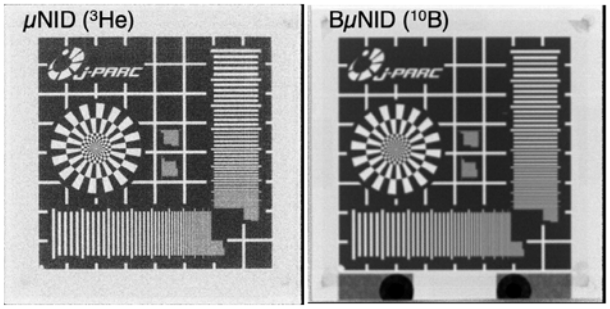

Figure 2. Comparison of image quality for μNID and BμNID. An image of a gadolinium test chart taken with the μNID (left) and BμNID (right) shows the good overall image quality of both detectors, while the BμNID displays a slightly reduced spatial resolution (0.3 mm) compared to the standard μNID (0.1 mm).

count rate. The performance characteristics of the μNID and BμNID are listed in Table 1.

Following a successful proof-of-principle study using a prototype detector [4], a dedicated BμNID detector was prepared, and its commissioning was completed in December 2020, with the first user experiments starting in January 2021.

4. Application of energy-selective imaging

A neutron imaging equipment consisting of a high-speed gated image intensifier unit and an sCMOS camera has been employed to the energy selective neutron imaging. With this equipment, it is possible to obtain an image of a given neutron energy because the image intensifier amplifies the light from the scintillator screen in a very short instant synchronizing the pulsed neutron's time-of-flight by its gate function. The gate timing can be easily controlled with an electric gate signal generated by using a delay generator. Hence, this system is suitable for experiments, which require a fine spatial resolution, a short exposure time and a coarse energy resolution. For example, the ice/water identification in a fuel cell for an automobile will be a good application of this imaging [5].

5. Summary and future plans

RADEN is used in various fields, not only scientific but also industrial, and the application spreads widely now. In addition to the user programs, the RADEN group continues to improve the instrument and develops imaging techniques, so as to provide state of the art neutron imaging environment to users and to perform application studies with it.

References

[1] T. Shinohoara et al., Rev. Sci. Instrum., **91**, 043302 (2020).
[2] K. Isegawa et al., J. Imaging, **7**, 232 (2021).
[3] J. D. Parker et al., Nucl. Inst. and Meth. Phys. Res. A, **726** 155 (2013).
[4] J. D. Parker et al., JPS Conf. Proc., **22**, 011022 (2018).
[5] Y. Higuchi et al., Phys. Chem. Chem. Phys., **23**, 1062 (2021).

T. Shinohara[1], T. Kai[1], K. Oikawa[1], Y. Tsuchikawa[1], K. Isegawa[1], K. Hiroi[1], Y. Su[2], H. Hayashida[3], J. D. Parker[3], Y. Matsumoto[3], and Y. Kiyanagi[4]

[1]Neutron Science Section, Materials and Life Science Division, J-PARC Center; [2]Technology Development Section, Materials and Life Science Division, J-PARC Center; [3]Neutron Science and Technology Center, CROSS; [4]Hokkaido University

Polarized Neutron Spectrometer POLANO

1. Introduction

POLANO is a direct geometry chopper spectrometer with middle energy and spatial resolution. For the purpose of highly efficient polarization experiments using the inelastic scattering technique, the POLANO was optimized for high transfer energy (HTE) polarization analysis [1–3]. The POLANO has been opened to a part of the user program since 2019 with only unpolarized neutron experiments. In order to realize the HTE polarization, we have made serious efforts to develop new devices with new ideas and concepts. The HTE polarization can be realized by combining a SEOP ^{3}He gas spin filter and a 5.5 Qc bending mirror analyzer, as described in the following section. However, even with this technique the utilized neutron energy is restricted up to around Ef = 45 meV for out-going analyzed neutron energy (final neutron energy) by the reflecting capability of mirrors. But our final goal for HTE is 100 meV beyond the reactor-based neutron polarization energy.

By 2019, some of the world's neutron facilities realized and planned time-of-flight (tof) polarization spectrometers, but all of them are focusing on polarization analysis with a low-energy region of the transfer energy up to several tens of meV. However, this energy range of polarization analysis had so far been done with reactor-based neutrons. In the research of the dynamical properties of atoms, spins, charges, orbitals, and so on, their energy scale could be over 100 meV. The POLANO was designed to realize polarization analysis with much higher energy by combining a SEOP ^{3}He spin filter and an analyzer mirror, as mentioned above. This enables us to reach higher transfer energy (Ef ~ 42 meV). As the second step, we plan to use a wide-angle SEOP/MEOP system as an analyzer. In this second step, we are targeting polarization analysis with neutron energy of up to 100 meV, covering absolutely wide momentum and energy region in the reciprocal space.

2. Polarization and other devices

1) Safety assessment:

To be approved for use in MLF, any newly installed device, especially when it is high-risk, must be assessed by a safety group or specific committee in J-PARC prior to use. The laser system used in the SEOP system is one of those devices. In addition to the laser, we also need to go through the facility safety assessment for a Helmholtz-coil system and comply with the general safety requirements for the system. All examinations for those safety issues were completed before the end of this year.

2) SEOP polarizer:

The SEOP system used as a polarizer in POLANO has been under development for a long time. We have been working consistently to realize a high-performance device for high-energy neutrons. The glass cell containing ^{3}He and other gases was originally made in-house using GE180 glass material and it reached 80% of ^{3}He spin polarization. Finally, the system has been installed on the beam line for practical use. Figure 1 shows the system on the POLANO beam line. A black box containing optical and laser devices addition to ^{3}He cell is the main component of the polarizer, as shown in Fig. 2. The

Figure 1. Newly installed setup of the SEOP system. The neutron beam goes directly through the black box (SEOP box), where the glass cell for the ^{3}He gas filter is positioned.

dimension of the SEOP box is about 60 cm square, which is a rather compact design. However, the beam line is significantly limited in space, as shown in Fig. 1. With less space on the beam line, it is especially hard to handle the beam line devices.

3) Magnetic system:

The spin polarization of the polarized neutron spins must be maintained all the way to the analyzer in order to know if the scattering processes are either in spin flip (SF) or non-spin flip (NSF). Also, the spin direction can be controlled to measure different spin direction scattering processes. The POLANO report last year introduced our new asymmetric Helmholtz magnet, which is able to apply magnetic field to any direction in the horizontal plane, and also a vertical field to the scattering plane. With this magnetic coil system, it is possible to control the quantization axis around the sample position.

4) Spin flipper:

In order to measure four spin states (uu, ud, du, dd) before and after the sample, the spin flipper is an indispensable device to flip the direction of neutron spins. The SEOP has a capability of spin flipping with NMR technique before the sample. We need another flipper after the sample. The flipper should be able to cover very wide scattering angle, almost 180˚, and a limited radial space. In the POLANO case, since there is a vacuum chamber in the flight path after the sample, the space for the flipper is quite limited. Currently, we are considering the use of Dabbs-foil (current sheet) type spin flipper. But still, many difficulties need to be overcome. We will continue to develop the device for future polarization analysis.

5) Data handling:

Once the set of scattering data is collected, some numerical treatments as data handling between the four spin configurations, background subtraction, data normalization, data correction and so on, are required. Also, the data visualization is crucial to deduce scientific results from the obtained data. New algorithm for analyzing the polarization data set should be prepared. In this year, we improved the data handling software HANA modifying the current version of HANA, designed for unpolarized data, to treat polarization data.

6) Analyzer:

As an analyzer of neutron spins, a neutron mirror is used in POLANO. A 5.5 Qc FeSi bending mirror can analyze the neutron energy up to about 42 meV, which can realize the highest energy polarization experiment ever. The problem is that the coverage of the installed mirror range is just 20˚ of the scattering angle. Several sets of scans (experiments) are necessary to see a wide Q and E area by scanning the analyzer mirror around the scattering angle. The 5.5 Qc mirror is currently the highest critical angle of neutron polarizing mirror that enables higher energy polarization. The cost, however, is also extremely high and the neutron energy is still not enough. The ^{3}He gas filter analyzer with a wide angle is now in the process of development for the future higher energy experiments.

3. Magnetic devices

We have several magnetic devices in order to keep the spin polarization, to control the spin direction, and to apply the magnetic field to the sample. One of these devices is what we call a fan-shaped magnet. The magnet has a very unique design, as shown in Fig. 3. The magnetic field is provided by a set of permanent magnets of NdFeB and it will be 60 Gauss at maximum

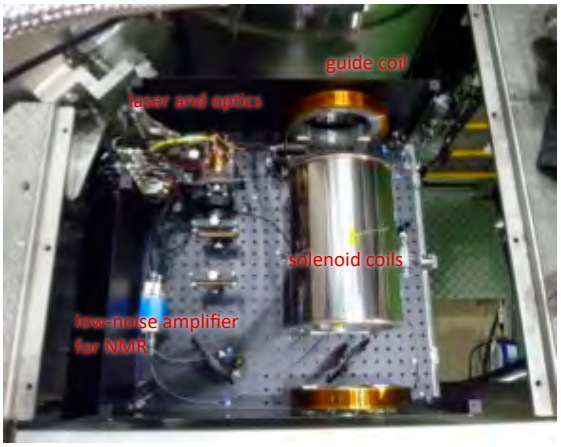

Figure 2. The suite of magnets, including the SEOP ^{3}He polarizer, Helmholtz coils, analyzer mirror, and guide fields.

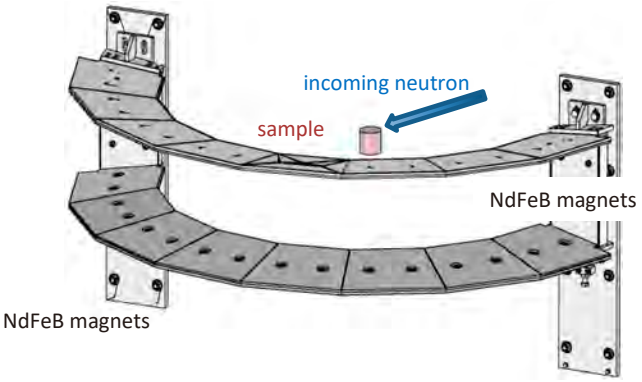

Figure 3. Newly designed fan-shaped magnet.

and 30 Gauss at minimum on the neutron path in wide scattering angle. In order not to obstruct the scattered neutron beam, the device is tapered to the beam direction. With this new concept, optimized for the wide-angle distribution measurement, homogeneous magnetic field can be applied.

4. In summary

Now the POLANO is almost ready to launch polarization experiments via an on-beam test at the MLF beamline BL23. In addition to beam commissioning, developments and updating devices and methods are indispensable to realize spherical polarimetry with the pulse neutron beam. In particular, we are working on the R&D of new devices, such as a spin flipper after the sample, high polarization ^{3}He filter, and large solid angle SEOP analyzer for the future HTE polarization.

References

[1] T. Yokoo, et al., EPJ Web of Conferences, **83** 03018 (2015).
[2] T. Yokoo, et al., AIP conference proceedings, **1969** 050001 (2018).
[3] MDPI Books, Quantum Beam Science 162 (2019).

T. Yokoo[1,2], N. Kaneko[1,2], S. Itoh[1,2], K. Hayashi[1], T. Ino[1,2], and M. Fujita[3]
[1]*Institute of Materials Structure Science, KEK;* [2]*Neutron Science Section, Materials and Life Science Division, J-PARC Center;* [3]*Institute for Materials Research, Tohoku University*

Sample Environment at MLF

1. Introduction

The MLF sample environment (SE) team provides the sample environment equipment commonly used among several beamlines and is also responsible for upgrading that equipment. The MLF SE team develops "cutting-edge" equipment that can function even under extreme sample conditions and also fulfills the growing users' needs. Our activities in JFY2020 are described below.

2. Cryogenics and magnets

We have supported users' experiments using the BL-common equipment. In JFY2020, the superconducting magnet was operated for 11 experiments, the ^{4}He cryostat for 8 experiments, the ^{3}He cryostat for 6 experiments, the dilution refrigerator insert for 3 experiments and the Gifford-McMahon (GM) cryofurnace for 1 experiment, including instrument proposals.

Recently, we purchased another ^{3}He cryostat as BL-common equipment. This is because the frequency of use is increasing and there is no alternative in case of failure. We are currently preparing a rotary stage and a control box for it. The new ^{3}He cryostat will be introduced to users' experiments in JFY2021.

3. High temperature and light irradiation

We have two furnaces as BL-common equipment: a niobium furnace and another furnace that is dedicated to small-angle neutron scattering (SANS) measurements. In JFY2020, the niobium furnace was used for two users' experiments on BL18. In addition, there was a request from BL21 to use the furnace. It was necessary to modify it to be able to use on BL21, because dimensions of the flange of the vacuum chamber are different from those of other BLs previously used. In this fiscal year, we finished this modification and are actually checking its installation on BL21. It will be used for users' experiment on BL21 in JFY2021. We also installed a remote monitoring system with IROHA2 to the furnace, as shown in Fig. 1. Until now, according to the regulations of the MLF, one user had to be near the furnace at all times to monitor the status whenever its heater was on. However, with this installation, we have received approval from the equipment safety team to operate the furnace under remote monitoring. This is expected to significantly reduce user's labor during their experiments.

Using the SANS furnace, we performed the light irradiation experiment at high temperatures up to 200°C on TAIKAN (BL15) as shown in Fig. 2 (Proposal No. 2020P0503). Ultraviolet light from a mercury lamp illuminated the sample in the furnace through the focusing lens system and the quartz glass window of the furnace on the incidence neutron side. Changes of the neutron scattering at the small-angle and middle-angle detector banks by the light illumination were successfully observed in the experiment.

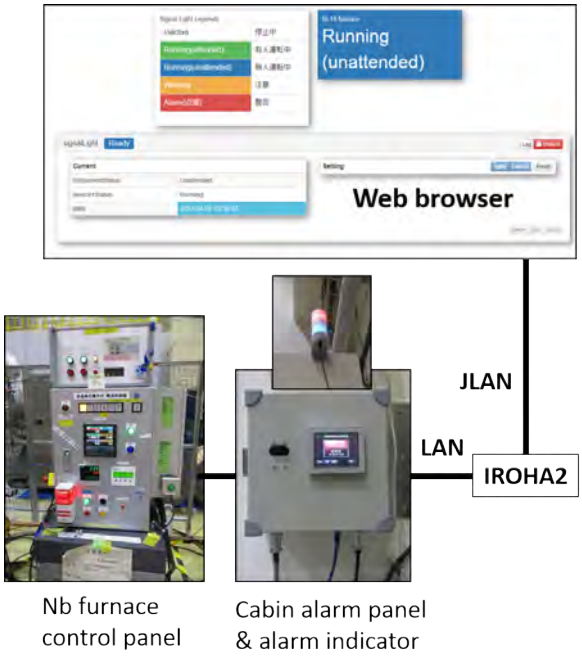

Figure 1. Remote monitoring system for the Nb furnace.

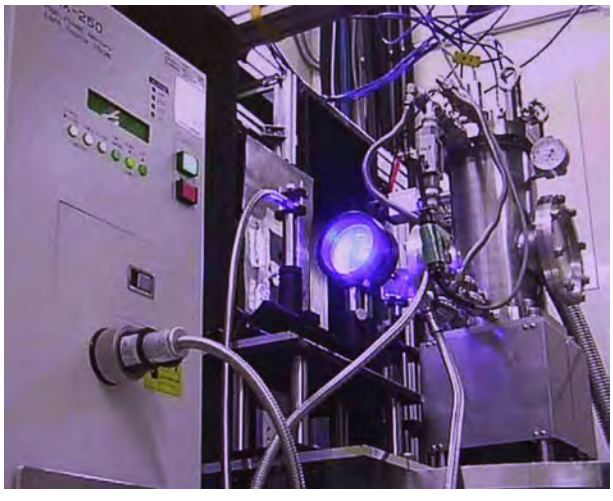

Figure 2. Light irradiation experiment at high temperatures on TAIKAN (BL15).

4. A pulsed magnet system

In JFY2020, neutron scattering experiments using a developed pulsed magnet system, which consists of a solenoid coil within the insert and a cryostat and a GM refrigerator to cool samples down to less than 4K, were performed at NOBORU (BL10). The samples we studied were $LiFePO_4$, which is generally employed as battery, and multiferroics $TbMnO_3$. Pulsed magnetic fields up to approximately 30 T were applied to the samples. A small solenoidal coil in the pulsed magnet system was immersed in liquid nitrogen to remove the heat generated by the magnetic field. So far, liquid nitrogen has been manually replenished every two hours during the experiment. A new device, automatic liquid nitrogen supply system, has been introduced this fiscal year. Figure 3 shows a photograph of the automatic liquid nitrogen supply system used in the BL10 for the neutron scattering experiments. As a result of using the new system, it was possible to reduce the time to supply it up to about 6 hours per day in maximum, compared to supplying it manually.

5. Humidity

The humidity experimental environment is being developed in cooperation with several beamline groups [1]. The two-way gas-flow method can generate up to 85% relative humidity within a temperature range of 5°C–85°C. To date, humidity experiments have been carried out in reflectivity, SANS, and quasi-elastic neutron scattering instruments.

In JFY2020, we started to develop a mixed humidity gas generator. The first goal is to develop an automatic system to generate mixed humidity gas of heavy and light water. This system will enable us to conduct automatic contrast variation humidity experiments.

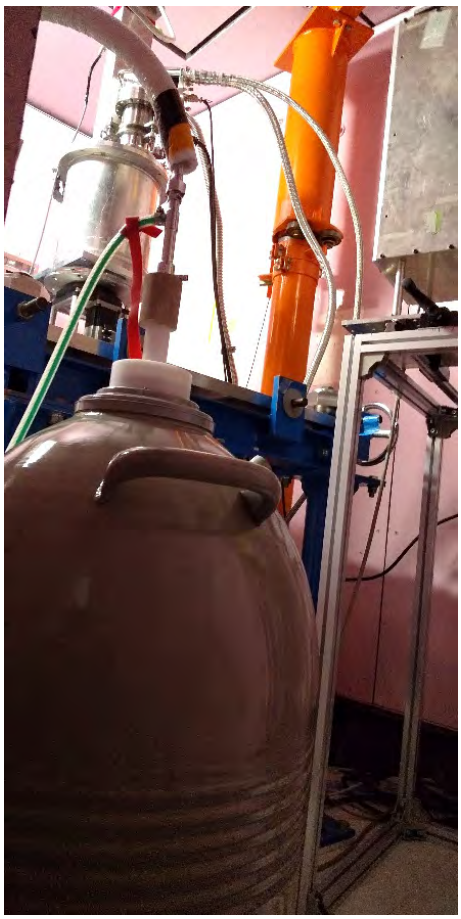

Figure 3. Automatic liquid nitrogen supply system.

Reference

[1] H. Arima-Osonoi, N. Miyata, T. Yoshida, S. Kasai, K. Ohuchi, S. Zhang, T. Miyazaki, H. Aoki, Rev. Sci. Instrum., **91**, 104103 (2020).

M. Watanabe[1], R. Takahashi[1], M. Ishikado[2], Y. Yamauchi[3], S. Ohira-Kawamura[1,4], M. Nakamura[3], H. Arima[2], S. Takata[1,4], Y. Su[1], S. Zhang[2], T. Morikawa[2], K. Ohuchi[2], Y. Sakaguchi[2], and T. Oku[1]

[1]Technology Development Section, Materials and Life Science Division, J-PARC Center; [2]Neutron Science and Technology Center, CROSS; [3]NAT Corporation; [4]Neutron Science Section, Materials and Life Science Division, J-PARC Center

A New Position-Sensitive Scintillation Neutron Detector for Obliquely Downward Scattering Bank in SENJU

1. Introduction

SENJU is a time-of-flight Laue single-crystal diffractometer installed in the BL18 of the J-PARC MLF [1]. This neutron instrument is equipped with 37 two-dimensional scintillation neutron detectors, and has been in service since 2012 [2]. One of the recent SENJU upgrades includes additional four new detector modules, which are placed in the obliquely downward scattering direction to increase the total angle coverage.

The purpose of this paper is to introduce our new detector module that has been developed to meet the required specifications for this specific bank. The thickness of the detector modules should be reduced to fit in the tight space constraint while maintaining the similar neutron-sensitive area and pixel size. Moreover, some detector components are developed and renewed to improve the count uniformity and detector efficiency. The detector specifications and experimental results of the prototype detector are presented.

2. A prototype detector

Figure 1 shows a photograph of the prototype detector module. The detector module is made based on ^{6}Li:ZnS scintillator and wavelength-shifting fiber technology, where each detector module maintains a neutron-sensitive area of 256 × 256 mm with a pixel size of 4 × 4 mm. To shorten the depth of the detector configuration of the optical fibers, multianode PMTs and electronic cards in the detector has been rearranged. The clear fibers are bent tightly with a smaller bending radius than the original one while keeping the light loss acceptably low. The depth of the detector has been successfully decreased to 170 mm, which is 60% of the original detector. Moreover, the scintillator screens, WLS fibers, and comparator electronics are also modified.

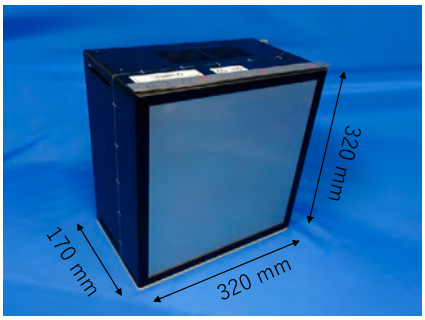

Figure 1. A photograph of the prototype detector.

To increase the light-collection yield, the scintillator screen and WLS fibers are selected; ^{6}Li:ZnS scintillator screen purchased from SINTACOR, UK and Y11 fiber from KURARAY, Japan. The thicknesses of the two scintillator screens are 0.25 and 0.45 mm for upstream and downstream of the WLS fibers arrays, respectively. New discriminator electronics cards are implemented to this detector [3]. The new discriminator circuit has a frequency bandwidth of ~500 MHz, which is 1.8-fold wider than the original one. These cards can pick up signals that are smaller in height and narrower in time than the original cards. Table 1 summarizes the detector specifications.

Table 1. Detector specifications.

Pixel size	: 4 × 4 mm
Neutron-sensitive area	: 256 × 256 mm
Physical size	: 320 × 320 × 170^{d} mm
Weight	: 16 kg
Detection efficiency	: 50 - 55% (@2 Å)
Gamma-ray sensitivity	: 1 × 10^{-5} (^{60}Co)
Count uniformity	: 3-5%
Pulse pair resolution	: 5 μs

3. Experimental results

The developed new discriminator cards help improve both high voltage characteristics and count uniformity. Figure 2 shows a comparison of the high voltage characteristics for the detector equipped with new or original discriminator cards. The count plateau has not been measured clearly in the original detector due to the insufficient frequency bandwidth of the original discriminator cards even when the multianode PMT voltage is applied at 96% of its maximum rating

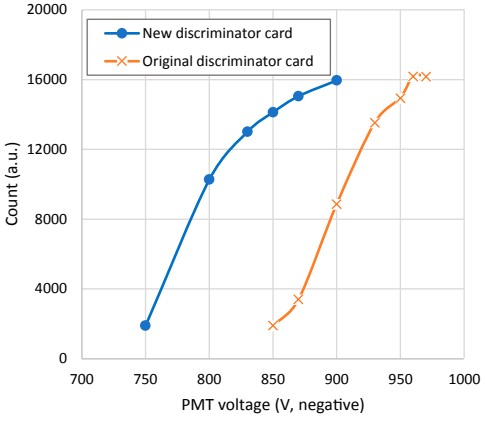

Figure 2. High voltage characteristics of the detector.

value. On the other hand, the detector with the new discriminator cards acknowledges neutrons at the applied voltage 100 V less compared with the original discriminator cards. These cards give an extra margin for adjustment to the PMT voltage. The count uniformities of the detector equipped with new or original discriminator cards are compared in Fig. 3. In both cases the detector components, except the discriminator cards, maintained the same in both detectors. The PMT voltages were set at -900 and -960 V for the new and original discriminator cards, respectively. With the new discriminator cards the count uniformity improved to 4.3% from 6.0%. This is attributed to the new discriminator cards picking up signals more efficiently than the original ones.

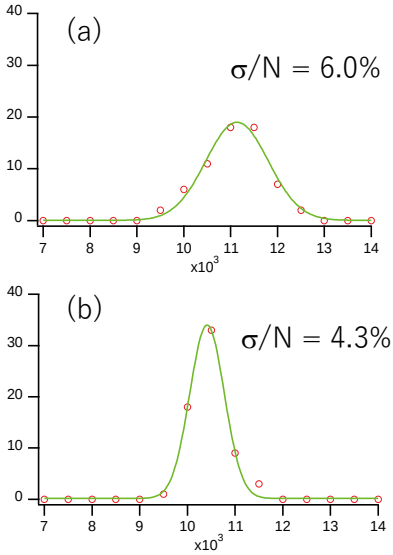

Figure 3. Count histogram distribution for the x-projection data (a) with original discriminator cards, and (b) with new discriminator cards. A whole detector area is irradiated with neutrons from a ^{252}Cf neutron source [4].

Figure 4 shows a typical detector count measured with (a) a flood neutron illumination and (b) projected count distributions for x and y directions. The detector exhibited similar count uniformity of 4-5% for x and y projections. The other three detector modules also exhibited count uniformities in between 3-5%. Regarding the detection efficiency all the four detector modules exceeded 1.0~1.2-fold compared with the original detector for neutron-wavelengths from 1 to 12 Å. The detection efficiencies become 50-55% for the 2-Å neutron.

The separate experiments revealed the ^{60}Co gamma-ray sensitivities are ~1×10^{-5} and background rate ~ 0.1 cps/hr, which are acceptable for use in the beam line.

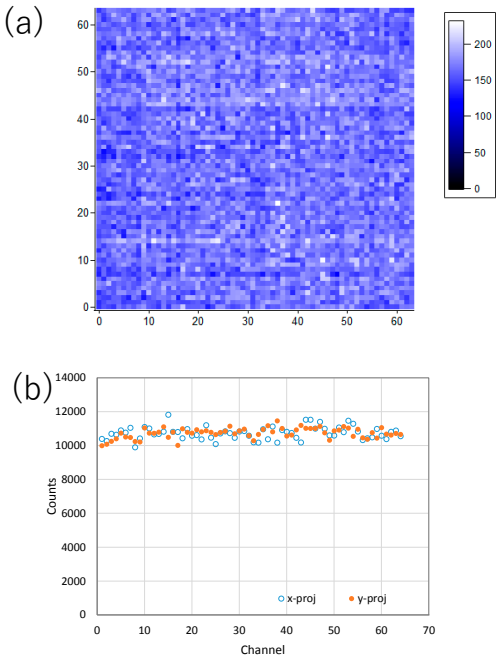

Figure 4. (a) Count distribution, and (b) projection of the x and y projection of the data of the det-4 (one of the produced detector modules) with a flood neutron irradiation [4].

4. Conclusions

The new two-dimensional scintillation detector was developed for the additional detector bank of the SENJU neutron instrument. The produced four detectors exhibited similar detector performances to each other with the improved count uniformities and detection efficiencies compared to the original detector. All these detectors have been implemented at the obliquely downward scattering bank in the SENJU.

References

[1] T. Ohhara, et al., J. Appl. Cryst., **49** 120 (2016).
[2] T. Kawasaki, et al., Nucl. Instrum. & Meth. A, **735** 444 (2014).
[3] T. Nakamura, et al., JPS Conf. Proc., **33** 011097 (2021).
[4] T. Nakamura, et al., Conference record, 2020 IEEE Nuclear Science and Medical Imaging Conference, N20-215.

T. Nakamura[1], K. Toh[1], R. Kiyanagi[2], T. Ohhara[2], and K. Sakasai[1]
[1]Neutron Instrumentation Section, Materials and Life Science Division, J-PARC Center; [2]Neutron Science Section, Materials and Life Science Division, J-PARC Center

Locally Adaptive Kernel Density Estimation on Quasi-Elastic Neutron Scattering Energy Profiles

1. Introduction

Shimazaki et al. reported a histogram bin-width optimization method [1] and a kernel band-width optimization method [2] on neuron firing time data approximated as Poisson point processes. Recently, the former was applied to inelastic neutron scattering (INS) data [3,4].

Quasi-elastic neutron scattering (QENS) data contain intense elastic scattering and their spectra generally have larger dynamic ranges than the region of interests in the INS, requiring to set the bin-widths or the band-widths locally in the data space. Usually, the researchers using QENS adopt histogramming to represent a QENS data set, setting the bin-widths according to conventional schemes. Because the bin-widths determine the residual constant background intensity and influence the final results of the curve fitting analyses, the bin-widths must be set accurately.

In [2], an adaptive kernel density estimation (KDE) was proposed, where the kernel band-widths were optimized locally in the data space. Moreover, the adaptive KDE on phantom data resulted in smaller deviations from the true probability density than the other methods including the histogram bin-width optimization. Therefore, the adaptive KDE seems promising for a QENS data representation.

In the present study, we tried the adaptive KDE on the QENS experimental data and analyzed a single linewidth from the estimated energy profile.

2. Method

We simply used the open-source library of the adaptive KDE [5]. The internal procedures are briefly described in this section.

In a kernel density estimation, underlying probability density λ is estimated based on the n observed data points $\{x_i\ (i = 1,..,n)\}$ as $\hat{\lambda} = \sum_{i=1}^{n} k(x - x_i)$ with k being a kernel, *e.g.*, a Gaussian of a standard deviation h, h regarded as the kernel bandwidth. $\{x_i\}$ is the set of the detected neutrons' energies. The method searches h minimizing the mean integrated square errors (MISE) between $\hat{\lambda}$ and λ [2]. Assuming the data points as a Poisson point process and the count in any part of the data space follows the Poisson distribution, MISE is separated into two terms, depending on λ and depending on the observed data set $\{x_i\}$, respectively. The latter is as follows:

$$\hat{C}(h) = \int \hat{\lambda}^2 - 2f\hat{\lambda} + \frac{k(x=0)\hat{\lambda}}{n} dx = \int \hat{c}(x,h)dx, \quad (1)$$

where $f = \sum_{i=1}^{n} \delta(x - x_i)$.

For h fixed over the whole data space, the optimal h is $\underset{h}{\operatorname{argmin}}\, \hat{C}(h)$.

For h optimized locally in the data space, we first consider h^* minimizing the local cost function.

$$h^*(W,x) = \underset{h}{\operatorname{argmin}} \int \rho(x - x', W)\hat{c}(x,h)dx' = \underset{h}{\operatorname{argmin}}\, \hat{c}^{local}(x,h), \quad (2)$$

where ρ is a window function with a width W, *e.g.*, a Gaussian function with a standard deviation W (Fig. 1b). We obtain one h^* for each of all possible configurations (W, x). In order to select one pair of h^* and W for each x, h^*/W is set as a constant value γ.

Since the data points are discrete, $h^*(x, \gamma)$ abruptly changes over x. Smooth band-widths h^γ are estimated by Nadaraya-Watson kernel regression,

$$h^\gamma(x) = \frac{\int h^*(x,\gamma)\rho(x-x', W(x',\gamma))dx'}{\int \rho(x-x', W(x',\gamma))dx'}. \quad (3)$$

Finally, by finding γ^* minimizing the cost function $\hat{C}[h^\gamma]$, the optimized band widths h^{γ^*} (Fig. 1c) and $\hat{\lambda}[h^{\gamma^*}]$ (Fig. 1d) are obtained.

3. Application of the method on QENS data

For the input data of the method, we obtained a histogram with a small bin-width of a QENS data set without the usual corrections in the data reduction processes, keeping the number of the detected neutrons in each of the bins. Because the method requires observed data points of energies as the input, we randomly generated energy points at each bin while keeping the count within the bin.

The locally adaptive KDE had the larger bin-widths at the low-count region (Fig. 1e). They resulted in a density curve being smoother in that region than the non-locally adaptive KDE (Fig. 1g).

We compared the results of a curve fitting on the usual histograms and the profiles by the locally adaptive KDE. We treated the QENS energy spectra collected from a sample at T = 50, 253, 303K. In the fitting, we regarded the spectrum at T = 50K as the device resolution function and fitted each of the other spectra by the convolution of a Lorentzian and a delta function with the device resolution function, and a constant background. HWHM of the Lorentzian corresponds to the inverse of the lifetime of the dynamical phenomenon invoked in the sample during the measurement. The HWHM values

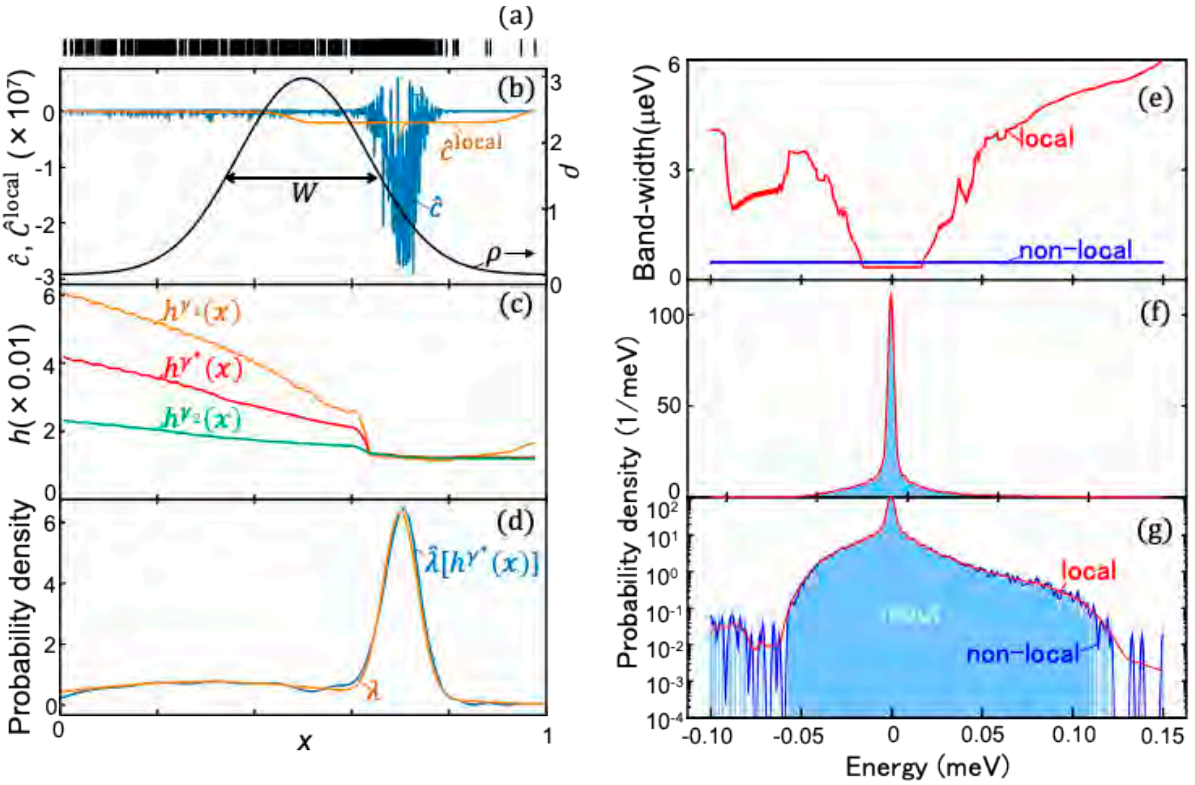

Figure 1. Schematic of the adaptive KDE with the band-widths locally optimized (a-d): an input data set of Poisson point process $\{x_i\ (i = 1, .., n)\}$ (a), integrand of global cost function $\hat{C}$, window function ρ, and local cost function $\hat{C}^{\text{local}}$ (b), smoothed band-widths h^{γ} with different flexible parameters γ (c), estimated density $\hat{\lambda}$ and true density λ generating the data (d). Trial application of the present method on a QENS data set (e-g): optimized band-widths (e), estimated density and input histogram in non-log (f) and log scales (g). Local and non-local are the results of the adaptive KDE with the band-widths locally and non-locally optimized, respectively.

were 12.4 ± 0.3 (303K) and 3.9 ± 0.08 (253K) in units of μeV for the histograms, while 12.3 ± 0.12 (303K) and 3.9 ± 0.03 (253K) for the adaptive KDE. The adaptive KDE showed lower uncertainties by factors than the usual histograms, probably because the adaptive KDE more accurately estimated λ.

4. Future plans

By extending the method to the 2D spectra on the momentum transfer and energy, and replacing the usual 2D histograms by the 2D adaptive KDE, more accurate time and space correlation functions might be obtained; the 2D adaptive KDE as the input data for the mode distribution analysis using a maximum entropy method [6] might be promising.

References

[1] H. Shimazaki et al., Neural Comput., **19** 1503 (2007).
[2] H. Shimazaki et al., J Comput. Neurosci. **29** 171 (2010).
[3] K. Muto et al., J. Phys. Soc. Jpn., **88** 044002 (2019).
[4] Manuscript in preparation
[5] https://github.com/cooperlab/AdaptiveKDE, http://github.com/shimazaki/density_estimation
[6] T. Kikuchi et al., Physica B, **567** 51 (2019).

K. Tatsumi[1], M. Matsuura[2], H. Shimazaki[3], and Y. Inamura[4]
[1]*Technology Development Section, Materials and Life Science Division, J-PARC Center;* [2]*Neutron Science and Technology Center, CROSS;* [3]*Center for Human Nature, Artificial Intelligence, and Neuroscience, Hokkaido University;* [4]*Neutron Science Section, Materials and Life Science Division, J-PARC Center*

Muon Science

MUSE Facility Overview

1.Development of real-time temperature monitoring system for the muon target

Real-time monitoring of the target temperature is extremely important to prevent the rotating target system from severe accidents. While thermocouples have been installed on the cooling jacket to measure the temperature rise due to thermal radiation from the rotating target, the slow response of thermocouples (typically in minutes) makes it difficult to detect a sudden temperature rise caused by some serious trouble, such as target rotation stop-page. For real-time temperature detection, we have been developing a monitoring system based on an infrared (IR) camera.

Figure 1(a) shows the temperature distribution of the rotating target during the 1 MW operation observed by the IR camera. The high-temperature part (shown in yellow) can be observed covering the area from the center of the target to the right (the direction of rotation). The measured temperature rise of the rotating target at the start of the beam operation is shown in Fig. 1(b), where it takes about one hour using thermocouples to reach the actual temperature inferred from the IR camera.

The real-time sensitivity of the IR camera is also demonstrated by the temperature fluctuations associated with the fluctuations of the irradiated beam shown in Fig. 1(b). The analysis regarding the relationship between the temperature change and thermal conductivity upon proton beam irradiation is in progress for the 1 MW operation.

2. Construction of the H-Line

The H-line is a new beamline under construction since FY2012 in Experimental Hall No.1 of the MLF building. Its layout drawing is shown in Fig. 2. It is a general-purpose beamline that can deliver both decay and surface muons and has branches to two experimental areas named H1 and H2. The designed surface muon flux reaches 108 muons/s with a proton beam power of 1 MW owing to a large acceptance (108 mSr) capture solenoid and other beamline magnets with large apertures.

In FY2020, construction of the main (upstream) part of the H-line and the first branch (to the H1 Area) progressed to secure the minimal components required to deliver muons to the H1 Area for beam commissioning. All vacuum devices were connected (see Fig. 2),

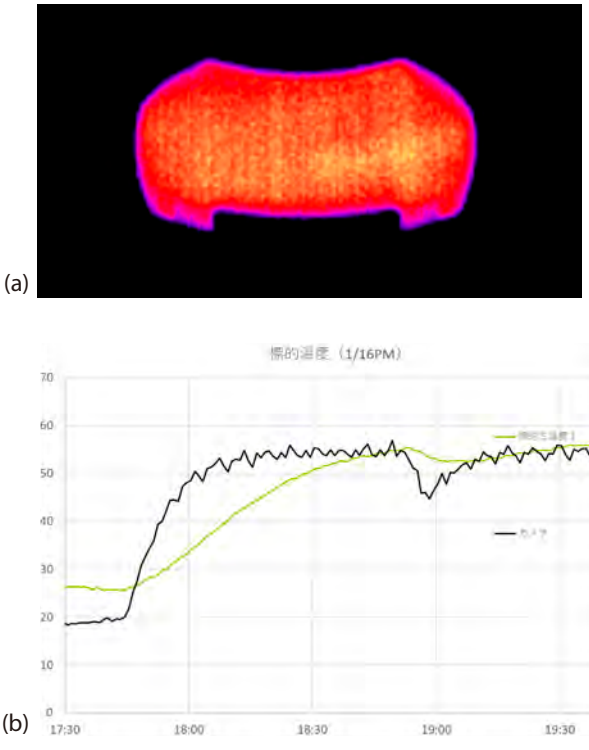

Figure 1. (a) An infrared (IR) camera image of the rotating target during 1 MW-beam operation. (b) Temperature of the rotating target rises upon the resumption of the beam operation. The temporary beam halt at around 18:50 is clearly identified by the target temperature monitored by the IR camera.

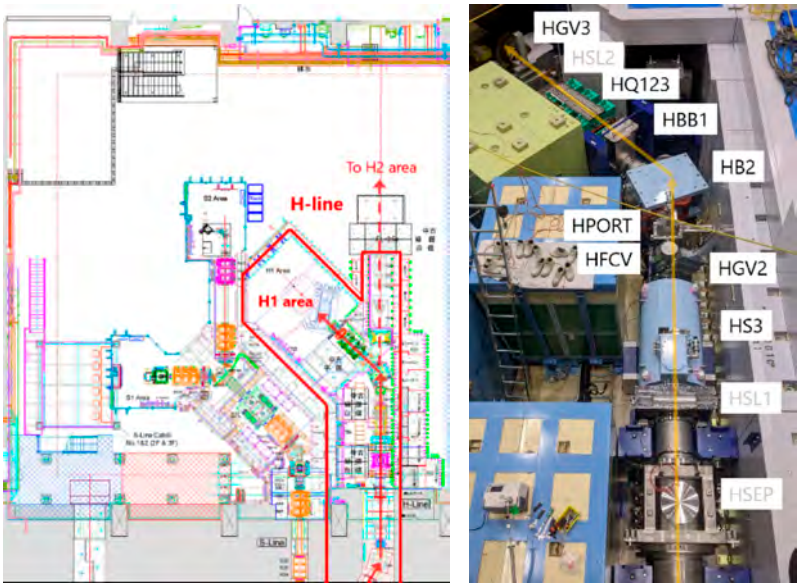

Figure 2. (a) A layout drawing of the H-line, and (b) a snapshot showing vacuum devices for the beamline to the first branch, which were connected during the summer shutdown in FY2020.

electrical cabling and cooling water piping for two bending magnets (HB1 and HB2) were conducted, and a safety interlock system was implemented to be incorporated into the whole MLF system. Although the capture solenoid (HS1), transportation solenoids (HS2 and HS3), focusing quadrupole triplets, and a DC-separator are not ready, the surface muon flux is expected to be 6×10^5 muons/s without these components. In the next summer shutdown, we plan to conduct the remaining works, such as electrical cabling and cooling water piping of all magnets and installation of a DC separator and beam slits, so that the design in-tensity of 10^8 muons/s will be achieved.

Progress was also made in preparing the second branch of the H-line (to the H2 Area). Since the muon g-2/EDM experiment proposed for the H2 Area requires a 50-meter LINAC to accelerate muons to 212 MeV, the construction of an extension building is planned on the east side of the MLF where the parking lot is located. In FY2020, the detailed design of the extension building was completed, and geotechnical investigation and buried cultural property research was conducted on the construction site.

3. Laser system for Ultra-slow muon

Ultra-slow muons can be generated by resonant optical ionization of thermal muonium from hot-W foil target. The light pulses of 122.09 nm (Lyman-α) and 355 nm are required for the 1s to 2p state excitation and 2p to ionization, respectively. The high power pulsed coherent Lyman-α light source is one of the key elements for the efficient generation of ultra-slow muons.

In FY2020, more than 10 μJ Lyman-α pulses have been stably generated from 212.556 nm and 820 nm light pulses using the two-photon-resonant four-wave-mixing method attained by nonlinear wavelength conversions of a 100 mJ 1062.78 nm pulse delivered from Nd:YGAG (1 at.% Nd doped Y3Ga2Al3O15) ceramic laser amplifiers. Although we are targeting 1J-level 1062.78 nm pulses to achieve the required Lyman-α out-put power, the problem of Ga inhomogeneity in Nd:YGAG has precluded for years to obtain the large-aperture laser medium (> 10 mm in diameter) for the amplifier required for this purpose.

To overcome this problem, we have been developing Nd:YSAG ceramic (Ga substituted with Sc), and a newly fabricated middle-size (φ9 mm, 112 mm long) Nd:YSAG ceramic was delivered for testing the amplification gain and wave-front distortion. While the amplification gain was satisfactory, the distortion of transmitted wavefront was revealed, which resulted in the reduction of the wavelength conversion efficiency in the sub-sequent stages due to the collapsed beam shape. In order to compensate for the distortion occurring inside the Nd:YSAG ceramic, we introduced an active 40-segment deformable mirror combined with the Shack-Hartmann wave-front sensor that was placed before and after amplifier, respectively. The measured wave-front distortion is shown in Fig. 3, where the distortion is removed after the compensation. The method obtained by these

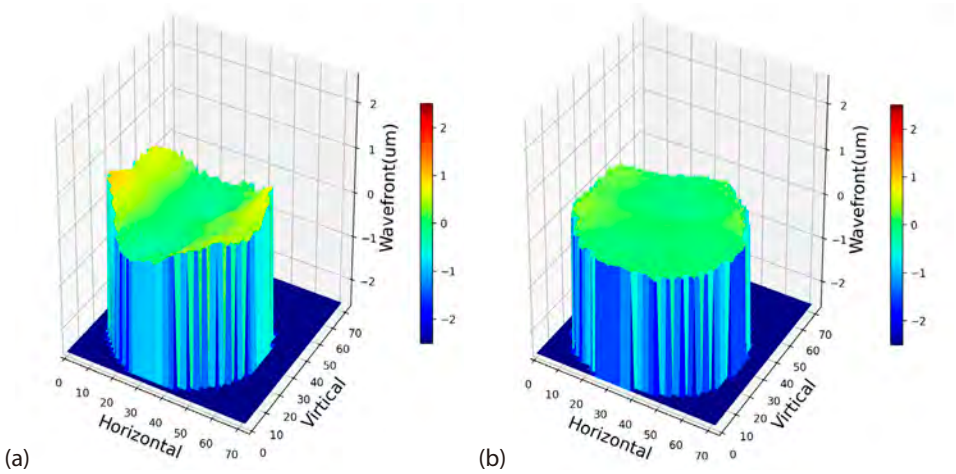

Figure 3. The wave-front distortion in Nd:YSAG ceramic for final amplifier before (a) and after (b) after the compensation by a deformable mirror system.

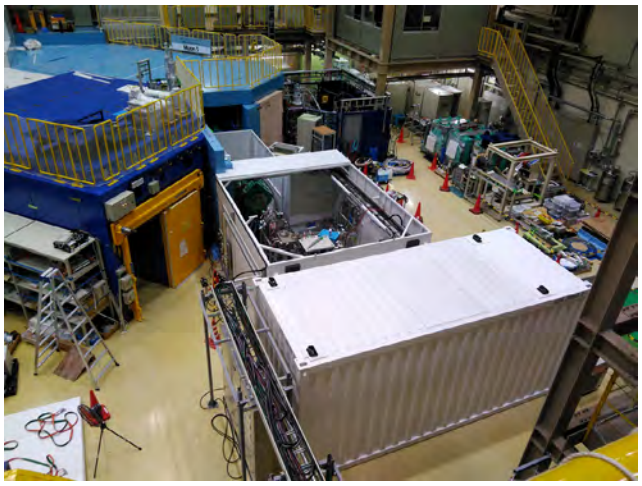

Figure 4. A snapshot of the S2 Area (with roofs temporally removed) and laser hut viewed from the downstream of the S-line.

studies will be applied to a practical laser system to implement the enhancement of Lyman-α optical intensity.

4. Construction of the S2 Area

The S2 Area is under construction for the precise measurement of the muonium 1s-2s transition energy by the resonant laser ionization (S1-type proposal by Okayama U. group, supported by Kakenhi). To allow for the laser experiment, the entire area is shaded by walls and removable roofs to ensure safety. The muon beam interlock system is almost the same as that for the S1 Area. A laser hut has been installed next to the S2 Area for the immediate access. The hut is made of a marine container, so that it can be easily moved by crane. The construction of the S2 Area was nearly completed in the summer shutdown of FY2020. The rest of the work will be completed after the approval from the Nuclear Regulatory Commission to deliver the first beam in the early FY2021.

R. Kadono[1,2], K. Shimomura[1,2], A. Koda[1,2], P. Strasser[1,2], T. Yamazaki[1,2], S. Kanda[1,2], S. Takeshita[1,2], Y. Ikedo[1,2], Y. Kobayashi[1,2], J. Nakamura[1,2], T. Yuasa[1,2], N. Kawamura[1,2], Y. Oishi[1,2], Y. Nagatani[1,2], S. Matoba[1,2], S. Nishimura[1,2], S. K. Dey[1,2], W. Higemoto[1,3], and T. U. Ito[2,3]

[1]Muon Science Section, Materials and Life Science Division, J-PARC Center; [2]Muon Science Laboratory, Institute of Material Structure Science, KEK; [3]Advanced Science Research Center, JAEA

Present Status of the Muon-Beam Source

1. Introduction

The muon production target and the front-end part of each muon beamline, as well as the primary beamline, are located in the M2 tunnel, as shown in Fig. 1. This area is crucial for the stable and safe operation of the whole MLF facility, which contains not only MUSE but also JSNS.

2. Muon production target

In FY2019, the rotating target was replaced with a new one due to trouble in the first rotating target. The second target has been operated without any essential troubles. So far, the new target has been working stably under the 500/600 kW proton-beam operation.

In addition to the conventional monitors like thermometers on the cooling jacket and the torque meter, an infra-red thermometer that monitors the target temperature more directly is under development. The details are reported separately [1]. The new monitor will be added to the target safety system to compose a layered system.

To secure a spare target in advance, fabrication of the third target starts in the next fiscal year under the multi-year plan.

3. Buffer tank system

Due to spallation reactions, lots of radioisotopes are generated in the target. The main residual activities in the target are tritium and ^{7}Be after a short cooling period. The tritium is generated by 0.5 TBq/year under the 1 MW operation according to a simulation. The radiation dose from the residual activities in the target is orders of magnitude lower than that in the surrounding metallic parts in the target assembly. In addition to this, tritium emits only low-energy β rays. Thus, the contribu-tion of the tritium to the external exposure is not serious, if it stays in the target. However, tritium can diffuse in the hot graphite and evaporate from the target surface. In general, tritium forms a volatile chemical state, easily spreads out and sticks to the surface of devices, and eventually increases the risk of internal exposure.

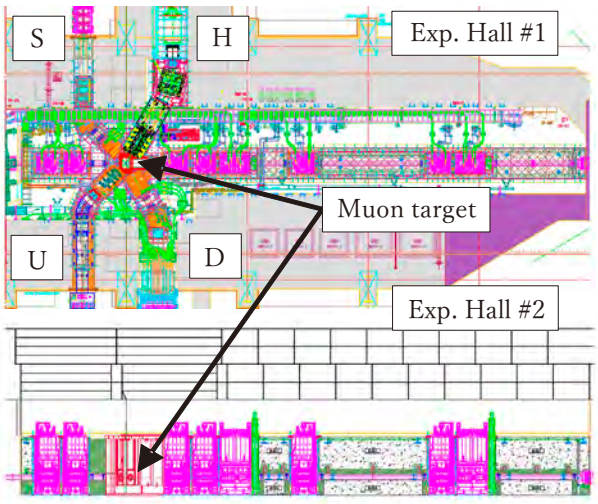

Figure 1. The horizontal (upper) and the vertical sectional view (lower) of the M2 tunnel. The proton beam is transported from the left side to the right side of the neutron target through the tunnel.

The buffer tank system [2] accumulated the operation data of the released tritium from the target. Since the second target's installation in the summer of 2019, the data of the fresh target was were obtained. Figure 2 shows the tritium release rate determined by the tritium contained in the vacuum exhaust gas. The emission rate is presumed to be proportional to the square root of the diffusion coefficient, $\sqrt{D}$, leading to the estimation that D is about 60 times greater at 1 MW (700˚C) than that at 600 kW (500˚C) . This seems consistent with the reported value of ~40 in similar isotropic graphite (IG-110 by TOYO TANSO Inc.) [3], although the absolute value of D seems different.

This kind of data accumulation is important for a safe and continuous operation. Toward a comprehensive understanding of tritium behavior, we are promoting collaboration with the experts in the Hydrogen Isotope Research Center (HRC), Toyama University. The elementary process is studied using the equipment in HRC. The results are fed back to the MUSE operation, not only to the regular operation, but also to the reconstruction of the scenario of storing the spent targets. The original scenario was considered at the early stage of the facility construction. Since then, the situation has changed: (1) early realization of the rotating target whose lifetime is expected to be around 10 years, (2) more serious contamination in the hot cell where the spent target will be cut into three pieces to reduce the volume, (3) potentially more serious effect of tritium in the target, and so forth. We will start to consider the new scenario taking all these issues into account.

4. The H line construction

The H line devices in the M2 tunnel were mainly installed in 2012 [4] and 2014 [5]. In this fiscal year, we

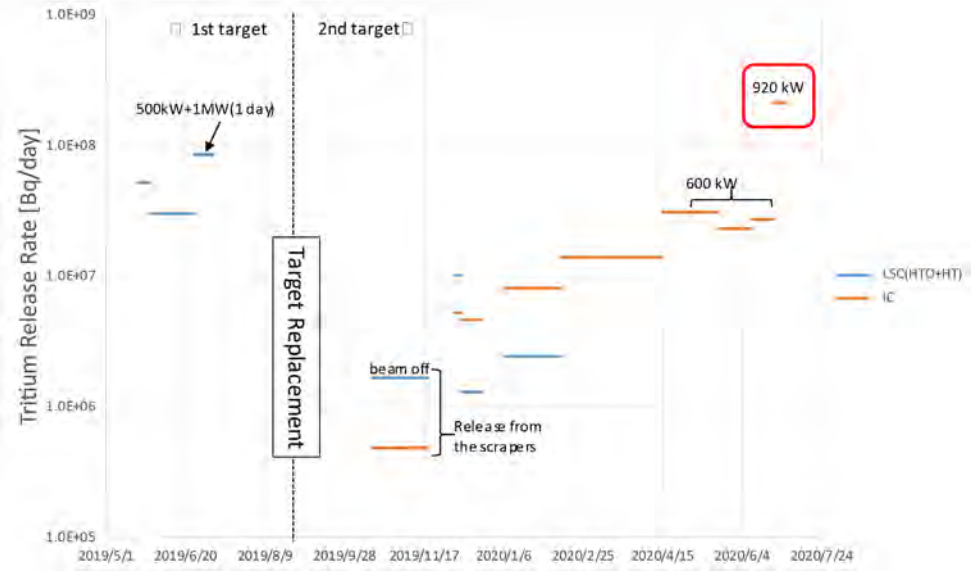

Figure 2. The released tritium from the target. The vacuum exhaust from the beamline around the muon target and its downstream is stored in the buffer tank during the beam operation and is exhausted on the maintenance day after the radiation survey with the liquid scintillator (blue lines) and the ionization chamber (orange lines). The tritium release rate was determined by the stored tritium in the buffer tank divided by the accumulation period, which corresponds to each line length. The amount of tritium was measured either by a liquid scintillator after pre-treatment of leachate in water (blue lines) or by an ionization chamber (orange lines).

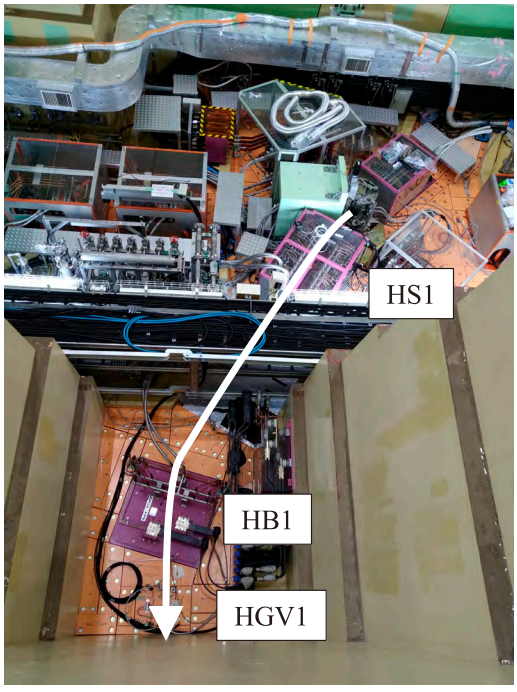

Figure 3. Top view of the H line taken on October 5, 2020.

performed the cabling and piping works connecting the line to the magnets and the vacuum components. Almost all the work on the H line in the M2 tunnel was completed in this fiscal year. Figure 3 shows a snapshot taken in the beginning of October, just before closing the radiation shield on the H line. Before releasing the first beam in the H line, the radiation application was submitted to the regulatory agency on October 5, 2020, and the permission was issued on June 15, 2021. Details of the present status in the H line are reported separately [6].

References

[1] S. Matoba et al., ibid.
[2] N. Kawamura et al., JPS Conf. Proc. **33** (2021) 011146, HTTPS:// doi.org/10.7566/JPSCP.33.011146.
[3] H. Atsumi et al., J. Vac. Soc. Jpn. **49** (2006) 49.
[4] N. Kawamura et al., KEK Prog. Rep. 2012.
[5] N. Kawamura et al., KEK Prog. Rep. 2014.
[6] T. Yamazaki et al., ibid.

S. Matoba[1,2] and N. Kawamura[1,2]
[1]Muon Science Section, Materials and Life Science Division, J-PARC Center; [2]Muon Science Laboratory, Institute of Material Structure Science, KEK

Development of Monitoring System for the Muon Rotating Target Using an Infrared Camera

It is important to measure the temperature of the muon-production rotating target (hereinafter referred to as "rotating target") in order to detect quickly problems in it.

Thermocouples have been installed on the cooling jacket to measure the temperature rise due to thermal radiation from the rotating target. Since the time constant of the thermocouples is in the order of minutes, it is not possible to stop the accelerator quickly in case of a significant temperature rise. In order to construct a rapid temperature detection system for rotating targets, we have installed an infrared camera (ULVVIPS-04171SL made by Vision-Sensing Co., Ltd.).

Figure 1 shows the temperature distribution of the rotating target during the 1 MW operation observed by the infrared camera. The high-temperature part (shown in yellow) can be observed flowing from the center of the target to the right, the direction of rotation.

Figure 2 shows the measured temperature rise of the rotating target at the start of the beam operation. The temperature rise is saturated in about one hour of using the thermocouples attached to the cooling jacket, while the temperature is constant in 30 minutes of using the infrared camera.

The infrared camera is also sensitive to the temperature change when the beam is temporarily stopped. As described above, rapid detection of temperature fluctuation by beam irradiation was achieved.

The beam power dependence of the temperature at the center of the rotating target is shown in Fig. 3, which is considered to be the beam spot temperature of the rotating target. As the beam power increases, the temperature of the rotating target also increases. We are analyzing the change of temperature and thermal conductivity by proton beam irradiation.

The infrared camera has been irradiated with cobalt-60 gamma rays and has been confirmed to be able to withstand up to 5 Gy of exposure. A glass dosimeter installed near the camera has been used to measure the radiation dose, which was estimated to be about 3 Gy at the end of March 2021. However, due to frequent errors in the electronic circuitry, which are presumably caused by the single event upset by neutrons, the camera operation time is low at about 30% of the available operation time. We are planning to develop a new infrared camera with measures such as shielding of the circuitry to increase the camera uptime.

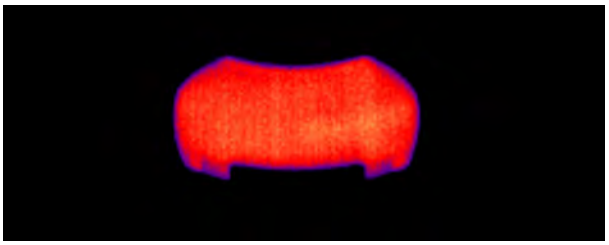

Figure 1. Infrared camera image of the rotating target during the 1 MW beam operation.

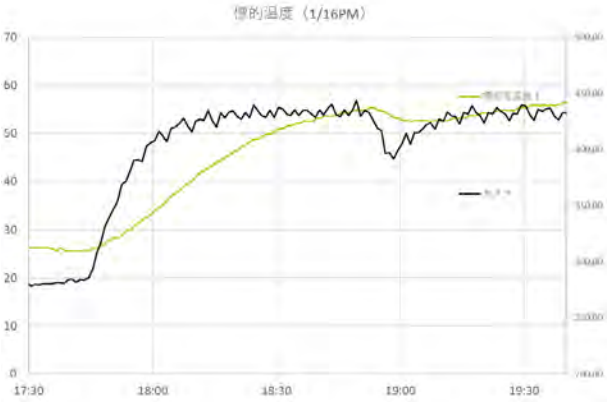

Figure 2. Temperature rise of the rotating target at the start of the beam operation. At around 18:50, the beam was temporarily stopped and the temperature of the target decreased.

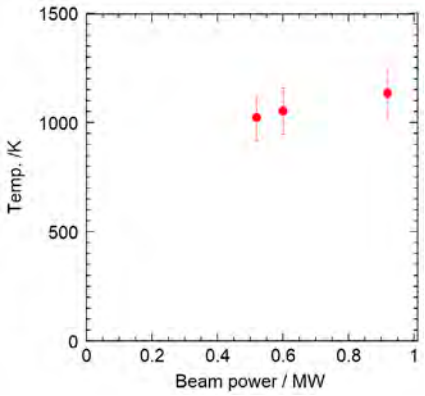

Figure 3. Beam power dependence of the temperature at the center of the rotating target.

S. Matoba[1,2] and N. Kawamura[1,2]

[1]*Muon Science Section, Materials and Life Science Division, J-PARC Center;* [2]*Muon Science Laboratory, Institute of Material Structure Science, KEK*

Muon Beamlines and Control System

1. Introduction

We report on the manufacturing of spare coils for a bending magnet in D-line and the installation of the personnel protection system (PPS) for the H1 experimental area.

The bending magnet DB2 is installed in the decay muon beamline (D-line) at the Materials and Life Science Facility (MLF) of J-PARC. The existing DB2 is a dipole magnet which has been manufactured over 40 years ago; therefore, we plan to exchange the degraded coils with new ones. The production and performance inspection of the new coils were carried out. The hollow conductor, which was produced last year, was used for the new coils as coil material [1].

The installation of the PPS equipment for the H1 area in the first experimental hall of MLF started in FY2020. The first experimental area constructed on the H-line is called H1 area. The PPS for the H1 area was installed, and status signals from the power supplies of the magnets, which bring muon beams to the H1 area, were connected to the PPS, and the existing PLC was update in the first experimental hall.

2. Manufacturing of spare coils

As shown in Fig. 1, DB2 bends muon beams by 40° and transports them to the downstream experimental areas. We calculated the field of DB2 with a 3-dimensional field analysis program OPERA-3d. The analysis model and actual DB2 are shown in Fig. 2.

In FY2020, we manufactured two spare coils with the same size as the existing coils so that they can be installed in the existing yoke and poles. The production drawing and the manufactured coils are shown in Figs. 3 and 4, respectively.

Table 1 shows the performance test results, and Fig. 5 shows a comparison between the measured and calculated central magnetic field values of the coil. The reason why the calculated and measured values do not match exactly is expected to be due to the presence of magnetic materials (reinforcing steel bars) under the floor at the measurement location.

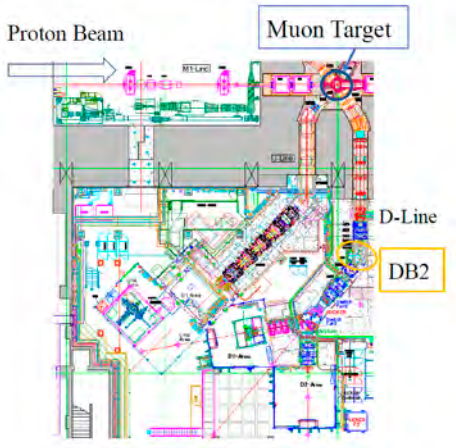

Figure 1. Decay muon beamline (D-line).

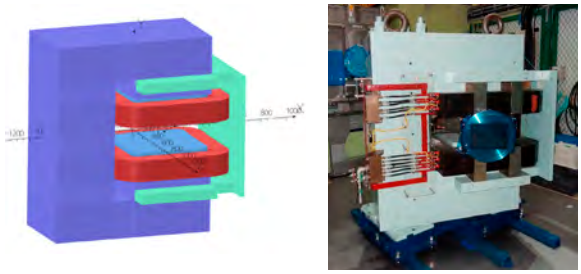

Figure 2. Analysis model (left) and existing DB2 (right).

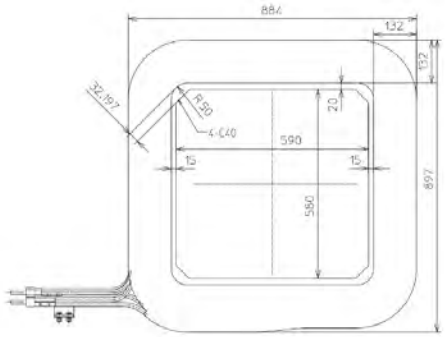

Figure 3. Drawing of the new coil.

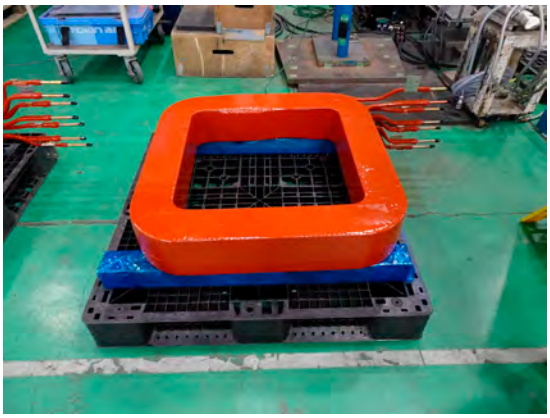

Figure 4. Manufactured coil.

3. Installation of PPS equipment for H1 area

3.1 PPS devices for H1 area

Similar to other muon experimental areas [2], the PPS for the H1 area comprises an emergency beam stop button (Panic Button), a search button, a muon blocker, a safety magnet and an entrance door to the experimental area, as shown in Fig. 6. The safety magnet for the H1 area is HB2 and the muon blocker is HBB1, as shown in Fig. 7.

3.2 Wiring of the PPS devices to H1 PPS

The PPS devices to display statuses and operate the PPS were wired to two control systems. One is the PPS panel located on the east side of the first experimental hall that is used to send the status signals from the PPS devices to the MLF control room, and the other is the PLC rack located on the west side of the hall. The PLC rack is equipped with three PLCs; magnet power supplies control panel, vacuum equipment control panel, and muon blocker drive panel, respectively. Regarding the magnet power supplies, it is necessary to be able to read all status signals of all the magnet power supplies. This fiscal year, the status signal of the safety magnet HB2 was added to the PPS, and the wiring for the magnet excitation permission signals was connected. The wiring system for each device is shown in Fig. 8.

3.3 Software modification

With the construction of the H1 area, it was also necessary to modify the software to properly display the new H1 area in the existing control panels. Figure 9 shows one of the screen of the control panel related to the H1 area.

Table 1. Result of the inspection test.

	measurement	calculation
Coil Resistance [mΩ] (at 20℃)	52.25	58.2
Inductance [mH] (at 120 kHz)	14.44	14.86
Inductance [mH] (at 1 MHz)	13.06	
Water pressure drop [MPa]	0.32	0.33
Water flow [ℓ/min] (at 0.5 MPa)	17.5	17.4
output current [A]	500	500
output voltage [V]	25.97	29
Temperature rise in cooling water Δt [℃]	7.9	12.0

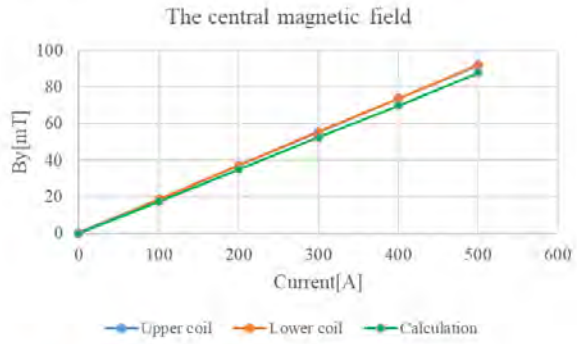

Figure 5. Comparison between measurement and calculation of the central magnetic field.

Figure 6. PPS devices at the H1 area: entrance door (left), panic button (top right) and search button (bottom right).

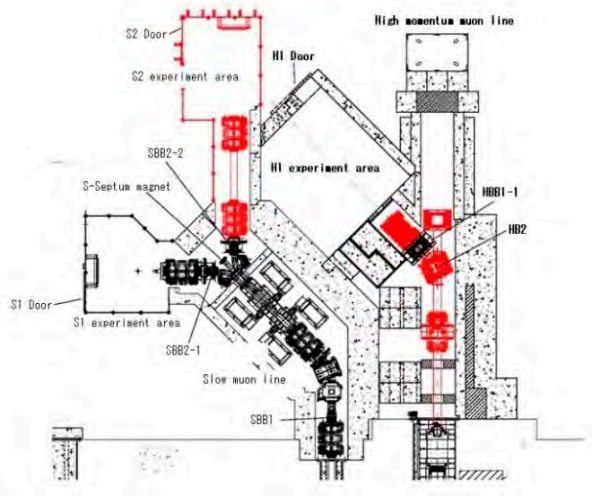

Figure 7. The H1 area in the first experimental hall of the MLF.

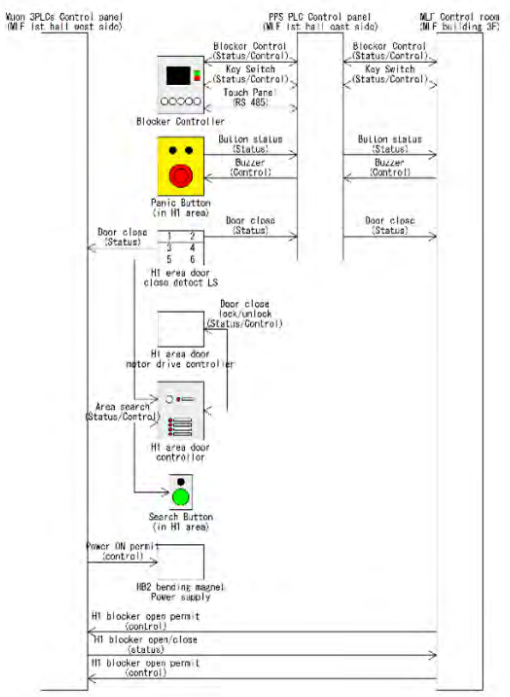

Figure 8. PPS wiring system diagram.

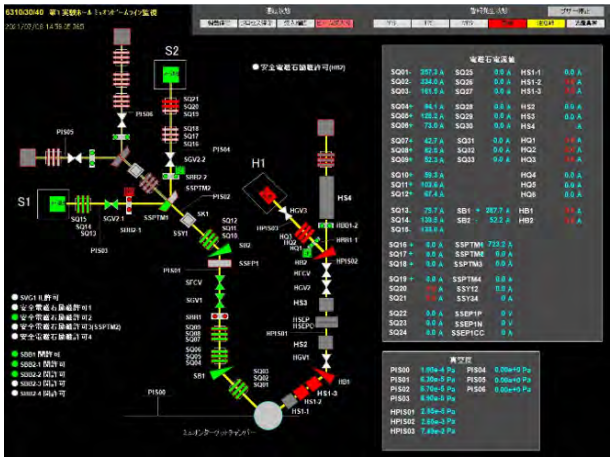

Figure 9. Screen of the magnet power supplies control panel for S-line & H-line.

4. Summary

We completed the manufacturing of the spare coils for DB2, and measured the magnetic field in FY2020. As a result, it was confirmed that the calculated and measured magnetic field values were almost identical. We plan to replace the existing coils with the newly manufactured coils in the summer of 2021. This project is currently in progress.

The installation of the PPS equipment for the H1 area was completed, and we updated the PPS wiring accordingly in the first experimental hall in FY2020. We are now ready to start experiments.

References

[1] H. Fujimori and T. Yuasa et al., Muon Beamlines and Target Control System, KEK-MSL REPORT 2019, KEK Progress Report 2020-4 (October 2020), pp. 13-15.

[2] K. Sakai, et al., Progress of General Control System for Materials and Life Science Experimental Facility at J-PARC JAEA-Technology 2018-011.

T. Yuasa[1,2], Y. Kobayashi[1,2], H. Fujimori[1,2], N. Kawamura[1,2], Y. Ikedo[1,2], T. Yamazaki[1,2], A. Koda[1,2], K. Sakai[3], A. Watanaebe[4], S. Sakata[4], M. Meguro[4], and K. Kawabata[4]

[1]*Muon Science Section, Materials and Life Science Division, J-PARC Center;* [2]*Muon Science Laboratory, Institute of Material Structure Science, KEK;* [3]*Japan Atomic Energy Agency, JAEA;* [4]*NAT Corporation*

Current Status of the μSR Experiment at D1

1. Introduction

At the D-line, muons are delivered to D1 and/or D2. At the D1-area, the μSR spectrometer is installed as a main and fixed instrument. Since high momentum muon, surface muon, and negatively charged muon are available at D1, all types of μSR measurements, except for the ultra-slow μSR, can be carried out. In particular, unique sample environments, such as very low temperature by using the dilution refrigerator, high pressure *etc.* were possible to carry out only at D1. Figure 1 shows the μSR spectrometer with the dilution refrigerator and the fly-past chamber. Here, we report the recent zero magnetic field condition of D1.

2. Zero-field condition at D1

Normally, a very weak magnetic field exists at the experimental hall. The main source of the magnetic field is the terrestrial magnetism with a magnitude of 0.2–0.3 G. In addition, normal and superconducting magnets are used to obtain muon beams, adding extra magnetic fields to the sample position. For a μSR experiment, a zero magnetic field condition at the sample position is one of the important experimental prerequisites to obtain information about the precise state of a sample. In particular, a superconductors are quite sensitive to an external magnetic field (by Meissner effect or formation of flux line lattice) and the reduction of a residual field is crucial to understand the essential properties of materials.

At D1, the magnetic fields at the sample position are estimated by using four triple-axis flux-gate magnetic probes, which are located near the center of the D1 spectrometer. To obtain a zero magnetic field condition, feedback currents are applied to three pairs of the correction coils. This feedback system was installed to the Iroha system, and a zero field can be obtained dynamically when we are measuring μSR data.

However, we found out recently that sometimes the zero-field feedback system is not working well and a finite residual magnetic field exists at the sample position. Unfortunately, this problem was discovered in 2020A and it was not possible to confirm the zero-field condition for some zero field μSR data. Currently, to check a magnetic field condition, we put another 3-axis magnetic probe close to the sample position.

We also checked the magnetic field distribution under the zero magnetic field condition. Figure 2 shows the position dependence of the residual magnetic fields. When the zero-field feedback system is working correctly, the residual magnetic field at the center of the D1 spectrometer is less than 0.02 G for all directions. This magnitude is small enough for the usual sensitivity of our measurements.

For μSR, a magnetic field condition is very important, and we need further development to monitor the magnetic status of the experiment.

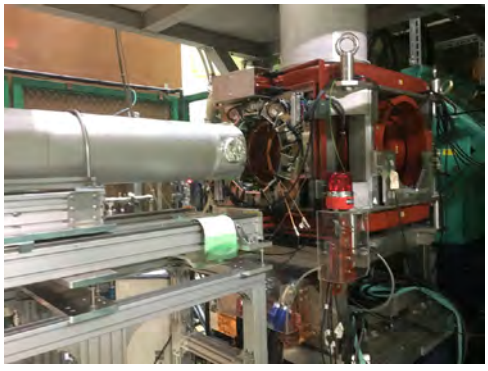

Figure 1. μSR spectrometer with the dilution refrigerator and the fly-past chamber at D1.

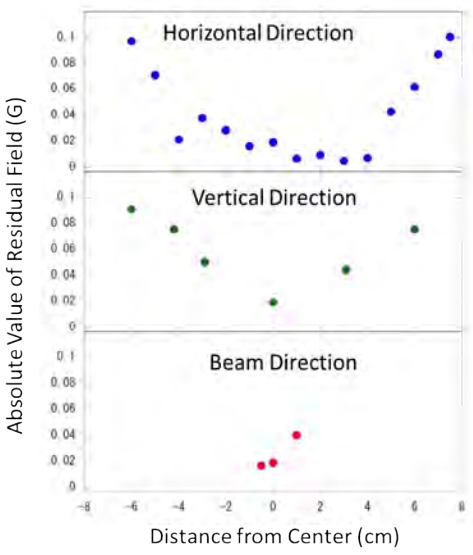

Figure 2. Position dependence of the residual magnetic field for each direction. For these measurements, no sample is mounted to the D1 spectrometer.

W. Higemoto[1,2,3] and A. Koda[2,4]

[1]Advanced Science Research Center, Japan Atomic Energy Agency; [2]Muon Section, Materials and Life Science Facility Division, J-PARC Center; [3]Department of Physics, Tokyo Institute of Technology; [4]Muon Science Laboratory, Institute of Materials Structure Science, High Energy Accelerator Research Organization (KEK)

Development of Sample Environment at the S1 Area

1. Introduction

SR experiments often use helium (He) as cryogen, which is collected in the recovery line after use. However, helium gas is a precious resource, and it is known that there is a global supply problem, so it is important to prepare a cryogen-free cryostat for the future sustainability of cryogenic experiments. In order to settle this issue, we have commissioned a new cryogen-free cryostat based on a commercially available model: the DRY ICE 1.5 K Beamline LEMON system (Dry Lemon), supplied by ICEoxford Ltd. [1]. It is a Gifford-McMahon (GM) cooled cryogen-free variable temperature cryostat. Figure 1 shows a snapshot of this cryostat.

The cryostat can be operated at a lowest temperature of ~1.5 K and a highest temperature of 500 K, whereas the lowest temperature achieved by existing cryogen-using top-load cryostats is 2 K [2]. The cryostat consists of a sample chamber with a variable temperature insert (VTI), a He circulation line, and a GM cryocooler operated by a dedicated compressor (Fig. 2).

Before reporting the specific work, we will de-scribe the regular cooling procedure. The GM refrigerator is operated in an outer vacuum chamber (OVC), and the circulation of He is started to cool VTI. In one day, GM stage 2 (GM2) temperature reaches approximately 4.2 K, which is slightly above the temperature at which He becomes liquid. After that, by adjusting the needle valve until the pressure gauge on the circulation line shows approximately 8 mbar, liquid He can be stored in a reservoir and VTI can be cooled at the same time. He gas is introduced into the sample chamber to provide heat exchange between VTI and the sample. The temperature of VTI is controlled by using PID heater parameters, and this process is not perfectly optimized yet. For high temperature operation (above room temperature), the sample chamber is kept in vacuum, and the sample rod for high temperature is also equipped with a heater near the sample.

Other features of this cryostat are the relatively large beam window size and the top-loading system. The former is for relatively low background of the μSR spectra, and the latter is for sample mounting without increasing the temperature up to room temperature. There are three beam windows in front of the sample. These window sizes are, from the outside, φ 55 mm: the OVC window (A), φ 50 mm: the 50K shield window (B), and φ 40 mm: the sample chamber window (C). As previously reported in the case of the 3He cryostat [3], all windows are φ 35 mm in size, and the cryostat is not designed for the top-loading sample rods but is using a dedicated sample holder, which is in contrast to the case of Dry Lemon.

With this top-loading cryostat, various sample rods can be used. Currently, in addition to one fixed sample rod for low temperature and one for high temperature, a rod for sample rotation was prepared for low

Figure 1. Snapshot of the new cryogen-free variable temperature cryostat placed at the test bench.

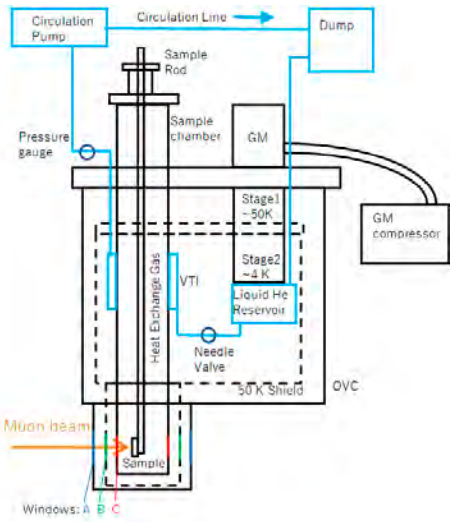

Figure 2. Schematic diagram of the cryostat with a blue line showing the He circulation line, where GM, VTI and OVC respectively denote the Gifford-McMahon refrigerator, the variable temperature insert and the outer vacuum chamber.

temperature. Figure 3 shows a schematic diagram and a snapshot of the rotating rod, on which the sample can be mounted on a φ 30mm aluminum disk, which can be rotated by a stepping motor in the radial direction.

We are currently commissioning this cryostat for user experiments and are dealing with the following problems. A typical problem in this cryostat is the vacuum leakage in two areas. One is a leak from the window, and the other is a leak from the He circulation line.

The most common leak at room temperature, the leak from the window, happens as follows. In the cryostat, there are two pairs of vacuum windows: A and C, shown in Fig. 2. The windows are aluminized polyimide films. The following procedure is used to leak-check before operation. First, all closed systems, i.e., He circulation line, sample chamber, and OVC, are evacuated. Then, while connecting the helium leak detector to OVC, He gas is introduced into the sample chamber using a gas bag. This is used to check for leaks from the sample chamber to OVC. Figure 4 shows schematic diagram of the trend of the leak detector. The red line is the case where there is a leak through the window C, and within 1–2 minutes, there is a sharp increase in the rate of e.g., 10^{-3} Pa m^3 s^{-1} for a typical pinhole. The black line shows the trend when there is no leak, and the rate increases slowly to approximately 10^{-6} Pa m^3 s^{-1}. This is because the He gas can gradually penetrate the window at room temperature. The leak rate increases both with and without leaks, but the quantitative difference makes it possible to distinguish the presence of a leak. When a 5 L gas bag is introduced, the pressure in the sample chamber increases to approximately 70 mbar at room temperature, but if there is a leak, the pressure decreases noticeably within a few minutes: e.g., to 30 mbar in 10 min for a typical pinhole.

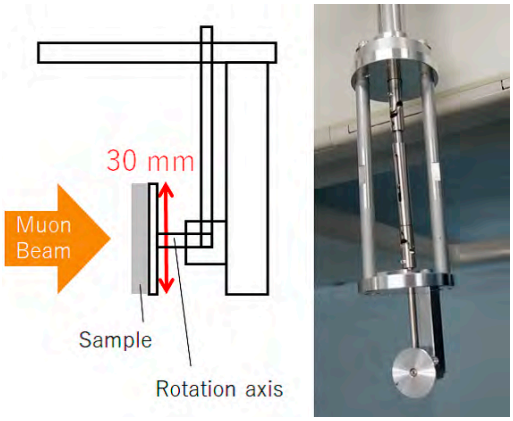

Figure 3. Schematic diagram (left) and snapshot (right) of the rotating sample rod for the top-loading cryostat.

Before circulating He, the leak detector connection is changed to the He circulation line and He gas is sprayed on the line from the outside to check for leaks. The leak-checking can be performed, because the background rate of the line is approximately 10^{-6} Pa m^3 s^{-1}, after the circulation line has been sufficiently evacuated. After connecting the leak detector to OVC again, the He circulation is started and we can check for leaks from the circulation line to OVC at room temperature. Then, He gas is sprayed on OVC from the outside to check for leaks. When leak-checking window A, the trend of the leak rate is similar to that shown in Fig. 4. In this outer window A, it is easier to identify the leak position compared to the inner window C, because the He sprayed position can be controlled. If there are leaks in these windows, it is necessary to repair them with epoxy glue: in window A, the glue can be applied from the outside, but in the window C, it is necessary to disassemble the cryostat (Fig. 5).

The next problem is a leak at low temperature, called a cold leak. If the leak is observed near the nitrogen liquefied temperature (~ 77 K), it is most likely due to thermal contraction. For example, if the leak is found after the VTI has reached at the low temperatures, it is likely to be a cold leak from the indium seal on a sample chamber flange.

As the cooling progresses and the VTI temperature decreases near the lowest level, another cold leak may be observed. Liquid He under saturated vapor pressure transitions to a superfluid state below 2.2 K. As a result, He has no viscosity and passes through a pinhole that viscous fluids cannot pass through, a phenomenon known as a super leak. Figure 6 shows an example of the temperature trend when the super leak was observed.

The initial temperature increases up to 7 K, as seen

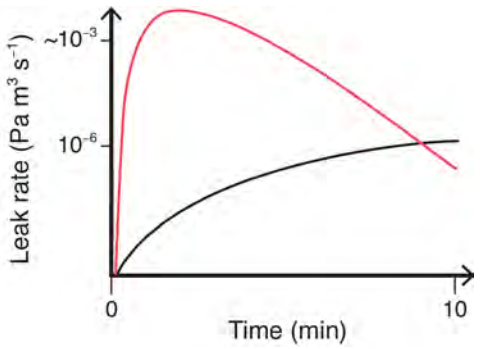

Figure 4. Schematic of the leak rate trends. The black line represents the case of gradual He gas penetration through a leakless window. The red line represents the case where there is a leak through the window.

in Fig. 6, was due to He gas leaked into OVC by the super leak, which acted as the heat exchange gas to increase the temperature of VTI. The heat shot also increased the temperature at the leak point above the superfluid transition temperature, and the leak was immediately stopped. The temperature increase of VTI stimulated release of He gas adsorbed on the vessel wall, which led to a further temperature increase (the second peak). Since evacuating was continued during this period, it is seen that the temperature increase of VTI was slowing down from around 20 K. Besides this, decreasing of the flow rate through the needle valve due to the temperature increase of VTI also reduced the heat load at GM2, suggested by the fact that the temperature of GM2 was slightly decreasing, as shown in Fig. 6. As a result, liquid He that started to accumulate in the He reservoir gradually cooled the needle valve, and when the liquid He began to flow through the needle valve (at the VTI temperature of 25 K), rapid cooling reoccurred.

In the case of the cold leak, as described above, the cryostat needs to be disassembled and the following procedure is used for maintenance. An indium sealed flange, used for the circulation line (lower right part of Fig. 5), should be replaced first during maintenance. At that time, for increasing the circulation line pressure to atmospheric pressure, He gas is introduced into the line to prevent air from contaminating the line and blocking it during cooling. In addition, stainless steel tubes with an outer diameter of 2–3 mm are used for the part of the circulation line in OVC (upper right part of Fig. 5). If there is an oxidized solder part (shown in Fig. 5), it is necessary to replace it using solder and flux for stainless steel. The old solder should be removed with sandpaper before soldering, and it is important to remove any remaining flux as it may cause oxidation.

Because the impedance (conductance) of the He circulation line is always important, it is necessary to confirm that the impedance has not changed before and after the maintenance as follows. First, a gas bag filled with He is connected to the circulation line on the GM refrigerator side (right side of Fig. 2), the needle valve is closed, and then the circulation line on the sample chamber side is evacuated with a vacuum pump. After the vacuum pump has been stopped, the needle valve is fully opened and the pressure rise in the circulation line is observed to roughly check the impedance. For example, a pressure rise of 300 mbar/10 sec can be checked before and after the maintenance.

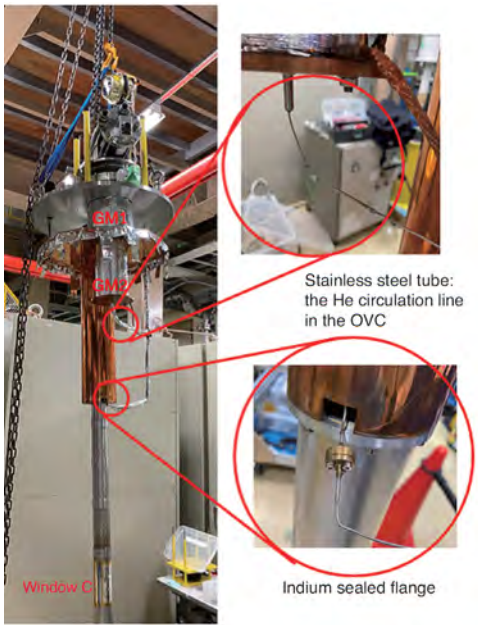

Figure 5. Snapshot of disassembling the cryostat. The sample chamber tail is shown by removing the 50 K shield.

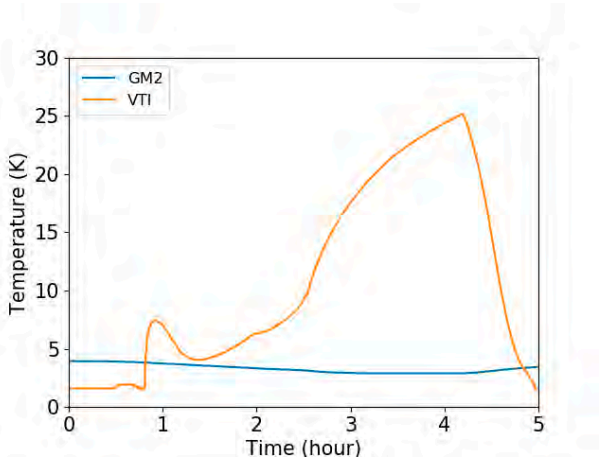

Figure 6. Temperature trend of VTI and GM 2nd stage (GM2) with the cold leak from a circulation line.

References

[1] https://www.iceoxford.com/

[2] https://mslnfo.jp/en/s1/se.html

[3] J.G. Nakamura et. al., KEK Progress Report 2019-3 KEK-MSL REPORT 2018 (2019) 23.

J. G. Nakamura[1,2], A. Koda[1,2], M. Hiraishi[1], S. Doiuchi[1], S. Nishimura[1,2], H. Okabe[1], A. Hashimoto[1], H. Li[1], and R. Kadono[1,2]

[1]Muon Science Section, Materials and Life Science Division, J-PARC Center; [2]Muon Science Laboratory, Institute of Material Structure Science, KEK

S2 Area Construction - Recent Progress

1. Introduction

To realize the precise measurement of the Mu 1s–2s transition frequency [1] (KAKENHI 19H05606), the construction of the S2 area has been started. The S2 area is an experimental area of the surface muon beamline (S-line) in experimental hall No.1 of the Materials and Life science experimental Facility (MLF) building. The S-line is designed to have four experimental areas; one area (S1 area) is already constructed and in operation [2, 3].

2. Overview of S2 area

The S2 area is located at the opposite side of the S-line from the S1 area. A top view of the S2 area is shown in Fig. 1. The kicker (SK12) can split a double-pulsed muon beam to two single-pulsed muon beams for both areas. A septum magnet (SSPTM2) leads muons to the S2 branch and two triplets (SQ16-18 and SQ19-21) guide them to the S2 area.

The Mu 1s–2s experiment uses lasers at the S2 area. So, the area is completely surrounded by walls and roofs, as shown in Fig. 2. The roofs are removable for installing experimental setups. LED lights (5000 lm, 6 units) and ventilation fans (900 m3/h, 2 units) are installed on the walls. A manifold of cooling water (50 l/min, 2 ports) and a power distribution board (100 V, 15 A, 4 ports) exist in the area. The beam interlock system is almost the same as the one at the S1 area. The door of the S2 area is hand-operated.

To provide lasers, a laser hut is located next to the S2 area. The laser hut is a custom-made 20-ft container, so that it can be easily craned and moved as necessary. The laser hut has no floor and the laser table or other instruments in the laser hut will be directly placed on the floor of the experimental hall. Figure 3 shows the laser hut hoisted with a crane. The laser hut has LED lights (2500 lm, 4 units), precision air-conditioner (Cooling power 7000 W), and double doors for light shielding.

3. Construction

The construction of the S2 areanwas almost finished in the summer shutdown of 2020. Figure 4 shows the experimental hall No.1 before and after the construction. The remaining construction works will be done after theepermit frof the Nuclear Regulation Authority. The first beam of the S2 area is expected early in fiscal year 2021.

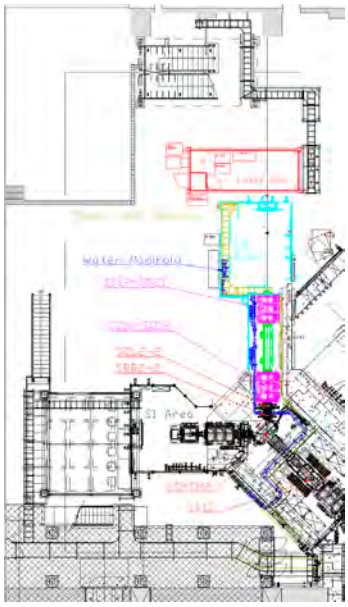

Figure 1. A top view of the S2 area. Beamline components toward the S2 area are a kicker (SK12), a septum magnet (SSPTM2), a beam blocker (SBB2-2), a set of slits (SSL2-2), and two triplets (SQ16-18 and SQ19-21).

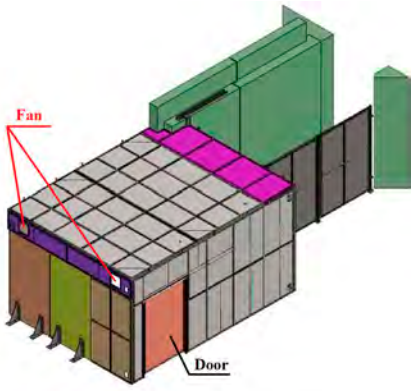

Figure 2. An aspect of the S2 area.

Figure 3. The laser hut hoisted with a crane. Large instruments like a laser table can be installed by moving the hut to another place.

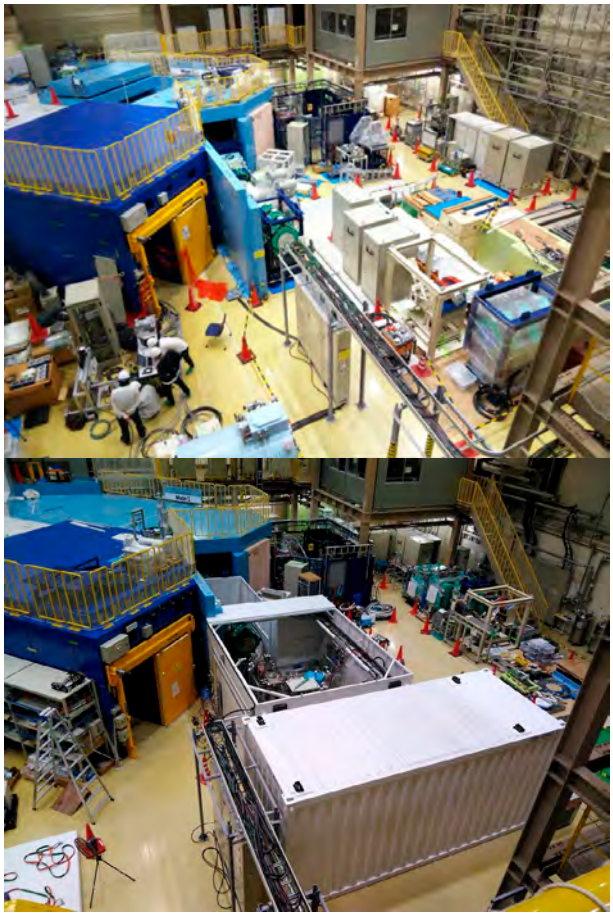

Figure 4. Experimental hall No.1 before (upper) and after (lower) the construction. The roofs of the S2 area are temporary removed.

References

[1] Ce Zhang et al., JPS Conf. Proc. **33** (2021) 011125.
[2] A. Koda et al., KEK-MSL REPORT **2013** (2014) 12-13.
[3] P. Strasser et al., KEK-MSL REPORT **2016** (2017) 17-18.

T. Adachi[1,2], N. Kawamura[1,2], A. Koda[1,2], T. Masuda[3], K. Shimomura[1,2], P. Strasser[1,2], S. Uetake[3], and T. Yamazaki[1,2]
[1]Muon Science Section, Materials and Life Science Division, J-PARC Center; [2]Muon Science Laboratory, Institute of Material Structure Science, KEK; [3]Division of Quantum Universe, Research Institute for Interdisciplinary Science, Okayama University

Commissioning of the μSR Spectrometer at U1A

1. Introduction

At J-PARC MLF, MUSE provides the world's highest flux of pulsed muon beams. U-Line, one of the four beamlines in the facility, features an intense surface muon beam from Super-Omega [1] and Ultra Slow Muon (USM) by laser ionization of thermal muonium. The beamline has two branches: U1A for μSR studies using USM and U1B for the transmission muon microscope.

The surface muon beam irradiates a resistively heated tungsten film to obtain thermal muonium atoms in a vacuum. Two laser beams resonantly ionize the muonium atoms with wavelengths of 355 nm and 122 nm. The ionized muonium has a thermal velocity corresponding to the target temperature of 2000 K, which results in a seven-digit cooling from 4 MeV to 0.2 eV. An electrostatic extractor and immersion lens focuses the ionized muonium and accelerates it to 30 keV. The extracted muons are transported to the experimental areas through a magnetic bend for mass separation, electric bends for energy selection, and electric quadrupoles for focusing. Micro channel plate (MCP) detectors are placed at focal points along the transport optics to measure the flux and profile of USM. In the U1A area, a muon spin spectrometer is placed on a high-voltage stage to control injection energy from zero to 30 keV.

2. The U1A μSR spectrometer

The muon spin spectrometer at U1A consists of a longitudinal field coil and a positron detector segmented into 16 modules, 512 channels. The coils can generate a magnetic field of up to 0.4 T along the beam axis. The USM spins are rotated 90 degrees at the magnetic bend during transport, so the longitudinal field at the spectrometer is orthogonal to the average muon spin vector. The detector consists of plastic scintillator blocks, silicon photomultipliers (SiPM), and dedicated front-end electronics. A sample is placed inside the main chamber surrounded by the coils, and a helium flow cryostat controls the temperature. A load lock chamber next to the main chamber allows sample exchange while maintaining a high vacuum.

3. Project status and tasks

Following the successful USM generation in 2016 [2] and the demonstration of USM-μSR at U1A in 2018 [3], preparations for the start of user experiments are steadily underway. In 2019, implantation depth control by the high-voltage stage was successfully demonstrated [4]. To proceed from the demonstration to the practical stage, several issues need to be addressed. The key issues are improving beam flux and quality, optimizing the spectrometer's performance, and preparing the sample environment.

For the USM flux, pulse energy improvement and spectral linewidth optimization are being studied. We are also working on a step-by-step study to quantify the generation rate of muonium and the extraction efficiency of the USM with sufficient precision. The typical USM flux is about 2×10^2 Hz after the first electric bend with the Lyman-α light's pulse energy of 5 μJ.

Concerning the beam quality, the beam profile, energy, and time-of-flight spread are the performance to be considered. A simulation study has been done to optimize the parameters of the transport optics, and a computational solution has been found [5]. Experimental validation is also being understood qualitatively, and further systematic comparison of measurements and calculations will be performed.

For the spectrometer, the signal-processing electronics have been upgraded to improve its performance. The operating parameters of the electronics and the SiPMs needed to be optimized, so they were determined in laboratory tests and commissioning with the beam. Positrons from the upstream of the beamline were observed at the spectrometer and reduced the μSR asymmetry. As a countermeasure for the positron background, additional lead shields were installed in front of the spectrometer. These details are described in the next section.

As of the sample environment, the electric noise from the power supply of the longitudinal field coils has been disturbing the deceleration potential of the high-voltage stage. The frequency of the noise was 50 Hz, and the amplitude was 28 V peak-to-peak. This noise level limits the implantation-depth resolution of the USM, so a countermeasure is required.

4. Progress in this fiscal year

In FY2020, the muon beam was delivered from Run84 to Run86 operation cycles. There was a period in April and May when the beam was stopped due to the spread of COVID-19. After the resumption of the accelerator operation, we continued to prepare the commissioning to start user programs while making efforts to prevent the spread of infection. In this section, we report on the three main results obtained during this fiscal year.

4.1. Tests of upgraded front-end electronics for the positron detector

The spectrometers of MUSE use the dedicated front-end electronics for the positron detector. A series of ASICs called VOLUME perform analog signal processing. This year, the U1A spectrometer has been upgraded from VOLUME2012 (V2012) to a new version named VOLUME2014 (V2014).

V2014 has a pole-zero-cancelation circuit in the amplifier, which provides an undershoot-free output with appropriate parameters. As a part of the commissioning, the biases given to the amplifier were determined by observing the output waveform. In addition, the comparator threshold was determined from the relationship between the threshold and the SiPM's dark count rate. The operating voltages of SiPMs were optimized from the pulse height distribution depending on the bias voltage.

The detection efficiency of the detector for decay positrons was almost 100%, the timing resolution was 2.5 ns in the standard deviation, and no significant pileup was observed.

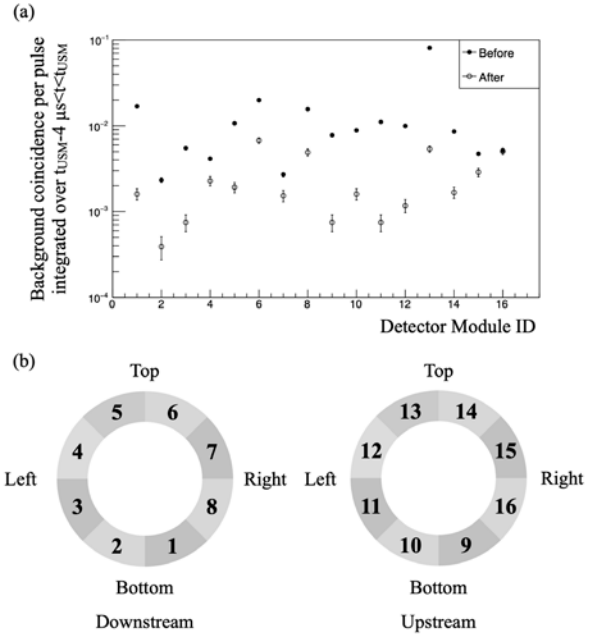

Figure 1. Background positrons at the spectrometer: (a) comparison of the background rate before and after the installation of shielding; (b) geometrical arrangement of the detector module. Directions are from the beam perspective.

4.2. Suppression of decay positron background by adding the lead shield

The muonium production target is made thick enough to stop half of the beam to maximize the muonium emission rate. Muons not stopping at the target are the origin of background events at the spectrometer. Since these background muons are spread by Coulomb multiple scattering, shielding the upstream side of the spectrometer is an effective countermeasure.

A lead shield with a thickness of 5 cm was installed to cover the detectors. The shield reduced the background rate, as shown in Fig.1. The integrated rate of background events was suppressed to about 1/5.

4.3. Improvement in the injection energy resolution by modifying the power supply wiring

Electrical noise at the high-voltage stage causes uncertainty in the USM implantation depth. We modified the power supply wiring to the longitudinal field coils. The noise level was reduced to 4 V peak-to-peak, i.e., improved by a factor of seven. This level of uncertainty is small compared to the energy spread due to the position dependence of the accelerating electric field for the USM extraction.

5. Summary and outlook

The commissioning in FY2020 completed the preparation of the U1A spectrometer for use in materials science using USM. To start user programs, the beam intensity needs to be improved, which will require optimization of the extraction and transport optics. We will attempt to increase the number of USMs and to evaluate the number precisely in parallel.

References

[1] The total beam flux is 6.4×107μ+/s at 212 kW. Y. Miyake et al., JPS Conf. Proc. 21, 011054 (2018).
[2] T. Adachi, A. D. Pant, and Y. Ikedo, KEK Prog. Rep. 2017-4 (2017) 12.
[3] T. Adachi, A. D. Pant, and Y. Ikedo, KEK Prog. Rep. 2018-2 (2018) 13.
[4] T. Adachi and Y. Ikedo, KEK Prog. Rep. 2019-3 (2019) 17.
[5] A. D. Pant et al., Nucl. Instrum. Methods Phys. Res. A 929 (2019) 129-133.

S. Kanda[1,2], T. Adachi[1,2], Y. Ikedo[1,2], Y. Oishi[1,2], H. Li[1,2], T. Yuasa[1,2], and H. Fujimori[1,2]
[1]*Muon Science Section, Materials and Life Science Division, J-PARC Center;* [2]*Muon Science Laboratory, Institute of Material Structure Science, KEK*

Construction of Transmission Muon Microscope at U1B

1. Introduction

At the U1B area, a 5 MeV transmission muon microscope is being constructed. It will visualize thick objects (>10 μm) in nanometer resolution. Quantum coherence of the ultraslow muon beam, and deep-penetration power of the muon beam accelerated over 5 MeV provide it with the necessary capabilities. In this fiscal year, we have constructed a 5 MeV AVF-type muon-cyclotron (see Fig. 1) using flat-top RF acceleration.

2. 3D magnetic field measurement and shimming of the cyclotron magnet

The cyclotron should have quite small energy dispersion ($\Delta E/E \sim 10^{-5}$) to reduce the chromatic aberration of the microscope. The magnet of the cyclotron should give us the precisely designed magnetic field, and the discrepancy should be reduced to the order of 10^{-5}. We have developed a 3D measurement system of the magnetic field, which uses a search coil (see Fig. 2). We iteratively tuned the magnet by iron-shims of 184-pieces with 0.1 mm precision after the field measurements. Finally, the expected energy dispersion simulated based on the final field-measurement became $\Delta E/E \sim 6 \times 10^{-5}$.

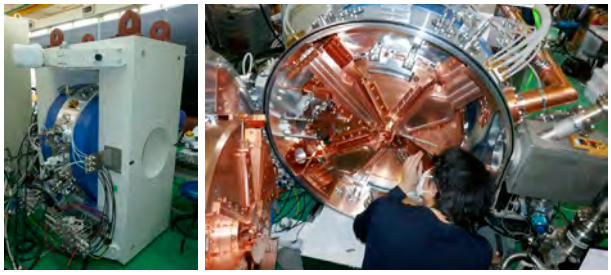

Figure 1. Muon-cyclotron (left) and its inside.

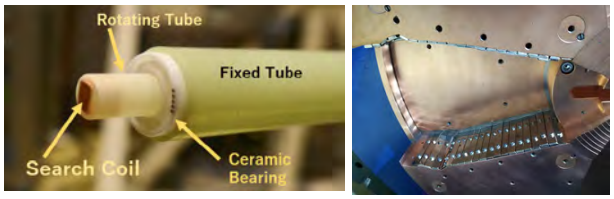

Figure 2. Search Coil (left) and iron-shims.

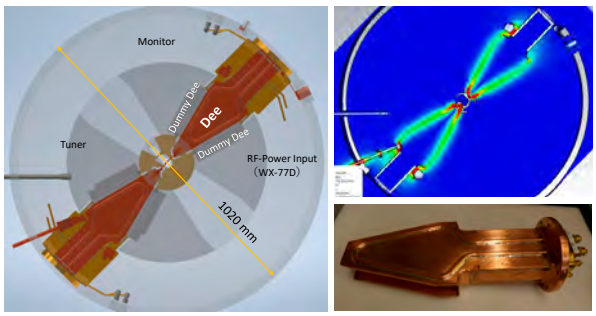

Figure 3. Design of the main Dees (left), RF fields by simulation (right-up) and the constructed body of the main Dee (right-down).

3. RF Cavities of the cyclotron

Two main RF-cavities of 108 MHz (main Dee) and a flat-top RF-cavity of 324 MHz (flat top Dee) for muon-cyclotron are being designed and constructed (see Fig. 3).

4. RF Power Amplifier

The cyclotron requires CW 108 MHz RF of 12–20 kW to accelerate the muon beam to 5 MeV energy. It also requires CW 324 MHz RF less than 1 kW for flat-top acceleration. The controlling system of the RFs is described in Fig. 4. The main RF is generated by combining 16 RF-amplifiers of 1.5 kW (Fig. 5 right-up) by using a 16-way RF-combiner (Fig. 5 center).

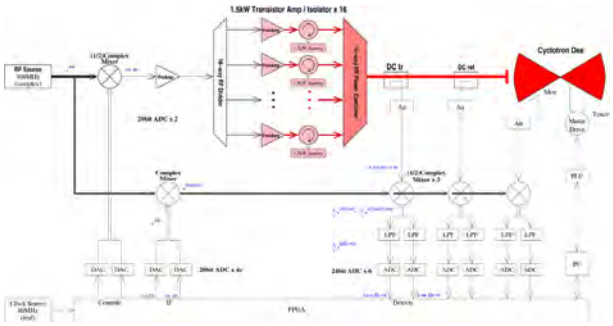

Figure 4. Block Diagram of the RF System.

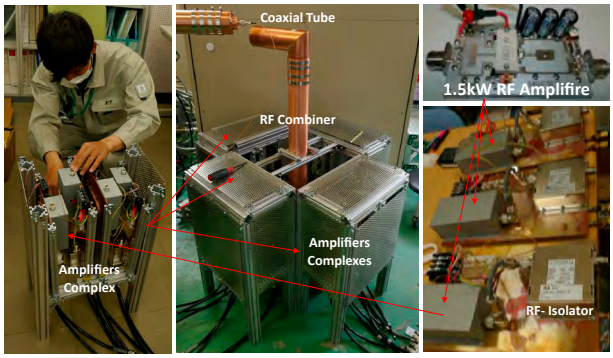

Figure 5. 108 MHz, 20 kW RF Amplifier System.

Y. Nagatani[1,2], T. Yamazaki[1,2], J. Ohnishi[3], A. Goto[2], T. Yuasa[1,2], S. K. Dey[1,2], T. Adachi[1,2], and Y. Ikedo[1,2]

[1]Muon Science Section, Materials and Life Science Division, J-PARC Center; [2]Muon Science Laboratory, Institute of Material Structure Science, KEK; [3]Nishina Center, RIKEN

The Progress of the Laser System for Ultralow Muon Generation

1. Introduction

The Lyman-α laser system for the ultra-slow muon generation is operating stably. In order to increase the output laser pulse energy, several kinds of laser gain medium for an additional laser amplifier are being developed.

2. Laser System for Ultra Slow Muon Generation

Ultra-slow muons can be generated by resonant optical ionization of thermal muonium from hot-W foil target. Light pulses of 122.09 nm and 355 nm are required for 1*s* to 2*p* state excitation and 2*p* to ionization, respectively. The high-energy pulsed coherent Lyman-α light (122.09 nm) source is one of the most important elements for the efficient generation of ultra-slow muons.

The design of the Lyman-α light source system is described in Ref. 1 and a schematic of the light source is shown in Fig.1. Lyman-α pulse of more than 10 μJ is stably generated in a krypton/argon mixture filled gas-cell by the method of two-photon-resonant four-wave-mixing. This method requires 212.556 nm and 820 nm pulses. These pulses are generated by nonlinear wavelength conversions of a 100 mJ 1062.78 nm pulse which is obtained by Nd:YGAG (1 at.% Nd doped Y3Ga2Al3O15) ceramic laser amplifiers. We intended to obtain 1 J level 1062.78 nm pulse in the initial design of the amplifiers' system, but there was a problem in a large-aperture laser medium (>10 mm diameter) for the final amplifiers. The fabrication of ceramic as a gain medium is very difficult due to the nature of Gallium in the Nd:YGAG. In order to overcome the difficulties, we have developed Nd:YSAG (1 at.% Nd doped Y3Sc2Al3O15) ceramic and optimized the composition ratio between Scandium and Aluminum which was reported in the last year's MSL progress report. Newly fabricated middle size (ø9 mm, 112 mm long) Nd:YSAG(1 at.% Nd doped Y3Sc1.5Al3.5O15) ceramic was delivered and inspected in the property of amplification gain at 1062.78 nm light and wavefront distortion. The amplification gain was satisfactory, but the transmitted wavefront distortion was still present, and the collapsed beam shape by the wavefront distortion caused the reduction of the wavelength conversion efficiency in the subsequent stages. The measured wavefront distortion is shown in Fig. 2.

3. Wavefront compensation

In order to compensate for the transmitted wavefront distortion inside the Nd:YSAG ceramic, we introduced an active deformable mirror. The deformable mirror was introduced with Shack-Hartmann wavefront sensor that placed before and after the amplifier, respectively, as shown in Fig. 3. While a deformable mirror can compensate for wavefront distortion, it can also focus the high-power laser beam to an arbitrary position in the laser system if it malfunctions, which can easily destroy not only exchangeable optical components but also expensive nonlinear crystals. Therefore, a preliminary wavefront compensation using a nearly practical optical configuration and a He-Ne laser was used to evaluate the performance. Initially, the wavefront of the optical system was measured without the laser ceramic and with a flat mirror in place of the deformable mirror.

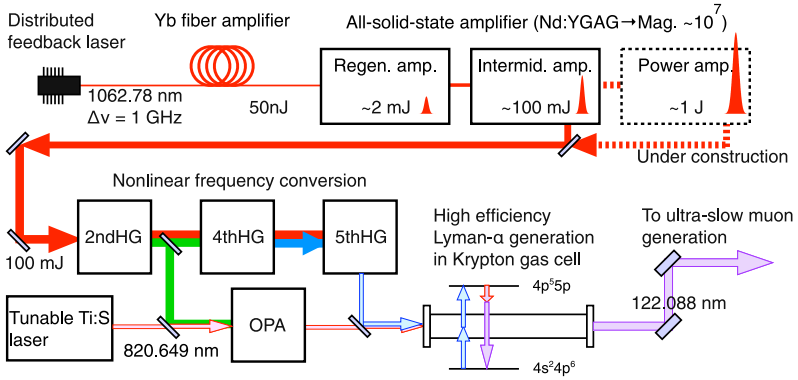

Figure 1. Schematic of the Lyman-α laser system for the Ultra-slow muon generation.

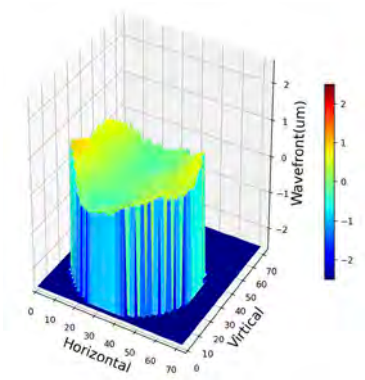

Figure 2. The measured wavefront distortion in newly fabricated Nd:YSAG ceramic for the final amplifier.

Next, the flat mirror was replaced by a deformable mirror and the wavefront was measured. Finally, the wavefront of the entire optical system was measured after inserting the laser ceramic into the optical path. The distorted wavefront was compensated to a plane wave by adaptively applying and controlling the voltage of each piezoelectric element of the 40-segment deformable mirror. The measured wavefront of every step is shown in Figs. 4(a)–(d).

It was shown that the wavefront distortion caused by the laser ceramic can be compensated to a plane wave using a deformable mirror. The method obtained by these studies will be applied to a practical laser system to implement the enhancement of the Lyman-α optical intensity.

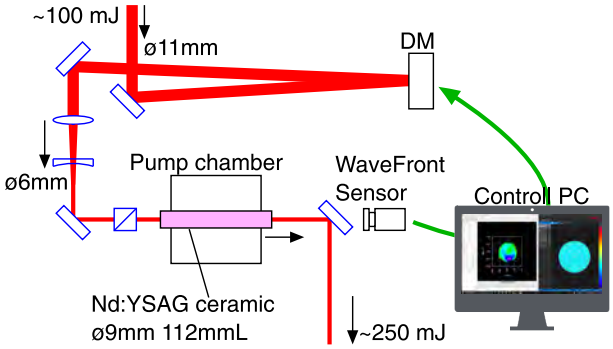

Figure 3. The experimental setup of the final amplifier and wavefront compensation system by a deformable mirror with wavefront sensor.

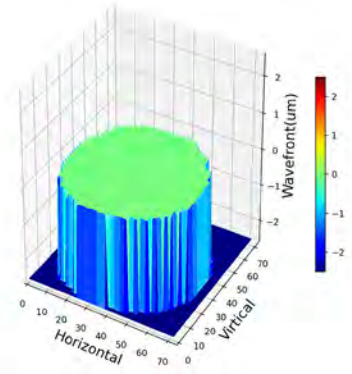

Figure 4(a). The measured initial optical system wavefront with a flat mirror.

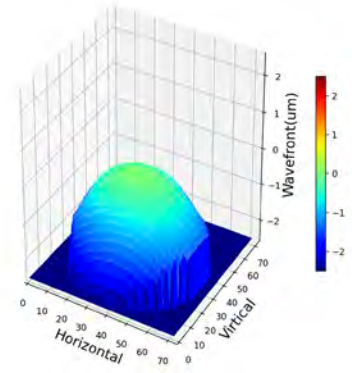

Figure 4(b). The measured wavefront with a deformable mirror.

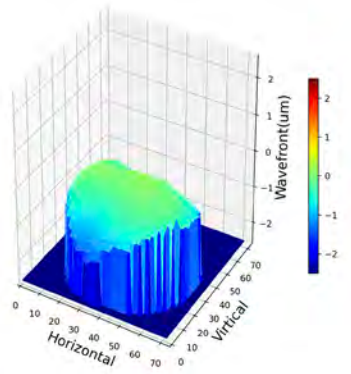

Figure 4(c). The measured wavefront with a deformable mirror and a laser ceramic.

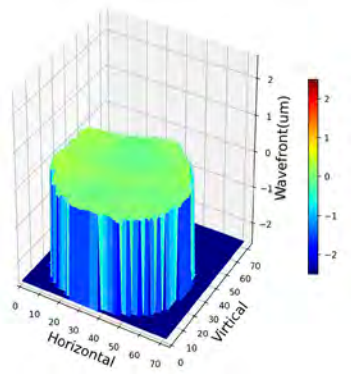

Figure 4(d). The measured wavefront after compensation.

Reference

[1] N. Saito et. al., Opt. Express 24, 7566-7574 (2016).

Y. Oishi[1,2]

[1]*Muon Science Section, Materials and Life Science Division, J-PARC Center;* [2]*Muon Science Laboratory, Institute of Material Structure Science, KEK*

H-Line Construction – Recent Progress

The H-line is a new beamline under construction in the east #1 experimental hall of the MLF. Its layout drawing is shown in Fig. 1. It is a general-purpose beamline [1] that can generate both decay and surface muons and has two branches named H1- and H2-area. Its design intensity of surface muons reaches 108 muons/s with a proton beam power of 1 MW thanks to a large acceptance (108 mSr) capture solenoid and other beamline magnets with large apertures.

At the H-line, precision measurements such as the hyperfine splitting measurement of muonium (MuSEUM experiment) [2] and the muon *g-2*/EDM experiment [3] are planned. Its intense beam is also suited to search for a rare process such as cLFV (charged Lepton Flavor Violation), which is forbidden in the Standard Model of particle physics (DeeMe experiment [4]). In addition, a transmission muon microscope (TμM) project, which enables us to observe thick samples non-destructively, is planned for the H2 area.

The construction of the H-line started in FY2012 and progressed intermittently. Its front-end devices, such as the capture solenoid, were installed in FY2012 and FY2014. Its radiation shields and beam blockers were installed in FY2016. From FY2017 to FY2019, a new electric substation for the H-line was constructed.

In FY2020, the core part and the first branch (H1 area) of the H-line were constructed. The construction was the minimum required to deliver muons to the H1 area and enable us to start beam commissioning. All vacuum apparatuses were connected (see Fig. 2), electrical cabling and cooling water piping for two bending magnets (HB1 and HB2) were conducted, and a safety interlock system was implemented and combined with the whole MLF system. Though the capture solenoid (HS1), transportation solenoids (HS2 and HS3), focusing quadrupole triplets, and a DC-separator are not available yet, the rate of surface muons is expected to be 6×10^5 muons/s. In the next summer shutdown, we plan to conduct the remaining works, such as electrical cabling and cooling water piping of all magnets, and the installation of a DC separator and beam slits, and then the design intensity of 10^8 muons/s will be achieved.

The preparation for the second branch of the H-line (H2 area) also progressed. An extension building must be built for the H2 area on the east side of the MLF, where a parking lot is located because the muon *g-2*/EDM experiment planned at the H2 area needs to accelerate muons up to 212 MeV using a linac of about 50 m. In FY2020, the design of the extension building was detailed, and geotechnical investigation (Fig. 3) and buried cultural property research of the construction site were conducted.

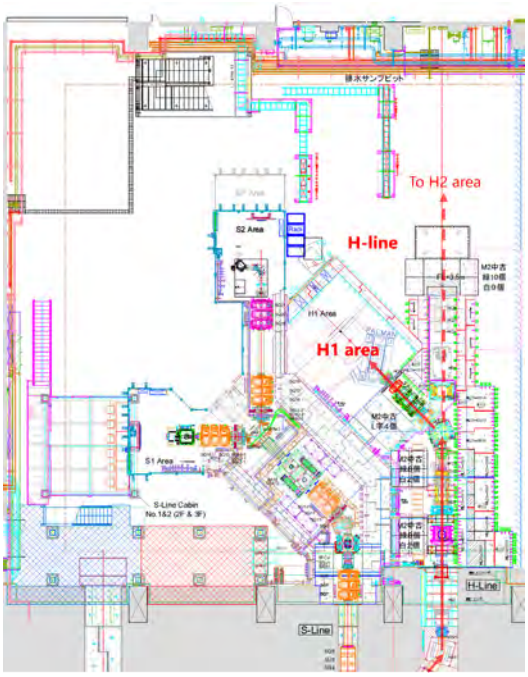

Figure 1. A layout drawing of the H-line.

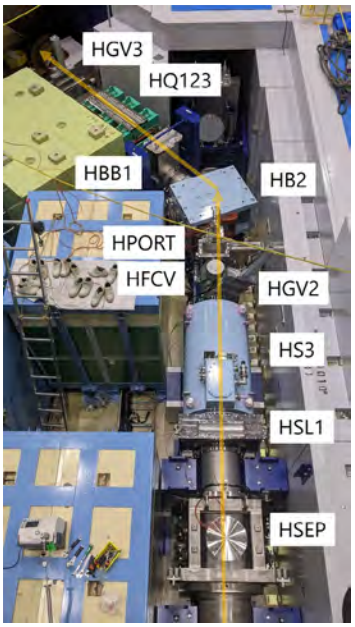

Figure 2. All vacuum apparatuses for the first branch of the H-line were connected during the summer shutdown in FY2020.

Figure 3. Geotechnical investigation of the construction site of the extension building for the H2 area.

References

[1] N. Kawamura, et al., Prog. Theor. Exp. Phys. **2018**, 113G01 (2018).
[2] K. Shimomura, AIP conf. proc. **1382**, 245 (2011).
[3] T. Mibe, et al., Chin. Phys. C **34**, 745 (2010).
[4] H. Natori, et al., Nucl. Phys. B (Proc. Suppl.) **248-250**, 52 (2014).

T. Yamazaki[1,2] and N. Kawamura[1,2]
[1]Muon Science Section, Materials and Life Science Division, J-PARC Center; [2]Muon Science Laboratory, Institute of Material Structure Science, KEK

MLF Safety

Research Safety

1. Radiation safety

Radiation safety for users and increase of radio-activated samples

The low-surface contamination area that has been adopted at the MLF experimental halls from November 2016 is essential for avoiding surface-contamination problems caused by a sample, an environmental atmosphere, and so on. Several experiments with gaseous or liquid samples or atmospheres have been conducted at the MLF, showing that it was useful to expand the flexibility of the experiments.

On the other hand, as the proton beam power increases, neutron flux proportionally rises, resulting in higher radioactivity in the sample. The MLF radiation team, in cooperation with CROSS, supports user experiments by measuring radio-activated samples and devices with Ge detectors. Co-60 ($T_{1/2}$ = 5.271 y) and Mn-54 ($T_{1/2}$ = 312.1 d) as radio-activated ferrous samples are the main contributors. Ag-110 m ($T_{1/2}$ = 249.8 d) and Ta-182 ($T_{1/2}$=114.4 d) are also usually found in radio-activated samples. Characteristics of these radio-active nuclides are the large reaction cross section and long lifetime. The easily activated nuclides should be avoided if the sample needs to be brought from the MLF.

Radiological license upgrade

The applications for radiological license upgrades in FY2020 were approved on April 28, 2020.

The following items were updated after the application approval in FY2020:

(1) Construction of High momentum decay muon instrument (H-line).
(2) Change of Accelerator experimental room followed by the construction of H-line.
(3) Extension of Surface muon instrument (S-line).

2. Chemical safety

This year, due to space limitations, only statistics of the chemical safety check are shown in Fig. 1. Their number decreased due to the effect of the COVID-19 pandemic.

3. Crane safety

Also, this year, due to space limitations, only statistics of the crane usage are shown in Fig. 2. The usage was not affected by the COVID-19 pandemic.

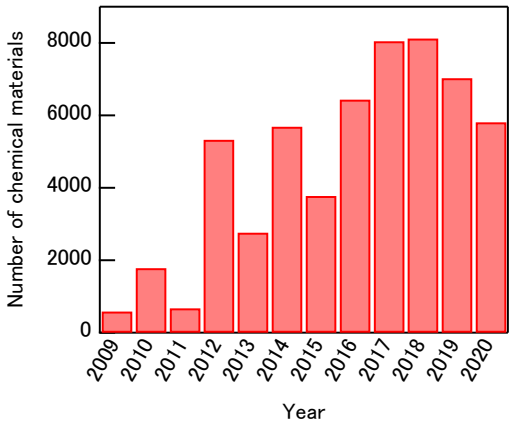

Figure 1. Trend of the amount of user-brought chemical materials for chemical safety check from the start of the MLF operation to the last year.

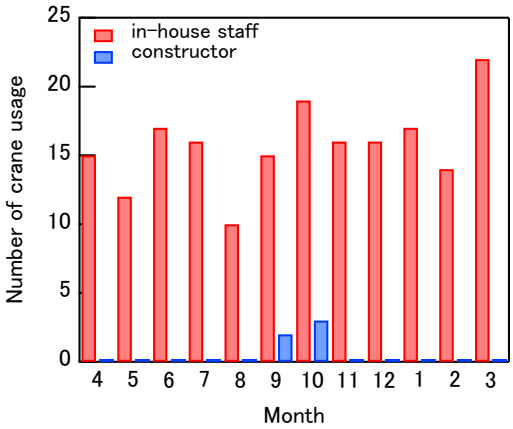

Figure 2. Trend of the total crane usage in one year.

4. COVID-19 pandemic measures

(1) General overview

The MLF division handled the COVID-19 pandemic under the guidelines of the JAEA and KEK measures. On March 1, the first COVID-19 infection occurred in Ibaraki prefecture, where Tokai-mura is located. After that, the number of infected persons gradually increased up to around 10 per day in the early April, so, on April 8, the MLF division decided to stop the users from coming to the MLF facility. Then, on April 20, J-PARC stopped all operations. In the case of the MLF, the operation was restarted on May 15, and the user access was restored on May 22, under the conditions of the individual measures mentioned below. As a result, there were no COVID-19 infections among the users and the pandemic did not affect the operation.

(2) Individual measures

First, when users came to the Users Office (U.O.), their physical condition and behavioral history were checked with interview sheets, behavioral history charts, health management charts, and contact person lists.

The basic measures for COVID-19 in the MLF are health check and avoidance of the following "Three Cs":

1. Closed spaces with poor ventilation.
2. Crowded places with many people nearby.
3. Close-contact settings, such as close-range conversations. Other actions included disinfection of the common areas, dissemination of information, and posting posters about COVID-19. Figure 3 shows various measures as a record for posterity.

Figure 3. Various measures for COVID-19, (a) automatic alcohol atomizer at the entrance of radiation-controlled area, (b) non-contact infrared forehead thermometer at the entrance of the radiation-controlled area, (c) access record book in the radiation-controlled area, (d) non-contact trash can, (e) users' own shoes for the radiation-controlled area, (f) collection box of used shoes for the radiation controlled area, (g) air cleaner in a cabin, (h), (i) UV locker for yellow robe for the radiation-controlled area in the experimental preparation room No. 3, (j) an example of a disinfection location: tables at the MLF entrance lobby, (k) an example of a disinfection location: doorknob in the radiation controlled area.

M. Harada[1], M. Ooi[1], M. Sekijima[1], K. Kawakami[2], K. Aizawa[2], A. Hori[2], H. Tanaka[2], W. Kambara[2], M. Sawabe[2], K. Suzuya[3], N. Kawamura[4], Y. Sakaguchi[5], R. Takahashi[2], Y. Yamaguchi[5], and K. Soyama[6]

[1]Neutron Source Section, Materials and Life Science Division, J-PARC Center, [2]Technology Development Section, Materials and Life Science Division, J-PARC Center, [3]Neutron Science Section, Materials and Life Science Division, J-PARC Center, [4]Muon Science Section, Materials and Life Science Division, J-PARC Center, [5]Neutron Science and Technology Center, CROSS, [6]Materials and Life Science Division

MLF Operations in 2020

Beam Operation Status at the MLF

1. Overall

In Japanese Fiscal Year (JFY) 2020, the beam operation at the MLF started on April 1, 2020 and ended on March 31, 2021. In JFY2020, the beam operation started with a power of 500 kW with a double-bunch beam. After May 18, the beam power was increased from 500 kW to 600 kW. For tuning the accelerator and the proton beam transport, the user beam operation was interrupted for 1 hour on May 18 morning. Table 1 shows the scheduled time and availability in JFY2020. In the schedule, the beam period of 2020A switched to 2020B on November 30. The records of the beam power and the availability are shown in Fig. 1. A long uninterrupted work period of 3,121 h was attained in JFY2020.

Due to the COVID-19 situation, the beam operation at the J-PARC was stopped from April 20 to May 14. The duration of the beam operation loss was 262 hours. The beam stop duration due to the COVID-19 was excluded from the beam operational schedule to evaluate the availability. Fortunately, the beam stop caused by the COVID-19 had less influence on the operation because we had planned to stop the operation during the national holidays from the end of April to the beginning of May.

As shown in Table 1, a stable beam operation with a 93% availability was maintained from April 1 to June 27, just before the summer outage. A high-intensity beam operation for users was carried out. To minimize the negative influence on the users' program caused by potential target failure, we made it before the summer outage period. In the last year, the high-intensity demonstration was achieved without any radiation issues, and the radiation safety group granted permission for the operation with a beam power of ~1 MW. Despite some failures at RCS, a successful high-intensity beam operational with 920 kW was accomplished with a fairy high beam availability of 69.6% for 3 days from June 25 to 27. It should be noted that the allowable high-intensity beam power is limited to ~920 kW because we must have a safety margin of the beam power against the beam power of 1 MW authorized by the radiation license. The personnel protection system (PPS) is limited

Table 1. Run cycle, scheduled time, actual beam time, and availability.

Run cycle	Duration	Scheduled time (h)	Beam time (h)	Avilability (%)
85	Apr 1 – Jun 27	1,337	1,244	93.0
86	Nov 9 – Dec 22	2,587	1,884	72.8
2020A	Apr 1 – Dec 12	2,031	1,465	72.2
2020B	Dec 13 – Mar 31	1,893	1,662	87.8
Overall	Apr 1 – Mar 31	3,924	3,127	79.7

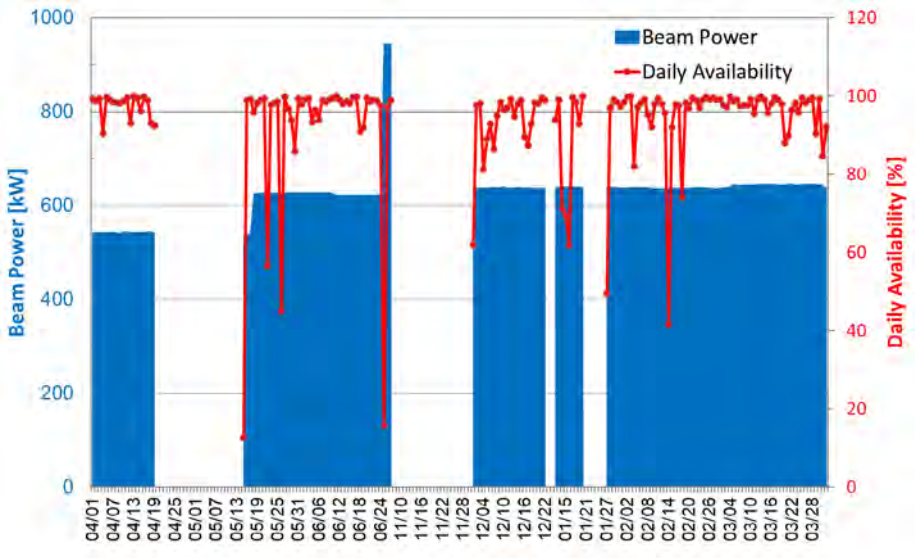

Figure 1. Beam power trend (blue line) at the MLF and availability per day (red line).

Table 2. Events that stopped the beam and reduced the daily availability to less than 80%.

Stop date	Cause of beam stop	Stop duration for each event [h]
Apr 20 - May 1 and May 11 – May 14	COVID-19	262.0
May 22	RCS RF power supply failure for RF2	10.4
May 26	3NBT power supply failure for B1U	13.2
June 25	RCS RF power supply failure for RF3 and RF8	7.0
Nov 9 – Dec 1	Delay of mercury target vessel replacement	456.2
Jan 14	RCS kicker magnet power supply failure for KM5	11.6
January 14 – January 15	LINAC klystron failure at HV4 for SDTL 9 to 12	7.0
Jan 22 – Jan 27	3NBT water pump annomaly at 20 system	141.0
Feb 14	LINAC klystron failure at HV9 for ACS 9 to 12	14.0
February 18	RCS charge exchange foil failure	3.9

to a beam power of 950 kW, which automatically stops the beam at the ion source when the power exceeds the limit. Another safety margin of 3% limits is required for the actual beam operation. To increase the beam power, the safety margin or the license must be changed.

After the summer outage period, the beam operation was planned to be resumed on November 9. Due to the failure of the target replacement, we failed to resume as scheduled. The spent target #9 had been planned to be replaced with new target #13. During replacement, mismatch position was found at the water cooling flange of target #13. Instead of target #13, another new target, #10, was used. The second replacement took a long time. As a matter of fact, the delay of the target replacement made the most impact on the overall availability in JFY2020. After the outage, the beam operation was resumed on December 6. Eventually, the overall availability in JFY2020 was 79.7%.

The beam operation was stopped on several occasions due to minor failures. Typical causes of the beam stop with daily availability of less than 80% are summarized in Table 2 and described below.

2. Causes of the beam stop

LINAC:

During JFY2020, there were no shortages of water flow for the magnet at LINAC, which had been the main reason for beam stops so far. In JFY2020, we had two failures on the klystron providing the RF to the cavities.

3 GeV Rapid Cycling Synchrotron (RCS):

During the high-intensity operation from June 25 to 27, failures of power supplies of Radio Frequency (RF) cavities occurred due to insufficient cooling power for the RF at RCS. The failure of the power supplies is not considered directly related to the beam power. We expect the cooling power to be improved by clearing the heat exchanger for the RF cooling water system. Except in the high-intensity operation, the power supplies for the RF cavities failed on two other occasions. Also, failures of the kicker magnet power supply and of the charge exchange foil introducing the H^- beam from LINAC to RCS also occurred.

Beam transport from RCS to the MLF (3NBT)

An anomaly was detected at the vibrator of the water pump for the 20 system on January 16. The 20 system serves the cooling water to the magnets and the beam scraper placed around at the muon production target. Because the water in the system was highly contaminated, mainly by tritium, it was difficult to replace quickly the pump with the new one. By changing the water pressure at the exit of the pump to sustain the flow, the vibration was decreased to be at the allowed level. It should be noted that the pump violation was rectified within a few days. When the anomaly happened, it was difficult to estimate the recovery period. Therefore, a longer than the expected stop period was announced to users, which affected the duration of the beam period.

Last summer, all clamps, vulnerable to cracking used for the coupler for the vacuum duct's flanges, were exchanged for robust ones. As a result, in JFY2020, the beam did not stop due to cracked clamps, which happened frequently in the past.

S. Meigo
Neutron Source Section, Materials and Life Science Division, J-PARC Center

Users at the MLF

In fiscal year (FY) 2020, the MLF was running stably with a beam power of 600 kW throughout the year, except for the first three weeks from April 1, when the operation ran at 500 kW. Due to the COVID-19 situation, the overall availability in JFY2020 was decreased to 79.7%. In addition, before the summer maintenance period, the 920 kW beam test was successfully operated from June 25 to 27, 2020, with a remarkably high beam delivery. The total number of users of the neutron and muon experimental facilities in FY2020 was 581, a decrease compared with FY2019, due to COVID-19.

The trend for the number of users at the MLF since the start of the operations in FY2008 is summarized in Table 1 and Fig. 1.

Table 1. The number of domestic and foreign users by fiscal year.

	FY2008		FY2009		FY2010		FY2011		FY2012		FY2013		FY2014	
	Domestic Users	Foreign Users	Domestic Users	Foreign Users	Domestic Users	Foreign Users	Domestic Users	Foreign Users	Domestic Users	Foreign Users	Domestic Users	Foreign Users	Domestic Users	Foreign Users
Neutron	107		317		476		259		708		449		824	
	95	12	303	14	432	44	238	21	628	80	399	50	711	113
Muon	18		40		50		23		56		61		91	
	18	0	38	2	42	8	21	2	46	10	50	11	78	13

	FY2015		FY2016		FY2017		FY2018		FY2019		FY2020	
	Domestic Users	Foreign Users	Domestic Users	Foreign Users	Domestic Users	Foreign Users	Domestic Users	Foreign Users	Domestic Users	Foreign Users	Domestic Users	Foreign Users
Neutron	559		852		927		965		940		489	
	476	83	744	108	742	185	789	176	827	113	448	41
Muon	69		99		179		161		138		92	
	59	10	83	16	149	30	146	15	127	11	88	4

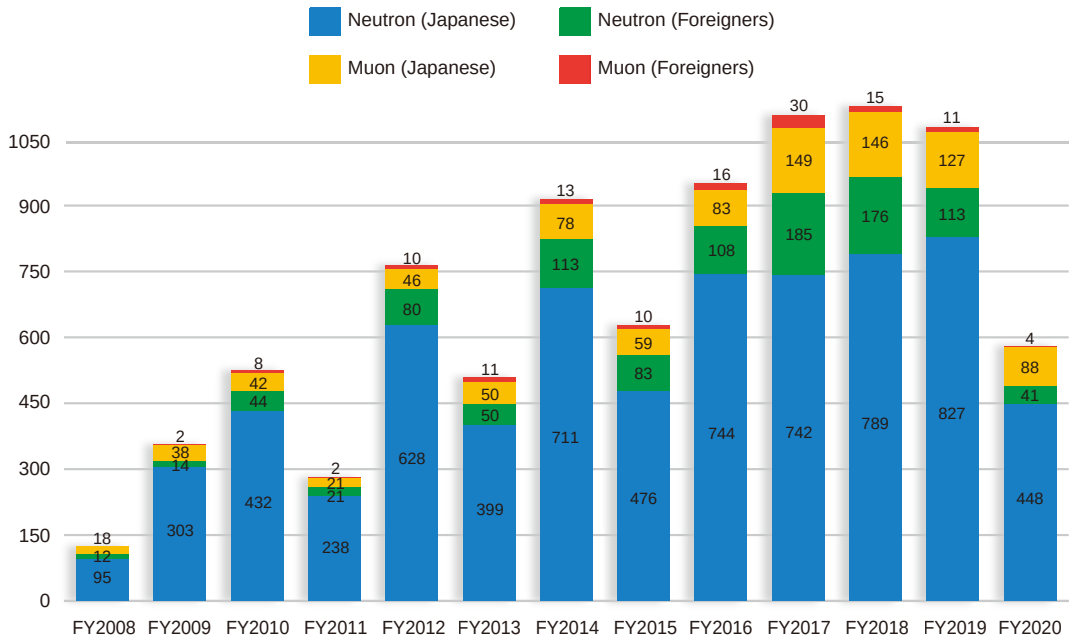

Figure 1. The number of domestic and foreign users by fiscal year.

MLF Proposals Summary – FY2020

Due to the COVID-19 situation, 2020B and 2021A were combined into one proposal round. The experiment period for the proposals for "2020B+2021A" was from December 2020 to July 2021. Therefore, the proposals for 2021A are included in the FY2020 data as they cannot be counted separately.

Table 1. Breakdown of Proposals Numbers for the 2020 Rounds.

Beam-line	Instrument		2020A		2020B+2021A		Full Year			
			Submitted	Approved	Submitted	Approved	Submitted		Approved	
			GU	GU	GU	GU	PU/S	IU	PU/S	IU
BL01	4D-Space Access Neutron Spectrometer - ***4SEASONS***		25(0)	10(0)	31(0)	11(0)	0	1	0	1
BL02	Biomolecular Dynamics Spectrometer - ***DNA***		24(0)	5(0)	36(2)	15(1)	2	2	2	2
BL03	IBARAKI Biological Crystal Diffractometer - ***iBIX***	(100–β)‡	0	0	3	3	0	0	0	0
		(β)†	0	0	0	0	48※	0	47※	0
BL04	Accurate Neutron-Nucleus Reaction Measurement Instrument - ***ANNRI***		5	4	11	5	1	1	1	1
BL05	Neutron Optics and Physics - ***NOP***		2	2	4	4	1	0	1	0
BL06	Village of Neutron Resonance Spin Echo Spectrometers - ***VIN ROSE***		1	1	7	4	1	0	1	0
BL08	Super High Resolution Powder Diffractometer - ***Super HRPD***		13	8	19	11	1	0	1	0
BL09	Special Environment Powder Diffractometer - ***SPICA***		2	2	1	1	1	0	1	0
BL10	Neutron Beamline for Observation and Research Use - ***NOBORU***		10	7	15	10	3	1	3	1
BL11	High-Pressure Neutron Diffractometer - ***PLANET***		21(0)	15(0)	14(0)	12(0)	0	1	0	1
BL12	High Resolution Chopper Spectrometer - ***HRC***		5	4	11	8	1	0	1	0
BL14	Cold-Neutron Disk-Chopper Spectrometer - ***AMATERAS***		25	8	36	7	3	1	3	1
BL15	Small and Wide Angle Neutron Scattering Instrument - ***TAIKAN***		35(0)	15(0)	50(2)	20(2)	2	3	2	3
BL16	Soft Interface Analyzer - ***SOFIA***		14	14	29	25	0	1	0	1
BL17	Polarized Neutron Reflectometer - ***SHARAKU***		18(2)	11(1)	20(1)	14(1)	2	3	2	3
BL18	Extreme Environment Single Crystal Neutron Diffractometer - ***SENJU***		18(0)	9(0)	28(0)	10(0)	1	1	1	1
BL19	Engineering Materials Diffractometer - ***TAKUMI***		14	11	31	21	1	1	1	1
BL20	IBARAKI Materials Design Diffractometer - ***iMATERIA***	(100–β)‡	9	6	8	6	0	0	0	0
		(β)†	26	26	36	36	22	0	22	0
BL21	High Intensity Total Diffractometer - ***NOVA***		25	19	20	10	1	0	1	0
BL22	Energy Resolved Neutron Imaging System - ***RADEN***		10(0)	10(0)	24(0)	16(0)	2	3	2	3
BL23	Polarized Neutron Spectrometer - ***POLANO***		1	1	2	2	1	0	1	0
D1	Muon Spectrometer for Materials and Life Science Experiments - ***D1***		15(0)	6(0)	20(0)	12(0)	1	1	1	1
D2	Muon Spectrometer for Basic Science Experiments - ***D2***		3(1)	3(1)	8(0)	4(0)	1	1	1	1
S1	General purpose μSR spectrometer - ***ARTEMIS***		22(2)	16(2)	46(0)	24(0)	1	1	1	1
U1A	Ultra Slow Muon Microscope - ***U1A***		0	0	0	0	0	1	0	1
U1B	Transmission Muon Microscope - ***U1B***		0	0	0	0	0	1	0	1
Total			**343**	**213**	**509**	**290**	**87**	**24**	**86**	**24**

GU : General Use **PU :** Project Use or Ibaraki Pref. Project Use **S :** S-type Proposals **IU :** Instrument Group Use
† : baraki Pref. Exclusive Use Beamtime (β = 80% in FY2020) **‡ :** J-PARC Center General Use Beamtime (100–β = 20% in FY2020)
( ) : Proposal Numbers under the New User Promotion (BL01, BL02, BL11, BL15, BL17, BL18, BL22) or P-type proposals (D1,D2, S1) in GU
※ **:** Proposal rounds are held twice per year (for each of the A and B periods), with only the yearly total shown above.
The actual total number of proposals in each beamline named in the table does not match the number shown in the "Total" cell, because some proposals are submitted or approved across multiple beamlines.

Table 2. Proposals Numbers of Long Term Proposal for the 2020 Rounds.

Application FY	Submitted	Approved
2018	9	5
2019	9	4
2020	13	3

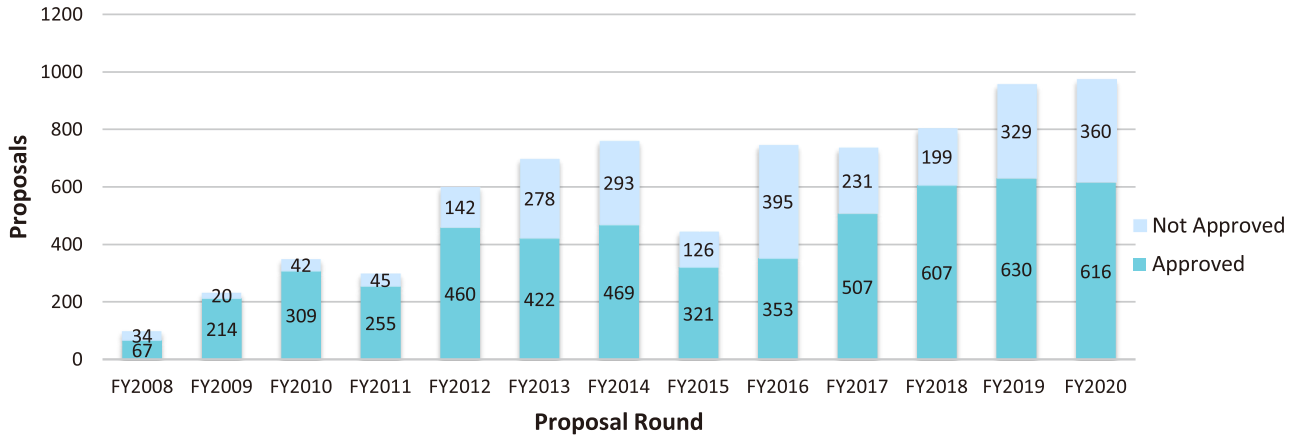

Figure 1. MLF Proposal Numbers over Time.

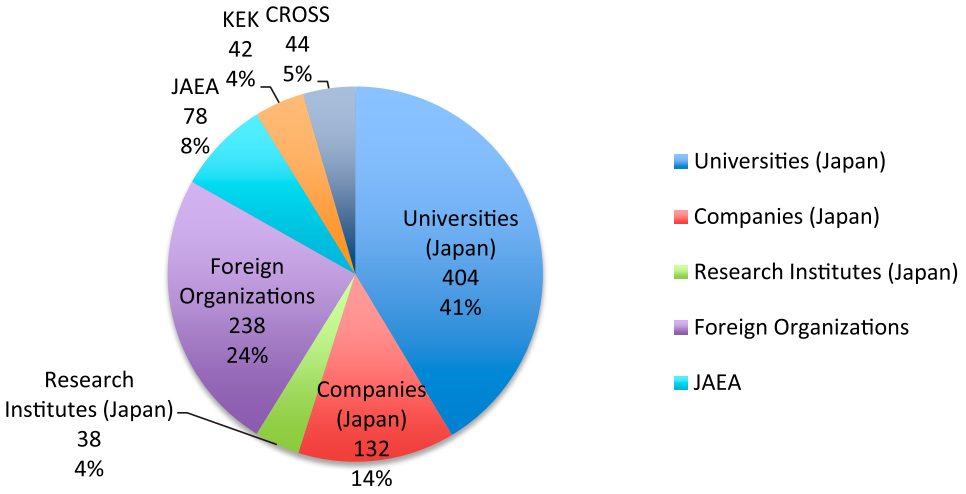

Figure 2. Origin of Submitted Proposals by affiliation - FY2020 (2020A, 2020B + 2021A).

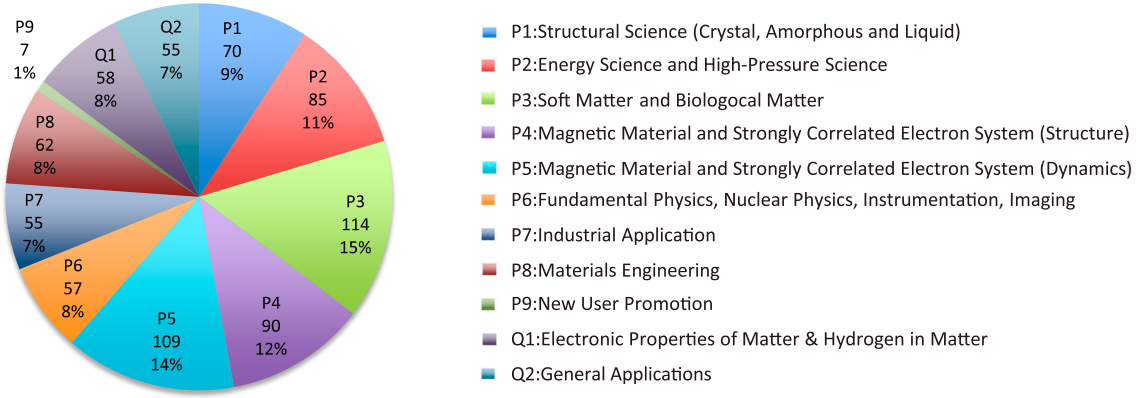

Figure 3. Submitted Proposals by Sub-committee/Expert Panel - FY2020 (2020A, 2020B + 2021A).

MLF Division Staff 2020

Toshiya Otomo (Head)
Kazuya Aizawa (Deputy Head)
Kenji Nakajima (Deputy Head)
Koichiro Shimomura (Deputy Head)
Eiichi Wakai
Izumi Kuwahara

Neutron Source Section

*: additional duties

<JAEA>

Katsuhiro Haga (Leader)
Kenji Sakai (Sub-Leader)
Makoto Teshigawara
Masahide Harada
Tomokazu Aso
Hiroyuki Kogawa
Hidetaka Kinoshita
Takashi Wakui
Motoki Ooi
Takashi Naoe
Masakazu Seki
Akira Shibata
Shiho Masuda
Yuji Yamaguchi
Toshiaki Uehara
Akihiko Watanabe
Hideki Muto
Akiyoshi Futakawa
Mitsuaki Sekijima
Yoshinori Kikuchi
Masakazu Nakamura
Hidemitsu Hosokawa
Atsushi Akutsu
Toshiyuki Yasuhara
Hiromi Inoue
Noriyuki Morikawa
Shigeto Tanaka
Shizuka Yoshinari
Rie Nemoto
Hiroshi Takada *
Shoichi Hasegawa *
Eiichi Wakai *
Shin-ichiro Meigo *
Kenichi Oikawa *
Tetsuya Kai *
Hiroyuki Uehara *

Neutron Science Section

*: additional duties

<JAEA>

Yukinobu Kawakita (Leader)
Mitsutaka Nakamura (Sub-Leader)
Kentaro Suzuya
Ryoichi Kajimoto
Takanori Hattori
Stefanus Harjo
Kenichi Oikawa
Takashi Ohhara
Takenao Shinohara
Hiroyuki Aoki
Tetsuya Kai
Seiko Kawamura
Shinichi Takata
Ryoji Kiyanagi
Kaoru Shibata
Asami Sano
Yasuhiro Inamura
Takuro Kawasaki
Maiko Kofu
Kousuke Hiroi
Naoki Murai
Hiromu Tamatsukuri
Yusuke Tsuchikawa
Kanae Ito
Kazuhisa Isegawa
Shigeki Uzuki
Hiroyuki Dannoshita
Tatsuya Kikuchi
Masashi Harada
Daigo Setoyama
Takeshi Harada
Hideaki Isozaki
Keiichi Inoue
Misono Fujii
Naoko Shimizu
Toshiko Goto
Itaru Tamura *
Kouji Kaneko *
Hiroshi Nakagawa *
Atsushi Moriai *
Satoshi Morooka *
Atsushi Kimura *
Shoji Nakamura *
Shunsuke Endo *
Yosuke Toh *
Mariko Segawa *
Masahide Harada *
Masao Watanabe *
Dai Yamazaki *
Kazuo Kurihara *
Tarou Tamada *
Yuu Hirano *
Takeshi Hiromoto *
Fumiaki Kono *

<KEK>

Testuya Yokoo (Sub-Leader)
Shinichi Ito
Hideki Seto
Toshiya Otomo *
Takashi Kamiyama
Hitoshi Endo
Takashi Ino
Norifumi Yamada
Takashi Honda
Naokatsu Kaneko
Shuki Torii
Hidetoshi Oshita
Kaoru Taketani
Kenji Mishima
Hiroyuki Aoki *
Asami Sano *
Kazutaka Ikeda
Masato Hagihala
Takashi Saito
Kwanghee CHO
Sara Yamauchi
Taichi Ueta
Go Ichikawa

Technology Development Section

*: additional duties

<JAEA>

Takayuki Oku (Leader)
Kazuyoshi Tatsumi
Takeshi Nakatani
Masao Watanabe
Yuhua Su
Ryota Komine
Takuya Okudaira
The Dang Vu
Wataru Kambara
Akihiro Hori
Hideaki Takahashi
Ryuta Takahashi
Wu Gong
Kazuhiro kawakami
Hiromichi Tanaka
Hiroyuki Asai
Yukiko Nagai
Kenji Sakai *
Tetsuya Kai *
Hiroyuki Kogawa *
Motoki Ooi *
Kentaro Suzuya *
Mitsutaka Nakamura *
Shinichi Takata *
Kaoru Sakasai *
Tatsuya Nakamura *
Yasuhiro Inamura *
Masahide Harada *
Tomokazu Aso *
Seiko Kawamura *
Rumi Shimizu *
Satoru Fujiwara *
Motoyasu Adachi *
Shigeki Arai *
Chie Shibazaki *

<KEK>

Tomohiro Seya
Setsuo Sato
Testuya Yokoo *
Shuki Torii *
Takashi Ino *
Naokatsu Kaneko *
Kaoru Taketani *
Naritoshi Kawamura *
Hiroshi Fujimori *
Shunsuke Makimura *

Neutron Instrumentation Section

*: additional duties

<JAEA>

Kaoru Sakasai (Leader)
Dai Yamazaki
Kentaro Toh
Tatsuya Nakamura
Ryuji Maruyama
Tomokatsu Koizumi
Yukio Hishinuma
Yukiko Uno

Muon Science Section

*: additional duties

<KEK>

Ryosuke Kadono (Leader)
Naritoshi Kawamura (Sub-Leader)
Koichiro Shimomura *
Akihiro Koda
Patrick Strasser
Takayuki Yamazaki
Sotaro Kanda
Yutaka Ikedo
Yasuo Kobayashi
Junpei Nakamura
Takashiro Yuasa
Yasuhiro Miyake
Yu Oishi
Yukinori Nagatani
Shiro Matoba
Soshi Takeshita
Hiroaki Natori
Shoichiro Nisimura
Sourav Kumar Dey
Hiroshi Fujimori
Masatoshi Hiraishi
Hirotaka Okabe
Motonobu Tanpo
Taihei Adachi
Amba Datt Pant
Tatsuhiko Tachibana
Hua Li
Shogo Doiuchi
Akiko Hashimoto
Yoshinori Ito
Izumi Umegaki

<JAEA>

Wataru Higemoto *
Takashi Ito *

CROSS Staff 2020

Director **Mitsuhiro Shibayama**

Science Coordinators

*: additional duties

Shamoto Shinichi
Jun Sugiyama
Takashi Noma *
Hibi Masaaki
Kazuhisa Kakurai
Midori Kamimura

Research & Development Division

*: additional duties

Jun-ichi Suzuki (Head)
Kenichi Funakoshi (Deputy Head)
Tsukasa Miyazaki * (Deputy Head)

<BL01 Group>
Kazuya Kamazawa (Leader)
Kazuki Iida
Kazuhiko Ikeuchi

<BL02 Group>
Masato Matsuura (Leader)
Takeshi Yamada
Taiki Tominaga

<BL11 Group>
Kenichi Funakoshi * (Leader)
Jun Abe
Shinichi Machida

<BL15 Group>
Kazuki Ohishi (Leader)
Jun-ichi Suzuki *
Hiroki Iwase
Yukihiko Kawamura

<BL17 Group>
Noboru Miyata (Leader)
Kazuhiro Akutsu
Takayasu Hanashima

<BL18 Group>
Akiko Nakao (Leader)
Koji Munakata
Yoshihisa Ishikawa

<BL22 Group>
Hirotoshi Hayashida (Leader)
Joseph Don Parker
Yoshihiro Matsumoto

<Technical Support Group>
Takayoshi Ito (Leader)
Koji Kiriyama * (Sub-Leader)
Keiichi Ohuchi
Masae Sahara
Yoshihiko Honda
Yoshifumi Sakaguchi
Hiroshi Kira
Motoyuki Ishikado
Shuoyuan Zhang
Toshiaki Morikawa
Hiroshi Arima
Nobuo Okazaki
Satoshi Kasai
Kentaro Moriyama

Safety Division

*: additional duties

Mitsuhiro Shibayama * (Head)
Koji Kiriyama (Leader)
Tazuko Mizusawa *
Masae Sahara *
Yasuhiro Yamaguchi

Utilization Promotion Division

*: additional duties

Takashi Noma (Head)
Tsukasa Miyazaki * (Deputy Head)
Seiya Konishi (Leader)
Toshiki Asai (Leader)
Junichi Sato (Leader)
Takayoshi Ito *
Miho Igarashi
Atsuko Irie
Kaoru Ohuchi
Emi Goto
Tazuko Mizusawa
Tomoko Ishikawa
Nobuo Okazaki *
Rie Kurosawa *
Taeko Ishikawa
Maya Endo
Hideyuki Niitsuma

Administration Division

Michihiko Murasawa (Head)
Takashi Hikita (Leader)
Rei Ito
Tomoko Sakuma
Mutsumi Shiraishi
Shinobu Matsumoto

Industrial Collaboration Promotion Division

*: additional duties

Tsukasa Miyazaki (Head)
Takashi Noma *
Seiya Konishi *
Noboru Miyata *
Jun Abe *
Takeshi Yamada *
Yoshihiro Matsumoto *
Hiroki Iwase *

Ibaraki Neutron Beamline Staff in 2020

Ibaraki Prefectural Government

<Senior Director for Neutron Promotion>
Hironori Kodama

<Neutron Beamline Coordinator>
Michiko Konno
Tetsuroh Minemura

Ibaraki University *

* Trustee of the Beamline operations

<BL03 iBIX Group>
Katsuhiro Kusaka (Leader)
Taro Yamada
Naomine Yano
Ichiro Tanaka
Takaaki Hosoya

<BL20 iMATERIA Group>
Toru Ishigaki (Leader)
Satoshi Koizumi
Akinori Hoshikawa
Shigeo Sato
Yusuke Onuki
Yohei Noda
Tomoki Maeda
Takeshi Matsukawa

<Technical Support Group>
Junichi Hiroki
Tomoyuki Nakazawa
Mitsuyuki Fujii
Shinju Shibata
Takumi Inada

Proposals Review System, Committees and Meetings

Proposal Review System

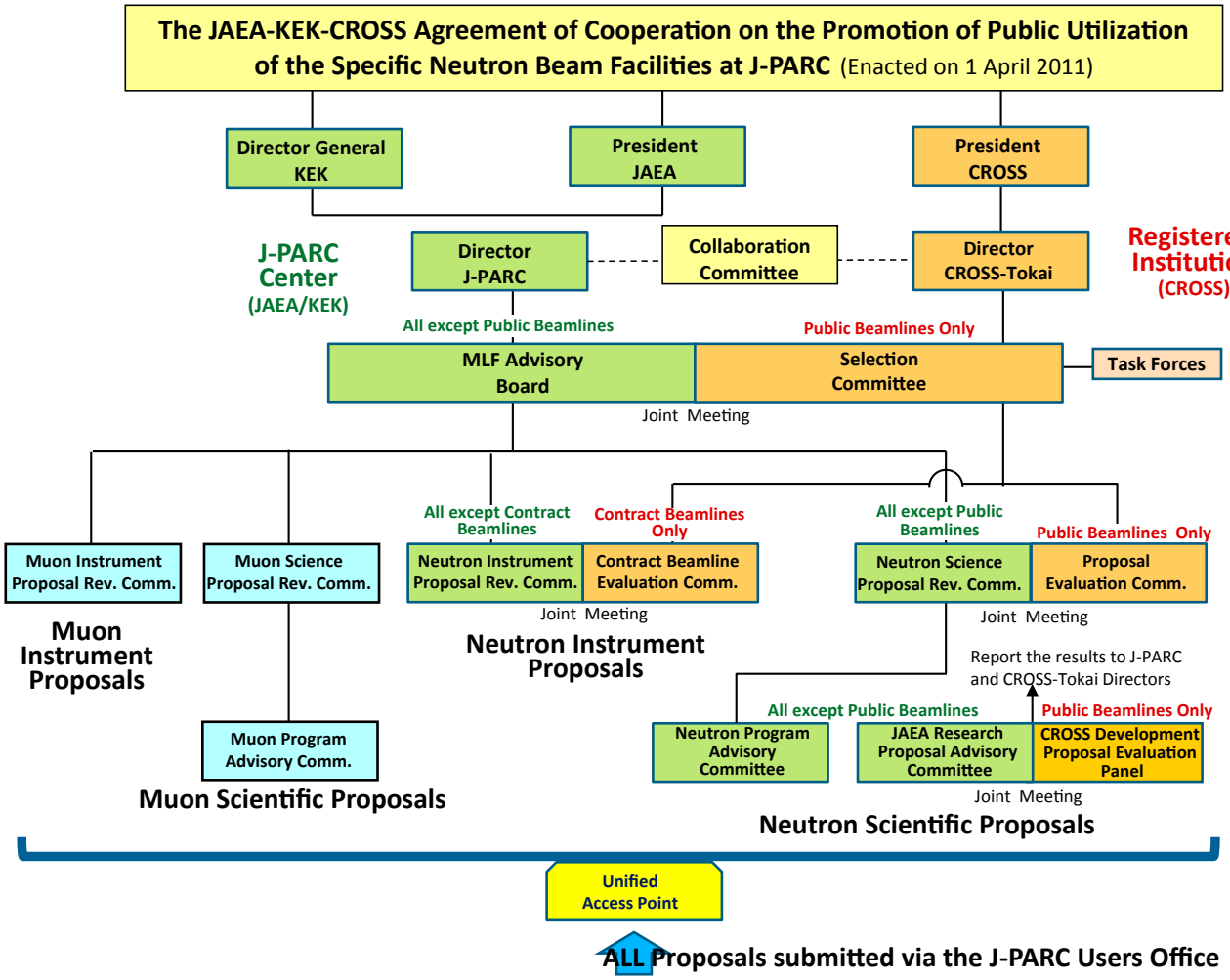

Figure 1. Proposals Review System Framework.

Materials and Life Science Facility Advisory Board

Kazuya Aizawa	Japan Atomic Energy Agency
Hiroshi Amitsuka	Hokkaido University
Taka-hisa Arima	The University of Tokyo
Shinich Itoh	High Energy Accelerator Research Organization
Ryosuke Kadono	High Energy Accelerator Research Organization
Kazuhisa Kakurai	Comprehensive Research Organization for Science and Society
Takashi Kamiyama	High Energy Accelerator Research Organization
Takashi Kamiyama	Hokkaido University
Yukinobu Kawakita	Japan Atomic Energy Agency
Takamitsu Kohzuma	Ibaraki University
Yoji Koike	Tohoku University
Kenya Kubo	International Christian University
Kenji Nakajima	Japan Atomic Energy Agency
Toshiya Otomo	High Energy Accelerator Research Organization
Yoshiharu Sakurai	Japan Synchrotron Radiation Research Institute
Taku Sato	Tohoku University
Hideki Seto	High Energy Accelerator Research Organization
Koichiro Shimomura	High Energy Accelerator Research Organization
Kazuhiko Soyama	Japan Atomic Energy Agency
Masaaki Sugiyama (chair)	Kyoto University
Jun-ichi Suzuki	Comprehensive Research Organization for Science and Society
Atsushi Takahara	Kyushu University
Masayasu Takeda	Japan Atomic Energy Agency
Toshio Yamaguchi	Fukuoka University
Osamu Yamamuro	The University of Tokyo

Term: through March 31, 2021

Neutron Science Proposal Review Committee

Hiroshi Abe	National Defense Academy of Japan
Taka-hisa Arima (chair)	The University of Tokyo
Hiroyuki Kagi	The University of Tokyo
Ryosuke Kadono	High Energy Accelerator Research Organization
Yukinobu Kawakita	Japan Atomic Energy Agency
Masaaki Kitaguchi	Nagoya University
Takatsugu Masuda	The University of Tokyo
Tsukasa Miyazaki	Comprehensive Research Organization for Science and Society
Jun'ichiro Mizuki	Kwansei Gakuin University
Kenji Ohoyama	Ibaraki University
Toyotaka Osakabe	Japan Atomic Energy Agency
Toshiya Otomo	High Energy Accelerator Research Organization
Hideki Seto	High Energy Accelerator Research Organization
Naoya Torikai	Mie University
Noriyuki Tsuchida	University of Hyogo

Term: through September 30, 2021

Muon Science Proposal Review Committee

Tadashi Adachi	Sophia University
Kenta Amemiya	High Energy Accelerator Research Organization
Hidehito Asaoka	Japan Atomic Energy Agency
Toshiyuki Azuma	RIKEN
Katsuyuki Fukutani	The University of Tokyo
Wataru Higemoto	Japan Atomic Energy Agency
Adrian Hillier	Rutherford Appleton Laboratory
Katsuya Inoue	Hiroshima University
Shinichi Itoh	High Energy Accelerator Research Organization
Ryosuke Kadono	High Energy Accelerator Research Organization
Yukinobu Kawakita	Japan Atomic Energy Agency
Naritoshi Kawamura	High Energy Accelerator Research Organization
Yasushi Kino	Tohoku University

Akihiro Koda	High Energy Accelerator Research Organization
Takamitsu Kohzuma	Ibaraki University
Kenya Kubo (chair)	International Christian University
Roderick Macrae	Marian University
Tsutomu Mibe	High Energy Accelerator Research Organization
Yasuhiro Miyake	High Energy Accelerator Research Organization
Chihiro Ohmori	High Energy Accelerator Research Organization
Toshiya Otomo	High Energy Accelerator Research Organization
Hideki Seto	High Energy Accelerator Research Organization
Tatsushi Shima	Osaka University
Koichiro Shimomura	High Energy Accelerator Research Organization
Yoko Sugawara	Kitasato University
Jun Sugiyama	Comprehensive Research Organization for Science and Society
Masaaki Sugiyama	Kyoto University
Toshiyuki Takayanagi	Saitama University

Term: through March 31, 2021

Selection Committee

Taka-hisa Arima	The University of Tokyo
Yasuhiro Iye (chair)	Japan Society for Promotion of Science
Takashi Kamiyama	Hokkaido University
Hiroyuki Kishimoto	Sumitomo Rubber Industries, LTD.
Hideaki Kitazawa	Research Center for Strategic Materials
Yoji Koike	Tohoku University
Takamitsu Kohzuma	Ibaraki University
Yoshiharu Sakurai	Japan Synchrotron Radiation Research Institute
Taku Sato	Tohoku University
Masaaki Sugiyama	Kyoto University
Atsushi Takahara	Kyushu University
Shinji Tsuneyuki	The University of Tokyo
Toshio Yamaguchi	Fukuoka University
Osamu Yamamuro	The University of Tokyo

Term: through March 31, 2021

Proposal Evaluation Committee

Hiroshi Abe	National Defense Academy of Japan
Taka-hisa Arima (chair)	The University of Tokyo
Hiroyuki Kagi	The University of Tokyo
Masaaki Kitaguchi	Nagoya University
Takatsugu Masuda	The University of Tokyo
Tsukasa Miyazaki	Comprehensive Research Organization for Science and Society
Jun'ichiro Mizuki	Kwansei Gakuin University
Kenji Ohoyama	Ibaraki University
Toshiya Otomo	High Energy Accelerator Research Organization
Naoya Torikai	Mie University
Noriyuki Tsuchida	University of Hyogo

Term: through September 30, 2021

Neutron Advisory Committee (NAC)

NAC convened online on the 17 and 22 of February 2021.

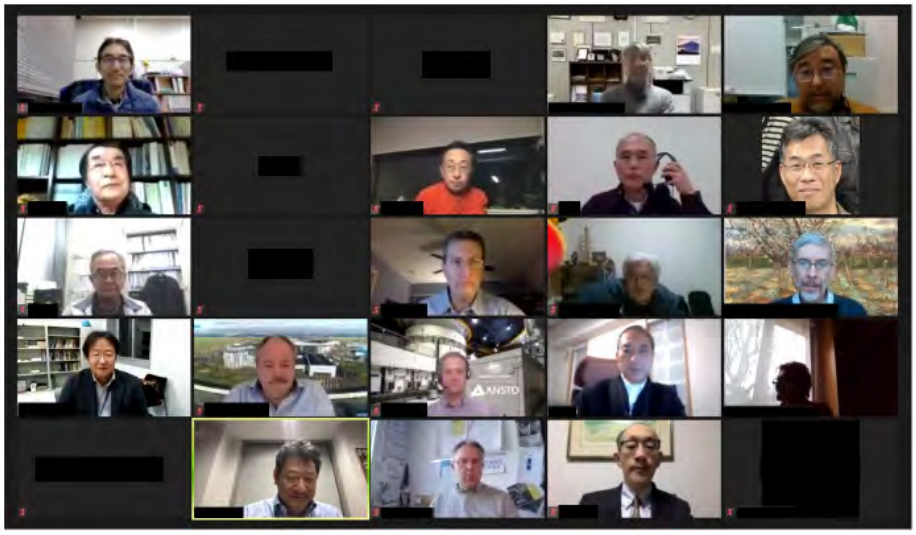

Screenshot of NAC

Robert McGreevy (chair)	Rutherford Appleton Laboratory
Christiane Alba-Simionesco	Laboratoire Léon Brillouin
Bertrand Blau	Paul Scherrer Institut
Sung-Min Choi	Korea Advanced Institute of Science and Technology
Michael Dayton	Oak Ridge National Laboratory
Yoshiaki Kiyanagi	Nagoya University
Yoshie Ohtake	RIKEN
Christian Rüegg	Paul Scherrer Institut
Andreas Schreyer	European Spallation Source
Jamie Schulz	Australian Nuclear Science and Technology Organization
Masaaki Sugiyama	Kyoto University

Muon Advisory Committee (MAC)

MAC convened online on the 1 and 4 of February 2021.

Screenshots of MAC

Thomas Prokscha (chair)	Paul Scherrer Institut
Hiroshi Amitsuka	Hokkaido University
Klaus Kirch	ETH Zurich and Paul Scherrer Institut
Kenya Kubo	International Christian University
Andrew Macfarlane	The University of British Columbia
Martin Månsson	KTH Royal Institute of Technology
Takashi Nakano	Osaka University
Tadayuki Takahashi	The University of Tokyo

Workshops, Conferences, Seminars and Schools in 2020

Conferences held jointly by J-PARC MLF and CROSS

2020 Z-Code Beginner Level Training Course
27 Aug.-28 Aug. 2020, Online

MRM2020
7-11 Dec. 2020, Online

2020 Z-Code Intermediate Level Training Course
25 Feb.-31 Mar. 2021, Online

The 7th Workshop on Pulsed Neutron Imaging
1-2 Mar. 2021, Online

2020 Quantum Beam Science Festa
(The 12th MLF Symposium and the 38th PF Symposium)
9 -11 Mar. 2021, Online

Screenshot of MLF Symposium
(photo courtesy of J-PARC Center)

Conferences held by J-PARC MLF and other organizations

The 3rd FC-Cubic Open Symposium
2 Feb. 2021, Tokyo International Exchange Center, J-PARC (Satellite), Online, YouTube

Conferences held by KEK

CIQuS 研究会 " 無機材料中の水素の存在状態と機能発現 "
27 Aug. 2020, Online

Screenshot of CIQuS 研究会
(photo courtesy of KEK)

第 3 回文理融合シンポジウム " 量子ビームで歴史を探る ー加速器が紡ぐ文理融合の地平ー "
25 Sep. 2020, Online

第 4 回文理融合シンポジウム " 量子ビームで歴史を探る ー加速器が紡ぐ文理融合の地平ー "
28 Jan. 2021, Online

Workshops held by KEK

Fundamental Physics Using Atoms (FPUA 2021)
4–5 Aug. 2021, Online

Analysis of ordered/disordered structure in functional materials with high intensity neutron total scattering technique (BL21)
13 Oct. 2020, Online

第 1 回 MCP 討論会
27 Oct. 2020, The University of Tokyo, Kashiwa

Study on slow dynamics by the neutron resonance spin echo spectrometers VIN ROSE (BL06)
25 Nov. 2020, Online

Studies on Dynamics in Condensed Matters by using the High Resolution Chopper Spectrometer (BL12)
25 Nov. 2020, Online

Workshop on Neutron Powder Diffraction using SuperHRPD (BL08) and SPICA (BL09)
30 Nov. 2020, Online

Study on Cross-correlated Physics by Polarized Neutron Spectrometer, POLANO (BL23)
1 Dec. 2020, Online

Fundamental Physics with Pulsed Cold Neutrons (BL05)
17–18 Dec. 2020, Online

第 11 回 Muon 科学と加速器研究
27 Jan. 2021, Online

第 2 回 MCP 討論会
31 Mar. 2021, The University of Tokyo, Kashiwa

Workshops and Seminars held by CROSS and other organizations

The 24th CROSSroads Workshop
“ 偏極中性子を使った磁性薄膜・多層膜研究 ”
30 Jun., 10 Jul., and 4 Aug. 2020, Online

Screenshot of CROSSroads
(photo courtesy of CROSS)

2020 Neutron Experiment Technique Training Course
21 Oct. 2020, Online

Workshop on Organic materials and Polymers
“Current status of structural analysis of Organic materials and Polymers by neutron small-angle scattering”
14 Dec. 2020, Online

Tohoku U x CROSS x JAEA Cooperative Seminar, 62nd REIMEI Workshop “New excitations for spintronics seen with quantum beams”
25 Feb. 2021, Online

Workshop on Metals
“Novel structural analysis of metals by neutron scattering -focused on light elements in metals-”
5 Mar. 2021, Online

2020 Workshop on Liquids and Amorphous Materials
16 Mar. 2021, Online

2020 Workshop on Neutron Structural Biology
30 Mar. 2021, Online

Schools in 2020

Hello Science from J-PARC “The Latest Battery Research at J-PARC for the Innovation of Lithium-ion Batteries”
25 Sep. 2020, iVil, Tokai

Hello Science from J-PARC “Looking into Lithium Ion Battery using J-PARC Negative Muon”
25 Dec. 2020, iVil, Tokai

Award List

Dean's Award, School of Engineering, The University of Tokyo
Exploration of quantum transport phenomena via engineering emergent magnetic fields in topological magnets
Y. Fujishiro (2021-03-19)

第38回高分子学会千葉地域活動若手セミナー 奨励ポスター賞
両親媒性ロフィンダイマーが形成する分子集合体を用いた可溶化能の高速光制御
田中理紗 (2021-03-02)

Springer Theses
Exploration of quantum transport phenomena via engineering emergent magnetic fields in topological magnets
Y. Fujishiro (2021-03)

The Tawara Award of the Iron and Steel Institute of Japan
Analysis of Tensile Deformation Behavior by in situ Neutron Diffraction Experiments of a 1 GPa-grade TRIP Steel with High ElongationAnalysis of Tensile Deformation Behavior by in situ Neutron Diffraction Experiments of a 1 GPa-grade TRIP Steel with High Elongation
N. Tsuchida, T. Tanaka, Y. Toji (2021-03)

The JSNS President's Choice
Localized Magnetic Excitations in the Almost Perfectly Frustrated Spin Dimer Quantum Magnet
N. Kurita, H. Tanaka (2020-11-10)

The JSNS President's Choice
Recent progress in the development of polarizing supermirror
R. Maruyama (2020-11-10)

The JSNS President's Choice
Ripple of Electronic Clouds
K. Matsuura, H. Sagayama, T. Arima (2020-11-09)

The JSNS Young Researcher Prize
Magnetic fluctuations in unconventional superconductivity by pulsed neutron
K. Iida (2020-11-09)

The JSNS Technology Prize
Development of Super High-Resolution Powder Diffractometer, SuperHRPD
S. Torii, K. Oikawa, M. Hagihara , K. Cho, T. Kamiyama (2020-11-09)

The JSNS Science Prize
Characterization of soft matter interfaces using neutron reflectometry
A. Takahara (2020-11-09)

The JSNS Outstanding Achievement Prize
Contribution to the development of neutron structure analysis and the development of the Japanese neutron science community
Y. Noda (2020-11-09)

The JSNS Technology Prize
Proton beam control technology for highintensity pulsed neutron production
S. Meigo, H. Fujimori, S. Sakamoto, M. Ooi (2020-11-09)

Japan Association of Mineralogical Sciences Award
Technical developments for high-pressure neutron diffraction and analyses of phase transitions of hydrogen-bearing minerals under pressure
K. Komatsu (2020-09-18)

JSNS: The Japanese Society for Neutron Science

MLF Publication 2020

1 T. Hirata, H. Taneda, K. Nishio, M. Inutsuka, N. L. Yamada, F. Nemoto, Y. Minagawa, H. Matsuno, K. Tanaka,
A Facile Surface Functionalization Method for Polymers Using a Non-solvent
ACS Appl. Bio Mater., **3** 2170-2176 (2020).

2 J.-H. Hong, M. Totani, D. Kawaguchi, H. Masunaga, N. L. Yamada, H. Matsuno, K. Tanaka,
Design of a Bio-inert Interface Using an Amphiphilic Block Copolymer Containing a Bottlebrush Unit of Oligo(oxazoline)
ACS Appl. Bio Mater., **3** 7363–7368 (2020).

3 K. Mori, A. Mineshige, T. Saito, M. Sugiura, Y. Ishikawa, F. Fujisaki, K. Namba, T. Kamiyama, T. Otomo, T. Abe, T. Fukunaga,
Experimental Visualization of Interstitialcy Diffusion Pathways in Fast-Fluoride-Ion-Conducting Solid Electrolyte $Ba_{0.6}La_{0.4}F_{2.4}$
ACS Appl. Energy Mater., **3** 2873 (2020).

4 M. Nitta, N. Nagao, Y. Nomura, T. Hirasawa, Y. Sakai, T. Ogata, M. Azuma, S. Torii, T. Ishigaki, Y. Inada,
High-Brightness Red-Emitting Phosphor $La_3(Si,Al)_6(O,N)_{11}:Ce^{3+}$ for Next-Generation Solid-State Light Sources
ACS Appl. Mater. Interfaces, **12** 31652–31658 (2020).

5 K. Shiino, T. Otomo, T. Yamada, H. Arima, K. Hiroi, S. Takata, J. Miyake, K. Miyatake,
Structural investigation of sulfonated polyphenylene ionomers for the design of better performing proton-conductive membranes
ACS Appl. Polym. Mater., **2** 5558-5565 (2020).

6 T. Sato, T. Mochizuki, K. Ikeda, T. Honda, T. Otomo, H. Sagayama, H. Yang, W. Luo, L. Lombardo, A. Züttel, S. Takagi, T. Kono, S. Orimo,
Crystal Structural Investigations for Understanding Hydrogen Storage Properties of $YMgNi_4$-Based Alloys
ACS Omega, **5** 31192 (2020).

7 S. Utsumi, S. Tanaka, K. Maruyama, N. Hatakeyama, K. Itoh, J. Koike, A. Horikawa, H. Iriyama, H. Kanamaru, Y. Amako, T. Iiyama, R. Futamura, R. Kiyanagi, A. Nakao, K. Moriyama, Y. Ishikawa, N. Momozawa,
Flux Growth and Magnetic Properties of Helimagnetic Hexagonal Ferrite $Ba(Fe_{1-x}Sc_x)_{12}O_{19}$ Single Crystals
ACS Omega, **5** 24890-24897 (2020).

8 M. Tanaka, K. Hayakawa, N. Ogawa, T. Kurokawa, K. Kitanishi, K. Ite, T. Matsui, Y. Mori, M. Unno,
Structure determination of the human TRPV1 ankyrin-repeat domain under nonreducing conditions
Acta Crystallogr. Sect. F Struct. Biol. Cryst. Commun., **F76** 130-137 (2020).

9 Y. Wang, Y. Tomota, T. Ohmura, S. Morooka, W. Gong, S. Harjo,
Real time observation of martensite transformation for a 0.4 C low alloyed steel by neutron diffraction
Acta Mater., **184** 30-40 (2020).

10 A. S. Tremsin, D. Perrodin, A. S. Losko, S. C. Vogel, T. Shinohara, K. Oikawa, G. A. Bizarri, E. D. Bourret, J. H. Peterson, K. P. Wang, J. J. Derby,
In-situ observation and analysis of solid-state diffusion and liquid migration in a crystal growth system: A segregation-driven diffusion couple
Acta Mater., **186** 434-442 (2020).

11 Y. Wang, Y. Tomota, T. Ohmura, W. Gong, S. Harjo, M. Tanaka,
Continuous and discontinuous yielding behaviors in ferrite-cementite steels
Acta Mater., **196** 565-575 (2020).

12 S. Harjo, S. Kubota, W. Gong, T. Kawasaki, S. Gao,
Neutron diffraction monitoring of ductile cast iron under cyclic tension–compression
Acta Mater., **196** 584-594 (2020).

13 D. Fukui, N. Nakada, S. Onaka,
Internal residual stress originated from Bain strain and its effect on hardness in Fe–Ni martensite
Acta Mater., **196** 660-668 (2020).

14 T.-N. Lam, S. Y. Lee, N.-T. Tsou, H.-S. Chou, B.-H. Lai, Y.-J. Chang, R. Feng, T. Kawasaki, S. Harjo, P. K. Liaw, A.-C. Yeh, M.-J. Li, R.-F. Cai, S.-C. Loh, E-W. Huang,
Enhancement of fatigue resistance by overload-induced deformation twinning in a CoCrFeMnNi high-entropy alloy
Acta Mater., **201** 412-424 (2020).

15 M. Morgano, N. Kalentics, C. Carminati, J. Capek, M. Makowska, R. Woracek, T. Maimaitiyili, T. Shinohara, R. Loge, M. Strobl,
Investigation of the effect of Laser Shock Peening in Additively Manufactured samples through Bragg Edge Neutron Imaging
Addit. Manuf., **34** 101201 (2020).

16 L. Kong, J. Gong, Q. Hu, F. Capitani, A. Celeste, T. Hattori, A. Sano-Furukawa, W. Yang, H.-k. Ma,
Suppressed Lattice Disorder for Large Emission Enhancement and Structural Robustness in Hybrid Lead Iodide Perovskite Discovered by High-pressure Isotope Effect
Adv. Funct. Mater., **31** 2009131 (2020).

17 K. Hayashi, W. Saito, K. Sugimoto, K. Ohoyama, K. Hayashi, N. Happo, M. Harada, K. Oikawa, Y. Inamura, Y. Miyazaki,
Preparation, thermoelectric properties, and crystal structure of boron-doped Mg_2Si single crystals
AIP Adv., **10** 35115 (2020).

18 Umegaki, Y. Higuchi, Y. Kondo, K. Ninomiya, S. Takeshita, M. Tampo, H. Nakano, H. Oka, J. Sugiyama, M. K. Kubo, Y. Miyake,
Nondestructive High-Sensitivity Detections of Metallic Lithium Deposited on a Battery Anode Using Muonic X-rays
Anal. Chem., **92** 8194 (2020).

19 T. Takami, T. Saito, T. Kamiyama, K. Kawahara, T. Fukunaga, T. Abe,
A new $Bi_{0.7}Fe_{1.3}O_{1.5}F_{1.7}$ phase: Crystal structure, magnetic properties, and cathode performance in fluoride-ion batteries
APL Mater., **8** 051103 (2020).

20 H. Seto, T. Yamada,
Quasi-elastic neutron scattering study of the effects of metal cations on the hydration water between phospholipid bilayers
Appl. Phys. Lett., **116** 133701 (2020).

21 Cho, H. Kim, S. Park,
Magnetic structure of undistorted hexagonal ferrites, $Lu_{0.2}In_{0.8}FeO_3$
Appl. Phys. Lett., **116** 202902 (2020).

22 H. Yamamoto, S. Sekikawa, H. Taniguchi, M. Matsukawa, K. Shigematsu, T. Honda, K. Yamauchi, K. Ikeda, T. Otomo, T. Sakakura, M. Azuma, S. Nimori, Y. Noda, H. Kimura,
Reversible thermally controlled spontaneous magnetization switching in perovskite-type manganite
Appl. Phys. Lett., **117** 112404 (2020).

23 Kitanishi, J. Igarashi, A. Matsuoka, M. Unno,
Identification and Characterization of a Redox Sensor Phosphodiesterase from Ferrovum sp. PN-J185 Containing Bacterial Hemerythrin and HD-GYP Domains
Biochemistry, **59** 983-991 (2020).

24 H. Kawaura, M. Harada, Y. Kondo, M. MIzutani, N. Takahashi, N. L. Yamada,
Operando Time-slicing Neutron Reflectometry Measurements of Solid Electrolyte Interphase Formation on Amorphous Carbon Surfaces of a Li-ion Battery
Bull. Chem. Soc. Jpn., **93** 854-861 (2020).

25 H. Uchiyama, M. Dowaki, K. Kadota, H. Arima, K. Sugiyama, Y. Tozuka,
Single-stranded β-1,3–1,6-glucan as a carrier for improved dissolution and membrane permeation of poorly water-soluble compounds
Carbohydr. Polym., **247** 116698 (2020).

26 Fujii, Y, Yoshida, Y. J. Shan, K. Tezuka, Y. Inaguma, M. Yashima,
Cation- and anion-ordered rutile-type derivative $LiTeO_3(OH)$
Chem. Commun., **56** 10042-10045 (2020).

27 J. Yamaura, S. Maki, T. Honda, T. Otomo, H. Abe, Y. Murakami, N. Ohashi,
Polar nano-region structure in oxynitride perovskite $LaTiO_2N$
Chem. Commun., **56** 1385-1388 (2020).

28 H. Yamauchi, D. P. Sari, I. Watanabe, Y. Yasui, L.-J. Chang, K. Kondo, T. U. Ito, M. Ishikado, M. Hagihara , M. D. Frontzek , S. Chi, J. A. Fernandez-Baca, J. S. Lord, A. Berlie, A. Kotani, S. Mori, S. Shamoto,
High-temperature short-range order in Mn_3RhSi
Commun. Mater., **1** 43 (2020).

29 R. Sei, H. Kawasoko, K. Matsumoto, M. Arimitsu, K. Terakado, D. Oka, S. Fukuda, N. Kimura, H. Kasai, E. Nishibori, K. Ohoyama, A. Hoshikawa, T. Ishigaki, T. Hasegawa, T. Fukumura,
Tetragonality induced superconductivity in anti-$ThCr_2Si_2$-type RE_2O_2Bi (RE = rare earth) with Bi square nets
Dalton Trans., **49** 3321-3325 (2020).

30 Kasai, R. Fujishima, N. Ishida, N. Kitamura, Y. Idemoto,
Effect of Separator and Anode on Electrochemical Characteristics and Crystal Structure of Lithium-ion Battery Cathode Material $0.4Li_2MnO_3$-$0.6LiMn_{1/3}Ni_{1/3}Co_{1/3}O_2$
Electrochemistry, **89** 148-156 (2020).

31 A. Kimura, S. Nakamura, O. Iwamoto, N. Iwamoto, H. Harada, T. Katabuchi, K. Terada, J. Hori, Y. Shibahara, T. Fujii,
Neutron capture and total cross-section measurements of ^{155}Gd and ^{157}Gd at ANNRI in J-PARC
EPJ Web Conf., **239** 1012 (2020).

32 G. Rovira, T. Katabuchi, K. Tosaka, S. Matsuura, K. Terada, O. Iwamoto, A. Kimura, S. Nakamura, N. Iwamoto,
Measurement of the neutron capture cross-section of ^{237}Np using ANNRI at MLF/J-PARC
EPJ Web Conf., **239** 1017 (2020).

33 T. Katabuchi, O. Iwamoto, J. Hori, A. Kimura, N. Iwamoto, S. Nakamura, Y. Shibahara, K. Terada, G. Rovira, S. Matsuura,
Fast Neutron Capture Reaction Data Measurement of Minor Actinides for Development of Nuclear Transmutation Systems
EPJ Web Conf., **239** 1044 (2020).

34 Iwamoto, S. Nakamura, A. Kimura, T. Katabuchi, G. Rovira, K. Y. Hara, O. Iwamoto,
Evaluation of gamma-ray strength function based on measured gamma-ray pulse-height spectra in time-of-flight neutron capture experiments
EPJ Web Conf., **239** 17016 (2020).

35 T. Yamada, H. Seto,
Quasi-Elastic Neutron Scattering Studies on Hydration Water in Phospholipid Membranes
Front. Chem., **8** 8 (2020).

36 J. Pallbo, M. Imai, L. Gentile, S. Takata, U. Olsson, E. Sparr,
NACore amyloid formation in the presence of phospholipids
Front. Physiol., **11** 592117 (2020).

37 K. Komatsu, S. Klotz, S. Nakano, S. Machida, T. Hattori, A. Sano-Furukawa, K. Yamashita, T. Irifune,
Developments of nano-polycrystalline diamond anvil cells for neutron diffraction experiments
High Press. Res., **40** 184-193 (2020).

38 T. Hattori, A. Sano-Furukawa, S. Machida, K. Ohuchi, H. Kira, J. Abe, K. Funakoshi,
Practical effects of pressure-transmitting media on neutron diffraction experiments using Paris-Edinburgh presses
High Press. Res., **40** 325-338 (2020).

39 S. Abe and T. Sato, J. Kuroda, S. Manabe, Y. Watanabe, W. Liao, K. Ito, M. Hashimoto, M. Harada, K. Oikawa, Y. Miyake,
Impact of Hydrided and Non-Hydrided Materials Near Transistors on Neutron-Induced Single Event Upsets
IEEE International Reliability Physics Symposium Proceedings, (2020).

40 W. Liao, M. Hashimoto, S. Manabe, Y. Watanabe, S. Abe, M. Tampo, S. Takeshita, Y. Miyake,
Impact of the Angle of Incidence on Negative Muon-induced SEU Cross Sections of 65-nm Bulk and FDSOI SRAMs
IEEE Trans. Nucl. Sci., **67** 1566-1572 (2020).

41 J. Kuroda, S. Manabe, Y. Watanabe, K. Ito, W. Liao, M. Hashimoto, S. Abe, M. Harada, K. Oikawa, Y. Miyake,
Measurement of Single-Event Upsets in 65-nm SRAMs Under Irradiation of Spallation Neutrons at J-PARC MLF
IEEE Trans. Nucl. Sci., **67** 1599-1605 (2020).

42 Matsubara, T. Masese, E. Suard, O. K. Forslund, E. Nocerino, R. Palm, Z. Guguchia, D. Andreica, A. Hardut, M. Ishikado, K. Papadopoulos, Y. Sassa, M. Månsson,
Cation distributions and magnetic properties of ferrispinel $MgFeMnO_4$
Inorg. Chem., **59** 17970-17980 (2020).

43 T. Yajima, H. Nakajima, T. Honda, K. Ikeda, T. Otomo, H. Takeda, Z. Hiroi,
Titanium Hydride Complex $BaCa_2Ti_2H_{14}$ with a 9-Fold Coordination
Inorg. Chem., **59** 4228-4233 (2020).

44 Y. Matsumoto, Y. Nambu, T. Honda, K. Ikeda, T. Otomo, H. Kageyama,
High-pressure Synthesis of $Ba_2CoO_2Ag_2Te_2$ with Extended CoO_2 Planes
Inorg. Chem., **59** 8121–8126 (2020).

45 Y. Hosoya, Y. Matsumura, Y. Tomota, Y. Onuki, S. Harjo,
Mechanism of Improved Ductility of 1500 MPa-class Ultra-high Strength Cold-rolled Steel Sheet Produced by Rolling and Partitioning Method
ISIJ International, **60** 2097 (2020).

46 H. Sato, K. Iwase, T. Kamiyama, Y. Kiyanagi,
Simultaneous Broadening Analysis of Multiple Bragg Edges Observed by Wavelength-resolved Neutron Transmission Imaging of Deformed Low-carbon Ferritic Steel
ISIJ International, **60** 1254-1263 (2020).

47 N. Tsuchida, T. Tanaka, Y. Toji,
Analysis of Tensile Deformation Behavior by in situ Neutron

Diffraction Experiments of 1 GPa-grade TRIP Steels with High Elongation
ISIJ International, **60** 1349-1357 (2020).

48 T. Wakisaka, K. Kusada, D. Wu, T. Yamamoto, T. Toriyama, S. Matsumura, H. Akiba, O. Yamamuro, K. Ikeda, T. Otomo, N. Palina, Y. Chen, L. S. R. Kumara, C. Song, O. Sakata, W. Xie, M. Koyama, Y. Kubota, S. Kawaguchi, R. L. Arevalo, S. M. Aspera, E. F. Arguelles, H. Nakanishi, H. Kitagawa,
Rational Synthesis for a Noble Metal Carbide
J. Am. Chem. Soc., **142** 1247 (2020).

49 Zhang, X. Tang, Y. Wang, X. Wang, D. Gao, Y. Li, H. Zheng, Y. Wang, X. Wang, R. Fu, M. Tang, K. Ikeda, P. Miao, T. Hattori, A. Sano-Furukawa, C. A. Tulk, J. J. Molaison, X. Dong, K. Li, J. Ju, H. Mao,
Distance-Selected Topochemical Dehydro-Diels-Alder Reaction of 1,4-Diphenylbutadiyne toward Crystalline Graphitic Nanoribbons
J. Am. Chem. Soc., **142** 17662-17669 (2020).

50 N. L. Yamada, T. Hosobata, F. Nemoto, K. Hori, M. Hino, J. Izumi, K. Suzuki, M. Hirayama, R. Kanno, Y. Yamagata,
Application of Precise Neutron Focusing Mirror for Neutron Reflectometry - Latest Results and Future Prospects
J. Appl. Crystallogr., **53** 1462-1470 (2020).

51 Y. Akahama, M. Miyakawa, T. Taniguchi, A. Sano-Furukawa, S. Machida, T. Hattori,
Structure refinement of black phosphorus under high pressure
J. Chem. Phys., **153** 014704 (2020).

52 J. Matsuno, T. Kanamaru, K. Arai, R. Tanaka, J.H. Lee, R. Takahashi, K. Sakurai, S. Fujii,
Synthesis and characterization of nanoemulsion-mediated core crosslinked nanoparticles, and in vivo pharmacokinetics depending on the structural characteristics
J. Control. Release, **324** 405 (2020).

53 Aggarwal, M. H. Meylan, B. P. Lamichhane, C. M. Wensrich,
Energy Resolved Neutron Imaging for Strain Reconstruction Using the Finite Element Method
J. Imaging, **6** 13 (2020).

54 T. Aoyagi, Y. Honda, H. Iked, M. Ikeno, K. Kawagoe, T. Kohriki, T. Kume, T. Mibe, K. Namba, S. Nishimura, N. Saito, O. Sasaki, N. Sato, Y. Sato, H. Sendai, K. Shimomura, S. Shirabe, M. Shoji, T. Suda, T. Suehara, T. Takatomi, M. Tanaka, J. Tojo, K. Tsukada, T. Uchida, T. Ushizawa, H. Wauke, T. Yamanaka, T. Yoshioka,
Performance evaluation of a silicon strip detector for positrons/electrons from a pulsed a muon beam
J. Instrum., **15** P04027 (2020).

55 S. Okada, T. Azuma, D. A. Bennett, P. Caradonna, W. B. Doriese, M. S. Durkin, J. W. Fowler, J. D. Gard, T. Hashimoto, R. Hayakawa, G. C. Hilton, Y. Ichinohe, P. Indelicato, T. Isobe, S. Kanda, M. Katsuragawa, N. Kawamura, Y. Kino, Y. Miyake, K. M. Morgan, K. Ninomiya, H. Noda, G. C. O'Neil, T. Okumura, C. D. Reintsema, D. R. Schmidt, K. Shimomura, P. Strasser, D. S. Swetz, T. Takahashi, S. Takeda, S. Takeshita, H. Tatsuno, Y. Ueno, J. N. Ullom, S. Watanabe, S. Yamada,
X-ray Spectroscopy of Muonic Atoms Isolated in Vacuum with Transition Edge Sensors
J. Low. Temp. Phys., 200 445-451 (2020).

56 T. E. Ashton, P. J. Baker, D. Bauer, A. R. Groves, C, Sotelo-Vazquez, T. Kamiyama, T. Matsukawa, K. M. Kojima, J. A. Darr,
Multiple diffusion pathways in $Li_xNi_{0.77}Co_{0.14}Al_{0.09}O_2$ (NCA) Li-ion battery cathodes
J. Mater. Chem. A, **8** 11545-11552 (2020).

57 H. Abe, A. Takeshita, H. Sudo, K. Akiyama,
CO_2 capture and surface structures of ionic liquid-propanol solutions
J. Mol. Liq., **301** 112445 (2020).

58 K. Sakai, M. Motoki, M. Teshigawara, T. Naoe, K. Haga, A. Watanabe,
Conceptual design of an abnormality sign determination system for the general control system of the Materials and Life Science Experimental Facility at J-PARC
J. Neutron Res., **22** 337-343 (2020).

59 Kajimoto, M. Nakamura, K. Iida, K. Kamazawa, K. Ikeuchi, Y. Inamura, M. Ishikado,
Energy resolution and neutron flux of the 4SEASONS spectrometer revisited
J. Neutron Res., **22** 99-107 (2020).

60 T. Ishida, E. Wakai, S. Makimura, A. M. Casella, D. J. Edwards, R. Prabhakaran, D. J. Senor, K. Ammigan, S. Bidhar, P. G. Hurh, F. Pellemoinee, C. J. Denshamf, M. D. Fitton, J. M. Bennett, D. Kim, N. Simos, M. Hagiwara, N. Kawamura, S. Meigo, K. Yonehara, On behalf of the RaDIATE COLLABORATION,
Tensile behavior of dual-phase titanium alloys under high-intensity proton beam exposure: Radiation-induced omega phase transformation in Ti-6Al-4V
J. Nucl. Mater., **541** 152413 (2020).

61 Y. Kameda, S. Saito, A. Saji, Y. Amo, T. Usuki, H. Watanabe, N. Ara, Y. Umebayashi, K. Fujii, K. Ueno, K. Ikeda, T. Otomo,
Solvation Structure of Li^+ in Concentrated Acetonitrile and N,N-Dimethylformamide Solutions Studied by Neutron Diffraction with $^6Li/^7Li$ Isotopic Substitution Methods
J. Phys. Chem. B, **124** 10456 (2020).

62 K. Yoshimoto, A. Masuno, I. Sato, Y. Ezura, H. Inoue, M. Ueda, M. Mizuguchi, Y. Yanaba, T. Kawashima, T. Oya, Y. Onodera, S. Kohara, K. Ohara,
Principal Vibration Modes of the La_2O_3–Ga_2O_3 Binary Glass Originated from Diverse Coordination Environments of Oxygen Atoms
J. Phys. Chem. B, **124** 5056-5066 (2020).

63 Y. Zhou, T. Yamaguchi, K. Ikeda, K. Yoshida, T. Otomo, C. Fang, W. Zhang, F. Zhu,
Dihydrogen Bonds in Aqueous $NaBD_4$ Solution by Neutron and X-Ray Diffraction
J. Phys. Chem. Lett., **11** 1622 (2020).

64 M. A. González, O. Borodin, M. Kofu, K. Shibata, T. Yamada, O. Yamamuro, K. Xu, D. L. Price, M.-L. Saboungi,
Nanoscale Relaxation in "Water-in-Salt" and "Water-in-Bisalt" Electrolytes
J. Phys. Chem. Lett., **11** 7279 (2020).

65 Z. Liu, C. Yang, L. Zhang, Y. Yu, M. Yu, V. G. Sakai, M. Tygai, T. Yamada, L. He, X. Zhang, L. Hong,
Heterogeneity of Water Molecules on the Free Surface of Thin Reduced Graphene Oxide Sheets
J. Phys. Chem. C Nanomater. Interfaces, **124** 11064-11074 (2020).

66 Hiroto, T. J Sato, H. Cao, T. Hawai, T. Yokoo, S. Itoh, R. Tamura,
Noncoplanar ferrimagnetism and local crystalline-electric-field anisotropy in the quasicrystal approximant $Au_{70}Si_{17}Tb_{13}$
J. Phys. Condens. Matter, **32** 415802 (2020).

67 M. Abe, T. Tanimori, A. Takada, Y. Mizumura, S. Komura, T. Kishimoto, T. Takemura, K. Yoshikawa, Y. Nakamura, Y. Nakamasu, T. Taniguchi, K. Onozaka, K. Saito, T. Mizumoto, S. Sonoda, J. D. Parker, K. Miuchi, T. Sawano,
Development of a μ-PIC with glass substrate aiming at high gas gain
J. Phys. Conf. Ser., **1498** 012002 (2020).

68 S. Ikeda, K. Kaneko, Y. Tanaka, T. Kawasaki, T. Hanashima, K. Munakata, A. Nakao, R. Kiyanagi, T. Ohhara, K. Mochizuki, A. Kondo, K. Kindo, Y. Homma, M. D. Frontzek, H. Kobayashi,
Multi-Step Magnetic Transitions in $EuNiIn_4$
J. Physical Soc. Japan, **89** 14707 (2020).

69 Otomo, K. Ikeda, T. Honda,
Structural Studies of Hydrogen Storage Materials with Neutron Diffraction: A Review
J. Physical Soc. Japan, **89** 51001 (2020).

70 T. U. Ito, W. Higemoto, K. Shimomura,
Negatively Charged Muonium and Related Centers in Solids
J. Physical Soc. Japan, **89** 51007 (2020).

71 K. Sato, K. Ikeuchi, R. Kajimoto, S. Wakimoto, M. Arai, M. Fujita,
Coexistence of Two Components in Magnetic Excitations of $La_{2-x}Sr_xCuO_4$ (x = 0.10 and 0.16)
J. Physical Soc. Japan, **89** 114703 (2020).

72 M. Komabuchi, D. Urushihara, T. Asaka, K. Fukuda, T. Ohhara, K. Munakata, Y. Ishikawa,
Crystal Structure and Cation Distribution of the X-type Hexaferrite $Sr_2Co_2Fe_{28}O_{46}$
J. Physical Soc. Japan, **89** 034601 (2020).

73 M. Kofu, O. Yamamuro,
Dynamics of Atomic Hydrogen in Palladium Probed by Neutron Spectroscopy
J. Physical Soc. Japan, **89** 051002 (2020).

74 K. Iida, M. Kofu, K. Suzuki, N. Murai, S. Ohira-Kawamura, R. Kajimoto, Y. Inamura, M. Ishikado, S. Hasegawa, T. Masuda, Y. Yoshida, K. Kakurai, K. Machida, S.-H. Lee,
Horizontal line nodes in Sr_2RuO_4 proved by spin resonance
J. Physical Soc. Japan, **89** 053702 (2020).

75 T. Noda, Y. Doi, Y. Ohta, S. Takata, A. Takano, Y. Matsushita,
Preparation, characterization, and dilute solution properties of four-branched cage-shaped poly (ethylene oxide)
J. Polym. Sci., **58** 2098-2107 (2020).

76 R. Iizuka-Oku, W. Gui, K. Komatsu, T. Yagi, H. Kagi,
High-pressure responses of alkali metal hydrogen carbonates, $RbHCO_3$and $CsHCO_3$: Findings of new phases and unique compressional behavior
J. Solid State Chem., **283** 121139 (2020).

77 J. Hendriks, N. O'Dell, A. Wills, A. Tremsin, C. Wensrich, T. Shinohara,
Bayesian non-parametric Bragg-edge fitting for neutron transmission strain imaging
J. Strain Anal. Eng. Des., (2020).

78 D. Kitahara, H. Arima, T. Kawamata, K. Sugiyama, T. Mikouchi,
The location of Mn and Fe in axinite–(Fe) from Nandan, China determined by anomalous X–ray scattering (AXS)
Journal of Mineralogical and Petrological Sciences, **115** 227-235 (2020).

79 M. Nagashima, Y. Sano, T. Kochi, M. Akasaka, A. Sano–Furukawa,
Crystal chemistry of Sr–rich piemontite from manganese ore deposit of the Tone mine, Nishisonogi Peninsula, Nagasaki, southwest Japan
Journal of Mineralogical and Petrological Sciences, **115** 391-406 (2020).

80 F. Funama, M. Hino, T. Oda, H. Endo, T. Hosobata, Y. Yamagata, S. Tasaki,
Observation of TOF-MIEZE Signals with Focusing Mirrors at BL06, MLF, J-PARC
Journal of Surface Investigation: X-ray, Synchrotron and Neutron Techniques, **14** S50-S55 (2020).

81 K. Kataoka,
Oxide single crystals with high lithium-ion conductivity as solid electrolytes for all-solid-state lithium secondary battery applications
Journal of the Ceramic Society of Japan, **128** 7-18 (2020).

82 Z. Xu, T. Sato, J. Nakamura, A. Koda, K. Shimomura, A. Filonov, D. Migas, T. Suemasu,
Hydrogen states in hydrogen-passivated semiconducting barium disilicide measured via muon spin rotation
Jpn. J. Appl. Phys., **59** 071004 (2020).

83 S. Makimura, J. Park, A. Sato, S. Matoba, N. Kawamura, T. Yamazaki, K. Ninomiya, D. Tomono, N. Nakazato, M. Calviani, I. L. Garcia,
Feasibility Study for NITE SiC/SiC as the Target Material for Pions/Muons Production at High-Power Proton Accelerator Facilities
JPS Conf. Proc., **28** 031005 (2020).

84 T. Naoe, S. Harjo, T. Kawasaki, Z. Xiong, M. Futakawa,
Change in Mechanical Properties by High-Cycle Loading Up to Gigacycle for 316L Stainless Steel
JPS Conf. Proc., **28** 061009 (2020).

85 N. Nakamura, R. Higashinaka, K. Fushiya, R. Tsubota, T. U. Ito, W. Higemoto, A. Nakao, R. Kiyanagi, T. Ohhara, K. Kaneko, T. D. Matsuda, Y. Aoki,
μSR and Neutron Scattering Studied on Possible Partially-Disordered Magnetic State Coexisting with Heavy Quasiparticles in $SmPt_2Si_2$
JPS Conf. Proc., **29** 012009 (2020).

86 D. Hirai, A. Koda, A. Matsuo, K. Kindo, T. Yajima, Z. Hiroi,
Muon Spin Rotation, High-Field Magnetization, and Structural Study on a Spin–Orbit-Entangled Mott Insulator Ba_2MgReO_6
JPS Conf. Proc., **30** 11143 (2020).

87 S. Tsunoda, K. Horigane, H. Okabe, K. Machida, M. Akimitsu, K. Kawashima, R. Horie, K. Kobayashi, A. Koda, R. Kadono, J. Akimitsu,
μSR study of the magnetic state in hole and electron doped Sr_2IrO_4
JPS Conf. Proc., **30** 11145 (2020).

88 N. Metoki, A. A. Aczel, D. Aoki, S. Chi, J. A. Fernandez-Baca, J.-C. Griveau, M. Hagihala, T. Hong, Y. Haga, K. Ikeuchi, Y. Inamura, K. Kamazawa, R. Kajimoto, H. Kitazawa, T. Masuda, M. Matsuda, M. Nakamura, J. Ohtsuki, D. Pajerowski, H. S. Suzuki, E. Yamamoto, H. Yamauchi,
The f-electron State of the Heavy Fermion Superconductor $NpPd_5Al_2$ and the Isostructural Family
JPS Conf. Proc., **30** 011123 (2020).

89 S. Nakazato, K. Iwasa, D. Hashimoto, M. Shiozawa, K. Kuwahara, H. Nakao, H. Sagayama, M. Ishikado, T. Ohhara, A. Nakao, K. Munakata, R. Kiyanagi,
Successive Phase Transitions in $R_3Ir_4Sn_{13}$ (R: La and Ce) Investigated Using Neutron and X-ray Diffraction
JPS Conf. Proc., **30** 011128 (2020).

90 K. Iba, T. Matsumura, A. Nakao, Y. Ishikawa, K. Ohishi, R. Kiyanagi, Y. Kousaka, S. Ohara,
Magnetic Structure of a Chiral Magnet $DyNi_3Al_9$
JPS Conf. Proc., **30** 011164 (2020).

91 K. Akutsu-Suyama, K. Park, R. Takakura, K. Tamura, M. Cagnes, T.A. Darwish, T. Yamada, Y. Sawama, H. Sajiki,
Metal catalyzed H-D exchange methods using D_2O as a deuterium source: A comparative study in different sealed devices
JPS Conf. Proc., **33** 011150 (2020).

92 T. Yoshimura, N. K. Kawano, S. Yada, H. Iwase,
Adsorption and aggregation properties of Gemini-type amphiphilic dendrimers
Langmuir, **36** 563 (2020).

93 Y. Higaki, M. Kobayashi, A. Takahara,
Hydration State Variation of Polyzwitterion Brushes through Interplay with Ions
Langmuir, **36** 9015 (2020).

94 K. Ito, M. Harada, N. L. Yamada, K. Kudo, H. Aoki, T. Kanaya,
Water Distribution in Nafion Thin Films on Hydrophilic and

Hydrophobic Carbon Substrates
Langmuir, **36** 12830–12837 (2020).

95 T. Miyazaki, K. Shimokita, K. Yamamoto, H. Aoki, N. L. Yamada, N. Miyata,
Neutron Reflectivity on the Mobile Surface and Immobile Interfacial Layers in the Poly(vinyl acetate) Adsorption Layer on a Si Substrate with Deuterated Toluene Vapor-Induced Swelling
Langmuir, **36** 15181-15188 (2020).

96 T. Miyazaki, N. Miyata, T. Yoshida, H. Arima, Y. Tsumura, N. Torikai, H. Aoki, K. Yamamoto, T. Kanaya, D. Kawaguchi, K. Tanaka,
Detailed Structural Study on the Poly(vinyl alcohol) Adsorption Layers on a Si Substrate with Solvent Vapor-Induced Swelling
Langmuir, **36** 3415-3424 (2020).

97 T. Sugahara, M. Akamatsu, H. Iwase, Y. Takamatsu, K. Sakai, H. Sakai,
Structural change of α-gel (α-form hydrated crystal) induced by temperature and shear flow in an oleic acid-based gemini surfactant system
Langmuir, **36** 4695-4701 (2020).

98 T. Kimura, T. Kawamoto, M. Aoki, T. Mizusawa, N. L. Yamada, K. Miyatake, J. Inukai,
Sublayered Thin Films of Hydrated Anion Exchange Ionomer for Fuel Cells Formed on SiO_2 and Pt Substrates Analyzed by Neutron Reflectometry under Controlled Temperature and Humidity Conditions
Langmuir, **36** 4955-4963 (2020).

99 K. Igata, T. Sakamaki, Y. Inutsuka, Y. Higaki, M. K. Okajima, N. L. Yamada, T. Kaneko, A. Takahara,
Cationic Polymer Brush/Giant Polysaccharide Sacran Assembly: Structure and Lubricity
Langmuir, **36** 6494-6501 (2020).

100 S. Yada, H. Shimosegawa, H. Fujita, M. Yamada, Y. Matsue, T. Yoshimura,
Microstructural Characterization of Foam Formed by a Hydroxy Group-Containing Amino Acid Surfactant Using Small-Angle Neutron Scattering
Langmuir, **36** 7808–7813 (2020).

101 C.I. Gupit, X. Li, R. Maekawa, N. Hasegawa, H. Iwase, S. Takata, M. Shibayama,
Nanostructures and viscosities of nafion dispersions in water/ethanol from dilute to concentrated regimes
Macromolecules, **53** 1464 (2020).

102 M. Ohira, Y. Tsuji, N. Watanabe, K. Morishima, E. P. Gilbert, X. Li, M. Shibayama,
Quantitative structure analysis of a near-ideal polymer network with deuterium label by small-angle neutron scattering
Macromolecules, **53** 4047 (2020).

103 T. Nishimura, L. de Campo, H. Iwase, K. Akiyoshi,
Determining the hydration in the hydrophobic layer of permeable polymer vesicles by neutron scattering
Macromolecules, **53** 7546 (2020).

104 Y. Oda, M. Inutsuka, R. Awane, M. Totani, N. L. Yamada, M. Haraguchi, M. Ozawa, H. Matsuno, K. Tanaka,
Dynamic Interface based on Segregation of an Amphiphilic Hyperbranched Polymer Containing Fluoroalkyl and Oligo(ethylene oxide) Moieties
Macromolecules, **53** 2380-2387 (2020).

105 A. Izumi, Y. Shudo, M. Shibayama, T. Yoshida, N. Miyata, T. Miyazaki, H. Aoki,
Interfacial Cross-Link Inhomogeneity of a Phenolic Resin on a Silica Surface As Revealed by X-ray and Neutron Reflection Measurements
Macromolecules, **53** 4082-4089 (2020).

106 K. Tashiro, K. Kusaka, H. Yamamoto, M. Hanesaka,
Introduction of Disorder in the Crystal Structures of Atactic Poly(vinyl Alcohol) and Its Iodine Complex To Solve a Dilemma between X-ray and Neutron Diffraction Data Analyses
Macromolecules, **53** 6656-6671 (2020).

107 Y. Cui, C. Li, S. Harjo, C. Zhang, R. Li, W. Zheng, Y. Wang,
A study on the micromechanical behavior of Ti-55531 titanium alloy with lamellar microstructure byin-situ neutron diffraction
MATEC Web of Conferences, **321** 11013 (2020).

108 Y. Tomota, T. Murakami, Y. X. Wang, T. Ohmura, S. Harjo, Y. H. Su, T. Shinohara,
Influence of carbon concentration and magnetic transition on the austenite T lattice parameter of 30Mn-C steel
Mater. Charact., **163** 110243 (2020).

109 D. Ma, P. Yang, X.-F. Gu, Y. Onuki, S. Sato,
In-situ neutron diffraction investigation on the martensite transformation, texture evolution and martensite reversion in high manganese TRIP steel
Mater. Charact., **163** 110244 (2020).

110 Z. Wei, P. Yang, X. Gu, Y. Onuki, S. Sato,
Transformation textures in pure titanium: Texture memory vs surface effect
Mater. Charact., **164** 110359 (2020).

111 K. Itoh, J. Saida, T. Otomo,
Structural study of $Ni_{67}Zr_{33}$ amorphous alloy: Interatomic space analysis approach
Mater. Chem. Phys., **240** 122214 (2020).

112 Woo, M. Naeem, J.-S. Jeong, C.-M. Lee, S. Harjo, T. Kawasaki, H. He, X.-L. Wang,
Comparison of dislocation density, twin fault probability, and stacking fault energy between CrCoNi and CrCoNiFe medium entropy alloys deformed at 293 and 140K
Mater. Sci. Eng. A Struct. Mater., **781** 139224 (2020).

113 S. Harjo, K. Aizawa, W. Gong, T. Kawasaki,
Neutron Diffraction Monitoring of As-Cast $Mg_{97}Zn_1Y_2$ during Compression and Tension
Mater. Trans., **61** 828-832 (2020).

114 J. W. Bae, J. Jung, J. G. Kim, J. M. Park, S. Harjo, T. Kawasaki, W. Woo, H. S. Kim,
On the phase transformation and dynamic stress–strain partitioning of ferrous medium-entropy alloy using experimentation and finite element method
Materialia, **9** 100619 (2020).

115 O. Holderer, M. Carmo, M. Shviro, W. Lehnert, Y. Noda, S. Koizumi, M.-S. Appavou, M. Appel, H. Frielinghaus,
Fuel Cell Electrode Characterization Using Neutron Scattering
Materials, **13** 1474 (2020).

116 T. Kai, K. Hiroi, Y. Su, M. Segawa, T. Shinohara, Y. Matsumoto, J. D. Parker, H. Hayashida, K. Oikawa,
Feasibility Study of Two-Dimensional Neutron-Resonance Thermometry using Molybdenum in 316 Stainless-Steel
Materials Research Forum LLC, **15** 149-153 (2020).

117 K. Oikawa, Y. Kiyanagi, H. Sato, K. Ohmae, A. H. Pham, K. Watanabe, Y. Matsumoto, T. Shinohara, T. Kai, S. Harjo, M. Ohnuma, S. Morito, T. Ohba, A. Uritani, M. Ito,
Pulsed Neutron Imaging Based Crystallographic Structure Study of a Japanese Sword made by Sukemasa in the Muromachi Period
Materials Research Forum LLC, **15** 207-213 (2020).

118 J. D. Parker, M. Harada, H. Hayashida, K. Hiroi, T. Kai, Y. Matsumoto, T. Nakatani, K. Oikawa, M. Segawa, T. Shinohara, Y. Su, A. Takada, T. Tanimori, Y. Kiyanagi,
Development of Event-Type Neutron Imaging Detectors at the Energy-Resolved Neutron Imaging System RADEN at J-PARC
Materials Research Proceedings, **15** 102-107 (2020).

119 Y. Oba, D. Ito, Y. Saito, Y. Onodera, J. D. Parker, T. Shinohara, K. Oikawa,
Neutron Transmission Spectrum of Liquid Lead Bismuth Eutectic
Materials Research Proceedings, **15** 160-164 (2020).

120 H. Sato, Y. Kiyanagi, K. Oikawa, K. Ohmae, A. H. Pham, K. Watanabe, Y. Matsumoto, T. Shinohara, T. Kai, S. Harjo, M. Ohnuma, S. Morito, T. Ohba, A. Uritani, M. Itoh,
Crystallographic Microstructure Study of a Japanese Sword made by Noritsuna in the Muromachi Period by Pulsed Neutron Bragg-Edge Transmission Imaging
Materials Research Proceedings, **15** 214-220 (2020).

121 Y. Matsumoto, K. Watanabe, K. Ohmae, A. Uritani, Y. Kiyanagi, H. Sato, M. Ohnuma, A. H. Pham, S. Morito, T. Ohba, K. Oikawa, T. Shinohara, T. Kai, S. Harjo, M. Ito,
Comparative Study of Ancient and Modern Japanese Swords using Neutron Tomography
Materials Research Proceedings, **15** 221-226 (2020).

122 K. Ohmae, Y.i Kiyanagi, H. Sato, K. Oikawa, A. H. Pham, K. Watanabe, Y. Matsumoto, T. Shinohara, T. Kai, S. Harjo, M. Ohnuma, S. Morito, T. Ohba, A. Uritani, M. Ito,
Crystallographic Structure Study of a Japanese Sword Masamitsu made in the 1969 using Pulsed Neutron Imaging
Materials Research Proceedings, **15** 227-232 (2020).

123 T.-N. Lam, C.-W. Tsai, B.-K. Chen, B.-H. Lai, H.-C. Liu, T. Kawasaki, S. Harjo, B.-H. Lin, E-W. Huang,
Element Effects of Mn and Ge on the Tuning of Mechanical Properties of High-Entropy Alloys
Metall. Mater. Trans. A Phys. Metall. Mater. Sci., **51** 5023-5028 (2020).

124 Tanaka, T. Chatake, S. Fujiwara, T. Hosoya, K. Kusaka, N. Niimura, T. Yamada, N. Yano,
Current status and near future plan of neutron protein crystallography at J-PARC
Methods Enzymol., **634** 101-123 (2020).

125 M. Budayova-Spano, K. Koruza, Z. Fisher,
Large crystal growth for neutron protein crystallography
Methods Enzymol., **634** 21-46 (2020).

126 S. Urakawa, T. Inoue, T. Hattori, A. Sano-Furukawa, S. Kohara, D. Wakabayashi, T. Sato, N. Funamori, K. Funakoshi,
X-ray and neutron study on the structure of hydrous SiO_2 glass up to 10 GPa
Minerals, **10** 84 (2020).

127 S. Kajiyama, H. Iwase, M. Nakayama, R. Ichikawa, D. Yamaguchi, H. Seto, T. Kato,
Shear-induced liquid-crystalline phase transition behaviour of colloidal solutions of hydroxyapatite nanorod composites
Nanoscale, **12** 11468-11479 (2020).

128 Watanabe, S. Katsuhara, H. Mamiya, Y. Kawamura, T. Yamamoto, K. Tajima, T. Isono, T. Satoh,
Highly asymmetric lamellar nanostructures from nanoparticle–linear hybrid block copolymers
Nanoscale, **12** 16526-16534 (2020).

129 Komatsu, S. Machida, F. Noritake, T. Hattori, A. Sano-Furukawa, R. Yamane, K. Yamashita, H. Kagi,
Ice Ic without stacking disorder by evacuating hydrogen from hydrogen hydrate
Nat. Commun., **11** 464 (2020).

130 Li, P. Liu, E. Zhao, Z. Zhang, T. Guidi, M. D. Le, M. Avdeev, K. Ikeda, T. Otomo, M. Kofu, K. Nakajima, J. Chen, L. He, Y. Ren, X.-L. Wang, B. Wang, Z. Ren, H. Zhao, F. Wang,
Ultralow Thermal Conductivity from Transverse Acoustic Phonon Suppression in Distorted Crystalline α-MgAgSb
Nat. Commun., **11** 942 (2020).

131 Zhang, K. Fujii, E. Niwa, M. Hagihala, T. Kamiyama, M. Yashima,
Oxide-ion conduction in the Dion–Jacobson phase $CsBi_2Ti_2NbO_{10-\delta}$
Nat. Commun., **11** 1224 (2020).

132 Q. Ren, C. Fu, Q. Qiu, S. Dai, Z. Liu, T. Masuda, S. Asai, M. Hagihala, S. Lee, S. Torri, T. Kamiyama, L. He, X. Tong, C. Felser, D. J. Singh, T. Zhu, J. Yang, J. Ma,
Establishing the carrier scattering phase diagram for ZrNiSn-based half-Heusler thermoelectric materials
Nat. Commun., **11** 3142 (2020).

133 Fujihala, K. Morita, R. Mole, S. Mitsuda, T. Tohyama, S. Yano, D. Yu, S. Sota, T. Kuwai, A. Koda, H. Okabe, H. Lee, S. Itoh, T. Hawai, T. Masuda, H. Sagayama, A. Matsuo, K. Kindo, S. Ohira-Kawamura, K. Nakajima,
Gapless spin liquid in a square-kagome lattice antiferromagnet
Nat. Commun., **11** 3429 (2020).

134 T. Yamamoto, A. Chikamatsu, S. Kitagawa, N. Izumo, S. Yamashita, H. Takatsu, M. Ochi, T. Maruyama, M. Namba, W. Sun, T. Nakashima, F. Takeiri, K. Fujii, M. Yashima, Y. Sugisawa, M. Sano, Y. Hirose, D. Sekiba, C. M. Brown, T. Honda, K. Ikeda, T. Otomo, K. Kuroki, K. Ishida, T. Mori, K. Kimoto, T. Hasegawa, H. Kageyama,
Strain-induced creation and switching of anion vacancy layers in perovskite oxynitrides
Nat. Commun., **11** 5923 (2020).

135 F. B. Li, M. Li, X. Xu, Z. C. Yang, H. Xu, C. K. Jia, K. Li, J. He, B. Li, H. Wang,
Understanding colossal barocaloric effects in plastic crystals
Nat. Commun., **11** 4190 (2020).

136 R. Bauer, J. S. Tse, K. Komatsu, S. Machida, T. Hattori,
Slow compression of crystalline ice at low temperature
Nature, **585** E10 (2020).

137 P. Wu, F.-R. Fan, M. Hagihala, M. Kofu, K. Peng, Y. Ishikawa, S. Lee, T. Honda, M. Yonemura, K. Ikeda, T. Otomo, G. Wang, K. Nakajima, Z. Sun, T. Kamiyama,
Strong lattice anharmonicity exhibited by the high-energy optical phonons in thermoelectric material
New J. Phys., **22** 083083 (2020).

138 Xu, G. Dai, Y. Li, Z. Yin, Y. Rong, L. Tian, P. Liu, H. Wang, L. Xing, Y. Wei, R. Kajimoto, K. Ikeuchi, D. L. Abernathy, X. Wang, C. Jin, X. Lu, G. Tan, P. Dai,
Strong local moment antiferromagnetic spin fluctuations in V-doped LiFeAs
NPJ Quantum Mater., **5** 11 (2020).

139 T. Okudaira, T. Oku, T. Ino, H. Hayashida, H. Kira, K. Sakai, K. Hiroi, S. Takahashi, K. Aizawa, H. Endo, S. Endo, M. Hino, K. Hirota, T. Honda, K. Ikeda, K. Kakurai, W. Kambara, M. Kitaguchi, T. Oda, H. Ohshita, T. Otomo, H.M. Shimizu, T. Shinohara, J. Suzuki, T. Yamamoto,
Development and application of a 3He neutron spin filter at J-PARC
Nucl. Instrum. Methods Phys. Res. A, **977** 164301 (2020).

140 T. Naoe, H. Kogawa, T. Wakui, M. Teshigawara, K. Haga, M. Futakawa,
Pressure wave induced sound measurement for diagnosing the operation status of the J-PARC pulsed spallation neutron source
Nucl. Instrum. Methods Phys. Res. A, **982** 164566 (2020).

141 Zhoua, T. Yamaguchi, W. Zhang, K. Ikeda, K. Yoshida, F. Zhu, H. Liu,
Structure of Aqueous H_3BO_3 Solutions by DFT and Neutron Scattering
Phys. Chem. Chem. Phys., **22** 17160-17170 (2020).

142 Kawano, K. Sadakane, H. Iwase, M. Matsugami, B. A. Marekha, A. Idrissi, T. Takamuku,
Mixing states of imidazolium-based ionic liquid, [C_4mim][TFSI], with cycloethers studied by SANS, IR, and NMR experiments and MD simulations
Phys. Chem. Chem. Phys., **22** 5332-5346 (2020).

143 Y. Higuchi, D. Setoyama, K. Isegawa, Y. Tsuchikawa, Y. Matsumoto, J. D. Parker, T. Shinohara, Y. Nagai,
Pulsed neutron imaging for differentiation of ice and liquid water towards fuel cell vehicle applications
Phys. Chem. Chem. Phys., **23** 1062-1071 (2020).

144 Nagashima, T. Armbruster, M. Akasaka, A. Sano-Furukawa, D. Nishio-Hamane, A. Malsy, T. Imaoka, K. Nakashima,
Multi-methodical study of the Ti, Fe_{2+} and Fe_{3+} distribution in chevkinite-subgroup minerals: X-ray diffraction, neutron diffraction, ^{57}Fe Mössbauer spectroscopy and electron-microprobe analyses
Phys. Chem. Miner., **47** 29 (2020).

145 T. Oda, M. Hino, H. Endo, H. Seto, Y. Kawabata,
Tuning Neutron Resonance Spin-Echo Spectrometers with Pulsed Beams
Phys. Rev. Appl., **14** 054032 (2020).

146 Cai, S. Bao, W. Wang, Z. Ma, Z.-Y. Dong, Y. Shangguan, J. Wang, K. Ran, S. Li, K. Kamazawa, M. Nakamura, D. Adroja, S.-L. Yu, J.-X. Li, J. Wen,
Spin dynamics of a magnetic Weyl semimetal $Sr_{1-x}Mn_{1-y}Sb_2$
Phys. Rev. B, **101** 134408 (2020).

147 M. M. R. Bhuiyan, X.-G. Zheng, M. Hagihala, S. Torii, T. Kamiyama, T. Kawae,
Spin order in the classical spin kagome antiferromagnet $MgxMn_{4-x}(OH)_6Cl_2$
Phys. Rev. B, **101** 134424 (2020).

148 S. Asai, T. Oyama, K. Nawa, A. Nakao, K. Munakata, K. Kuwahara, M. Hagihala, S. Itoh, Z. Hiroi, T. Masuda,
Helical and collinear spin density wave order in the S=1/2 one-dimensional frustrated chain compound $NaCuMoO_4(OH)$ investigated by neutron scattering
Phys. Rev. B, **101** 144437 (2020).

149 H. Masuda, H. Sakai, H. Takahashi, Y. Yamasaki, A. Nakao, T. Moyoshi, H. Nakao, Y. Murakami, T. Arima, S. Ishiwata,
Field-induced spin reorientation in the antiferromagnetic Dirac material $EuMnBi_2$ revealed by neutron and resonant x-ray diffraction
Phys. Rev. B, **101** 174411 (2020).

150 C. Tan, Z. F. Ding, J. Zhang, Z. H. Zhu, O. O. Bernal, P. C. Ho, A. D. Hillier, A. Koda, H. Luetkens, G. D. Morris, D. E. MacLaughlin, L. Shu,
Slow magnetic fluctuations and critical slowing down in $Sr_2Ir_{1-x}Rh_xO_4$
Phys. Rev. B, **101** 195108 (2020).

151 S. Bao, Z. Cai, W. Si, W. Wang, X. Wang, Y. Shangguan, Z. Ma, Z.-Y. Dong, R. Kajimoto, K. Ikeuchi, S.-L. Yu, J. Sun, J.-X. Li, J. Wen,
Evidence for magnon-phonon coupling in the topological magnet Cu_3TeO_6
Phys. Rev. B, **101** 214419 (2020).

152 M. Soda, S. Itoh, T. Yokoo, G. Ehlers, H. Kawano-Furukawa, T. Masuda,
Magnetic correlations in $YBaCo_4O_7$ on kagome and triangular lattices
Phys. Rev. B, **101** 214444 (2020).

153 E. Fogh, T. Kihara, R. Toft-Petersen, M. Bartkowiak, Y. Narumi, O. Prokhnenko, A. Miyake, M. Tokunaga, K. Oikawa, M. K. Sørensen, J. C. Dyrnum, H. Grimmer, H. Nojiri, N. B. Christensen,
Magnetic structures and quadratic magnetoelectric effect in $LiNiPO_4$ beyond 30 T
Phys. Rev. B, **101** 024403 (2020).

154 T. Uchino, N. Teramachi, R. Matsuzaki, E. Tsushima, S. Fujii, Y. Seto, K. Takahashi, T. Mori, Y. Adachi, Y. Nagashima, Y. Sakaguchi, K. Ohishi, A. Koda, T. Sakurai, H. Ohta,
Proximity coupling of superconducting nanograins with fractal distributions
Phys. Rev. B, **101** 035146 (2020).

155 T. Sato, Y. Araki, A. Miyake, A. Nakao, N. Abe, M. Tokunaga, S. Kimura, Y. Tokunaga, T. Arima,
Magnetic phase diagram enriched by chemical substitution in a noncentrosymmetric helimagnet
Phys. Rev. B, **101** 054414 (2020).

156 S. Klotz, K. Komatsu, A. Polian, S. Machida, A. Sano-Furukawa, J. Itié, T. Hattori,
Crystal structure and magnetism of MnO under pressure
Phys. Rev. B, **101** 064105 (2020).

157 K. H. Lee, I. Y. Hwang, J.-H. Chung, H. Ishibashi, Y. Kubota, S. Kawaguchi, S. Lee, S. Torii, M. Hagihala, T. Kamiyama,
Stabilization of orthorhombic distortions in Cu- and Co-doped ferrimagnetic Mn_3O_4
Phys. Rev. B, **101** 085126 (2020).

158 H. Ueda, S. Onoda, Y. Yamaguchi, T. Kimura, D. Yoshizawa, T. Morioka, M. Hagiwara, M. Hagihala, M. Soda, T. Masuda, T. Sakakibara, K. Tomiyasu, S. Ohira-Kawamura, K. Nakajima, R. Kajimoto, M. Nakamura, Y. Inamura, N. Reynolds, M. Frontzek, J. S. White, M. Hase, Y. Yasui,
Emergent spin-1 Haldane gap and ferroelectricity in a frustrated spin-1/2 ladder
Phys. Rev. B, **101** 140408(R) (2020).

159 Abe, S. Shiozawa, K. Matsuura, H. Sagayama, A. Nakao, T. Ohhara, Y. Tokunaga, T. Arima,
Magnetically induced electric polarization in $Ba_3Fe_2O_5Cl_2$ with tunable direction in three dimensions
Phys. Rev. B, **101** 180407(R) (2020).

160 M. Hirschberger, T. Nakajima, M. Kriener, T. Kurumaji, L. Spitz, S. Gao, A. Kikkawa, Y. Yamasaki, H. Sagayama, H. Nakao, S. Ohira-Kawamura, Y. Taguchi, T. Arima, Y. Tokura,
High-field depinned phase and planar Hall effect in the skyrmion host Gd_2PdSi_3
Phys. Rev. B, **101** 220401(R) (2020).

161 K. Iida, H. K. Yoshida, A. Nakao, H. O. Jeschke, Y. Iqbal, K. Nakajima, S. Ohira-Kawamura, K. Munakata, Y. Inamura, N. Murai, M. Ishikado, R. Kumai, T. Okada, M. Oda, K. Kakurai, M. Matsuda,
$q=0$ long-range magnetic order in centennialite $CaCu_3(OD)_6Cl_2 \cdot 0.6D_2O$: A spin-1/2 perfect kagome antiferromagnet with $J_1-J_2-J_d$
Phys. Rev. B, **101** 220408(R) (2020).

162 S. Uechi, K. Ohoyama, Y. Fukumoto, Y. Kanazawa, N. Happo, M. Harada, Y. Inamura, K. Oikawa, W. Matsuhra, F. Iga, A. K. R. Ang, K. Hayashi,
Behavior of Sm in the boron cage of Sm-doped RB_6 (R =Yb, La) observed by multiple-wavelength neutron holography
Phys. Rev. B, **102** 54104 (2020).

163 Y. Araki, T. Sato, Y. Fujima, N. Abe, M. Tokunaga, S. Kimura, D. Morikawa, V. Ukleev, Y. Yamasaki, C. Tabata, H. Nakao, Y. Murakakmi, H. Sagayama, K. Ohishi, Y. Tokunaga, T. Arima,
Metamagnetic transitions and magnetoelectric responses in the chiral polar helimagnet Ni_2InSbO_6

Phys. Rev. B, **102** 54409 (2020).

164 J. Sugiyama, I. Umegaki, S. Takeshita, H. Sakurai, S. Nishimura, O. K. Forslund, E. Nocerino, N. Matsubara, M. Månsson, T. Nakano, I. Yamauchi, K. Ninomiya, M. K. Kubo, K. Shimomura,
Nuclear magnetic field in $Na_{0.7}CoO_2$ detected with μ–SR
Phys. Rev. B, **102** 144431 (2020).

165 H. Takahashi, K. Aono, Y. Nambu, R. Kiyanagi, T. Nomoto, M. Sakano, K. Ishizaka, R. Arita, S. Ishiwata,
Competing spin modulations in the magnetically frustrated semimetal EuCuSb
Phys. Rev. B, **102** 174425 (2020).

166 C. Kim, J. Jeong, P. Park, T. Masuda, S. Asai, S. Itoh, H.-S. Kim, A. Wildes, J.-G. Park,
Spin waves in the two-dimensional honeycomb lattice XXZ-type van der Waals antiferromagnet $CoPS_3$
Phys. Rev. B, **102** 184429 (2020).

167 D. Zhang, X. Hu, T. Chen, D. L. Abernathy, R. Kajimoto, M. Nakamura, M. Kofu, B. J. Foley, M. Yoon, J. J. Choi, S.-H. Lee,
Temporally decoherent and spatially coherent vibrations in metal halide perovskites
Phys. Rev. B, **102** 224310 (2020).

168 H. Tamatsukuri, Y. Murakami, Y. Kuramoto, H. Sagayama, M. Matsuura, Y. Kawakita, S. Matsuishi, Y. Washio, T. Inoshita , N. Hamada, H. Hosono,
Magnetism induced by interlayer electrons in the quasi-two-dimensional electride Y_2C: Inelastic neutron scattering study
Phys. Rev. B, **102** 224406 (2020).

169 S. Gao, F. Xiao, K. Kamazawa, K. Ikeuchi, D. Biner, K. W. Krämer, C. Rüegg, T. Arima,
Crystal electric field excitations in the quantum spin liquid candidate $NaErS_2$
Phys. Rev. B, **102** 024424 (2020).

170 M. Fujita, K. M. Suzuki, S. Asano, H. Okabe, A. Koda, R. Kadono, I. Watanabe,
Magnetic behavior of T′-type Eu_2CuO_4 revealed by muon spin rotation and relaxation measurements
Phys. Rev. B, **102** 045116 (2020).

171 N. Katayama, H. Takeda, T. Yamaguchi, Y. Yamada, K. Iida, M. Takigawa, Y. Ohta, H. Sawa,
Robust atomic orbital in the cluster magnet $LiMoO_2$
Phys. Rev. B, **102** 081106(R) (2020).

172 T. Yamamoto, T. Okudaira, S. Endo, H. Fujioka, K. Hirota, T. Ino, K. Ishizaki, A. Kimura, M. Kitaguchi, J. Koga, S. Makise, Y. Niinomi, T. Oku, K. Sakai, T. Shima, H. M. Shimizu, S. Takada, Y. Tani, H. Yoshikawa, T. Yoshioka,
Transverse asymmetry of γ rays from neutron-induced compound states of ^{140}La
Phys. Rev. C, **101** 064624 (2020).

173 H. Singh, D. Ray, S. Kumar, S. Takata, V. K. Aswal, H. Seto,
Probing the adsorption of nonionic micelles on different-sized nanoparticles by scattering techniques
Phys. Rev. E, **102** 62601 (2020).

174 S. Allenspach, A. Biffin, U. Stuhr, G. S. Tucker, S. Ohira-Kawamura, M. Kofu, D. J. Voneshen, M. Boehm,B. Normand, N. Laflorencie, F. Mila, Ch. Rüegg,
Multiple Magnetic Bilayers and Unconventional Criticality without Frustration in $BaCuSi_2O_6$
Phys. Rev. Lett., **124** 177205 (2020).

175 J. Guo, X. Zhao, S. Ohira-Kawamura, L. Ling, J. Wang, L. He, K. Nakajima, B. Li, Z. Zhang,
Magnetic-field and composition tuned antiferromagnetic instability in the quantum spin-liquid candidate $NaYbO_2$
Phys. Rev. Mater., **4** 64410 (2020).

176 K. Kuramochi, T. Shimano, T. Nishio, H. Okabe, A. Koda, K. Horigane, J. Akimitsu, H. Ogino,
Synthesis and physical properties of the new iridium oxyfluoride $Sr_2Ir(O,F)_{6-d}$ using a topochemical reaction method
Phys. Rev. Mater., **4** 013403 (2020).

177 R. Takahama, T. Ishii, D. Indo, M. Arizono, C. Terakura, Y. Tokura, N. Takeshita, M. Noda, H. Kuwahara, T. Saiki, T. Katsufuji , R. Kajimoto, T. Okuda,
Structural, magnetic, transport and thermoelectric properties of the pseudobrookite $AlTi_2O_5$-Ti_3O_5 system
Phys. Rev. Mater., **4** 074401 (2020).

178 S. Shamoto, Y. Yasui, M. Matsuura, M. Akatsu, Y. Kobayashi, Y. Nemoto, J. Ieda,
Ultralow-energy magnon anomaly in yttrium iron garnet
Phys. Rev. Res., **2** 33235 (2020).

179 T. Nakajima, T. Oda, M. Hino, H. Endo, K. Ohishi, K. Kakurai, A. Kikkawa, Y. Taguchi, Y. Tokura, T. Arima,
Crystallization of magnetic skyrmions in MnSi investigated by neutron spin echo spectroscopy
Phys. Rev. Res., **2** 43393 (2020).

180 K. Nawa, D. Hirai, M. Kofu, K.i Nakajima, R. Murasaki, S. Kogane, M. Kimata, H. Nojiri, Z. Hiroi, T. J. Sato,
Bound spinon excitations in the spin- 1/2 anisotropic triangular antiferromagnet $Ca_3ReO_5Cl_2$
Phys. Rev. Res., **2** 043121(11pages) (2020).

181 Y. Sakaguchi, T. Hanashima, A.-A. A. Simon, M. Mitkova,
Excitation Light Energy Dependence of Silver Photodiffusion into Amorphous Germanium Sulfide: Neutron and X-Ray Reflectivity and X-Ray Diffraction
Phys. Status Solidi. B Basic Solid State Phys., **257** 2000178 (2020).

182 N. Kitamura, Y. Araki, N. Ishida, Y. Idemoto,
Local Structures in Disordered Rocksalt-Type Li_3NbO_4- Based Positive Electrode Materials for a Lithium-Ion Battery
Phys. Status Solidi. B Basic Solid State Phys., **257** 2000112-1-7 (2020).

183 H. Saitoh, A. Machida, T. Hattori, A. Sano-Furukawa, K. Funakoshi, T. Sato, S. Orimo, K. Aoki,
Neutron diffraction study on the deuterium composition of nickel deuteride at high temperatures and high pressures
Physica B Condens. Matter., **587** 412153 (2020).

184 Y. Sue, M. Yotsuzuka, K. Futatsukawa, K. Hasegawa, T. Iijima, H. Iinuma, K. Inami, K. Ishida, N. Kawamura, R. Kitamura, Y. Kondo, T. Mibe, Y. Miyake, T. Morishita, Y. Nakazawa, M. Otani, N. Saito, K. Shimomura, Y. Takeuchi, T. Ushizawa, T. Yamazaki, H. Yasuda,
Development of a bunch-width monitor for low-intensity muon beam below a few MeV
Physical Review Accelerators and Beams, **23** 022804 (2020).

185 S. Meigo, M. Ooi, H. Fujimori,
Two-parameter model for optimizing target beam distribution with an octupole magnet
Physical Review Accelerators and Beams, **23** 062802 (2020).

186 Y. Kimura, M. Ouchi, T. Terashima,
Folded amphiphilic homopolymer micelles in water: uniform self-assembly beyond amphiphilic random copolymers
Polym. Chem., **11** 5156 (2020).

187 D. Ito, Y. Kimura, M. Takenaka, M. Ouchi, T. Terashima,
Single-chain crosslinked polymers via the transesterification of

folded polymers: from efficient synthesis to crystallinity control
Polym. Chem., **11** 5181 (2020).

188 K. Akutsu-Suyama, H. Kira, N. Miyata, T. Hanashima, T. Miyazaki, S. Kasai, D. Yamazaki, K. Soyama, H. Aoki,
Fine-structure analysis of perhydropolysilazane-derived nano layers in deep-buried condition using polarized neutron reflectometry
Polymers, **12** 2180 (2020).

189 S. Makimura, S. Matoba, N. Kawamura,
Status and Future Prospect of Muon Target at J-PARC MLF
PoS (NuFACT2019), **369** 124 (2020).

190 H. Natori,
Development of very slow negative muon beam
PoS (NuFACT2019), **369** 090 (2020).

191 T. Murakawa, K. Kurihara, M. Shoji, C. Shibazaki, T. Sunami, T. Tamada, N. Yano, T. Yamada, K. Kusaka, M. Suzuki, Y. Shigeta, R. Kuroki, H. Hayashi, T. Yano, K. Tanizawa, M. Adachi, T. Okajima,
Neutron crystallography of copper amine oxidase reveals keto/enolate interconversion of the quinone cofactor and unusual proton sharing
Proc. Natl. Acad. Sci. U. S. A., **117** 10818-10824 (2020).

192 Y. Fukuda, Y. Hirano, K. Kusaka, T. Inoue, T. Tamada,
High-resolution neutron crystallography visualizes an OH-bound resting state of a copper-containing nitrite reductase
Proc. Natl. Acad. Sci. U. S. A., **117** 4071-4077 (2020).

193 K. Komatsu, S. Klotz, S. Machida, A. Sano-Furukawa, T. Hattori, H. Kagi,
Anomalous hydrogen dynamics of the ice VII-VIII transition revealed by high-pressure neutron scattering
Proc. Natl. Acad. Sci. U. S. A., **117** 6356-6361 (2020).

194 K. Moriyama, T. Nakatani,
Public cloud-based remote access infrastructure for neutron scattering experiments at MLF, J-PARC
Proceedings of the 17th International Conference on Accelerator and Large Experimental Physics Control Systems, 707-713 (2020).

195 J. Beare, G. Beer, J. H. Brewer, T. Iijima, K. Ishida, M. Iwasaki, S. Kamal, K. Kanamori, N. Kawamura, R. Kitamura, S. Li, G. M. Luke, G. M. Marshall, T. Mibe, Y. Miyake, Y. Oishi, K. Olchanski, A. Olin, M. Otani, M. A. Rehman, N. Saito, Y. Sato, K. Shimomura, K. Suzuki, M. Tabata, H. Yasuda,
Study of muonium emission from laser-ablated silica aerogel
Prog. Theor. Exp. Phys., **2020** 123C01 (2020).

196 K. Hirota, G. Ichikawa, S. Ieki, T. Ino, Y. Iwashita, M. Kitaguchi, R. Kitahara, J. Koga, K. Mishima, A. Morishita, N. Nagakura, H. Oide, H. Okabe, H. Otono, Y. Seki, D. Sekiba, T. Shima, H. M. Shimizu, N. Sumi, H. Sumino, T. Tomita, H. Uehara, T. Yamada, S. Yamashita, M. Yokohashi, T. Yoshioka,
Neutron lifetime measurement with pulsed cold neutrons
Prog. Theor. Exp. Phys., **2020** 123C02 (2020).

197 T. Tanaka, K. Hagiwara, E. Gazzola, A. Ali, I. Ou, T. Sudo, P. K. Das, M. S. Reen, R. Dhir, Y. Koshio, M. Sakuda, A. Kimura, S. Nakamura, N. Iwamoto, H. Harada, G. Collazuol, S. Lorenz, M. Wurm, W. Focillon, M. Gonin, T. Yano,
Gamma-ray spectra from thermal neutron capture on gadolinium-155 and natural gadolinium
Progress of Theoretical and Experimental Physics, **2020** 043D02 (2020).

198 A. Momose, H. Takano, Y. Wu, K. Hashimoto, T. Samoto, M. Hoshino, Y. Seki, T. Shinohara,
Recent Progress in X-ray and Neutron Phase Imaging with Gratings
Quantum Beam Science, **4** 9 (2020).

199 O. Takahashi, Y. Shibui, P. G. Xu, S. Harjo, T. Suzuki, Y. Tomota,
Microstructural Features and Ductile-Brittle Transition Behavior in Hot-Rolled Lean Duplex Stainless Steels
Quantum Beam Science, **4** 16 (2020).

200 Y. Wang,
Phase Stress Measurement of Centrifugally Cast Duplex Stainless Steel by Neutron Diffraction
Quantum Beam Science, **4** 28 (2020).

201 Y. Noda, H. Izunome, T. Maeda, T. Inada, S. Ueda, S. Koizumi,
The Large-Area Detector for Small-Angle Neutron Scattering on iMATERIA at J-PARC
Quantum Beam Science, **4** 32 (2020).

202 Y. Noda, T. Maeda, T. Oku, S. Koizumi, T. Masui, H. Kishimoto,
First Experiment of Spin Contrast Variation Small-Angle Neutron Scattering on the iMATERIA Instrument at J-PARC
Quantum Beam Science, **4** 33 (2020).

203 K. Nakagawa, M. Hayashi, K. Takano-Satoh, H. Matsunaga, H. Mori, K. Maki, Y. Onuki, S. Suzuki, S. Sato,
Characterization of Dislocation Rearrangement in FCC Metals during Work Hardening Using X-ray Diffraction Line-Profile Analysis
Quantum Beam Science, **4** 36 (2020).

204 S. Koizumi, Y. Noda, T. Maeda, T. Inada, S. Ueda, T. Fujisawa, H. Izunome, R. A. Robinson, H. Frielinghaus,
Advanced Small-Angle Scattering Instrument Available in the Tokyo Area. Time-of-Flight, Small-Angle Neutron Scattering Developed on the iMATERIA Di ractometer at the High Intensity Pulsed Neutron Source J-PARC
Quantum Beam Science, **4** 42 (2020).

205 Y. Onuki, S. Sato,
In Situ Observation for Deformation-Induced Martensite Transformation (DIMT) during Tensile Deformation of 304 Stainless Steel Using Neutron Diffraction. PART I: Mechanical Response
Quantum Beam Science, **4** 44227 (2020).

206 V. Sonnenschein, Y. Tsuji, S. Kokuryu, W. Kubo, S. Suzuki, H. Tomita, Y. Kiyanagi, T. Iguchi, T. Matsushita, N. Wada, M. Kitaguchi, H. M. Shimizu, K. Hirota, T. Shinohara, K. Hiroi, H. Hayashida, W. Guo, D. Ito, Y. Saito,
An experimental setup for creating and imaging $^4He_2^*$ excimer cluster tracers in superfluid Helium-4 via neutron-^{3}He absorption reaction
Rev. Sci. Instrum., **91** 33318 (2020).

207 T. Shinohara , T. Kai , K. Oikawa , T. Nakatani, M. Segawa, K. Hiroi, Y. Su, M. Ooi, M. Harada, H. Iikura, H. Hayashida, J. D. Parker , Y. Matsumoto, T. Kamiyama, H. Sato, Y. Kiyanagi,
The energy-resolved neutron imaging system, RADEN
Rev. Sci. Instrum., **91** 043302 (2020).

208 K. Arai, Y. Horikawa, T. Shikata, H. Iwase,
Reconsideration of the conformation of methyl cellulose and hydroxypropyl methyl cellulose ethers in aqueous solution
RSC Adv., **10** 19059 (2020).

209 M. Naeem, H. He, F. Zhang, H. Huang, S. Harjo, T. Kawasaki, B. Wang, S. Lan, Z. Wu, F. Wang,
Cooperative deformation in high-entropy alloys at ultralow temperatures
Sci. Adv., **6** eaax4002 (2020).

210 Y. K. Kshetri, T. Kamiyama, S. Torii, S. H. Jeong, T.-H. Kim, H. Choi, J. Zhou, Y. P. Feng, S. W. Lee,
Electronic structure, thermodynamic stability and high temperature sensing properties of Er-a-SiAlON ceramics
Sci. Rep., **10** 4952 (2020).

211 H. Saitoh, A. Machida, R. Iizuka-Oku, T. Hattori, A. Sano-Furukawa,

K. Funakoshi, T. Sato, S. Orimo, K. Aoki,
Crystal and Magnetic Structures of Double Hexagonal Close-Packed Iron Deuteride
Sci. Rep., **10** 9934 (2020).

212 S. Sato, S. Irie, Y. Nagamine, T. Miyazaki, Y. Umeda,
Antiferromagnetism in perfectly ordered $L1_0$-MnAl with stoichiometric composition and its mechanism
Sci. Rep., **10** 12489 (2020).

213 S. Yamamoto, K. Ninomiya, N. Kawamura, Y. Hirano,
Optical imaging of muons
Sci. Rep., **10** 20790 (2020).

214 R. Inoue, T. Oda, H. Nakagawa, T. Tominaga, T. Saio, Y. Kawakita, M. Shimizu, A. Okuda, K. Morishima, N. Sato, R. Urade, M. Sato, M. Sugiyama,
Dynamics of proteins with different molecular structures under solution condition
Sci. Rep., **10** 21678 (2020).

215 W. Woo, J. S. Jeong, D.-K. Kim, C. M. Lee, S.-H. Choi, J.-Y. Suh, S. Y. Lee, S. Harjo, T. Kawasaki,
Stacking Fault Energy Analyses of Additively Manufactured Stainless Steel 316L and CrCoNi Medium Entropy Alloy Using In Situ Neutron Diffraction
Sci. Rep., **10** 43845 (2020).

216 E. Shoji, S. Isogai, R. Suzuki, M. Kubo, T. Tsukada, T. Kai, T. Shinohara, Y. Matsumoto, H. Fukuyama,
Neutron computed tomography of phase separation structures in solidified CuCo alloys and investigation of relationship between the structures and melt convection during solidification
Scr. Mater., **175** 29 (2020).

217 T. Yamashita,S. Morooka, S. Harjo, T. Kawasaki, N. Koga, O. Umezawa,
Role of retained austenite in low alloy steel at low temperature monitored by neutron diffraction
Scr. Mater., **177** 43992 (2020).

218 K. Cho, R. Morioka, S. Harjo, T. Kawasaki, H. Y. Yasuda,
Study on formation mechanism of {332} < 113 > deformation twinning in metastable β-type Ti alloy focusing on stress-induced α"martensite phase
Scr. Mater., **177** 106-111 (2020).

219 Z. Deng, K. Chu, Q. Li, Y. Onuki, Q. Sun,
Elinvar property of cold-rolled NiTi alloy
Scr. Mater., **187** 197-201 (2020).

220 M. Naeem, H. He, S. Harjo, T. Kawasaki, F. Zhang, B. Wang, S. Lan, Z. Wu, Y. Wu, Z. Lu,
Extremely high dislocation density and deformation pathway of CrMnFeCoNi high entropy alloy at ultralow temperature
Scr. Mater., **188** 21-25 (2020).

221 N. Ishida, Y. Nakamura, T. Mandai, N. Kitamura, Y. Idemoto,
Synthesis, cathode property and crystal, electronic and local structures of $Mg_2Mo_3O_8$ as Mg rechargeable battery cathode material
Solid State Ion., **354** 115413 (2020).

222 R. Li, Z. Liu, L. Li, J. Huang, T. Yamada, V. G. Sakai, P. Tan, L. Hong,
Anomalous sub-diffusion of water in biosystems: From hydrated protein powders to concentrated protein solution to living cells
Struct. Dyn., **7** 054703 (2020).

223 J. Kim, S. Yamanaka, I. Murayama, T. Katou, T. Sakamoto, T. Kawasaki, T. Fukuda, T. Sekino, T. Nakayama, M. Takeda,
Pyroelectric power generation from the waste heat of automotive exhaust gas
Sustain. Energy Fuels, **4** 1143 (2020).

224 Y. Onuki, T. Masumura, T. Tsuchiyama, S. Sato, T. Tomida, S. Takaki,
Mutual Verification of Phase Fraction Analysis Techniques for Steels Comprising Deformation Induced Martensite Phases: Neutron-Diffraction-Based Rietveld Texture Analysis and Saturation Magnetization Measurement
Tetsu to Hagane, **106** 457 (2020).

225 Y. Hosoya, Y. Matsumura, Y. Tomota, Y. Onuki, S. Harjo,
Mechanism of improved ductility of 1,500 MPa-class ultra-high strength cold-rolled steel sheet produced by rolling and partitioning method
Tetsu to Hagane, **106** 154-164 (2020).

226 Y. Tomota, Y. X. Wang, T. Ohmura, N. Sekido, S. Harjo, T. Kawasaki, W. Gong, A. Taniyama,
In situ Neutron Diffraction on Ferrite and Pearlite Transformations for a 1.5Mn-1.5Si-0.2C Steel
Tetsu to Hagane, **106** 262-271 (2020).

227 Y. Sakaguchi, T. Hanashima, A.-A. A. Simon, M. Mitkova,
Silver photodiffusion into amorphous Ge chalcogenides - Excitation photon energy dependence of the kinetics probed by neutron reflectivity
The European Physical Journal Applied Physics, **90** 30101 (2020).

228 Y. Sakaguchi, K. Tamura,
Photo-induced effects on amorphous and liquid selenium by pulsed laser illumination -Photo-induced structural changes in a network of selenium chains
Z. Phys. Chem., **235** 189-212 (2020).

Editorial Board - MLF Annual Report 2020

Chief Editor
Kazuhiro Akutsu
CROSS

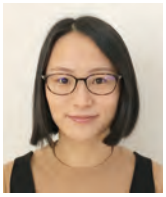

Yuhua Su
Technology Development Section

Kazuki Iida
CROSS

Takashi Naoe
Neutron Source Section

Miho Igarashi
CROSS

Yukinori Nagatani
Muon Science Section

Takashi Ino
Neutron Science Section

Takeshi Matsukawa
Ibaraki University

Kenichi Oikawa
Neutron Science Section

Dai Yamazaki
Neutron Instrumentation Section

J-PARC

JAPAN PROTON ACCELERATOR RESEARCH COMPLEX

High Energy Accelerator Research Organization (KEK)
Japan Atomic Energy Agency (JAEA)

http://j-parc.jp/

Materials and Life Science Division
J-PARC Center

https://mlfinfo.jp/en

CROSS

Comprehensive Research Organization for Science and Society

https://neutron.cross.or.jp/en

J-PARC 21-02